



Provided by the author(s) and University of Galway in accordance with publisher policies. Please cite the published version when available.

Title	Wave-structure interaction of offshore wave energy converters
Author(s)	Finnegan, William
Publication Date	2013-11-04
Publication Information	Finnegan, William. (2013). Wave-structure interaction of offshore wave energy converters.
Item record	http://hdl.handle.net/10379/5898

Downloaded 2024-04-18T00:54:16Z

Some rights reserved. For more information, please see the item record link above.



Wave-structure interaction of offshore wave energy converters

by William Finnegan

Supervisor: Dr. Jamie Goggins



A thesis submitted in partial fulfillment of the requirements for the degree of
Doctor of Philosophy,
in the College of Engineering and Informatics

01-11-2013

Abstract

With the continuing rise in oil prices and greater concern for the damage to the atmosphere, the world is continually looking for a cleaner and more sustainable form of energy. Ocean wave energy as a renewable source of energy, which as of yet is relatively unexploited, offers a possible solution to this energy crisis. The concept of harnessing ocean wave energy is by no means a new idea. However, the topic only gained international interest in the 1970s with the publication of Stephen Salter's ground-breaking paper on his Wave Energy Duck.

The current research study aims to aid the exploitation of this resource by developing robust and reliable analytical and numerical models. These numerical models will provide a platform for designers to optimise their marine renewable energy devices, in particular wave energy converters, before venturing into large scale physical testing, which is a very costly procedure. Therefore, the main objective associated with the current research is to develop numerical models which can accurately perform the interaction between an ocean wave and a structure to assist in the design of wave energy converters. However, in order to achieve this, two subtasks must be completed, which are: (1) to derive an analytical approximation in order to determine the wave excitation forces on a floating truncated cylinder in water of infinite depth and (2) to develop a computational fluid dynamics numerical model for a wave tank that can accurately simulate interaction between an irregular water wave and a floating structure.

In the derivation of the analytical approximation, the method of separation of variables was employed in solving the appropriate boundary value problem to derive the velocity potentials. Graphical representations of the analytical approximation for the truncated vertical cylinder and the cylinder of infinite depth are presented. The presented analytical approximation was found to be in good agreement when compared with the results from computational fluid dynamics analysis, using a commercial boundary element package, and with independent experimental data. The novel contribution of the presented analytical approximation is that it provides a solution which is far easier to use and implement than already available analytical solutions.

A methodology for developing a numerical model for a wave tank, commonly known as a numerical wave tank (NWT), that can accurately simulate linear regular waves and perform linear wave-structure interaction was then derived. In the current study, the finite volume commercial software ANSYS CFX, which uses a solver based on the Reynolds-averaged Navier-Stokes equations, was used to perform the numerical analysis. This methodology was validated by comparing the outputs to physical experimental studies performed using the in-house wave flume and good agreement between the two were found. The state-of-the-art contribution is the methodology for the development of an optimum numerical model of a wave tank, in terms of the desired wave period generated.

The numerical model was then advanced in order to generate linear irregular water waves. The waves generated are simulated measured real sea waves, which were recorded at the Atlantic marine energy test site (AMETS) off the west coast of Ireland. Finally, a breakwater type floating structure was introduced into the model to explore the interaction between an irregular ocean wave and a structure. The results of this study were found to be in good agreement with the prediction from a hydrodynamic analysis of the structure. The ability of the model to accurately model measured ocean waves and their interaction with a floating structure is the novel aspect here.

Finally, numerical CFD models were developed to aid in the design of offshore wave energy converters (WECs). One application is in the development of a methodology to optimise the dynamic heave response of the floating oscillating part of the WEC through

form finding of the geometric configuration of its structure. The state-of-the-art aspect lies within the methodology itself. It offers a designer a method of optimising the performance of a WEC, in terms of its geometric configuration, at a given location using a single wave energy spectrum as the input. In this study, the wave energy spectrum was derived from three years of data recorded at the Atlantic marine energy test site.

Table of contents

Abstract	iii
Table of contents	vi
List of tables	xii
List of figures.....	xiii
Declarations	xxiii
Acknowledgments.....	xxiv
Nomenclature	xxvi
Chapter 1 Introduction	1
1.1 General introduction	2
1.2 Harnessing of ocean wave energy	4
1.2.1 Ocean wave energy in an Irish context.....	4
1.2.2 Current ocean wave energy technologies	5
1.3 Scope and objectives of the current research	10
1.4 List of publications produced as part of the current study	11
1.5 Structure of the thesis	13
Chapter 2 Literature review.....	15
2.1 Introduction.....	16

2.2	Airy's linear wave theory	16
2.3	Energy in an ocean wave.....	19
2.3.1	Wave energy spectrum.....	21
2.4	Hydrodynamic force on a structure	23
2.4.1	Equation of motion.....	23
2.4.2	Water-wave problem.....	25
2.4.3	Formulation of radiation problem	27
2.4.4	Formulation of scattering problem.....	30
2.5	Analytical wave-structure interaction studies.....	32
2.6	Numerical simulation of linear regular and irregular waves and the interaction of these with structures.....	34
2.7	Linear regular and irregular wave generation and wave-structure interaction through physical experiments	37
2.8	Optimisation of wave energy converters.....	42
2.9	Summary.....	44
Chapter 3 The wave excitation forces on a truncated vertical cylinder in water of infinite depth		45
3.1	Introduction.....	46
3.2	Methodology.....	46
3.2.1	Derivation of velocity potential for the interior domain	50
3.2.2	Derivation of velocity potential in the exterior domain	51
3.2.3	Analytical approximations for the coefficient $q_{m,0}$ and functions $p_m(\xi)$ and $q_m(\xi)$	54
3.3	Results.....	58
3.3.1	Wave excitation forces on a truncated cylinder	59

3.3.2	Wave excitation forces on a cylinder of infinite depth.....	67
3.4	Discussion and conclusions	69
Chapter 4	Development of a numerical model for a wave tank.....	72
4.1	Introduction.....	73
4.2	Methodology.....	74
4.2.1	Wave generation techniques	76
4.2.2	Wave energy dissipation.....	78
4.2.3	The governing equations.....	78
4.2.4	Optimisation of the length/height of the model.....	79
4.2.5	Optimisation of the mesh for the model.....	81
4.2.6	Time-step interval and total time.....	83
4.3	Results	85
4.3.1	Beach slope study.....	85
4.3.2	Validation of CFD wave with LWT.....	87
4.3.3	Validation of CFD wave with WMT.....	91
4.3.4	Comparison of turbulence models	94
4.3.5	Scaling laws in deep water wave modelling.....	94
4.4	Time-domain wave-structure interaction	96
4.4.1	Introduction	96
4.4.2	Wave-structure interaction in a numerical model for a wave tank	96
4.4.3	Analysis of a floating structure.....	97
4.4.3.1	Analysis with floating structure held in a fixed position.....	98
4.4.3.2	Analysis when the floating structure is allowed to oscillate	101
4.5	Discussions and conclusions.....	104

Chapter 5 Frequency-domain wave-structure interaction using CFD	106
5.1 Introduction	107
5.2 BEM analysis methodology	107
5.3 Properties calculation for a vertically axisymmetric structure	108
5.4 Mathematical formulation of the BEM	110
5.5 Determining the locations of high stresses on a floating structure to aid in the structural health monitoring of wave energy converters	113
5.5.1 Introduction	113
5.5.2 Methodology for identifying locations of high stress.....	114
5.5.3 Case study of a floating WEC.....	115
5.5.4 Discussions and conclusions.....	120
5.6 Structural dynamics of a heaving two-body wave energy converter	123
5.6.1 Introduction	123
5.6.2 Mathematical formulation	124
5.6.3 Mooring system design	127
5.6.4 Case study	128
5.6.5 Discussion and conclusions	131
Chapter 6 Validation of numerical models using experimental data	133
6.1 Introduction.....	134
6.2 NUI Galway experimental wave flume.....	135
6.3 Determining the parameters associated with the NUI Galway wave flume	138
6.4 Validation of NWT model for wave generation.....	142
6.4.1 NWT model of NUI Galway experimental wave flume.....	142
6.4.2 Comparison of numerical and experimental output.....	143

6.5	Validation of NWT model for wave-structure interaction.....	147
6.5.1	Experimental floating structure set-up.....	147
6.5.2	NWT model of floating structure.....	149
6.5.3	Comparison of numerical and experimental output.....	150
6.6	Discussions and conclusion.....	154
Chapter 7	Irregular linear wave generation in a numerical wave tank.....	156
7.1	Introduction.....	157
7.2	Methodology.....	158
7.2.1	CFD model set-up.....	160
7.2.2	CFD input wave.....	162
7.3	Results of linear irregular wave generation.....	165
7.4	Interaction of a structure with a linear irregular wave.....	173
7.5	Discussion and conclusions.....	179
Chapter 8	Shape optimisation of a floating wave energy converter.....	181
8.1	Introduction.....	182
8.2	Wave energy and data processing.....	183
8.2.1	Wave energy.....	183
8.2.2	Estimating the wave energy spectrum at a given location.....	191
8.3	Geometrical shape optimisation.....	193
8.3.1	Geometric configuration optimisation methodology.....	195
8.3.2	Case study and findings.....	198
8.4	Mean power output calculation.....	204
8.5	Discussion and conclusions.....	207
Chapter 9	Conclusions and recommendations for further work.....	209

9.1	Introduction	210
9.2	Summary and conclusions	210
9.2.1	The wave excitation force on a floating truncated vertical cylinder in water of infinite depth.....	211
9.2.2	Development of a numerical wave tank.....	212
9.2.3	Linear regular wave-structure interaction using computational fluid dynamics 213	
9.2.4	Validation of numerical models using experimental data.....	213
9.2.5	Irregular linear wave generation in a numerical wave tank	214
9.2.6	Shape optimisation of a floating wave energy converter.....	214
9.2.7	Overview of the impact of current research study	215
9.3	Recommendations for further work.....	216
9.3.1	Analytical approximations using similar techniques.....	216
9.3.2	3-D the interaction between an irregular ocean wave and a structure in a NWT 217	
9.3.3	Structural health monitoring of WEC's	217
9.3.4	The experimental wave flume at NUI Galway.....	217
	References	220
	Appendix A Full analytical derivation of the unknown functions for the wave excitation forces on a truncated vertical cylinder in water of infinite depth	229
	Appendix B MATLAB code for the analytical approximation.....	235
	Appendix C Time-domain comparison between the analytical approximation and results from the CFD analysis	238
	Appendix D Validation comparison of NWT model and experimental data	243
	Appendix E Shape optimisation algorithm programme code.....	254

List of tables

Table 4.1: Summary of parametric study of mesh set-up	82
Table 4.2: Summary of applicable scaling factors in deep water wave modelling.....	95
Table 6.1: Summary of breaking limit of waves study, where T is the minimum wave period to induce wave breaking at a given stroke length, S . The average value and coefficient of variation, c_v , are included.	141
Table 6.2: Summary of comparison of NWT model and experimental results.....	145
Table 8.1: Number of occurrences of significant wave height and average wave period at AMETS for 2010.	187
Table 8.2: Number of occurrences of significant wave height and average wave period at AMETS for 2011.	189
Table 8.3: Number of occurrences of significant wave height and average wave period at AMETS for 2012.	190
Table 8.4: Description of the various geometry options in the geometry library.....	196
Table 8.5: Matrix representation of the mean power output (in Watts per year) for the optimum structural configuration at AMETS for 2010 to 2012.....	207

List of figures

Figure 1.1: Approximate wave power levels in kW/m of wave front (Thorpe, 1999).	4
Figure 1.2: Summary of the various wave energy converters, image reproduced from Falcão (2010).	6
Figure 1.3: Schematic of the AWS working principle, where the arrows describe the pressure on the floater. (Adapted from: Beirao et al. (2007)).....	8
Figure 1.4: Elevation of the Pelamis WEC (Henderson, 2006).....	8
Figure 1.5: Plan: Main components of the Wave Dragon. Section: Basic principle of the Wave Dragon. (Adapted from: Kofoed et al. (2006)).....	9
Figure 2.1: Mathematical summary of Airy’s linear wave theory.	18
Figure 2.2: Part of a sinusoidal gravity wave in deep water. λ is wavelength; H is trough to crest height; Cgc is centre of gravity of the crest of the wave; CgT is centre of gravity of the trough of the wave. Adapted from Salter (1974).	21
Figure 2.3: Six degrees of freedom of a floating structure; surge(1), sway(2), heave(3), roll(4), pitch(5) and yaw(6). Reproduced from: Falnes (2002).	24
Figure 2.4: Illustration of the unit normal vector, n , and the displacement vector, u , of a floating structure. Included is the polar cylindrical coordinate system used.	27
Figure 2.5: Free surface wave fields around a ship hull derived from a numerical simulation by Mousaviraad et al. (2010).	36

Figure 2.6: Experimental setups of various studies which have been described in this section. (a): Overview schematic of Akyildiz (2002) (b): Pulley and structure schematic of Stallard et al. (2009) (c): Fixed cylinder rig of Fonseca et al. (2011).	41
Figure 2.7: Hull shape optimisation framework used by Birk and Claus (2001).	43
Figure 3.1: Definition sketch for the boundary value problem for a truncated vertical cylinder.	47
Figure 3.2: The normalised surge (or horizontal) excitation force, which is normalised by $\pi\rho g A a^2$, as a function of $k_0 a = \omega^2 a/g$, for various draft-to-radius ratios compared to a numerical CFD analysis (ANSYS AQWA). The shaded region denotes where a valid solution is possible.	61
Figure 3.3: The phase angle for surge and heave, in the frequency domain, as a function of $k_0 a = \omega^2 a/g$, compared to a numerical analysis	62
Figure 3.4: The normalised heave (or vertical) excitation force, which is normalised by $\pi\rho g A a^2$, as a function of $k_0 a = \omega^2 a/g$, for various draft-to-radius ratios compared to a numerical CFD analysis (ANSYS AQWA). The shaded region denotes where a valid solution is possible.	62
Figure 3.5: The normalised pitch (or torque) excitation force, which is normalised by $\pi\rho g A a^3$, as a function of $k_0 a = \omega^2 a/g$, for various draft-to-radius ratios.	64
Figure 3.6: The normalised surge (or horizontal) excitation force, which is normalised by $\pi\rho g A a^2$, as a function of $k_0 a = \omega^2 a/g$, for various draft-to-radius ratios compared to Bhatta and Rahman (1995; 2003) and to the corresponding numerical CFD analysis (ANSYS AQWA).	65
Figure 3.7: The normalised heave (or vertical) excitation force, which is normalised by $\pi\rho g A a^2$, as a function of $k_0 a = \omega^2 a/g$, for various draft-to-radius ratios compared to Bhatta and Rahman (1995; 2003) and to the corresponding numerical CFD analysis (ANSYS AQWA).	66

Figure 3.8: Comparison of the normalised heave and surge wave excitation forces, which is normalised by $\pi\rho g A d^2$ with the experimental results of Fonseca et al. (2011) , as a function of $k_0 a = \omega^2 a/g$. The draft-to-radius ratio, $b/a = 0.62$	67
Figure 3.9: Normalised surge excitation force, which is normalised by $\pi\rho g A d^2$, as a function of $k_0 a = \omega^2 a/g$, and compared to the results from a finite depth numerical CFD analysis (ANSYS AQWA).	69
Figure 4.1: Overall dimensions of model. S , H and d are discussed in Section 4.2 and ‘ <i>Device Diameter</i> ’ refers to the horizontal length of the structure being analysed.....	74
Figure 4.2: Physical wavemakers explored in this study (a) the paddle-type (b) flap-type (c) wedge-shaped plunger-type.	77
Figure 4.3: Minimum still water level as the wave period varies.	81
Figure 4.4: Comparison of wave elevation at 5 m, or $3d$, from the wavemaker for various mesh set-ups given in Table 4.1.	82
Figure 4.5: Typical longitudinal elevation of the mesh for CFD model with refinement along the SWL, which is illustrated in the schematic.....	83
Figure 4.6: The normalised amplitude wave profile for various wave periods at a distance $3d$ from the wavemaker for the first ten cycles.....	84
Figure 4.7: Results from a parametric study comparing the effect of the time-step on the wave height for a wave period of 1.35s.....	85
Figure 4.8: A comparison of the wave elevations for various beach slopes at 1.5m from the beach along the still water level.....	86
Figure 4.9: A comparison of the wave elevation at 5m from the wavemaker and 1.5m from the end of the beach.	87
Figure 4.10: For a wave period of 5 s and a wave height of 1.12 m (i.e. $0.03L_0$) and at a distance of 60 m, or $3d$ from the wavemaker (a) Comparison of wave elevations of CFD generated wave to a linear wave (b) Comparison of CFD water velocity to LWT velocity for deep water.	89

Figure 4.11: For a wave period of 8 s and a wave height of 2.92 m (i.e. $0.03L_0$) and at a distance of 150 m, or $3d$ from the wavemaker (a) Comparison of wave elevations of CFD generated wave to a linear wave (b) Comparison of CFD water velocity to LWT velocity for deep water. 90

Figure 4.12: Comparison of CFD results to wavemaker theory (WMT) for the wavemaker flap hinged at the base of the model. 91

Figure 4.13: Comparison of CFD results to wavemaker theory (WMT) with the wavemaker hinged at a height, $l = 0.5d$, from the base of the model. 92

Figure 4.14: The wave-structure interaction from CFD analysis (ANSYS CFX) after 24 s. The free surface and a fixed truncated cylinder are shown. 97

Figure 4.15: Time domain comparison between the heave excitation forces obtained from the analytical approximation presented in Chapter 3 (Eqn. (3.45)) and CFD models with $k_0a = 0.3$, where (a): $b = a$ and (b): $b = a/2$ and the mass of the structure is 47 kg and 23 kg, respectively. 99

Figure 4.16: Time domain comparison between the heave excitation forces obtained from the analytical approximation presented in Chapter 3 (Eqn. (3.45)) and CFD models with $k_0a = 0.6$, where (a): $b = a$ and (b): $b = a/2$ and the mass of the structure is 336 kg and 168 kg, respectively. 100

Figure 4.17: Comparison of the normalised vertical, or heave, excitation force for the analytical approximation presented in Chapter 3 (Eqn. (3.45)), the solution of Bhatta and Rahman (1995, 2003) and CFD models with ratios of $a = b$ and $a = 2b$ 101

Figure 4.18: Summary of the various forces on a floating truncated vertical cylinder with $a=b$, which is allowed to oscillate in a vertical, or heave, motion from the numerical CFD analysis (ANSYS CFX). 103

Figure 4.19: The incident wave and the dynamic response of a floating truncated vertical cylinder with $a=b$, which is allowed to oscillate in a vertical, or heave, motion from the numerical CFD analysis (ANSYS CFX). 103

Figure 5.1: The normalised hydrodynamic coefficients for the case study using ANSYS AQWA.....	116
Figure 5.2: The normalised wave excitation forces, in the heave and surge motion, for the case study using ANSYS AQWA.....	116
Figure 5.3: The normalised dynamic response, and its phase angle, for the case study using ANSYS AQWA.....	117
Figure 5.4: The normalised maximum pressure (Eqn. (5.22)) and depth at which it occurs below the still water level against wave frequency. Derived from the ANSYS AQWA analysis of the structure.	117
Figure 5.5: Hydrodynamic pressure distribution on the structure when it is oscillating at resonance with an incident wave coming from left to right. (a): Front elevation (b): Right end elevation (c): Left end elevation (Units in N/m^2). Structure analysed using ANSYS AQWA.	119
Figure 5.6: The maximum stress and the locations at which it occurs for incident waves of different frequencies. (a): $f = 0.04$ Hz (b): $f = 0.08$ Hz (c): $f = 0.12$ Hz (Units in N/m^2). Structure analysed using ANSYS AQWA.	122
Figure 5.7: Free body diagram of the two-body system where only heaving motions are being considered.....	124
Figure 5.8: Restoring force of the mooring lines on the WEC	128
Figure 5.9: The hydrodynamic analysis, using BEM (ANSYS AQWA), for the floating buoy and intermediate buoy, detailing (a): the added mass (b): the wave radiation damping (c): the heave excitation force.....	130
Figure 5.10: The response amplitude operator for each of the buoys and the relative response.....	131
Figure 6.1: The experimental wave flume located at the National University of Ireland, Galway.	135

Figure 6.2: Schematic of the experimental wave flume at NUI Galway (Including positioning of wave elevation probes). Dimensions are in mm.....	137
Figure 6.3: Linear relation between the output voltage and the wave elevation which was determined during the calibration of the wave elevation gauges.	138
Figure 6.4: Normalised comparison of wave height and wave length for different stroke lengths and the experimental estimated wavemaker relation for (a) 2.35m and (b) 4.75m from the wavemaker.....	140
Figure 6.5: Normalised comparison between the experimental estimate for wavemaker relation and the results of the CFD numerical model for a wave tank for (a) 2.35 m and (b) 4.75 m from the wavemaker.....	144
Figure 6.6: Comparison between the output from the NWT model and the experimental output from the NUIG wave flume, for $S = 240$ mm and $T = 1.2$ s, at a distance from the wavemaker: (a): 2.35 m and (b) 4.75 m.....	146
Figure 6.7: Schematic of the laboratory set up for the floating structure, including horizontal mooring lines. (a) Section A-A. (b) Plan of structure. Dimensions are in mm.....	149
Figure 6.8: Comparison between experimental results and BEM hydrodynamic analysis using ANSYS AQWA.....	151
Figure 6.9: Comparison between the results from the numerical model and the experimental simulation for an incident wave with a period of 1.2 s and a height of 37mm.	152
Figure 6.10: Comparison between the experimental test and the numerical simulation at Top: 13.2 s. Middle: 13.5 s. Bottom: 13.9 s.	153
Figure 7.1: Map showing the location of the wave data buoy at AMETS, Ireland. Adapted from: (Marine Institute, 2012).....	158
Figure 7.2: Typical longitudinal elevation of the mesh for CFD model with refinement along the SWL. Included is a schematic of the location of the wave input boundary, the SWL and the dissipation zone.	161

Figure 7.3: Measured wave elevation at AMETS beginning at: (a) 10:30 on 17-12-2010 (b) 4:30 on 04-10-2010 and (c) 17:00 on 02-09-2011.....	166
Figure 7.4: Comparison between the measured wave at AMETS and the filtered analytical approximation beginning at: (a) 10:30 on 17-12-2010 (b) 4:30 on 04-10-2010 and (c) 17:00 on 02-09-2011.....	168
Figure 7.5: Comparison between the filtered analytical approximation wave and the output wave from the CFD model beginning at: (a) 10:30 on 17-12-2010 (b) 4:30 on 04-10-2010 and (c) 17:00 on 02-09-2011.....	170
Figure 7.6: Longitudinal wave profile along the full length of the wave tank for different time-steps for the simulation of the wave record beginning at 10:30 on 17-12-2010 (beginning at 115.4 s in equal time intervals of 3 s).....	171
Figure 7.7: Comparison between the wave energy spectrum of the measured wave and output wave from CFD model beginning at: (a) 10:30 on 17-12-2010 (b) 4:30 on 04-10-2010 and (c) 17:00 on 02-09-2011.....	173
Figure 7.8: Wave profile and dynamic response of the structure for different time steps beginning at 17:00 on 02-09-2011 (beginning at 128.4 s in equal 4 s time intervals).....	175
Figure 7.9: The normalised heave motion dynamic response and associated phase angle from the hydrodynamic analysis of the structure.....	177
Figure 7.10: Comparison of the heave motion dynamic response of the rectangular prism from the CFD NWT analysis and analytical hydrodynamic analysis beginning at: (a) 10:30 on 17-12-2010 (b) 4:30 on 04-10-2010 and (c) 17:00 on 02-09-2011.....	178
Figure 8.1: Probability of occurrence at AMETS for 2010, 2011 and 2012 of (a): average wave period and (b): significant wave height.....	186
Figure 8.2: Surface chart representation of the wave power level, in kWh/m year, for significant wave height and average wave period at AMETS for 2010.....	187
Figure 8.3: Surface chart representation of the wave power level, in kWh/m year, for significant wave height and average wave period at AMETS for 2011.....	188

Figure 8.4: Surface chart representation of the wave power level, in kWh/m year, for significant wave height and average wave period at AMETS for 2012.	188
Figure 8.5: The monthly average significant wave height at AMETS for 2010, 2011 and 2012.	189
Figure 8.6: The monthly average wave period at AMETS for 2010, 2011 and 2012.....	190
Figure 8.7: Wave energy spectra for AMETS for 2010, 2011 and 2012 and the resulting average spectrum for the site, which are calculated using Eqn. (8.11). A modified P-M spectrum for AMETS, using Eqn. (8.8), is also included.	193
Figure 8.8: Flowchart of the shape optimisation procedure.....	197
Figure 8.9: The significant force as a function of radius for the average spectrum over a two year period (2010-2011) for AMETS obtained by imposing the following maximum restrictions on the RAO: (a): no restriction, (b): a restriction of 5, (c): a restriction of 4, (d): a restriction of 3.	200
Figure 8.10: The significant force as a function of radius for the 2010 spectrum for AMETS with no restriction on the maximum value of RAO, which also details the optimum geometric shapes as the radius is varied.	201
Figure 8.11: The significant force as a function of radius for the 2011 spectrum for AMETS with no restriction on the maximum value of RAO, which also details the optimum geometric shapes as the radius is varied.	202
Figure 8.12: The significant force as a function of radius for the 2012 spectrum for AMETS with no restriction on the maximum value of RAO, which also details the optimum geometric shapes as the radius is varied.	202
Figure 8.13: The dynamic response spectrum of the optimum structure for an input of the average wave energy spectrum for AMETS. The wave height spectrum is also displayed and, both, have a frequency step, $\Delta f = 0.005$ Hz.....	203
Figure 8.14: Variation of the response amplitude operator for various values of the PTO damping coefficient, b_r	206

Figure 8.15: Variation of mean power output for a range of values of the PTO damping coefficient.	206
Figure C.1: Time domain comparison between the heave excitation forces obtained from the analytical and CFD models with $k_{\theta a} = 0.8$, where (a): $b = a$ and (b): $b = a/2$	239
Figure C.2: Time domain comparison between the heave excitation forces obtained from the analytical and CFD models with $k_{\theta a} = 1$, where (a): $b = a$ and (b): $b = a/2$	240
Figure C.3: Time domain comparison between the heave excitation forces obtained from the analytical and CFD models with $k_{\theta a} = 1.25$, where (a): $b = a$ and (b): $b = a/2$	241
Figure C.4: Time domain comparison between the heave excitation forces obtained from the analytical and CFD models with $k_{\theta a} = 1.5$, where (a): $b = a$ and (b): $b = a/2$	242
Figure D.1: Comparison between the output from the NWT model and the experimental output from the NUIG wave flume, for $S = 240\text{mm}$ and $T = 1.6667\text{s}$, at a distance from the wavemaker: (a): 2.35m and (b) 4.75m	244
Figure D.2: Comparison between the output from the NWT model and the experimental output from the NUIG wave flume, for $S = 240\text{mm}$ and $T = 1.05\text{s}$, at a distance from the wavemaker: (a): 2.35m and (b) 4.75m	245
Figure D.3: Comparison between the output from the NWT model and the experimental output from the NUIG wave flume, for $S = 240\text{mm}$ and $T = 0.9375\text{s}$, at a distance from the wavemaker: (a): 2.35m and (b) 4.75m	246
Figure D.4: Comparison between the output from the NWT model and the experimental output from the NUIG wave flume, for $S = 90\text{mm}$ and $T = 1.6667\text{s}$, at a distance from the wavemaker: (a): 2.35m and (b) 4.75m	247
Figure D.5: Comparison between the output from the NWT model and the experimental output from the NUIG wave flume, for $S = 90\text{mm}$ and $T = 1.2\text{s}$, at a distance from the wavemaker: (a): 2.35m and (b) 4.75m	248
Figure D.6: Comparison between the output from the NWT model and the experimental output from the NUIG wave flume, for $S = 300\text{mm}$ and $T = 2\text{s}$, at a distance from the wavemaker: (a): 2.35m and (b) 4.75m	249

Figure D.7: Comparison between the output from the NWT model and the experimental output from the NUIG wave flume, for $S = 300\text{mm}$ and $T = 1.6667\text{s}$, at a distance from the wavemaker: (a): 2.35m and (b) 4.75m.250

Figure D.8: Comparison between the output from the NWT model and the experimental output from the NUIG wave flume, for $S = 300\text{mm}$ and $T = 1.2\text{s}$, at a distance from the wavemaker: (a): 2.35m and (b) 4.75m.251

Figure D.9: Comparison between the output from the NWT model and the experimental output from the NUIG wave flume, for $S = 180\text{mm}$ and $T = 1.35\text{s}$, at a distance from the wavemaker: (a): 2.35m and (b) 4.75m.252

Figure D.10: Comparison between the output from the NWT model and the experimental output from the NUIG wave flume, for $S = 180\text{mm}$ and $T = 1.05\text{s}$, at a distance from the wavemaker: (a): 2.35m and (b) 4.75m.253

Declarations

This thesis or any part thereof, has not been, or is not currently being submitted for any degree at any other university.

William Finnegan

The work reported herein is as a result of my own investigations, except where acknowledged and referenced.

William Finnegan

Acknowledgments

First and foremost, I would like to thank, my supervisor, Dr. Jamie Goggins for his invaluable assistance and direction throughout the course of this project. Furthermore, he provided me with the necessary support and encouragement, without which the completion of this PhD study would be no more than a mere dream.

I would also like to express my gratitude to Dr. Martin Meere, of the School of Mathematics, Statistics and Applied Mathematics, whose assistance and support showed no bounds. His mathematical guidance and perseverance with the derivation of the analytical approximation provided in this thesis was essential for its completion.

My gratitude is also due to my parents, Tom and Carmel, and my sisters, Sarah, Rebecca and Rachel, for the support they have shown me through the course of my studies.

I would like to thank the Marine Institute for the AMETS wave-buoy data provided and to acknowledge the financial support from the National University of Ireland, Galway under the College of Engineering & Informatics Postgraduate Fellowship.

Finally, I would like to thank the staff, students and my fellow post-graduate students (especially the lads from R-Block) and researchers in the College of Engineering and Informatics at NUI Galway. Their camaraderie, both professionally and socially, has made my time here most enjoyable and an experience that I will never forget. A special mention must go to the lab technicians, Dermot McDermott and Edward Kilcullen, for their tireless efforts in the recommissioning of the wave flume and willingness to help

throughout the experimental aspects of the project. Furthermore, I would like to thank the members of my Graduate Research Committee, Prof. Padraic O'Donoghue and Prof. Michael Hartnett, for their advice throughout the research study.

Nomenclature

$(2s)_s$	Significant force or double amplitude motion	m
A	Wave amplitude	m
A_S	Pierson-Moskovitz spectrum coefficient	
\hat{A}_n	Fourier transform coefficient	
a	Radius of a vertical cylinder	m
a_m	Added mass	
B_S	Pierson-Moskovitz spectrum coefficient	
\hat{B}_n	Fourier transform coefficient	
b	Draft of a vertical cylinder	m
c	Mechanical damping in a structure	Ns/m
Ggc	Centre of gravity of the crest of the wave	
Ggt	Centre of gravity of the trough of the wave	
d	Water height at the SWL	m
g	Acceleration due to gravity	m/s^2
E	Total stored energy in a wave per unit area of sea surface	J/m^2
E_K	Kinetic energy in a wave per unit area of sea surface	J/m^2
E_P	Potential energy in a wave per unit area of sea surface	J/m^2
F_i	Force i-component	N
F_c	Fourier cosine transform	
F_D	Diffraction force	N
$F_{1,ext}$	Surge excitation force	N
$F_{3,ext}$	Heave excitation force	N
$F_{5,ext}$	Pitch excitation force	N
F_{FK}	Froude-Krylov force	N

F_H	Hydrodynamic force	N
F_{hs}	Hydrostatic force	N
F_R	Radiation force	N
f	Frequency (1/T)	s^{-1}
f_m	Modal (most likely) frequency	s^{-1}
H	Wave height	m
$H_m^{(1)}$	Hankel function of the first kind of order m	
h	Height of wavemaker flap from hinge to SWL	m
Δh	Change in water height level	m
I	Moment of inertia	m^4
I_m	Modified Bessel function of the first kind of order m	
I_{xx}	Moment of inertia about the x-axis	m^4
I_{yy}	Moment of inertia about the y-axis	m^4
I_{zz}	Moment of inertia about the z-axis	m^4
J_m	Bessel function of the first kind of order m	
k	Mechanical stiffness in a structure	N/m
k_0	Deep water wavenumber	m^{-1}
l	Height of wavemaker flap hinge from base of model	m
L_0	Deep water wavelength	m
M	Mass of the structure	kg
m	Integer	
m_{wave}	Mass per unit area of sea surface	kg
N	Number of time-steps	
\mathbf{n}	Unit normal from the structure	

n_j	j-component of the unit normal from the structure	
P	Power level per unit width of wave front	W/m
P_{av}	Average power	W
p	Pressure	Pa
p_{max}	Maximum pressure	Pa
p_0	Coefficient	
$p_m(\xi)$	Coefficient	
q_i	Volume fraction of the fluid i	
q_{m0}	Coefficient	
$q_m(\xi)$	Coefficient	
R	Radius of gyration	m
\mathbf{r}	Position vector of the point measured from the centre of rotation	
r	Radius	m
r	Radial polar coordinate	m
S	Stroke length	m
$S(f)$	Wave energy spectral density with respect to frequency	Js
S_B	Wetted surface	
$S_{ss}(f)$	Dynamic response spectral density with respect to frequency	
s	Scaling factor	
T	Location of pitch	
T	Wave period	s
T_{av}	Average wave period	s
T_{tot}	Total time of a record/simulation	s
T_z	Mean zero up-crossing wave period	s

t	Time	s
t_m	Time at m^{th} time-step	s
$U(y)$	Prescribed horizontal velocity of the wavemaker	m/s
\mathbf{u}	Dynamic displacement response of a structure	m
$\dot{\mathbf{u}}$	Dynamic velocity response of a structure	m/s
$\ddot{\mathbf{u}}$	Dynamic acceleration response of a structure	m/s^2
u_i	Flow velocity i-component	m/s
u_j	j-component of the dynamic displacement response	m
V	Volume of a structure	m^3
V_n	Component of the structural velocity in the same direction as the normal	m/s
v	Water particle velocity	m/s
v_g	Group velocity	m/s
$\hat{X}(t)$	Fourier transform	
x	Distance from wavemaker	m
x	Horizontal coordinate	m
$\bar{x}(t)$	Specified displacement of the wavemaker wall boundary	m
y	Increases from the SWL with depth	m
z	Vertical coordinate	m
α	JONSWAP wave energy spectrum constant	
γ	Breath of the wavemaker plunger at the SWL	m
ε_0	Initial phase angle	
ε_m	Neumann symbol	
ε_n	Phase angle of the n th wave	
ν	Radiation, wave, damping	Ns/m

ξ	Separation constant	
θ	Angular polar coordinate	<i>rads</i>
μ	Dynamic viscosity of a fluid	<i>Pa.s</i>
$\eta(t)$	Wave elevation in the time domain	<i>m</i>
ρ	Fluid density	<i>Kg/m³</i>
ρ_s	Density of a structure	<i>Kg/m³</i>
τ	Hydrostatic stiffness of a structure	<i>N/m</i>
Φ	Time domain velocity potential	<i>m/s</i>
Φ_D	Time domain diffraction velocity potential	<i>m/s</i>
Φ_I	Time domain incident velocity potential	<i>m/s</i>
Φ_R	Time domain radiation velocity potential	<i>m/s</i>
Φ_S	Time domain scattering velocity potential	<i>m/s</i>
φ	Frequency domain velocity potential	<i>m/s</i>
φ_R	Frequency domain radiation velocity potential	<i>m/s</i>
φ_j	Wave field due to oscillations in mode <i>j</i> with unit velocity amplitude	<i>m/s</i>
φ_I	Incident wave velocity potential	<i>m/s</i>
φ_s^i	Interior scattering velocity potential	<i>m/s</i>
φ_d^e	Exterior diffraction velocity potential	<i>m/s</i>
φ_s^e	Exterior scattering velocity potential	<i>m/s</i>
χ^i	Interior condensed function	
χ^e	Exterior condensed function	
ω	Wave angular frequency	<i>s⁻¹</i>
ω_n	Wave angular natural frequency	<i>s⁻¹</i>

Chapter 1

Introduction

1.1 General introduction

With the continuing rise in oil prices and greater concern for the damage to the atmosphere, the world is continually looking for a cleaner and more sustainable form of energy. In 2008, considerable interest in the price of oil and gas was cultivated when there was a nominal peak of over \$140 per barrel of crude oil in July, with a subsequent collapse in the price to just under \$40 per barrel by December (Kruckow, 2010). Furthermore, imported fossil fuels make up 86% of Ireland's total energy requirement between electricity, heat and transport (Marine Institute, 2006). However, the Government White Paper (Irish Government, 2007) details how Ireland aims to generate 33% of the electricity consumption from renewable sources by 2020 and this progress in the green energy revolution is set to continue with the aim of being carbon neutral by 2035 (Reilly, 2010).

Ocean wave energy is a renewable source of energy, which is relatively unexploited and offers a possible solution to the world's energy crisis. Furthermore, if Ireland is to achieve its aims of being carbon neutral, the exploitation of ocean wave energy is vital. In addition, this solution will reduce the use of these imported fossil fuels, while being friendly to the environment.

Ocean wave energy is one of the world's most powerful forms of energy and the energy density in ocean waves is the highest among renewable energy sources (Clément et al., 2002). In addition, Falnes (2007) shows that the power flow intensity of ocean waves is up to five times larger than for the wind that creates these waves and, thus, is an indirect form of solar power. Furthermore, ocean wave energy is a far more dependable source of energy when compared to the other renewable energy resources. Another advantage of ocean wave energy is, since most of these waves travel long distances, they are usually out of phase with the winds that create them, and, consequently, wave energy converters may easily and efficiently be integrated with other renewable technologies, such as offshore wind energy generation.

Introduction

However, as with any form of energy, there is a number of drawbacks when trying to harness it. In turn, one of the main reasons why this major natural resource has remained unexploited is that it is very variable and largely random over several time-scales; from wave to wave, with sea state and seasonal variations (Falcão, 2010). Another challenge in harnessing this form of energy is the harsh and secluded environment where the most power dense waves exist; that is in deep water (generally more than 40 metres) that are several kilometres offshore. This affects a number of integral factors, including the initial deployment of devices, as deep sea moorings are required or anchoring to a submerged platform. In addition, the loadings on these structures vary greatly and storms can generate loads of up to 100 times greater than the average wave loading and, as a result, additional survivability measures and factors of safety must be incorporated in their design. Furthermore, they require long underwater electrical cables and maintenance of these devices is difficult as they are not easily accessed. In addition, there may be a significant long term environmental affect. However, as of yet, the extent of this affect is not known but the areas that may be affected is sea life migration, silt build up and sediment deposits.

Thus, the main aim of this research is to develop a computational fluid dynamics numerical model for a wave tank that can accurately simulate the interaction of irregular ocean waves with a structure, which is outlined in more detail in Section 1.3. However, first a brief introduction into the harnessing of ocean wave energy in an Irish context and, also, a summary of the variety of wave energy converters, and examples of each, are presented. The chapter concludes with a brief summary of the objectives of the current research and an outline of the structure of the thesis.

1.2 Harnessing of ocean wave energy

1.2.1 Ocean wave energy in an Irish context

Ireland's advantage in developing this resource primarily lies in its location. It is well situated at the end of a long stormy fetch and its energetic climate is only bettered by the southern parts of South America and the Antipodes, which is due to the circumpolar storms near Antarctica (Thorpe, 1999). This is evident in Figure 1.1, where the wave power levels around Ireland are approximated at 70kW/m of wave front. In 2005, ESB International carried out a comprehensive assessment of the offshore wave energy resource off the coast of Ireland and found that the accessible wave energy resource is up to 20.76 TWh/year (Marine Institute, 2006). Furthermore, in the 2009 Construction Industry Federation publication it was stated that if all of the Irish coastline was developed, the total potential for wave energy is 48 TWh/year (Construction Industry Federation, 2009). Furthermore, Ireland has about 220 million acres of underwater continental shelf between the Atlantic Ocean and the Irish Sea, which provides the required area for the development of this sector (Reilly, 2010).

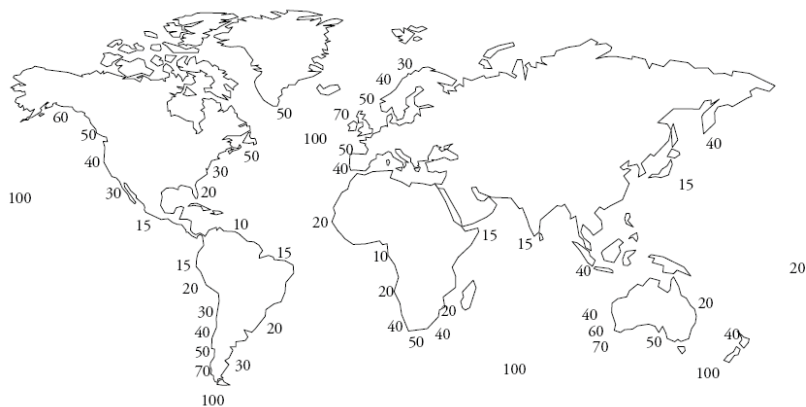


Figure 1.1: Approximate wave power levels in kW/m of wave front (Thorpe, 1999).

Introduction

In terms of becoming a European and World leader in the exploitation of wave energy, Ireland has huge potential as it has the highest wave energy resource in Europe. According to the Smart Ocean Consultation Document (Marine Institute, 2010), Ireland has an estimated generation capacity of 60 GW, which is one fifth of Europe's resource. The Smart Ocean Consultation Document was published, in 2010, by the Marine institute and aims to make Ireland a world leader in ocean energy technology by 2020.

1.2.2 Current ocean wave energy technologies

The concept of harnessing ocean wave energy is by no means a new idea. However, the topic only gained international interest in the 1970's with the publication of Stephen Salter's groundbreaking paper on his Wave Energy Duck (Salter, 1974). Since then, over a thousand patents have been issued for wave energy converters (WECs) (The United States Patent and Trademark Office, 2013), incorporating a variety of methods. However, as of yet, no 'winning' WEC design has been established.

One of the unique features of ocean wave energy extraction that differs from the other renewable energy resources is the fact that there are so many different approaches, in terms of designing an efficient energy converter. This is the case as wave energy conversion occurs at varying locations and at a variety of depths, including shoreline, near-shore and offshore. Clement et al. (2002) summarised the variety of devices into just four main types of WECs: oscillating water columns, point absorbers, surging devices, and overtopping devices. Since then, Falcão (2010) has schematically created a more comprehensive summary of the various wave energy converters with examples of each type, as shown in Figure 1.2. Currently, there are four wave energy prototype developers in Ireland; Sea Power, Ocean Energy, Hydam and Wavebob. Aquamarine Power also has operations in Ireland, although its head offices are based in Scotland, as it does some work in conjunction with Queens University, Belfast.

Introduction

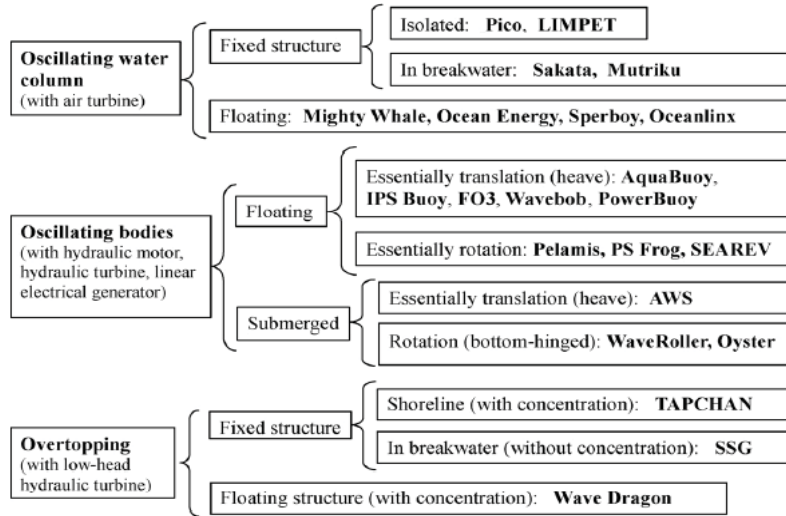


Figure 1.2: Summary of the various wave energy converters, image reproduced from Falcão (2010).

An oscillating water column (OWC) type WEC uses the increase and decrease in pressure within a partially submerged column, which is caused by the heave motion of the waves, to pull and push air through a turbine, thus powering the turbine and creating electricity. The most common type of turbine used is the Wells turbine. French (2006) describes the inefficiency of a device that relies on the hydrostatic force for energy capture. He does this by taking a wave of period 10 s and amplitude, A , of 1.14 m. The surface water particle velocity, v is $A\omega$, where ω is the angular frequency and is estimated at 0.72 s^{-1} . Thus, the kinetic energy of the wave, $0.5\rho v^2$, is 267 Pa and the hydrostatic force, $\rho g\Delta h$, is 11 kPa, Δh is the change in height and is given as $\Delta h = A$ in this calculation. Therefore, vertical axis turbines working on the particle velocity of the water can only capture 1/43 of the power available, which can be calculated by dividing the hydrostatic force in the column by the kinetic energy of the wave. However, a number of prototypes of OWC WECs are currently being developed and are leading in the race to make ocean wave energy commercially viable. The European Pilot Plant (Falcão, 2000) is an OWC type wave energy converter prototype, which is located on the island of Pico, Azores, Portugal. It was designed as a full scale testing facility, where testing began in

Introduction

August 1999. Furthermore, it supplies a sizable proportion of the Pico Island's electricity requirement. This 400kW plant was developed by the Instituto Superior Tecnico of Lisbon, Portugal as part of the European Commission's JOULE programme. An Irish example of an OWC WEC is the Ocean Energy Buoy (Ocean Energy, 2010). It is a floating near-shore type device which has been developed to a quarter scale model.

Oscillating body systems may be classified as floating offshore or submerged near-shore devices and there are, generally, two kinds. These are point absorbers and surging devices. Heave motion point absorbers use the heave motion, or vertical movement, of the wave to extract energy by opposing this motion with a reaction force. In general, point absorbers are anchored to the seabed or an intermediate device, which anchors a number of such devices to the seabed. Surging devices use the pitch or surge motion, or the horizontal movement, of the incident wave to create pneumatic power to be converted to electric energy. It usually does this by using a paddle that is free to rotate but in doing so resists the force of the incident wave. The Archimedes Wave Swing (AWS) (Beirao et al., 2007) is an offshore, fully submerged, heave motion point absorber wave energy converter. It is made up of two main parts; the silo and the floater. When the AWS is under the crest of a wave, the floater moves down condensing the air inside the AWS and, when the AWS is under a trough, the floater moves up causing the air to expand. The working principle is shown in Figure 1.3. This heave motion is converted into electricity using an Electrical Linear Generator. A 2 MW prototype has been built and tested at the Portuguese northern coast in 2004 and then decommissioned (Valério et al., 2007).

Introduction

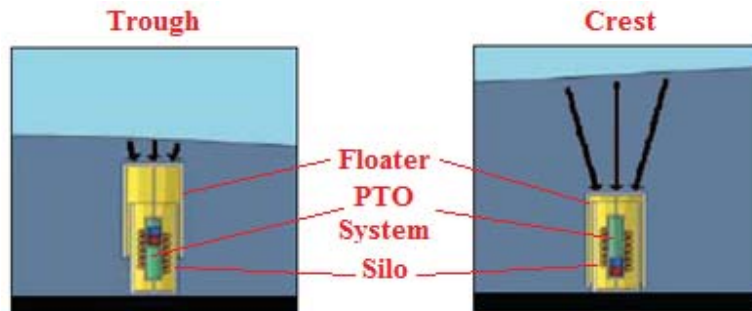


Figure 1.3: Schematic of the AWS working principle, where the arrows describe the pressure on the floater. (Adapted from: Beirao et al. (2007))

The Pelamis Wave Energy Converter (Henderson, 2006) is an offshore, floating, wave energy converter that absorbs energy from the rotational motion of the waves, as shown in Figure 1.4. The development of the device is carried out by Ocean Power Delivery Ltd in Edinburgh. The Pelamis is comprised of a string of cylinder sections whose joints are free to move in two degrees of freedom. These two axes that comprise each of its joints are inclined to the horizontal so as to allow a net inclined response to be induced. This inclined response offers a hydrostatic stiffness that is dependent on the slope of each segment. As a result of this dependence, the device can be designed to match the dominant frequency of the wave climate and, thus, create a resonant response. Wavebob (2010) prototype and the Sea Power prototype are two examples of oscillating body WEC's, which use the heave motion, being developed in Ireland. Aquamarine Power (2010) have tested a full-scale prototype of their Oyster, which is a near shore oscillating body WEC using the surge motion and is fixed to the seabed.

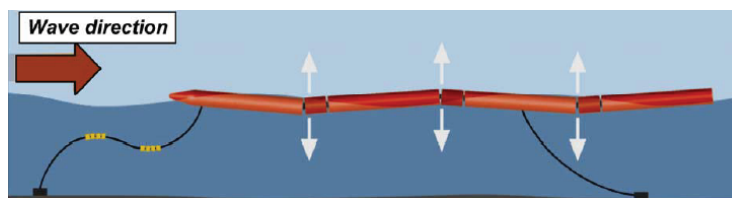


Figure 1.4: Elevation of the Pelamis WEC (Henderson, 2006).

Introduction

Overtopping devices force water to gather in a reservoir on top of the device. As the pressure head is greater in the reservoir than at the sea level, the water flows through a turbine, which converts this hydraulic head to electricity. The Wave Dragon (Soerensen, 2000) is a slack-moored offshore wave energy converter of the overtopping type, as can be seen in Figure 1.5. It uses a pair of patented reflectors to focus the waves towards a ramp, which then overtop into a reservoir. The hydraulic head in this reservoir is higher than that of the water causing the water to flow through a set of Kaplan-propeller hydro turbines and, thus, creating electric energy. The Wave Dragon is envisaged to be deployed in arrays of up to 200 units and this will minimise both grid connections and maintenance costs. Each unit will be of 4 MW and will be located in water deeper than 20 m and preferably in water more than 40 m deep so as to take advantage of the waves before energy is lost to shoreline effects.

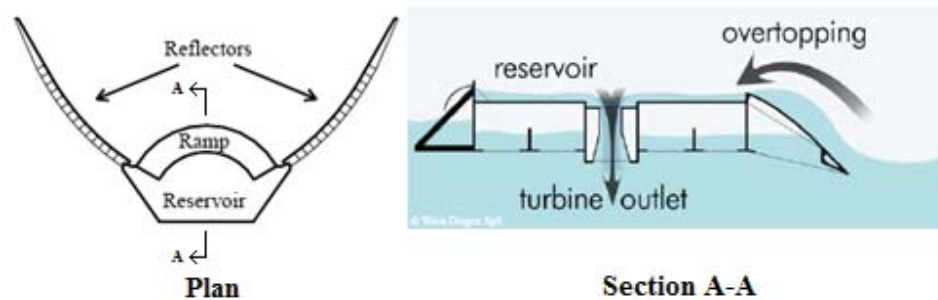


Figure 1.5: Plan: Main components of the Wave Dragon. Section: Basic principle of the Wave Dragon. (Adapted from: Kofoed et al. (2006))

1.3 Scope and objectives of the current research

The main objective associated with the current research is to develop numerical models which can accurately compute wave-structure interaction to assist in the design of wave energy converters. However, in order to achieve this, two subtasks must be completed. The first is to derive an analytical approximation in order to determine the wave excitation forces on a floating truncated cylinder in water of infinite depth. The second aim is to develop a computational fluid dynamics numerical model for a wave tank which can accurately simulate the interaction between an irregular ocean wave and a structure.

The numerical models developed through the course of this study provide a forum for exploring the interaction between real ocean waves and any floating offshore structure. Therefore, these models may be used to investigate any of the WECs detailed in Section 1.2.2. However, the analysis may need to be altered depending on the desired output from the investigation. Furthermore, in order to insure the accuracy of the numerical model, the outputs from the model have been validated against experimental data.

In the current study, the finite volume commercial software ANSYS CFX is used to perform the numerical analysis in developing a computational fluid dynamics numerical model for a wave tank which can accurately simulate the interaction between an irregular ocean wave and a structure. The solver is based on the Reynolds-averaged Navier-Stokes equations. One of the major advantages which this type of solver has over the alternative options, such as the boundary element method which is based on the small amplitude water wave theory, is that it includes higher order effects and, therefore, can incorporate some non-linearities. In developing the computational fluid dynamics numerical model for a wave tank, a number of steps and validation techniques are employed. These steps are individual objectives of the current study.

Therefore, the objectives of the current study are summarized as follows:

- Derive an analytical approximation in order to determine the wave excitation forces on a floating truncated cylinder in water of infinite depth.

Introduction

- Develop a computational fluid dynamics numerical model for a wave tank which can accurately generate linear regular waves and simulate wave-structure interaction.
- Perform experimental simulations in order to validate the methodology used to develop the numerical model for a wave tank in the generation of regular waves and simulating wave-structure interaction.
- Progress the computational fluid dynamics numerical model for a wave tank in order to generate linear irregular waves that can replicate real ocean waves and accurately simulate wave-structure interaction.
- Use computational fluid dynamics to develop techniques which will aid in the structural health monitoring of wave energy converters.
- Develop a methodology for the optimisation of the structural geometric configuration of a wave energy converter to maximize the power generation for a given site and detail a case study using this methodology.

1.4 List of publications produced as part of the current study

In this section, the journal and conference publications which have been produced as part of the current study are listed. These publications form the core of this thesis and the chapters and sections which they relate to are detailed in Section 1.5.

- Finnegan, W. and J. Goggins, 2012a. Numerical simulation of linear water waves and wave-structure interaction. *Ocean Engineering*. 43(0): p. 23-31.

Introduction

- Finnegan, W., M. Meere and J. Goggins, 2013. The wave excitation forces on a floating truncated vertical cylinder in water of infinite depth. *Journal of Fluids and Structures*. 40(0): p. 201-213. DOI: 10.1016/j.jfluidstructs,2013.04.007
- Finnegan, W. and J. Goggins, 2013. Numerical modelling to aid in the structural health monitoring of wave energy converters. *Key Engineering Materials*. 569-570: p. 595-602. DOI: 10.4028/www.scientific.net/KEM.569-570.595
- Goggins, J. and W. Finnegan. Shape optimisation of floating wave energy converters for a specified wave energy spectrum. Under review: *Renewable Energy*.
- Finnegan, W. and J. Goggins. Numerical simulation of the interaction of linear irregular water waves with a structure. Under review: *Ocean Engineering*.
- Finnegan, W., M. Meere and J. Goggins, 2011. The wave excitation forces on a floating vertical cylinder in water of infinite depth. *World Renewable Energy Congress 2011. Linkoping Sweden*.
- Finnegan, W. and J. Goggins, 2012b. The structural dynamics of a two-body wave energy converter. *4th International Conference on Ocean Energy. Dublin, Ireland*.
- Finnegan, W. and J. Goggins, 2012c. Determining the locations of high stresses on a floating concrete structure to aid in the structural health monitoring of wave

energy converters. *Bridge and Concrete Research in Ireland 2012, Dublin, Ireland.*

1.5 Structure of the thesis

In this section, a detailed description of the structure of this thesis is presented. Furthermore, the publications listed in Section 1.4, which are related to chapters of this thesis, are detailed in this section.

Chapter 2 presents a review of published literature containing similar or related topics to those discussed in the current study. Furthermore, reviews of Airy's linear wave theory, the mathematical description of energy in a wave, and the mathematical formulation of the hydrodynamic forces on a floating structure are detailed.

In Chapter 3, an analytical approximation for the wave excitation forces on a floating truncated vertical cylinder in water of infinite depth is derived. The initial mathematical formulation of the approximation is detailed in Finnegan et al. (2011) and the complete mathematical formulation of the approximation, along with comparison to other analytical, numerical and experimental results are detailed in Finnegan et al. (2013).

The methodology used in the development of a numerical model for a wave tank which accurately generates linear regular waves using a commercial computational fluid dynamics software, ANSYS CFX (ANSYS Inc., 2009) is outlined in Chapter 4. Furthermore, this methodology is also described in detail in Finnegan and Goggins (2012a).

Chapter 5 describes the evolution of the numerical model for a wave tank in order to accurately simulate linear wave-structure interaction in the time domain, which is detailed in Finnegan and Goggins (2012a). The hydrodynamic analysis of a floating structure in the frequency domain is also discussed and two case study examples have been described. These examples are also detailed in Finnegan and Goggins (2012b) and Finnegan and Goggins (2012c).

Introduction

In Chapter 6, physical measurements from the wave flume, located at the National University of Ireland, Galway, are used to validate the numerical model for a wave tank methodology presented in Chapter 4. Furthermore, linear regular wave-structure interaction using the experimental wave flume is performed and compared to the results of the linear regular wave-structure interaction simulated using the numerical model for a wave tank.

Chapter 7 describes the advancing of the numerical model for a wave tank in order to accurately generate linear irregular waves, which is then used to accurately perform wave-structure interaction on a floating rectangular prism structure. The details of this model are also briefly described in Finnegan and Goggins (2013).

Chapter 8 details the methodology used to optimise the geometry of a floating axisymmetric wave energy converter. A case study location of the Atlantic marine energy test site (AMETS) is used to demonstrate the presented methodology.

Finally a concluding chapter details a summary of the main findings and undertakings and discusses the conclusions of the current study. Furthermore, recommendations for future research which may stem from this current study are outlined.

Literature review

Chapter 2
Literature review

2.1 Introduction

As discussed in Chapter 1, there are two main objectives to this current research study; to develop an analytical approximation for calculating the wave excitation forces on a truncated cylinder in water of infinite depth and develop a computational fluid dynamics numerical model for a wave tank which can accurately simulate the interaction between an irregular ocean wave and a structure. Therefore, in this chapter, a critical review of the literature on these two topics is presented. Furthermore, a review of the literature relating to the other topics detailed in this research study, including the experimental simulation of the interaction between regular and irregular ocean waves and a structure and the structural optimization of wave energy converters, is detailed.

2.2 Airy's linear wave theory

Airy's linear wave theory (LWT) is the simplest form of mathematical representation of a regular wave. It assumes the waves are small in amplitude, sinusoidal and progressive in a constant water depth. Once the waves are larger, this theory may not remain a good representation. The main assumptions that relate to the theory are summarised in Newell (2010), as follows:

- The fluid is homogeneous and incompressible.
- Surface tension may be neglected.
- The Coriolis effect due to the Earth's rotation may be neglected.
- Pressure at the free surface is uniform and constant.
- The fluid is ideal and inviscid.
- The flow is irrotational.

Literature review

- The particular wave being considered does not interact with any other water motion.
- The bottom boundary, or bed, is a horizontal, fixed impermeable boundary.
- The wave amplitude is small with respect to the water depth and the waveform is invariant in time and space.
- Waves are plane or long-crested.

The theory describes the wave motions, including water particle displacement, water particle velocities and water particle accelerations, their kinematics and dynamics, which include wave pressures and their resultant forces and moments. A summary of the mathematical equations which have been derived using the theory is given in Figure 2.1.

LWT is mainly used to determine engineering design estimates. However, it does provide quite accurate results in a wide range of circumstances. The theory has been used to derive analytical solutions for wave-structure interaction problems. For example, it was used in the analytical studies reviewed in Section 2.5, and also in the development of many ship seakeeping techniques since its inception in 1841 by George Biddell Airy. An example of its use in the seakeeping of ships is detailed in Faltinsen (1993). Within this current study, LWT is used as the basis of the analytical approximation for the wave excitation forces on a truncated vertical cylinder in water of infinite depth, which is derived in Chapter 3. Furthermore, the theory is used as an analytical comparison of the results of the numerical model for a wave tank, developed in Chapter 4.

Literature review

	Shallow water $\frac{d}{L} < \frac{1}{20}$	Transitional water $\frac{1}{20} < \frac{d}{L} < \frac{1}{2}$	Deep water $\frac{d}{L} > \frac{1}{2}$
1. Wave profile	Same as >	$\eta = \frac{H}{2} \cos \left[\frac{2\pi x}{L} - \frac{2\pi t}{T} \right] = \frac{H}{2} \cos \theta$	< Same as
2. Wave celerity	$C = \frac{L}{T} = \sqrt{gd}$	$C = \frac{L}{T} = \frac{gT}{2\pi} \tanh \left(\frac{2\pi d}{L} \right)$	$C_0 = \frac{L}{T} = \frac{gT}{2\pi}$
3. Wavelength	$L = T\sqrt{gd} = CT$	$L = \frac{gT^2}{2\pi} \tanh \left(\frac{2\pi d}{L} \right)$	$L_0 = \frac{gT}{2\pi} = C_0T$
4. Group velocity	$C_g = C = \sqrt{gd}$	$C_g = \frac{1}{2} \left[1 + \frac{4\pi d/L}{\sinh(4\pi d/L)} \right] C$	$C_g = \frac{C_0}{2} = \frac{gT}{4\pi}$
5. Water particle velocity			
(a) Horizontal	$u_1 = \frac{H}{2} \sqrt{\frac{g}{d}} \cos \theta$	$u_1 = \frac{H}{2} \frac{gT}{L} \frac{\cosh[2\pi(z+d)/L]}{\sinh[2\pi d/L]} \cos \theta$	$u_1 = \frac{\pi H}{T} e^{\left(\frac{2\pi z}{L}\right)} \cos \theta$
(b) Vertical	$u_2 = \frac{H\pi}{T} \left(1 + \frac{z}{d} \right) \sin \theta$	$u_2 = \frac{H}{2} \frac{gT}{L} \frac{\sinh[2\pi(z+d)/L]}{\sinh[2\pi d/L]} \sin \theta$	$u_2 = \frac{\pi H}{T} e^{\left(\frac{2\pi z}{L}\right)} \sin \theta$
6. Water particle accelerations			
(a) Horizontal	$a_1 = \frac{\pi H}{T} \sqrt{\frac{g}{d}} \sin \theta$	$a_1 = \frac{g\pi H}{L} \frac{\cosh[2\pi(z+d)/L]}{\sinh[2\pi d/L]} \sin \theta$	$a_1 = 2H \left(\frac{\pi}{T}\right)^2 e^{\left(\frac{2\pi z}{L}\right)} \sin \theta$
(b) Vertical	$a_2 = -2H \left(\frac{\pi}{T}\right)^2 \left(1 + \frac{z}{d} \right) \cos \theta$	$a_2 = -\frac{g\pi H}{L} \frac{\sinh[2\pi(z+d)/L]}{\sinh[2\pi d/L]} \cos \theta$	$a_2 = -2H \left(\frac{\pi}{T}\right)^2 e^{\left(\frac{2\pi z}{L}\right)} \cos \theta$
6. Water particle displacements			
(a) Horizontal	$\xi = -\frac{HT}{4\pi} \sqrt{\frac{g}{d}} \sin \theta$	$\xi = -\frac{H}{2} \frac{\cosh[2\pi(z+d)/L]}{\sinh[2\pi d/L]} \sin \theta$	$\xi = -\frac{H}{2} e^{\left(\frac{2\pi z}{L}\right)} \sin \theta$
(b) Vertical	$\zeta = \frac{H}{2} \left(1 + \frac{z}{d} \right) \cos \theta$	$\zeta = \frac{H}{2} \frac{\sinh[2\pi(z+d)/L]}{\sinh[2\pi d/L]} \cos \theta$	$\zeta = \frac{H}{2} e^{\left(\frac{2\pi z}{L}\right)} \cos \theta$
8. Subsurface pressure	$p = \rho g(\eta - z)$	$p = \rho g\eta \frac{\cosh[2\pi(z+d)/L]}{\cosh[2\pi d/L]} - \rho g z$	$p = \rho g\eta e^{\left(\frac{2\pi z}{L}\right)} - \rho g z$

Figure 2.1: Mathematical summary of Airy's linear wave theory.

2.3 Energy in an ocean wave

The concept of energy in an ocean wave is an idea which has been studied and explored for decades. Since the 1940s, in Japan, Yoshio Masuda has been at the forefront of exploiting ocean wave energy (McCormick and Kraemer, 2001; Falcão, 2010). However, the topic only gained international interest in the 1970s with the publication of Stephen Salter's groundbreaking paper on his Wave Energy Duck (Salter, 1974). The rate of transport of energy across some line in the sea is known as the power and, therefore, the power of a wave can be calculated from the stored energy per unit width of the wave. For a sinusoidal gravity wave, which can be seen in Figure 2.2, the mass per unit area of sea surface, m_{wave} , in the half above the still water level is:

$$m_{wave} = \left(\frac{\rho}{2}\right) \left(\frac{H}{2\sqrt{2}}\right) \quad (2.1)$$

where ρ is the density of sea water and H is the height of the wave from trough to crest. The potential energy per unit area of sea surface, E_p , can then be calculated as follows:

$$E_p = m_{wave} g \Delta h = \left(\frac{\rho}{2}\right) \left(\frac{H}{2\sqrt{2}}\right) g \left(\frac{H}{2\sqrt{2}}\right) = \frac{\rho g H^2}{16} \quad (2.2)$$

where g is acceleration due to gravity and Δh is change in height of the centre of gravity of the wave, which is detailed in Figure 2.2. The kinetic energy per unit area of sea surface, E_k , of a wave is calculated from the total moving part of the wave using the Airy's linear wave theory velocity, v , as follows:

$$E_k = \frac{m_{wave} v^2}{2} = \frac{\rho}{2} \int_0^\infty A^2 \omega^2 e^{-2k_0 z} dz = \frac{\rho g H^2}{16} \quad (2.3)$$

where A is the wave amplitude ($= H/2$), ω is the wave angular frequency, k_0 is the wavenumber and z is the vertical distance from the still water level. Therefore, the total stored energy in a wave per unit area of sea surface, E , is given as:

$$E = E_k + E_p = \frac{\rho g H^2}{8} \quad (2.4)$$

Literature review

From the above equation, the power level per unit width of a wave, P , can be calculated. It is calculated using the group velocity, v_g , and the relation, $P = v_g E$, as follows:

$$P = v_g E = \frac{gT}{4\pi} \frac{\rho g H^2}{8} = \frac{\rho g^2 H^2 T}{32\pi} \quad (2.5)$$

where T is the wave period and for deep water waves, the group velocity is given as:

$$v_g = \frac{g}{2\omega} = \frac{gT}{4\pi} \quad (2.6)$$

When describing the energy in real sea waves, the wave energy spectrum, $S(f)$, is the most commonly used method. The wave energy spectrum is a plot of the energy density at specific frequency intervals against frequency used to quantify the sea state at a given location. Real sea waves can also be described in terms of their significant wave height, H_s , the average height of the top one third highest of the waves, and their average wave period, T_{av} . Therefore, Falnes (2007) describes the total stored energy in a wave per unit area of sea surface in terms of H_s and in terms of the wave energy spectrum, $S(f)$, which is detailed in Section 2.3.1, as follows:

$$E = \rho g \int_0^{\infty} S(f) df = \frac{\rho g H_s^2}{16} \quad (2.7)$$

where f is the frequency of the waves and $H_s = H\sqrt{2}$ (McCormick, 1973). The wave power level per unit width in a wave is, therefore, given as:

$$P = \rho g \int_0^{\infty} v_g(f) S(f) df = \frac{\rho g^2 H_s^2 T_{av}}{64\pi} \quad (2.8)$$

For example, a sea with a significant wave height, $H_s = 3$ m, and an average wave period, $T_{av} = 8$ s, has a wave power level per unit width of about 36 kW/m.

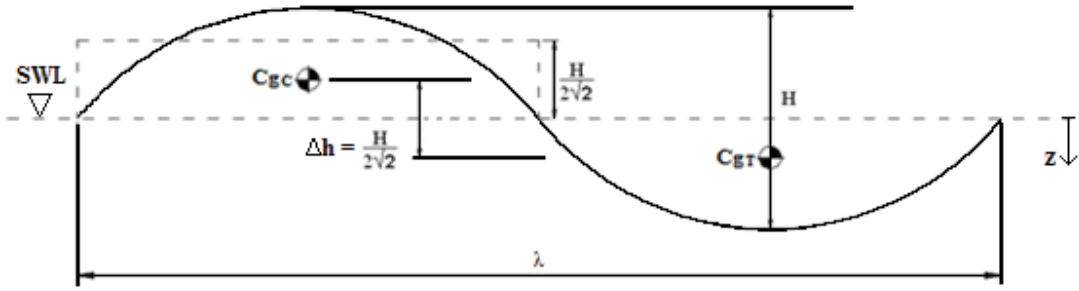


Figure 2.2: Part of a sinusoidal gravity wave in deep water. λ is wavelength; H is trough to crest height; C_{gc} is centre of gravity of the crest of the wave; C_{gt} is centre of gravity of the trough of the wave. Adapted from Salter (1974).

2.3.1 Wave energy spectrum

The wave energy spectrum, $S(f)$, is a distribution of the wave energy of a given location as a function of frequency. As the sea state of a given location is changing constantly, this method provides a clear analysis of the energy distribution at a certain location over a given time span. The spectrum also provides a convenient method of describing the dominant wave conditions of a given location.

The spectrum itself is derived from the Fourier transform (Morita, 1995) of a wave elevation record. For a given wave elevation record, $\eta(t)$, the Fourier transform, $\hat{X}(f)$, is given as:

$$\hat{X}(f) = \int_{-\infty}^{\infty} \eta(t) e^{-i2\pi ft} dt \quad (2.9)$$

Therefore, using the inverse Fourier transform (Morita, 1995),

$$\eta(t) = \int_{-\infty}^{\infty} \hat{X}(f) e^{-i2\pi ft} df \quad (2.10)$$

The wave energy spectrum is then calculated from the following relation:

Literature review

$$S(f) = \frac{\hat{X}(f)\hat{X}^*(f)}{T_{tot}} \quad (2.11)$$

where $\hat{X}^*(f)$ is the complex conjugate of the Fourier transform and T_{tot} is the total time of the wave elevation record.

There are a number of analytical techniques used in constructing the wave energy spectrum of a given location. These techniques are dependent on a combination of the fetch, the wind-speed, the significant wave height, the modal frequency, the average period or the zero-crossing period. Examples of these include, JONSWAP spectrum (Kim, 2008), Pierson-Moskowitz spectrum (Perez, 2005) and Bretschneider spectrum (Bretschneider, 1959). However, the technique used during the course of this study is the modified Pierson-Moskowitz spectrum.

In 1978, the 15th International Towing Tank Conference recommended the use of the modified Pierson-Moskowitz Spectrum (Perez, 2005), which has parameters that are a function of the significant wave height, H_s , and the wave period statistics, which are average wave period, T_{av} , and zero up-crossing period, T_z . The average wave period, T_{av} , is the average period of all waves passing a given point and the zero up-crossing wave period, T_z , is the average time between successive crossings of the mean water level in an upward direction. The spectrum is given in terms of frequency, as follows:

$$S(f) = \frac{A_S}{(2\pi)^4 f^5} \exp\left(\frac{-B_S}{(2\pi)^4 f^4}\right)$$

$$A_S = \frac{173H_s^2}{T_{av}^4} = \frac{123H_s^2}{T_z^4} \quad (2.12)$$

$$B_S = \frac{691}{T_{av}^4} = \frac{495}{T_z^4}$$

And in terms of angular frequency, ω , as,

$$S(\omega) = \frac{A_S}{\omega^5} \exp\left(\frac{-B_S}{\omega^4}\right)$$

$$A_S = \frac{173H_s^2}{T_{av}^4} = \frac{123H_s^2}{T_z^4} \quad (2.13)$$

Literature review

$$B_S = \frac{691}{T_{av}^4} = \frac{495}{T_z^4}$$

In this study, the Pierson-Moskowitz spectrum has been selected as the wave energy density spectrum model to be used as it is suitable for describing fully developed seas. It has been employed in the case study described in Section 5.5 and it is also suggested as the input model for the methodology described in Chapter 8 where a measured spectrum at the design location is not available.

2.4 Hydrodynamic force on a structure

2.4.1 Equation of motion

In this study, the equation of motion is used to describe the oscillating motions of the floating structure as it responds to the incident wave, which causes the hydrodynamic loading or force on the structure. In offshore hydrodynamics, a vessel, or structure, is a system with six degrees of freedom; surge, sway, heave, roll, pitch and yaw. The axes x , y and z corotate with the ship and the roll, pitch and yaw can be represented by a set of Euler angles. These are illustrated in Figure 2.3. Since, axisymmetric structures are mainly being dealt with in this study, this is reduced to just three degrees of freedom; surge, heave, and pitch, which will be represented by the subscripts; 1, 3 and 5, respectively, so as to retain the conventional numbering scheme.

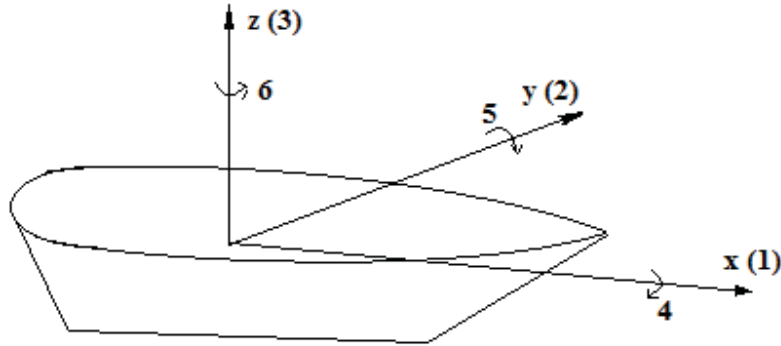


Figure 2.3: Six degrees of freedom of a floating structure; surge(1), sway(2), heave(3), roll(4), pitch(5) and yaw(6). Reproduced from: Falnes (2002).

The total pressure on a floating body is given by Bernoulli's equation (McCormick, 1973), as follows:

$$p = -\rho \frac{\partial \Phi}{\partial t} - \rho g z \quad (2.14)$$

where p is pressure, ρ is the density of water, g is gravity, Φ is the velocity potential, t is time and z is the downwards distance from the still water level (SWL). The first term refers to the pressure effect of the incident wave and the second term in the equation refers to the buoyancy pressure on the body in still water. Therefore, the first term in the equation is the pressure term that contributes to the force of the wave on the body and, thus, the part of interest in this study.

In this study, it is assumed that forces on the floating structures being analysed may be derived from diffraction theory so that the viscous force is neglected, as it will be insignificant. The use of diffraction theory is bounded by the Keulegan-Carpenter parameter (Dean and Dalrymple, 1984), or the period parameter, which was first derived by Keulegan and Carpenter in 1958. It defines the importance of drag and inertia forces depending on the magnitude of its value. At large values, the drag forces dominate, while at small values the inertia forces dominate. Therefore, the hydrodynamic force on the structure is made up of the hydrostatic force, the excitation force and the radiation force.

Literature review

The 6 degree of freedom equation of motion for the system can be summarised as follows:

$$([M] + [a_m])\{\ddot{u}\} + ([c] + [v])\{\dot{u}\} + ([k] + [\tau])\{u\} = \{F_{ext}\} \quad (2.15)$$

where $\{u\}$ is the dynamic response vector, $[M]$ is the mass matrix, $[a_m]$ is the added mass matrix, $[c]$ is the structural damping matrix, $[v]$ is the radiation wave damping matrix, $[k]$ is the structural stiffness matrix, $[\tau]$ is the hydrostatic stiffness matrix and $\{F_{ext}\}$ is the excitation force vector on the structure. Further details on this, along with an example of a heaving buoy WEC, may be found in Falnes (2002).

When calculating the excitation forces and radiation forces, which is a combination of the added mass and radiation wave damping, the problem is divided into two problems; the radiation problem and the scattering problem. These two forces are to be calculated by using the techniques of the water-wave problem, along with a boundary value problem that describes the problem for which a solution is sought, to evaluate the velocity potential, Φ .

2.4.2 Water-wave problem

The water-wave problem is a set of equations which are derived from Airy's linear wave theory that are used to solve problems relating to water waves. Therefore, the assumptions used in the derivation of the solution to the problem are congruent with those detailed in Section 2.2. In this section, the water-wave problem is used to derive the velocity potential within the fluid domain for the case of small amplitude waves interacting with a floating structure. The fluid velocity, v , may be expressed as a gradient of the scalar velocity potential, Φ , where $v = \nabla\Phi$. From the conservation of mass, the divergence of the velocity is zero to satisfy Laplace's equation, given by Eqn. (2.16). Thus, the governing equation, throughout the fluid domain:

$$\nabla^2\Phi = 0 \quad (2.16)$$

Literature review

Since mainly axisymmetric bodies are being explored in this study (e.g. the problem detailed in Chapter 3), it is convenient to specify a coordinate system, including time, t , comprising (r, θ, z, t) . For clarity, this coordinate system is illustrated in Figure 2.4. For time-harmonic motions with an angular frequency, ω , the time, t , can be omitted, thus, transforming the equation to the frequency domain, as follows:

$$\Phi(r, \theta, z, t) = \text{Re}[\varphi(r, z, \theta)e^{-i\omega t}] \quad (2.17)$$

At the wetted body surface, S_B , of floating body, the normal component, defined outward from the fluid domain, of the structural velocity must be equal to the velocity component of an adjacent fluid particle, in the same direction. Therefore:

$$\frac{\partial \Phi}{\partial n} = V_n \quad (2.18)$$

where \mathbf{n} is the unit normal vector to the structure and V_n is the component of the structural velocity in the same direction as the normal, as shown in Figure 2.4. As the incident wave interacts with a structure, it is caused to diffract and, also, causes the structure to oscillate and, thus, create a radiated wave field. Therefore, the velocity potential, Φ , is decomposed into two parts: the scattering velocity potential, Φ_S , and the radiation velocity potential, Φ_R . The scattering velocity potential is made up of an incident wave velocity potential, Φ_I , and a diffraction velocity potential, Φ_D , as follows:

$$\Phi = \Phi_S + \Phi_R = \Phi_I + \Phi_D + \Phi_R \quad (2.19)$$

Therefore, since the incident wave velocity potential is already known, the problem is divided up into two problems; the radiation problem, which solves for the radiation velocity potential derived in Section 2.4.3, and the scattering problem, which solves for the diffraction velocity potential derived in Section 2.4.4.

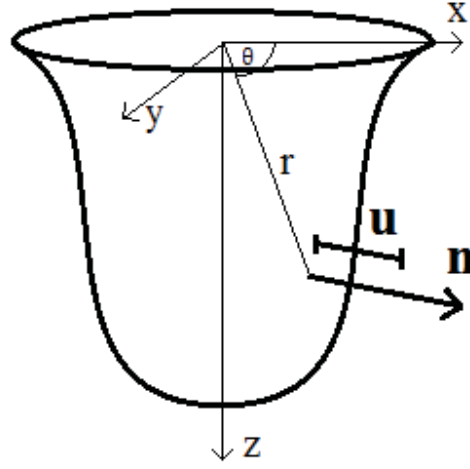


Figure 2.4: Illustration of the unit normal vector, \mathbf{n} , and the displacement vector, \mathbf{u} , of a floating structure. Included is the polar cylindrical coordinate system used.

2.4.3 Formulation of radiation problem

The radiation problem details when the structure is forced to oscillate harmonically in the absence of the incident wave. From this analysis, the radiation velocity potential is derived. Subsequently, by integrating the radiation velocity potential over the wetted surface of the structure, the hydrodynamic coefficients, the added mass and radiation wave damping associated with the structure, are derived. The structural boundary condition, which is to be imposed for this problem, is given as follows:

$$\frac{\partial \Phi_R}{\partial n} = V_n \text{ on } S_B \quad (2.20)$$

where

$$\Phi_R = \text{Re}[\varphi_R e^{-i\omega t}] = \text{Re} \left[\left[\sum_{j=1}^6 u_j \varphi_j \right] e^{-i\omega t} \right] \quad (2.21)$$

Literature review

where φ_R is the radiation velocity potential in the frequency domain, u_j is the complex amplitude of the oscillations in mode j and φ_j describes the wave field due to oscillations in mode j with unit velocity amplitude. Similar decomposition of the problem to Linton and McIver (2001) is used here, where $j = 1, 2, \dots, 6$, which includes both the translational and rotational modes of motion of the structure. For the radiation problem, $V_n = -i\omega u_j n_j$ (Zheng et al., 2008), hence:

$$\frac{\partial \varphi_j}{\partial n} = -i\omega n_j \text{ on } S_B, \quad j = 1, 2, \dots, 6 \quad (2.22)$$

where $n_j; j = 1, 2, 3$ are the x, y, z components of the unit normal outward from the structure, \mathbf{n} , while $n_j; j = 4, 5, 6$ are the corresponding components $\mathbf{r} \times \mathbf{n}$, where \mathbf{r} is the position vector of the point measured from the centre of rotation. The potential, φ_j , must satisfy Laplace's equation within the fluid, the free-surface boundary condition and the structural boundary condition, such that:

$$|\nabla \varphi_j| \rightarrow 0 \text{ as } z \rightarrow -\infty, \quad j = 1, 2, \dots, 6 \quad (2.23)$$

$$\frac{\partial \varphi_j}{\partial n} = k_0 \varphi_j \text{ on } z = 0, \quad j = 1, 2, \dots, 6 \quad (2.24)$$

Further, Linton and McIver (2001) describe how the free-surface boundary condition can be written as:

$$\frac{\partial^2 \varphi_j}{\partial t^2} + g \frac{\partial \varphi_j}{\partial z} = 0 \text{ on } z = 0, \quad j = 1, 2, \dots, 6 \quad (2.25)$$

$$\Rightarrow \omega^2 \varphi_j - g \frac{\partial \varphi_j}{\partial z} = 0 \text{ on } z = 0, \quad j = 1, 2, \dots, 6 \quad (2.26)$$

Also, to create a unique solution for the radiation problem, the following condition must be satisfied:

$$\lim_{r \rightarrow \infty} \sqrt{r} \left(\frac{\partial \varphi_j}{\partial r} - ik_0 \varphi_j \right) = 0, \quad j = 1, 2, \dots, 6 \quad (2.27)$$

Literature review

where r is the radial polar coordinate and $k_0 = \omega^2/g$. This boundary condition is known as the radiation condition. It ensures that the radiated wave dissipates as it travels away from the structure, i.e. as $r \rightarrow \infty$.

From Bernoulli's equation (Kim, 2008), the linear radiation hydrodynamic pressure, omitting the time factor, $e^{-i\omega t}$, is given as:

$$p_j = i\rho\omega\varphi_j, \quad j = 1, 2, \dots, 6 \quad (2.28)$$

The radiation velocity potential is then used to derive the radiation force on the floating structure. Thus, the complex force and moment on the domain due to radiation hydrodynamic pressure, with the unit normal directed outward from the fluid domain, is given as:

$$\hat{F}_{jk} = i\rho\omega \iint_{S_B} \varphi_j \frac{\partial \varphi_k}{\partial n} dS = i\rho\omega \iint_{S_B} \varphi_j n_k dS, \quad j, k = 1, 2, \dots, 6 \quad (2.29)$$

This is the force and moment due to unit velocity amplitude. For generalised displacement amplitude, u_k , and, thus, a velocity amplitude of $-i\omega u_k$ (Kim, 2008), the radiation hydrodynamic force and moment is given as follows:

$$\hat{F}_{jk} = \rho\omega^2 u_k \iint_{S_B} \varphi_j n_k dS, \quad j, k = 1, 2, \dots, 6 \quad (2.30)$$

The radiation hydrodynamic force and moment consists of an added mass, a_m , which is proportional to the acceleration and a radiation damping, ν , which is proportional to the velocity, as follows:

$$\hat{F}_{jk} = -\omega^2 u_k a_{mjk} - i\omega u_k \nu_{jk}, \quad j, k = 1, 2, \dots, 6 \quad (2.31)$$

Therefore,

$$a_{mjk} + \frac{i}{\omega} \nu_{jk} = -\rho \iint_{S_B} \varphi_j n_k dS, \quad j, k = 1, 2, \dots, 6 \quad (2.32)$$

Literature review

Since Green's theorem holds for the two harmonic functions in the fluid domain, we have:

$$\iint_{S_B} \varphi_j n_k dS = \iint_{S_B} \varphi_k n_j dS, \quad j, k = 1, 2, \dots, 6 \quad (2.33)$$

Hence, there are the following symmetry relations:

$$a_{m_{jk}} = a_{m_{kj}}, \quad v_{jk} = v_{kj}, \quad j, k = 1, 2, \dots, 6 \quad (2.34)$$

2.4.4 Formulation of scattering problem

The scattering problem deals with the scenario where the structure is held in a fixed position in the presence of an incident wave. From this analysis, the diffraction velocity potential is derived. Subsequently, by integrating the scattering velocity potential over the wetted surface of the structure, the wave excitation force on the structure is determined. The appropriate structural boundary condition, which is to be imposed is (Linton and McIver, 2001):

$$\frac{\partial \varphi_S}{\partial n} = 0 \quad \text{or} \quad \frac{\partial \varphi_D}{\partial n} = -\frac{\partial \varphi_I}{\partial n} \quad \text{on } S_B \quad (2.35)$$

The solution of the Laplace's equation in the fluid domain, the surface boundary condition and the free-surface condition, that must be satisfied, and, to ensure a unique solution, the following boundary conditions apply (Kim, 2008):

$$\frac{\partial \varphi_S}{\partial n} = k_0 \varphi_S \quad \text{on } z = 0 \quad (2.36)$$

$$\lim_{r \rightarrow \infty} \sqrt{r} \left(\frac{\partial \varphi_S}{\partial n} - ik_0 \varphi_S \right) = 0 \quad (2.37)$$

where $r = \sqrt{x^2 + y^2}$ but as y is taken as zero and, hence, $r = x$ and $k_0 = \omega^2/g$. The boundary condition given in Eqn. (2.37) is known as the radiation condition. It ensures that the diffracted wave dissipates as it travels away from the structure, i.e. as $r \rightarrow \infty$.

Literature review

The incident wave potential $\varphi_I e^{-i\omega t}$ for deep water in an oblique sea is given as:

$$\begin{aligned}\phi_I(r, \theta, z) &= -i \frac{gA}{\omega} e^{k_0 z} e^{ik_0 r \cos \theta} \\ &= -\frac{gA}{\omega} e^{-k_0 z} \sum_{m=0}^{\infty} \epsilon_m i^{m+1} J_m(k_0 r) \cos m\theta\end{aligned}\quad (2.38)$$

From Bernoulli's equation, the linear scattering hydrodynamic pressure, omitting the time factor, $e^{-i\omega t}$, is given as:

$$p = i\rho\omega(\varphi_I + \varphi_D) \quad (2.39)$$

The scattering velocity potential is then used to derive the wave excitation force on the floating structure. Therefore, the complex force and moment on the domain due to scattering hydrodynamic pressure, with the unit normal directed outward from the fluid domain, is given as:

$$\begin{aligned}\hat{F}_j &= i\rho\omega \iint_{S_B} (\varphi_I + \varphi_D) \frac{\partial \varphi_j}{\partial n} dS = i\rho\omega \iint_{S_B} (\varphi_I + \varphi_D) n_j dS, \\ j &= 1, 2, \dots, 6\end{aligned}\quad (2.40)$$

The above wave excitation force is made up of two forces: the Froude-Krylov force, \hat{F}_{FK} , and the Diffraction force, \hat{F}_D , as follows:

$$\hat{F}_{FKj} = i\rho\omega \iint_{S_B} \varphi_I n_j dS, \quad j = 1, 2, \dots, 6 \quad (2.41)$$

$$\hat{F}_{Dj} = i\rho\omega \iint_{S_B} \varphi_D n_j dS, \quad j = 1, 2, \dots, 6 \quad (2.42)$$

Using the Haskind-Newman Relation, the integral part of the Diffraction Force as follows:

$$\iint_{S_B} \varphi_D \frac{\partial \varphi_j}{\partial n} dS = - \iint_{S_B} \varphi_j \frac{\partial \varphi_I}{\partial n} dS, \quad j = 1, 2, \dots, 6 \quad (2.43)$$

In Chapter 3, the scattering problem for a truncated vertical cylinder in water of infinite depth is solved in order to derive an analytical approximation of the wave excitation forces on the structure.

2.5 Analytical wave-structure interaction studies

The solution of the scattering and radiation problem for floating bodies, in finite or infinite depth water, has been explored for decades for various shapes of bodies. Ursell (1949) explored the forces on an infinitely long horizontal floating cylinder in infinitely deep water using a polynomial set of stream functions to derive the analytical solution. Havelock (1955) employed a similar technique to solve the radiation problem for a floating half-immersed sphere in infinitely deep water. MacCamy and Fuchs (1954) derived the analytical solution of a bottom mounted cylinder which penetrates the water surface in water of finite depth. Garrett (1971) formulated the solution for the scattering problem of oblique waves around a circular dock in water of finite depth and presented numerical results detailing the vertical force, horizontal force and torque. Leppington (1973) examined the radiation properties of partially immersed three-dimensional bodies. A short-wave asymptotic limit was imposed in order to derive the velocity potential of the outgoing wave of a heaving and rolling circular dock and a heaving hemisphere. Bai (1975) developed a numerical method of linearizing the boundary value problem by using a variational principle equivalent in order to determine the diffraction of oblique waves by a horizontal infinitely long floating cylinder. This constructed variational form is employed by a finite element discretisation of the fluid domain and the numerical results are presented. Black (1975) investigated the wave forces on bodies which are vertically axisymmetric using an integral equation formulation in water of finite depth. Yeung (1981) presented a set of theoretical added mass and damping coefficients for a floating

Literature review

cylinder in water of finite depth and, also, truncated the solution for the infinite depth problem. Hsu and Wu (1997) developed a boundary element method to study the sway and heave motion of a 2-D floating rectangular structure in water of finite depth and an analytical solution for the problem was also presented. Mansour (2002) developed an analytical and Boundary Integral Method (BIM) solution for a bottom-mounted uniform vertical cylinder with cosine-type radial perturbations which penetrates the water surface in water of finite depth and compared the numerical results to that of a circular cylinder. Bhatta and Rahman (1995; 2003) used the method of separation of variables, which is similar to that employed by Havelock (1955), to analyse the scattering and radiation problem for a floating vertical cylinder in water of finite depth and presented the formulation for the surge, heave and pitch motion solutions. Liu et al. (2012) developed an analytical solution using a matched eigenfunction expansion for the wave scattering by a submerged porous plate with finite thickness in water of finite depth and a boundary element method solution is also presented to confirm the analytical solution. Hassan and Bora (2012) employed the method of separation of variables to derive the exciting forces on a pair of coaxial hollow cylinder and bottom mounted cylinder in water of infinite depth and presented numerical results for a variety of radius to water depth ratios. Kang et al. (2012) proposed an analytical model for analysing the annular flow induced vibration of a simply supported cylinder, while also taking into account the effects of friction. Liu et al. (2012) used the multipole expansion method to obtain the analytical solution for the diffraction and radiation problem for a submerged sphere in water of infinite depth and presented a set of numerical solutions for a variety of submerged depths. Similarly, Chatjigeorgiou (2012) employed the multipole expansion method in order to derive a solution for the hydrodynamic diffraction problem for a submerged oblate spheroid which is being excited by regular waves in deep water. Mohapatra et al. (2013) explored the effects of compressive flow on the wave diffraction on a 2-D floating elastic plate. The solution is derived for both the infinite and finite water depth cases using an integro-differential equation method.

However, an analytical study of the wave scattering problem of a floating truncated cylinder in water of infinite depth has not been previously published. Based on the

literature review presented in this section, a number of reasons why this problem has not been attempted previously have become clear: the infinite depth boundary condition increases the complexity greatly in 3-D problems and, therefore, a finite depth boundary condition has been used, e.g. Bhatta and Rahman (1995; 2003), Yeung (1981); the infinite depth boundary condition introduces an integral version of the Fourier transform that causes integrals which may not converge to arise and, thus, creates a problem which is difficult to solve. Furthermore, the solutions derived from previous authors require an extensive numerical procedure to derive useful results. Consequently, a solution which may be easily implemented by a user is also sought. Therefore, in Chapter 3, an analytical approximation for the wave excitation forces on a floating truncated vertical cylinder in water of infinite depth is derived.

2.6 Numerical simulation of linear regular and irregular waves and the interaction of these with structures

With the advances of computational methods and computational power, numerical simulations have become an efficient and cost effective solution for performing complex simulations in the early stages of development of a marine structure. In the studies described in this section, a numerical model for a wave tank is used to perform the analysis. In the current research study, a numerical model for a wave tank is developed, as detailed in Chapter 4 and Chapter 7, and this model is used to explore wave-structure interaction, as detailed in Chapter 5 and Chapter 7.

Contento (2000) used a 2-D numerical wave tank, which was based on the boundary element method (BEM) technique, to simulate the nonlinear motions of arbitrary shaped bodies in order to develop improved seakeeping techniques. Boo (2002) utilises a higher order boundary element method to explore the diffracted wave of linear and non-linear irregular waves on a truncated vertical cylinder. The scheme is first verified by accurately modelling linear regular and irregular waves. Kim et al. (2001) and Park et al. (2004) numerically simulated 3-D non-linear multi-directional waves using a finite difference

Literature review

method. The waves were generated using a numerical wavemaker by specifying the water particle velocities at the wavemaker boundary. Koo and Kim (2004) expanded the process to fluid-structure interaction in order to explore the effects of a nonlinear wave on a freely floating body for the 2-D case. Sun and Faltinsen (2006) developed a 2-D numerical tank using the BEM in order to simulate the impact of a horizontal cylinder on the free surface. Ning and Teng (2007) used a three-dimensional higher order boundary element model to simulate a fully nonlinear irregular wave tank. Ning et al. (2008) expanded this study to infinite water depth for nonlinear regular and focused waves. On the other hand, Yan and Lui (2011) developed a 3-D numerical wave tank using a high-order boundary element method (HOBEM) in order to simulate nonlinear wave-wave and wave-body interactions. The fluid motion inside a sphere was an example of wave-body interaction that they explored.

Wu and Hu (2004) used a finite element method (FEM) numerical wave tank (NWT) with a wavemaker to simulate the nonlinear interaction between water waves and a floating cylinder. Hadzic et al. (2005) created a 2-D NWT using a commercial CFD software package to explore the motion of a floating rigid body with up to 6 degrees of freedom as it is subjected to large amplitude waves. Turnbull et al. (2003) investigated the effects of inviscid gravity waves on a submerged fixed horizontal cylinder in a 2-D FEM numerical wave tank. Sriram et al. (2006) used a piston type wavemaker to generate 2-D nonlinear waves using FEM. Sriram et al. (2006) used a cubic spline approximation with the finite element approach when discretising the domain and had a fully reflecting wall at the end of the boundary. Mousaviraad et al. (2010) developed a harmonic group single run seakeeping procedure, which was solved using a general purpose unsteady Reynolds-averaged Navier-Stokes (URANS) solver. A linear potential solution was specified at the input boundary in order to generate linear input waves. An image showing the free surface wave fields around a ship hull derived from this numerical simulation is shown in Figure 2.5. Lal and Elangovan (2008) explored the CFD simulation of linear water waves for a flap type wavemaker using the same finite volume package described in this study. However, the dimension of the model was taken as an experimental wave tank and simulations were only carried out for the shallow water case.

Literature review

Anbarsooz et al. (2013) explored fully nonlinear viscous wave generation using both a paddle and a flap type wavemaker, in a numerical wave tank. The unsteady two-dimensional Navier-Stokes equations were solved and the results were compared to those of experiments and were found to be in good agreement.

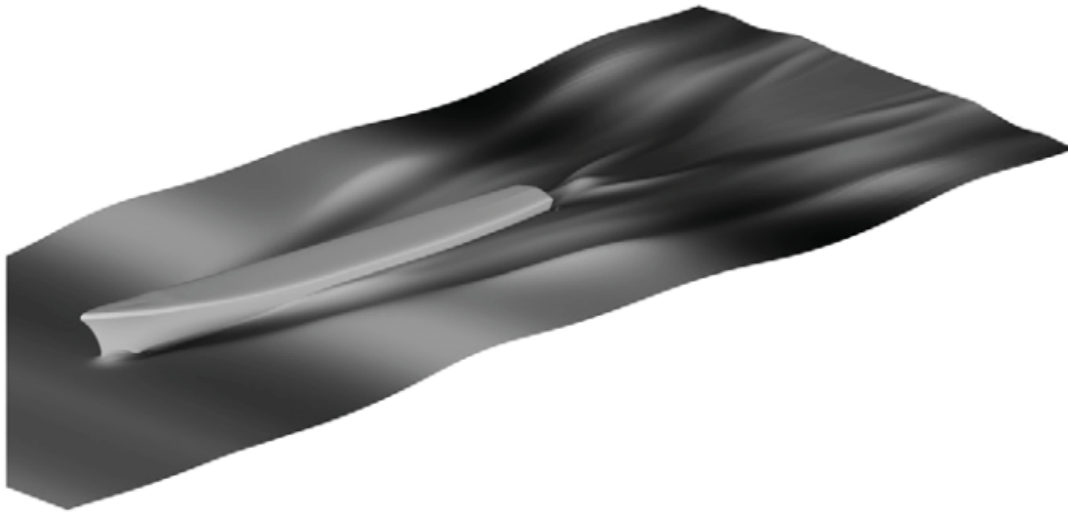


Figure 2.5: Free surface wave fields around a ship hull derived from a numerical simulation by Mousaviraad et al. (2010).

Liang *et al.* (2010) explored the use of a piston type wavemaker to generate an irregular wave train using the finite volume method, using FLUENT, and compared the results to the results from that of an experimental wave tank. Elangovan (2011) extended the work of Lal and Elangovan (2008) to simulate irregular linear waves using a flap-type wavemaker in a wave tank, which is based on an actual experimental wave tank. The method is validated by comparing the output wave spectrum to the original. Agamloh et al. (2008) used a commercial CFD software package to develop a 3-D numerical wave tank, which allowed fluid-structure interaction of a water wave and a cylindrical ocean wave energy device to be explored. Both the response of a single device and the response of an array of devices were investigated.

Literature review

From the above review of the literature, it is evident that the previous studies relating to the development of numerical models of wave tanks have aimed, in general, to either model a physical wave tank in order to replicate a physical experiment or to explore the interaction of a wave on a specified structure or process. As a result, there is no reliable methodology in place for the development of an optimum numerical model of a wave tank, in terms of the desired wave period generated. Therefore, in Chapter 4, a methodology is presented for the development of an optimum numerical model of a wave tank, in terms of the design of the mesh and the overall dimensions, which can accurately generate linear water waves, using a commercial CFD software package that incorporates Reynolds-averaged Navier-Stokes (RANS) solver.

As a comparison, in the current study, two commercial CFD software packages, one based on the RANS solver and one on the BEM solver, are used. The BEM solver offers a frequency domain solution for the forces and displacements of a floating structure over a range of frequencies. However, this solver is based on diffraction theory and only solves for first order, Airy's linear wave theory, and second order, Stokes wave theory, wave-structure interactions. The RANS solver is suitable for time domain calculations and may be used to model non-linear effects, including waves breaking, extreme wave conditions and non-linear, including viscous, wave-structure interactions. However, the RANS solver is much more time consuming and computationally expensive than the BEM solver.

2.7 Linear regular and irregular wave generation and wave-structure interaction through physical experiments

Although numerical models are proving a cost effective and efficient alternative to physical testing, there is still a need for experimental simulations. These experimental simulations are used to validate the performance that numerical models along with providing a greater insight into other non-linearities which the numerical model may not accurately represent, but may have a major impact in real full scale conditions. The

Literature review

numerical models developed in this study and the wave-structure interaction is validated with experimental testing in a wave flume, as detailed in Chapter 6. A schematic of the wave tank used in the experiments of Akyildiz (2002) is detailed in Figure 2.6 (a). It shows the main features of a wave tank/flume, including the wavemaker, the wave probes for recording wave elevation, the structure being studied and the method of wave energy dissipation, which in this case is a sloped beach.

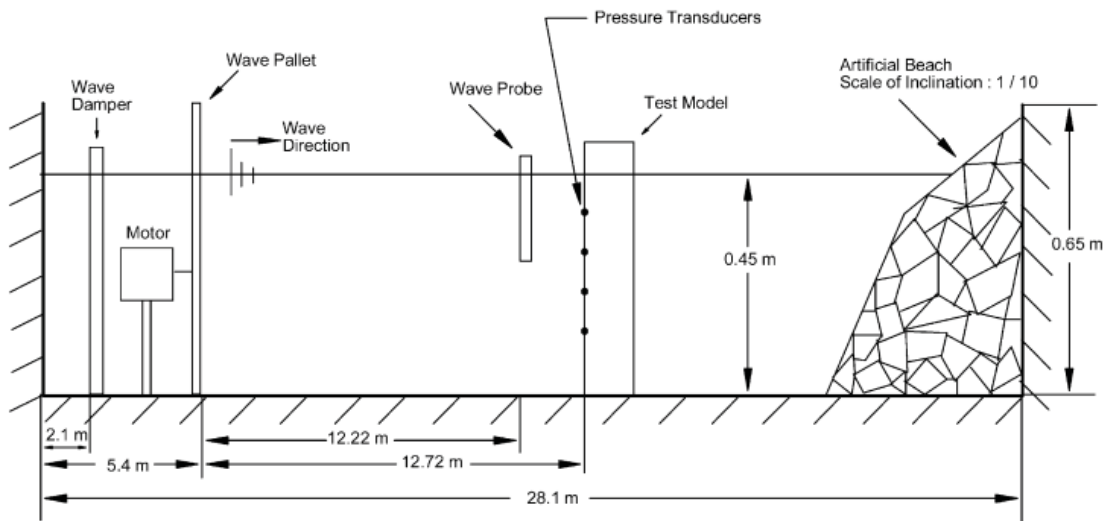
Ursell et al. (1960) validated the wavemaker theory for a piston-type wavemaker experimentally using a 100 m x 0.75 m x 0.9 m wave channel. Small amplitude waves were generated and measured using a combination hook and point gauge system in order to determine the wave height accurately. Wang (1974) explored the theory for plunger-type wavemakers and derived an deep water asymptotic expression for wave height to stroke length ratio. This deep water asymptotic expression was also compared to experimental results for a triangular wedge plunger-type wavemaker. Wu (1991) developed a numerical model of a plunger type wavemaker based on the boundary element method in order to study wave generation in water of shallow depth. Two types of analysis were performed, one with a wall behind the wavemaker and one without, and the results were compared to wavemaker theory of Wang (1974) and experimental results. Jensen et al. (2003) carried out an examination of the wave run-up at a steep beach using a particle image velocimetry (PIV) technique to capture the velocity fields in a wave flume, which is 0.5 m wide with a still water level of 0.2 m, and the results were compared to a boussinesq-type model. Henderson et al. (2006) explored the generation of two-dimensional, progressive, surface waves on deep water in a wave basin, which is 1.8m wide with a still water level of 0.2 m. Khalilabadi and Bidokhti (2012) detailed the design and construction of a wave flume at the Ocean Research Center of Shiraz. The experimental results of wave generation using a flap-type wavemaker are compared to the wavemaker theory to determine the efficiency of the wavemaker mechanism. The details of a survey of 43 laboratory facilities in relation to wave absorber design are also included.

Literature review

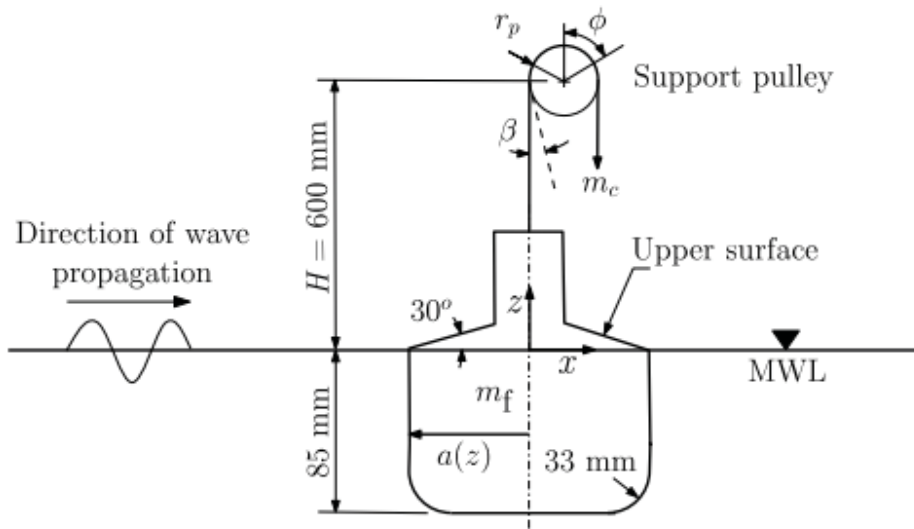
Akyildiz (2002) carried out experiments to investigate the pressure distribution due to diffraction on a bottom fixed cylinder which pierced the surface in water of finite depth, a schematic detailing the experimental setup in a wave tank is shown in Figure 2.6 (a). Akyildiz was mainly concerned with the second-order pressures on the cylinder and compared the results to a numerical solution. Kumar and Subramanian (2007) performed a study on the tank wall influences in drag estimation. In order to carry out this study experimentally, two scale model prototypes of a floating barge were examined to quantify the pressure and drag variations due to tank width in a 3.2m wide wave tank. Stallard et al. (2009) explored draft adjustment, which included upper surface immersion, of a wave energy device in order to limit heave response. Experimental trials were performed in regular and irregular waves at different drafts. Experimental simulations with focused waves were also performed to explore the response of the device in extreme conditions. The vertical dynamic response of the device is measured by a pulley system and a schematic of the pulley and structure is detailed in Figure 2.6 (b). This system is also employed to record the vertical response of the structure analysed in Section 6.5. Weller et al. (2013) extended the study to experimentally measure the complex motions of the structure in regular and near-focused waves.

Flocard and Finnigan (2010) experimentally investigated the performance of a bottom pivoting pitching wave energy device in water of intermediate depth in the presence of both regular and irregular waves. Their conclusions also detailed the performance of the device in 25m water at full scale. Fonseca et al. (2011) carried out experiments on a fixed vertical truncated cylinder in three depths of water; shallow, intermediate and deep water conditions. The objective of the study was to determine the slowly varying wave exciting drift forces in bi-chromatic waves, as well as, the first order surge and heave excitation forces. Fonseca et al. (2011) highlighted that it was necessary to use a cylinder with the bottom edges rounded in order to minimise the viscous effects that arise from vortex shedding from the transition between the sides and bottom associated with the oscillatory flow. A picture of the rig used to hold the cylinder in a fixed position is shown in Figure 2.6 (c). The structure being studied is connected to the rig using a load cell which records the vertical and horizontal force of the wave on the structure.

Literature review



(a)



(b)



(c)

Figure 2.6: Experimental setups of various studies which have been described in this section. (a): Overview schematic of Akyildiz (2002) (b): Pulley and structure schematic of Stallard et al. (2009) (c): Fixed cylinder rig of Fonseca et al. (2011).

In this study, the results of Fonseca et al. (2011) are used in Chapter 3 to experimentally validate the analytical approximation derived. Furthermore, the pulley system used to measure the vertical motion of the structure used by Stallard et al. (2009) is employed in the experimental work of the current research study, which is detailed in Chapter 6

2.8 Optimisation of wave energy converters

In order for a wave energy converter (WEC) to perform at maximum efficiency, it is necessary to optimise the design of many aspects of the device. In their design, it is necessary to maximise the dynamic response of wave energy converters for the majority of the time. In this study, the structural design of the geometric configuration of the device is explored in order to optimise its efficiency, as detailed in Chapter 8.

Traditionally, structural optimisation techniques were employed for sea keeping of ships and minimising of the dynamic response of the vessel when moored. Clauss and Birk (1996; 2001; 2002; 2009) have developed numerous automated optimisation procedures for the design of offshore structure hulls. A schematic of the hull shape optimisation framework which is utilised by Birk and Clauss (2001) is shown in Figure 2.7. A set of free variables, along with fixed parameters, are inputted into the framework. Wave data of the desired location, together with a number of constraints, are part of the framework and are used in deriving the optimum set of free variables of the structure, which is the output of the framework. This framework summarises the necessary aspects of a successful optimisation program. The structures involved in their studies include gravity base structures, tension leg platforms, caisson semisubmersibles and semisubmersibles with minimum downtime. Elchahal et al. (2007) used the structure's density distribution to optimise the internal geometry of floating breakwaters and explored a case study of a breakwater appearing in a port's construction far from the shore.

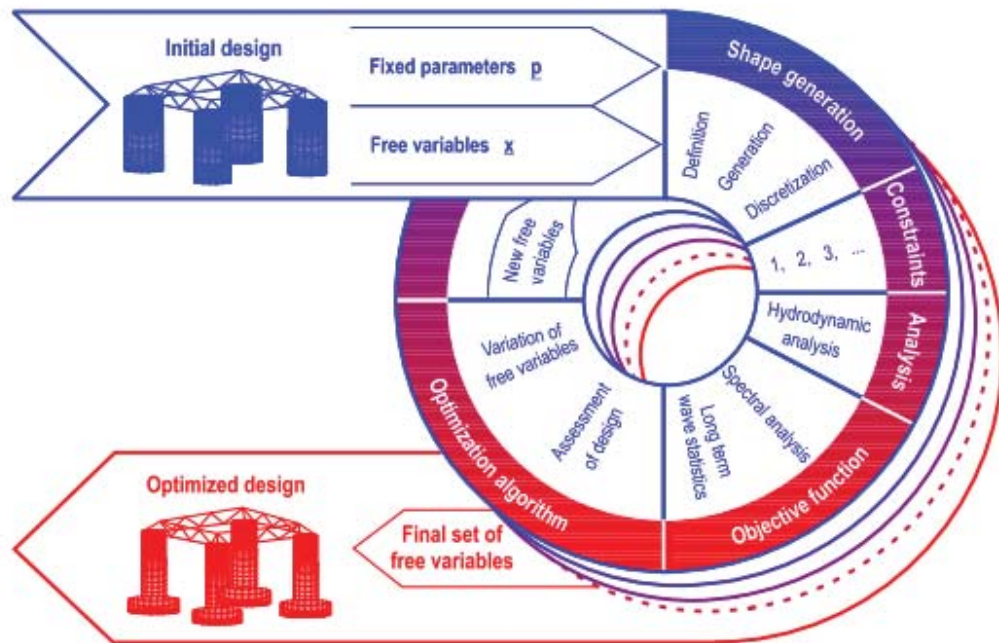


Figure 2.7: Hull shape optimisation framework used by Birk and Claus (2001).

Recently, with the increased interest in wave energy, designers have begun to increase the efficiency of their designs by improving the design of certain aspects or all of its structural shape. For example, Kramer and Frigaard (2002) explored the orientation and angle of the wave reflectors on the Wave Dragon to amplify the wave energy being absorbed. Vantorre et al. (2004) examined a number of geometries while exploring the hydraulic modelling of a heaving WEC being designed for the Belgian coast of the North Sea. Ruellan et al. (2010) describes the methodology involved in the design of the SEAREV WEC, which is a rotational point absorber.

2.9 Summary

In this chapter, a comprehensive review of the literature and studies undertaken related to the current research study has been presented. Furthermore, a background into Airy's linear wave theory and a mathematical description of both the energy in a water wave and the hydrodynamic characteristics of a floating structure are detailed.

Since deriving an analytical approximation for the wave excitation forces on a floating vertical cylinder in water of infinite depth is one of the main aims of the current study, a review of other analytical derivations and solutions has been undertaken and presented. From this review, it is clear that there is a gap in the research and a genuine need for deriving such an approximation.

A detailed account of the numerical analyses undertaken that involve wave generation and explore wave-structure interaction is given. In this review, particular attention is paid to exploring methods for the development of numerical wave tanks and their uses and applications. It is evident from this exploration that a methodology for the development of an optimised numerical wave tank using commercial computational fluid dynamics software is still required and this is undertaken as part of the current research study.

Since a number of numerical models are being developed during this study, a review of experimental data and experimental research undertakings using wave tanks and flumes has been presented. From this, experimental data which may be used to validate and verify the analytical and numerical models developed are identified. Furthermore, experimental procedures using the in-house wave flume are determined based on the reviewed work, which has already been carried out in other research facilities, in order to further validate the numerical models developed in the current research study.

Finally, since the structural optimisation of the geometric configuration of a wave energy converter is being explored in this study, a review of possible techniques used for other applications which may be employed for the extraction of wave energy is presented.

The wave excitation forces on a truncated vertical cylinder in water of infinite depth

Chapter 3

**The wave excitation forces on a truncated vertical
cylinder in water of infinite depth**

3.1 Introduction

One of the main stages in the design of wave energy converters (WECs) is the numerical modelling of a given converter. In this chapter, an analytical approximation for the wave excitation forces on a floating truncated vertical cylinder in water of infinite depth is provided. This approximation provides a method for validating the results of numerical models of WECs, since it may be used to estimate the forces on an arbitrary shaped axisymmetric WEC by analysing an equivalent cylinder representation of the structure.

In this chapter, the method of separation of variables is employed to construct approximate analytical expressions for the wave excitation forces, by considering the wave scattering problem, on a floating truncated vertical cylinder in water of infinite depth. The results are compared with the output from a numerical computational fluid dynamics (CFD) analysis that was undertaken using the boundary element method package, ANSYS AQWA (2010). The presented analytical approximation is, also, compared to a curtailed version of the finite depth solution of Bhatta and Rahman (2003), where the water depth was set to a value which is considered deep, $d = 200a$, where h is the height of the still water level and a is the radius of the cylinder, in order to be comparable to the infinite depth approximation presented here. Furthermore, the presented approximation is compared with the experimental results given in Fonseca et al. (2011).

3.2 Methodology

Since the desired solution deals with the scattering problem, the wave excitation forces on a fixed truncated vertical cylinder are considered with an incident wave of amplitude, A , and angular frequency, ω . A definition sketch depicting the set-up for the truncated vertical cylinder case is shown in Figure 3.1. The wave progresses in the positive x -direction with $z = 0$ corresponding to the still water level (SWL) and the positive z -direction being taken to point directly down into the water. In this analysis, Airy's linear

The wave excitation forces on a truncated vertical cylinder in water of infinite depth wave theory is used. Therefore, the following assumptions are made in the derivation of the governing mathematical model:

- The water is both incompressible, as frequencies are low, and effectively inviscid.
- As the air has such a small density relative to the water, pressure change as a result of the air is negligible and, thus, the air is at constant pressure.
- Surface tension at the air-water interface is negligible.
- The water is at constant density and temperature.
- The Reynolds number for the flow is sufficiently small for the flow to remain laminar.
- The waves are progressive and only travel in one direction and the wave motion is irrotational.
- The incident waves are of small amplitude compared to their wave length.
- The displacements of the body are sufficiently small that there is no need to distinguish the basis corotating with the cylinder from its fixed Cartesian counterpart.

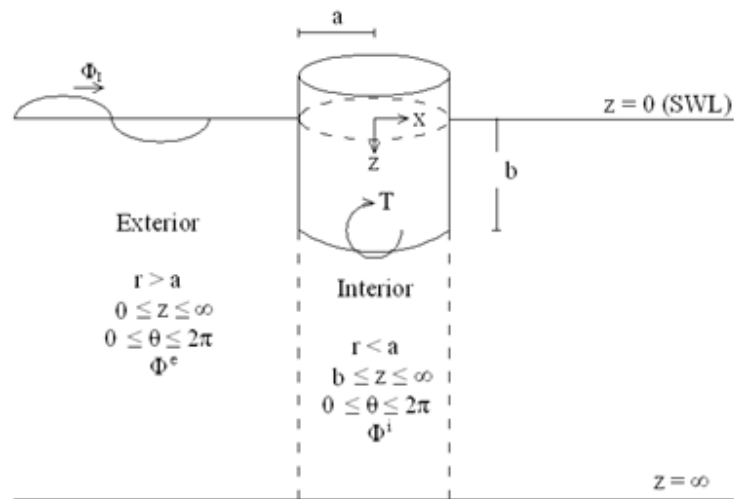


Figure 3.1: Definition sketch for the boundary value problem for a truncated vertical cylinder.

The wave excitation forces on a truncated vertical cylinder in water of infinite depth

Following Yeung (1981) and Bhatta and Rahman (2003), the fluid domain was divided into an interior region and an exterior region. The interior region corresponds to the area underneath the cylinder and the exterior region constitutes the remainder of the domain (Figure 3.1). The formulation of the problem presented is standard; the solution however is new. Therefore, additional details relating to the formulation may be sought from Linton and McIver (2001), among others. The problem is solved in the frequency domain. Therefore, the time domain velocity potential, Φ , to be solved is transformed to the frequency domain, as follows:

$$\Phi(r, \theta, z, t) = \text{Re}[\varphi(r, \theta, z)e^{-i\omega t}], \quad (3.1)$$

where r is the radial distance from the z -axis, θ is the angle about the x -axis, i is the standard imaginary unit, ω is the wave angular frequency of the wave, t is time and φ is the frequency domain velocity potential. Applied forces to the cylinder are then calculated by integrating the relevant velocity potential over the wetted surface area of the cylinder, S_B , using the following equation:

$$\hat{F}_j = i\rho\omega \iint_{S_B} \varphi n_j dS, \quad (3.2)$$

where ρ is water density, n_j is the j -component of the normal and \hat{F}_j is defined implicitly by $F_j = \text{Re}\{\hat{F}_j e^{-i\omega t}\}$, where F_j is the force in the j -direction. The equations and boundary conditions, in cylindrical coordinates, that need to be satisfied are: Laplace's equation, the deep water condition, the free surface equation and the radiation condition, respectively (Linton and McIver, 2001):

$$\nabla^2 \varphi = \frac{1}{r} \frac{\partial \varphi}{\partial r} + \frac{\partial^2 \varphi}{\partial r^2} + \frac{1}{r^2} \frac{\partial^2 \varphi}{\partial \theta^2} + \frac{\partial^2 \varphi}{\partial z^2} = 0, \quad (3.3)$$

$$|\nabla \varphi| \rightarrow 0 \text{ as } z \rightarrow \infty, \quad (3.4)$$

$$\omega^2 \varphi + g \frac{\partial \varphi}{\partial z} = 0 \text{ on } z = 0, r \geq a, \quad (3.5)$$

$$\lim_{r \rightarrow \infty} \sqrt{r} \left(\frac{\partial \varphi_d}{\partial r} - ik_0 \varphi_d \right) = 0, \quad (3.6)$$

The wave excitation forces on a truncated vertical cylinder in water of infinite depth

where ∇ is the gradient, g is the acceleration due to gravity, a is the radius of the cylinder, φ_d is the diffraction velocity potential and $k_0 = \omega^2/g$ is the wavenumber. Since the motion is irrotational and incompressible, Laplace's equation was arrived at by substituting $\mathbf{v} = \nabla\varphi$ into $\nabla \cdot \mathbf{v} = 0$, where \mathbf{v} is the flow velocity. The solution being developed is for infinitely deep water. Thus, the deep water condition defines the flow velocity near the sea bed. The free surface equation defines the velocity potential at the free surface away from the floating body. The radiation condition provides a constraint on the form of the velocity potential of the wave at distances from the body where the effect of the body on the wave has dissipated.

The velocity potential, φ , is a combination of the scattering velocity potential, φ_S , and the radiation velocity potential, φ_R , i.e. $\varphi = \varphi_S + \varphi_R$. The wave excitation forces are derived from the scattering velocity potential and the radiation velocity potential determines the radiation forces on an oscillating body. Therefore, only the scattering velocity potential needs to be derived as it is the wave excitation force which is being sought. The truncated vertical cylinder problem considers a vertical cylinder of radius, a , and of draft, b , with an incident wave of amplitude, A , and angular frequency, ω , as depicted in Figure 3.1. Since the scattering problem deals with the excitation force on a fixed body, the following structural boundary conditions must be imposed:

$$\frac{\partial \varphi_S^i}{\partial \bar{z}} = 0 \text{ on } \bar{z} = 0, \quad \text{where } \bar{z} = z - b, \quad (3.7)$$

$$\frac{\partial \varphi_S^e}{\partial r} = 0 \text{ at } r = a, \quad 0 < z < b, \quad (3.8)$$

where φ_S^i and φ_S^e are the interior and exterior scattering velocity potentials, respectively (see Figure 3.1). The unknown coefficients are then determined by matching the interior and exterior scattering velocity potentials and their radial derivatives along their common boundary, $r = a$.

The wave excitation forces on a truncated vertical cylinder in water of infinite depth

3.2.1 Derivation of velocity potential for the interior domain

The method of separation of variables is used to formulate an expression for the velocity potential. Since the problem deals with infinite depth, a Fourier sine/cosine transform is employed when dealing with the vertical or z -component. For the interior region, in order to satisfy the Neumann boundary condition on $\bar{z} = 0$ (Eqn. (3.7)), a Fourier cosine transform is required. Thus, the Fourier cosine transform of the interior scattering velocity potential, φ_S^i , is defined as follows:

$$F_c \left(\varphi_S^i(r, \theta, \bar{z}) \right) = \sqrt{\frac{2}{\pi}} \int_0^\infty \varphi_S^i(r, \theta, \bar{z}) \cos \xi \bar{z} d\bar{z} \equiv \chi^i(r, \theta, \xi), \quad (3.9)$$

where $0 < \xi < \infty$ and F_c is the Fourier cosine transform. The inverse transform is then:

$$\varphi_S^i(r, \theta, \bar{z}) = \sqrt{\frac{2}{\pi}} \int_0^\infty \chi^i(r, \theta, \xi) \cos \xi \bar{z} d\xi. \quad (3.10)$$

The method of separation of variables is used to solve the Laplace's equation (Eqn. (3.3)) in order to formulate an expression for φ_S^i . Taking the Fourier cosine transform of each part of Eqn. (3.3) gives:

$$\frac{1}{r} \frac{\partial \chi^i}{\partial r} + \frac{\partial^2 \chi^i}{\partial r^2} + \frac{1}{r^2} \frac{\partial^2 \chi^i}{\partial \theta^2} - \xi^2 \chi^i = 0. \quad (3.11)$$

Seeking separable variable solutions to Eqn. (3.11) of the form $\chi^i(r, \theta) = R(r)P(\theta)$ yields the following pair of ordinary differential equations:

$$r^2 R'' + rR' - (\xi^2 r^2 + \kappa)R = 0, \quad (3.12)$$

$$P'' + \kappa P = 0, \quad (3.13)$$

where κ is a separation constant. Solving Eqn. (3.13) and imposing 2π periodicity yields $\kappa = m^2$ and:

$$P_m(\theta) = A_m \cos m\theta \quad \text{for } m = 0, 1, 2, 3, \dots \quad (3.14)$$

The wave excitation forces on a truncated vertical cylinder in water of infinite depth

where the A_m are arbitrary constants. Solving Eqn. (3.12) and imposing boundedness as $r \rightarrow 0$, gives:

$$R_m(r) = \begin{cases} B_{m0}r^m & \text{if } \xi = 0 \\ B_m I_m(\xi r) & \text{if } \xi > 0 \end{cases} \quad (3.15)$$

where the B_{m0} and B_m are arbitrary constants and I_m is the modified first Bessel function of order m . The separable variable solutions are thus:

$$\chi_m^i(r, \theta, \xi) = R_m(r)P_m(\theta) = \begin{cases} \frac{p_{m0}}{2} \left(\frac{r}{a}\right)^m \cos m\theta & \text{if } \xi = 0 \\ p_m(\xi) \frac{I_m(\xi r)}{I_m(\xi a)} \cos m\theta & \text{if } \xi > 0 \end{cases}, \quad (3.16)$$

where $p_{m0} = a^m A_0 B_{m0}/2$ and $p_m(\xi) = A_m B_m I_m(\xi a)$. Superposing these gives:

$$\chi_m^i(r, \theta, \xi) = \sum_{m=0}^{\infty} \left[\frac{p_{m0}}{2} \left(\frac{r}{a}\right)^m + p_m(\xi) \frac{I_m(\xi r)}{I_m(\xi a)} \right] \cos m\theta, \quad (3.17)$$

$$r < a,$$

and taking the inverse transform yields:

$$\varphi_S^i(r, \theta, \bar{z}) = \sum_{m=0}^{\infty} \left[\sqrt{\frac{2}{\pi}} \int_0^{\infty} p_m(\xi) \frac{I_m(\xi r)}{I_m(\xi a)} \cos \xi \bar{z} d\xi \right] \cos m\theta, \quad r < a, \quad (3.18)$$

where the choice $p_{m0} = 0$ has been made to remove a Dirac delta function from φ_S^i .

3.2.2 Derivation of velocity potential in the exterior domain

Next the exterior domain, $r > a$, is considered. The exterior scattering velocity potential is the sum of the incident and diffraction velocity potentials (i.e. $\varphi_S = \varphi_I + \varphi_d$). In this problem, a plane incident wave of amplitude, A , coming from $x = -\infty$ and propagating in the x -direction is considered, so that:

The wave excitation forces on a truncated vertical cylinder in water of infinite depth

$$\varphi_I(r, \theta, z) = -i \frac{gA}{\omega} e^{-k_0 z} e^{ik_0 r \cos \theta}, \quad (3.19)$$

since $x = r \cos \theta$. MacCamy and Fuchs (1954) defines an expansion in cylindrical harmonics of Eqn. (3.19) having the form:

$$\varphi_I(r, \theta, z) = -\frac{gA}{\omega} e^{-k_0 z} \sum_{m=0}^{\infty} \epsilon_m i^{m+1} J_m(k_0 r) \cos m\theta, \quad (3.20)$$

where J_m is a Bessel function of the first kind of order m and ϵ_m is the Neumann symbol, defined by $\epsilon_0 = 1$ and $\epsilon_m = 2$ for $m \geq 1$. It is convenient to use this form of the incident velocity potential (Eqn. (3.20)) as it is a function of $\cos m\theta$ and, therefore, is easily combined with exterior diffraction velocity potential (Eqn. (3.25)) to yield the exterior scattering velocity potential, given in Eqn. (3.31). Similar to the interior domain, when dealing with infinite depth in the method of separation of variables a Fourier sine/cosine transform is used. In order to satisfy the free surface equation (Eqn. (3.5)), a combination of the Fourier sine and Fourier cosine transform is required. Thus, the Fourier cosine transform of the exterior diffraction velocity potential, φ_d^e , is defined as follows:

$$\begin{aligned} F(\varphi_d^e(r, \theta, z)) &= \sqrt{\frac{2}{\pi}} \int_0^{\infty} \varphi_d^e(r, \theta, z) [\xi \cos \xi z - k_0 \sin \xi z] dz \\ &= \chi^e(r, \theta, \xi), \end{aligned} \quad (3.21)$$

where $0 < \xi < \infty$. In order to obtain the inverse Fourier transform, Havelock's expansion theorem (Chakrabarti, 2000) is used, which states that if:

$$\begin{aligned} f(z) &= C_0 e^{-Kz} + \sqrt{\frac{2}{\pi}} \int_0^{\infty} \frac{C(\xi)}{(\xi^2 + K^2)} [\xi \cos \xi z - K \sin \xi z] d\xi, \\ &0 < \xi < \infty, \end{aligned} \quad (3.22)$$

then

$$C_0 = 2K \int_0^{\infty} f(z) e^{-Kz} dz, \quad (3.23)$$

The wave excitation forces on a truncated vertical cylinder in water of infinite depth

$$C(\xi) = \sqrt{\frac{2}{\pi}} \int_0^{\infty} f(z) [\xi \cos \xi z - K \sin \xi z] dz, \quad (3.24)$$

where C_0 and K are constants and $f(z)$ and its derivatives are continuous and integrable in the range $(0, \infty)$. Therefore, the inverse Fourier transform of Eqn.(3.21) is given as:

$$\begin{aligned} \varphi_d^e(r, \theta, z) = & \chi_0(r, \theta) e^{-k_0 z} \\ & + \sqrt{\frac{2}{\pi}} \int_0^{\infty} \frac{\chi^e(r, \theta, \xi)}{\xi^2 + k_0^2} [\xi \cos \xi z - k_0 \sin \xi z] d\xi, \end{aligned} \quad (3.25)$$

where

$$\chi_0(r, \theta) = 2k_0 \int_0^{\infty} \varphi_d^e(r, \theta, z) e^{-k_0 z} dz. \quad (3.26)$$

Now χ^e also satisfies Eqn. (3.11) and the variables are separated as before to obtain Eqn.(3.14). Insisting that the solution remain bounded as $r \rightarrow \infty$, the following is then obtained:

$$R_m(r) = A_m K_m(\xi r), \quad (3.27)$$

where K_m is the modified second Bessel function of order m . Superposing the separated solutions gives:

$$\chi^e(r, \theta, \xi) = \sum_{m=0}^{\infty} \left[q_m(\xi) \frac{K_m(\xi r)}{K_m(\xi a)} \right] \cos m\theta, \quad r > a. \quad (3.28)$$

In Eqn. (3.25), $\chi_0(r, \theta)$ corresponds to $\zeta = -ik_0$, which refers to the imaginary roots of Eqn. (3.21), and so the corresponding radial dependence is given by Linton and McIver (2001):

$$K_m(\xi r) = K_m(-ik_0 r) = \frac{1}{2} \pi i^{m+1} H_m^{(1)}(k_0 r), \quad (3.29)$$

where $H_m^{(l)}$ is a Hankel function of the first kind of order m . Hence, the appropriate expansion for $\chi_0(r, \theta)$ is of the form:

The wave excitation forces on a truncated vertical cylinder in water of infinite depth

$$\chi_0(r, \theta) = \sum_{m=0}^{\infty} \left[q_{m,0} \frac{H_m^{(1)}(k_0 r)}{H_m^{(1)}(k_0 a)} \right] \cos m\theta, \quad r > a. \quad (3.30)$$

Therefore, since the scattering velocity potential is the sum of the incident and diffraction velocity potentials (i.e. $\varphi_S = \varphi_I + \varphi_d$) and incorporating $-gA\omega^{-1}\epsilon_m i^{m+1}$ into the $\varphi_d^e(r, \theta, z)$ term in Eqn. (3.25), the scattering velocity potential for the exterior problem takes the form:

$$\begin{aligned} \varphi_S^e(r, \theta, z) = & -\frac{gA}{\omega} \sum_{m=0}^{\infty} \epsilon_m i^{m+1} \left[\left\{ J_m(k_0 r) + q_{m,0} \frac{H_m^{(1)}(k_0 r)}{H_m^{(1)}(k_0 a)} \right\} e^{-k_0 z} \right. \\ & \left. + \sqrt{\frac{2}{\pi}} \int_0^{\infty} \frac{K_m(\xi r)}{K_m(\xi a)} \frac{q_m(\xi)}{\xi^2 + k_0^2} [\xi \cos \xi z - k_0 \sin \xi z] d\xi \right] \cos m\theta. \end{aligned} \quad (3.31)$$

3.2.3 Analytical approximations for the coefficient $q_{m,0}$ and functions $p_m(\xi)$ and $q_m(\xi)$

The unknown coefficients $p_m(\xi)$ in Eqn. (3.18), and $q_{m,0}$ and $q_m(\xi)$ in Eqn. (3.31) are found by matching the velocity potentials and normal velocities across the boundary at $r = a$, and imposing the structural boundary condition. The conditions which are to be satisfied at the boundary are:

$$\left. \frac{\partial \varphi_S^e(r, \theta, z)}{\partial r} \right|_{r=a} = 0, \quad \text{if } 0 \leq z \leq b, \quad (3.32)$$

$$\varphi_S^e(r, \theta, z)|_{r=a} = \varphi_S^i(r, \theta, \bar{z})|_{r=a}, \quad \text{if } b \leq z \leq \infty, \quad (3.33)$$

$$\left. \frac{\partial \varphi_S^e(r, \theta, z)}{\partial r} \right|_{r=a} = \left. \frac{\partial \varphi_S^i(r, \theta, \bar{z})}{\partial r} \right|_{r=a}, \quad \text{if } b \leq z \leq \infty. \quad (3.34)$$

Imposing Eqn. (3.32)-(3.34) on Eqn. (3.18) and Eqn. (3.31) leads to a singular integral equation for determining the unknown function $q_m(\xi)$. The algebra arising in this

The wave excitation forces on a truncated vertical cylinder in water of infinite depth calculation is quite heavy and, as a result, the numerical work associated with this program is not attempted here. Furthermore, the details associated with this calculation have been relegated to Appendix A. The formulation detailed in Appendix A is the continuous analog for water of infinite depth to the discrete formulation given by Bhatta and Rahman (1995; 2003) for water of finite depth, and to the author's knowledge, it has not appeared in the literature previously. Therefore, although the analysis described above and in the appendix does lead to an interesting integral formulation for the unknown coefficients, it does not unfortunately yield convenient analytical expressions for the excitation forces.

However, in order to derive an analytical approximation, an alternative approach is presented. Leppington (1973) derives the velocity potential along the free surface in the outer region, as the majority of the velocity potential of significant magnitude is at the free-surface for high-frequency waves. Leppington (1973) then expands from this velocity potential to derive the full field outer velocity potential. In dealing with the inner region, a rescaling of coordinates is performed so a solid body (i.e. a dock) having a semi-infinite extent is being solved for. A similar technique is employed in this chapter in approximating the exterior scattering velocity potential, as the majority of this potential with significant magnitude is near the free-surface in the region $0 < z < b$. Since the presented study is not restricted to high-frequency waves, this assumption is deemed valid by ensuring that the draft-to-radius ratio remains greater than unity, i.e. $b/a > 1$, throughout the analysis.

In order to derive an analytical approximation for the interior and exterior velocity potentials, the following procedure is adopted. Closed form expressions for $q_{m,0}$ and $q_m(\xi)$ (and consequently φ_S^e) are constructed by taking $b = \infty$ in the boundary condition, given in Eqn. (3.32), which corresponds to calculating the exterior scattering velocity potential for a cylinder of infinite draft. The matching condition, given in Eqn. (3.33), is then imposed to determine $p_m(\xi)$ and φ_S^i . Finally, the surge and heave excitation forces are then found using the calculated forms for φ_S^e and φ_S^i , respectively. The justification for this approach lies in the comparison with corresponding numerical CFD results,

The wave excitation forces on a truncated vertical cylinder in water of infinite depth

which can be seen in Figure 3.2 and Figure 3.4. The parameter space for the problem under consideration here is two dimensional and may be represented by the region $0 < k_0 a, b/a < \infty$ in the $(k_0 a, b/a)$ plane. Extensive CFD work conducted for the current study indicates the analytical expressions for the surge and heave forces derived are acceptable provided the non-dimensional parameters $(k_0 a, b/a)$ lie in the region $0 < k_0 a < \infty, 1 < b/a < \infty$.

The procedure just described is now implemented. In the exterior region, the condition which is to be satisfied is given in Eqn. (3.32), where $b = \infty$, and is then applied to Eqn. (3.31), yielding:

$$\begin{aligned} -\frac{gA}{\omega} \epsilon_m i^{m+1} k_0 \left\{ J_m'(k_0 a) + q_{m,0} \frac{H_m^{(1)'}(k_0 a)}{H_m^{(1)}(k_0 a)} \right\} e^{-k_0 z} \\ -\frac{gA}{\omega} \epsilon_m i^{m+1} \sqrt{\frac{2}{\pi}} \int_0^\infty \frac{\xi K_m'(\xi a)}{K_m(\xi a)} \frac{q_m(\xi)}{(\mu^2 + k_0^2)} [\xi \cos \xi z \\ - k_0 \sin \xi z] d\xi = 0, \end{aligned} \quad (3.35)$$

which is then rearranged to give

$$\begin{aligned} k_0 q_{m,0} \frac{H_m^{(1)'}(k_0 a)}{H_m^{(1)}(k_0 a)} e^{-k_0 z} \\ + \sqrt{\frac{2}{\pi}} \int_0^\infty \frac{\xi K_m'(\xi a)}{K_m(\xi a)} \frac{q_m(\xi)}{(\mu^2 + k_0^2)} [\xi \cos \xi z - k_0 \sin \xi z] d\xi \\ = -k_0 J_m'(k_0 a) e^{-k_0 z}, \end{aligned} \quad (3.36)$$

where the prime is the derivative. Havelock's expansion theorem (Chakrabarti, 2000) is then applied to Eqn. (3.36) in order to determine the unknown coefficients. Therefore,

$$\begin{aligned} q_{m,0} \frac{H_m^{(1)'}(k_0 a)}{H_m^{(1)}(k_0 a)} = -2k_0 \int_0^\infty J_m'(k_0 a) e^{-k_0 z} e^{-k_0 z} dz \\ = -2k_0 J_m'(k_0 a) \frac{1}{2k_0} [e^{-2k_0 z}]_0^\infty = -J_m'(k_0 a), \end{aligned} \quad (3.37)$$

The wave excitation forces on a truncated vertical cylinder in water of infinite depth

and

$$\begin{aligned}
 q_m(\xi) &= \sqrt{\frac{\pi}{2}} \frac{2}{\pi(\xi^2 + k_0^2)} \int_0^\infty J_m'(k_0 a) e^{-k_0 z} [\xi \cos \xi z - k_0 \sin \xi z] dz \\
 &= \sqrt{\frac{2 J_m'(k_0 a)}{\pi \xi^2 + k_0^2}} \left[\xi \frac{k_0}{\xi^2 + k_0^2} - k_0 \frac{\xi}{\xi^2 + k_0^2} \right] = 0.
 \end{aligned} \tag{3.38}$$

Next, using this result, taking Eqn. (3.18) and Eqn. (3.31) and the condition in Eqn. (3.33) yields:

$$\begin{aligned}
 &\sqrt{\frac{2}{\pi}} \int_b^\infty p_m(\xi) \cos \xi(z - b) d\xi \\
 &= -\frac{gA}{\omega} \epsilon_m i^{m+1} \{J_m(k_0 a) + q_{m,0}\} e^{-k_0 z}.
 \end{aligned} \tag{3.39}$$

Therefore, inverting the Fourier cosine transform gives:

$$\begin{aligned}
 p_m(\xi) &= \sqrt{\frac{2}{\pi}} \int_b^\infty \left\{ -\frac{gA}{\omega} \epsilon_m i^{m+1} \{J_m(k_0 a) + q_{m,0}\} e^{-k_0 z} \right\} \cos \xi(z - b) dz \\
 &= -\frac{gA}{\omega} \epsilon_m i^{m+1} \sqrt{\frac{2}{\pi}} \left\{ J_m(k_0 a) \right. \\
 &\quad \left. - J_m'(k_0 a) \frac{H_m^{(1)}(k_0 a)}{H_m^{(1)'}(k_0 a)} \right\} \frac{e^{-k_0 b} k_0}{\xi^2 + k_0^2}.
 \end{aligned} \tag{3.40}$$

Consequently, the interior scattering velocity potential, given in Eqn. (3.18), is written as:

$$\begin{aligned}
 &\varphi_S^i(r, \theta, \bar{z}) \\
 &= -\frac{gA}{\omega} \frac{2}{\pi} \sum_{m=0}^\infty \left[\epsilon_m i^{m+1} \left\{ J_m(k_0 a) \right. \right. \\
 &\quad \left. \left. - J_m'(k_0 a) \frac{H_m^{(1)}(k_0 a)}{H_m^{(1)'}(k_0 a)} \right\} \int_0^\infty \frac{e^{-k_0 b} k_0}{\xi^2 + k_0^2} \frac{I_m(\xi r)}{I_m(\xi a)} \cos \xi \bar{z} d\xi \right] \cos m\theta,
 \end{aligned} \tag{3.41}$$

and the exterior scattering velocity potential, given in Eqn. (3.31), is written as:

The wave excitation forces on a truncated vertical cylinder in water of infinite depth

$$\varphi_S^e(r, \theta, z) = -\frac{gA}{\omega} \sum_{m=0}^{\infty} \epsilon_m i^{m+1} \left[\left\{ J_m(k_0 r) - J'_m(k_0 a) \frac{H_m^{(1)}(k_0 r)}{H_m^{(1)'}(k_0 a)} \right\} e^{-k_0 z} \right] \cos m\theta . \quad (3.42)$$

In this section, the scattering velocity potentials for the exterior region, $r > a$, and interior region, $r < a$, were formulated and the unknown coefficients were approximated by matching these velocity potentials at $r = a$. Therefore, for the truncated cylinder case, the interior scattering velocity potential (Eqn. (3.41)) and the exterior scattering velocity potential (Eqn. (3.42)) are now approximated.

3.3 Results

In this section, the wave excitation forces for both the truncated and infinite draft cylinder cases are derived using the relevant velocity potentials and Eqn. (3.2). The three motions from which the wave excitation forces are been calculated for the truncated cylinder case are the surge, heave and pitch. Since for the infinite draft cylinder case there is no vertical, or heave motion, only the surge excitation force is calculated. These solutions are presented for a range of frequencies and, for the truncated cylinder case, for a range of draft-to-radius ratios also. In addition, the MATLAB code for calculating the presented approximation and the associated plots is given in Appendix B. In order to verify the accuracy of the analytical solution, the wave excitation forces are compared to the output from a numerical CFD analysis that was undertaken using the boundary element method package, ANSYS AQWA (2010). Since the numerical CFD analysis uses a finite depth solution, it is necessary to set the water depth in the model to $200a$, in order to be comparable to the presented infinite depth analytical approximation.

The wave excitation forces on a truncated vertical cylinder in water of infinite depth

3.3.1 Wave excitation forces on a truncated cylinder

When calculating the surge, or horizontal, excitation force the only non-zero contribution is for $m = 1$, as this gives the only non-zero value in the integral $\int_0^{2\pi} \cos m\theta \cos\theta d\theta$, which occur in the force calculation. Furthermore, when integrating the velocity potential over the surface area, the integration is performed only over the curved surface of the cylinder and, hence, the exterior velocity potential at the surface boundary, $r = a$, given in Eqn. (3.42), is used. Therefore, the surge excitation force, $\hat{F}_{1,\text{ext}}$, is given as:

$$\begin{aligned}
 \hat{F}_{1,\text{ext}} &= i\rho\omega \iint_{S_B} \varphi_S^e(r, \theta, z) n_1 dS = -i\rho\omega \int_0^{2\pi} \int_0^b \varphi_S^e(a, \theta, z) \cos\theta a dz d\theta \\
 &= -\frac{\rho g A a}{k_0} \sum_{m=0}^{\infty} \varepsilon_m i^m \left\{ J_m(k_0 a) - J_m'(k_0 a) \frac{H_m^{(1)}(k_0 a)}{H_m^{(1)'}(k_0 a)} \right\} \\
 &\quad (1 - e^{-k_0 b}) \int_0^{2\pi} \cos m\theta \cos\theta d\theta \tag{3.43} \\
 &= -\frac{2\pi i \rho g A a}{k_0} \left\{ J_1(k_0 a) - J_1'(k_0 a) \frac{H_1^{(1)}(k_0 a)}{H_1^{(1)'}(k_0 a)} \right\} \\
 &\quad (1 - e^{-k_0 b}),
 \end{aligned}$$

where $n_1 = -\cos\theta$, which is the x-component of the unit normal, \mathbf{n} . Graphical representations of surge excitation forces as functions of incident wave frequency for various draft-to-radius ratios of truncated vertical cylinders are shown in Figure 3.2. As can be seen, the presented analytical solution and the numerical CFD solution are in good agreement even for quite modest draft-to-radius ratios, i.e. greater than unity. The correspondence between the analytical and numerical CFD solutions improves as the draft-to-radius ratio increases as would be expected, since the exterior velocity potential is derived assuming that the cylinder in question has infinite draft. The shaded region on the graph indicates where all the possible choices of draft-to-radius ratio which will return a valid solution. The upper bound is calculated where the draft is set to infinity and the lower bound is where the draft is set to zero, for a very thin plate, in the presented

The wave excitation forces on a truncated vertical cylinder in water of infinite depth approximation for the surge excitation force, given in Eqn. (3.43). Furthermore, the phase angle of the excitation forces as k_0a varies is shown in Figure 3.3, where the phase angle, β , is defined in the equation:

$$F(t) = |\hat{F}| \cos(\omega t + \beta), \quad (3.44)$$

where \hat{F} is the relevant excitation force. As can be seen from Figure 3.3, there is good agreement between the analytical solutions and the numerical CFD solutions for the phase angle over a range of normalised wave frequencies $k_0a = \omega^2 a/g$.

When calculating the heave, or vertical, excitation force from the velocity potential, the only non-zero value occurs when $m = 0$ as it gives the only non-vanishing term in the integral: $\int_0^{2\pi} \cos m\theta d\theta$. Furthermore, when integrating the velocity potential over the surface area, the integration is performed only over the base of the cylinder and, hence, the interior velocity potential, at $\bar{z} = 0$, given in Eqn. (3.41), is used. Therefore, the heave excitation force, $\hat{F}_{3,\text{ext}}$, is given as:

$$\begin{aligned} \hat{F}_{3,\text{ext}} &= i\rho\omega \iint_{S_B} \varphi_S^i(r, \theta, \bar{z}) n_3 dS = i\rho\omega \int_0^{2\pi} \int_0^a \varphi_S^i(r, \theta, 0) n_3 r dr d\theta \\ &= -i\rho\omega \sqrt{\frac{2}{\pi}} \sum_{m=0}^{\infty} \int_0^{2\pi} \int_0^a \int_0^{\infty} p_m(\xi) \frac{I_m(\xi r)}{I_m(\xi a)} d\xi r dr \cos m\theta d\theta \\ &= -2\pi i\rho\omega a \sqrt{\frac{2}{\pi}} \int_0^{\infty} p_0(\xi) \frac{I_1(\xi a)}{\xi I_0(\xi a)} d\xi, \end{aligned} \quad (3.45)$$

where $n_3 = -1$, which is the y-component of the unit normal, \mathbf{n} . Graphical representations of heave excitation forces as functions of incident wave frequency for various draft-to-radius of truncated vertical cylinders are shown in Figure 3.4 and the phase angle of the heave excitation forces is shown in Figure 3.3. Again, in Figure 3.4, as with Figure 3.2, the agreement between the presented analytical solution and the numerical CFD solutions is good and improves as the draft-to-radius ratio increases. However, in Figure 3.4, the upper bound for the normalised heave is calculated where the draft is set to zero, for a

The wave excitation forces on a truncated vertical cylinder in water of infinite depth

very thin plate, and the lower bound is where the draft is set to infinity in the presented approximation, given in Eqn. (3.45). This is to be expected as the water particle velocity decreases exponentially from the still water level downwards and, therefore, the vertical force on the base will, in turn, decrease as the draft-to-radius ratio increases.

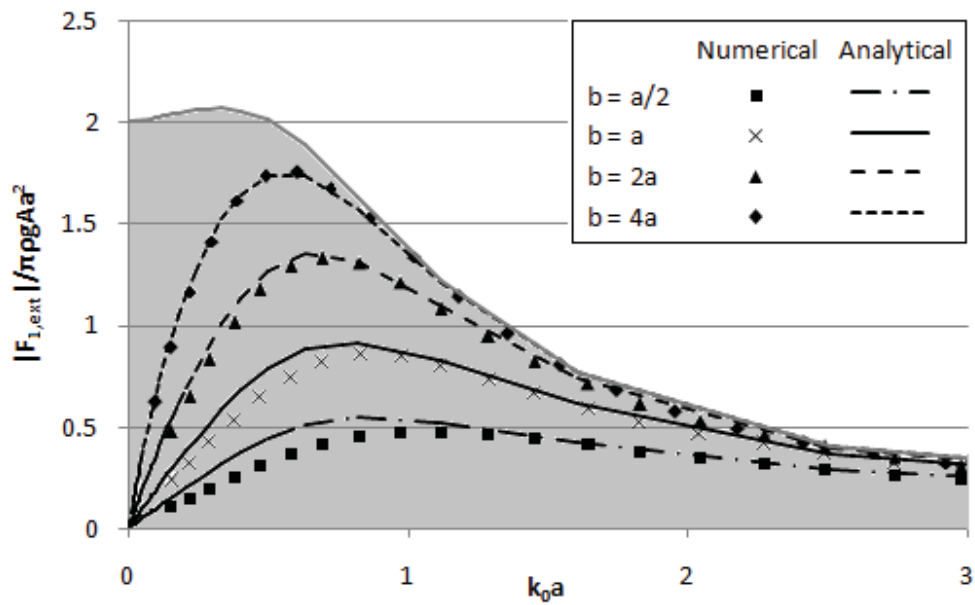


Figure 3.2: The normalised surge (or horizontal) excitation force, which is normalised by $\pi \rho g A a^2$, as a function of $k_0 a = \omega^2 a / g$, for various draft-to-radius ratios compared to a numerical CFD analysis (ANSYS AQWA). The shaded region denotes where a valid solution is possible.

The wave excitation forces on a truncated vertical cylinder in water of infinite depth

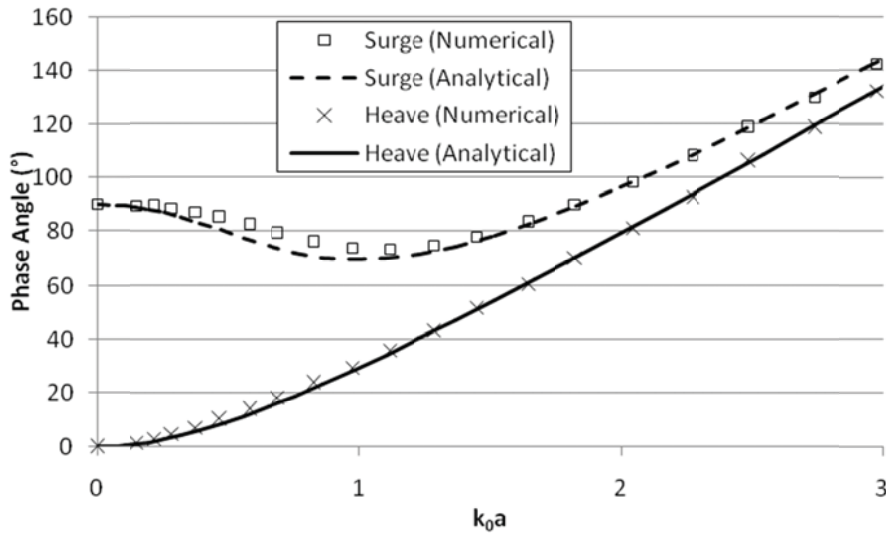


Figure 3.3: The phase angle for surge and heave, in the frequency domain, as a function of $k_0a = \omega^2 a/g$, compared to a numerical analysis

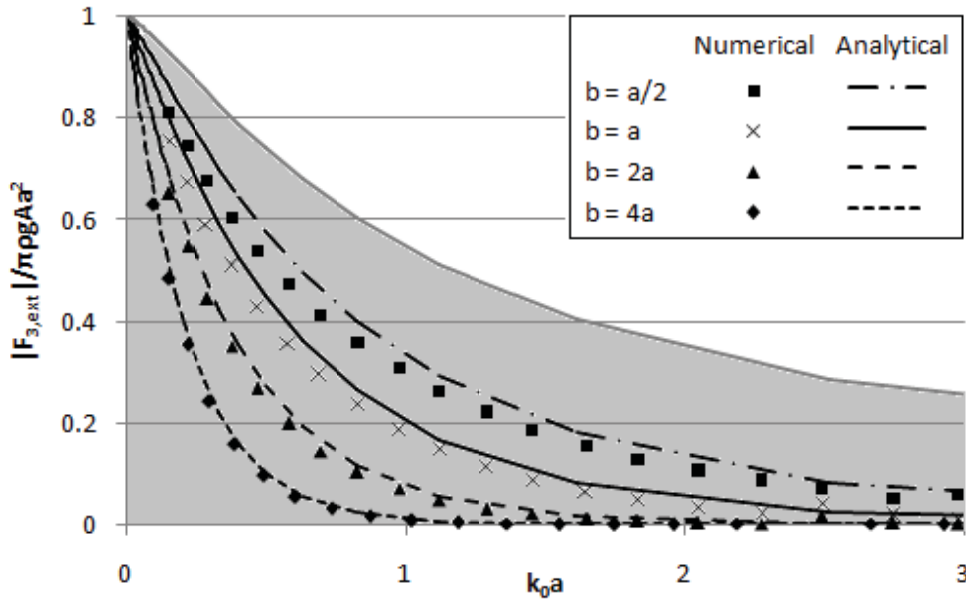


Figure 3.4: The normalised heave (or vertical) excitation force, which is normalised by $\pi \rho g A a^2$, as a function of $k_0a = \omega^2 a/g$, for various draft-to-radius ratios compared to a numerical CFD analysis (ANSYS AQWA). The shaded region denotes where a valid solution is possible.

The wave excitation forces on a truncated vertical cylinder in water of infinite depth

The pitch, or torque, excitation force arises from the surge and heave forces on the wetted surface of the cylinder. The pitch is taken about the axis which is transverse to the incident wave at the centre of the base, as shown by T in Figure 3.1. When calculating the pitch the only non-zero contribution, similar to surge, is from $m = 1$. Therefore, the pitch excitation force, $\hat{F}_{5,\text{ext}}$, is given as:

$$\begin{aligned}
\hat{F}_{5,\text{ext}} &= i\rho\omega \iint_{S_B} \varphi_S(r, \theta, z) n_5 dS \\
&= i\rho\omega \int_0^{2\pi} \int_0^b \varphi_S^e(a, \theta, z)(z - b) \cos \theta \, adz d\theta \\
&\quad - i\rho\omega \int_0^{2\pi} \int_0^a \varphi_S^i(r, \theta, 0)r^2 \cos \theta \, dr d\theta \\
&= -2\pi i\rho g A a \left\{ J_1(k_0 a) \right. \\
&\quad \left. - J_1'(k_0 a) \frac{H_1^{(1)}(k_0 a)}{H_1^{(1)'}(k_0 a)} \right\} \frac{1 - k_0 b - e^{-k_0 b}}{k_0^2} \\
&\quad + \pi i\rho\omega a^2 \sqrt{\frac{2}{\pi}} \int_0^\infty p_1(\xi) \frac{I_2(\xi a)}{\xi I_1(\xi a)} d\xi,
\end{aligned} \tag{3.46}$$

where

$$n_5 = (z - b)n_1 - r \cos \theta n_3 \tag{3.47}$$

Eqn. (3.47) is a rotational component $\mathbf{r} \times \mathbf{n}$ corresponding to the unit normal, \mathbf{n} , where \mathbf{r} is the distance from the centre of rotation to a point on the surface of the structure. Graphical representations of the analytical pitch excitation forces as functions of incident wave frequency for various draft-to-radius ratios of truncated vertical cylinders are shown in Figure 3.5. The trends of Figure 3.5 are very similar to that of Figure 3.2 as the magnitude of the pitch increases as the draft of the cylinder increases and the lower bound is where the draft is zero, for a very thin plate. However, since it is pitch that is being calculated and that is proportional to the draft an upper limit for the problem cannot

The wave excitation forces on a truncated vertical cylinder in water of infinite depth

be calculated. This is to be expected in view of the choice of axis about which the pitch is taken. It is also noted that the phase angle of the pitch excitation forces is the same as that for the surge excitation forces, as shown in Figure 3.3, and this was also observed by Garrett (1971) for the finite depth case.

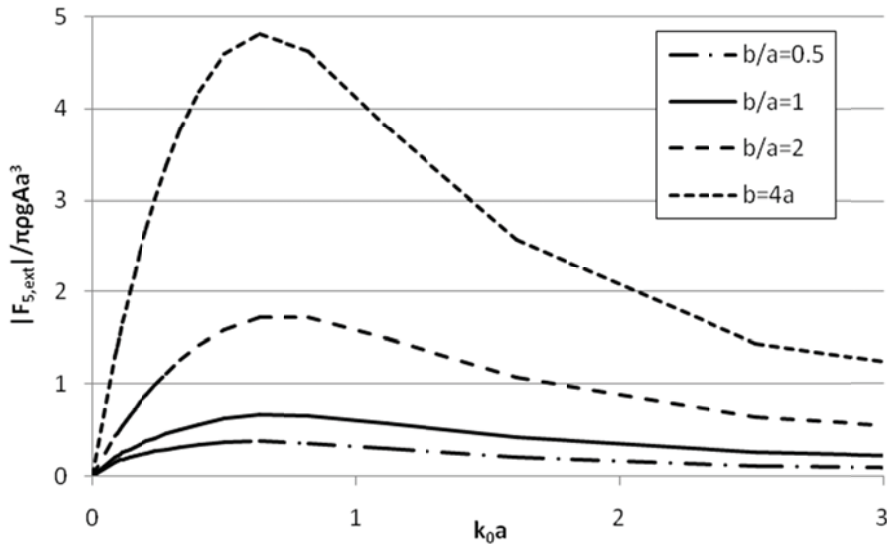


Figure 3.5: The normalised pitch (or torque) excitation force, which is normalised by $\pi \rho g A a^3$, as a function of $k_0 a = \omega^2 a/g$, for various draft-to-radius ratios.

The analytical approximation presented in this chapter is compared to a curtailed version of the finite depth solution of Bhatta and Rahman (1995; 2003) in Figure 3.6 and Figure 3.7 for the normalised surge and heave excitation forces, respectively. In order to ensure the two sets of results are comparable, the water depth was set to a value which is considered deep, $200a$, in the finite depth solution of Bhatta and Rahman (1995; 2003). The results from the corresponding numerical CFD analysis are also included in Figure 3.6 and Figure 3.7. It is clear to see from this comparison that the numerical model and analytical approximation yield similar trends of normalised force varying with normalised wave frequency $k_0 a = \omega^2 a/g$. As the draft-to-radius ratio increases, the two sets of results are found to be in very good agreement. Furthermore, it may be noted that the presented analytical approximation converges quicker to the numerical CFD than the

The wave excitation forces on a truncated vertical cylinder in water of infinite depth finite depth solution from Bhatta and Rahman (1995; 2003) in the case of the surge wave excitation force calculation.

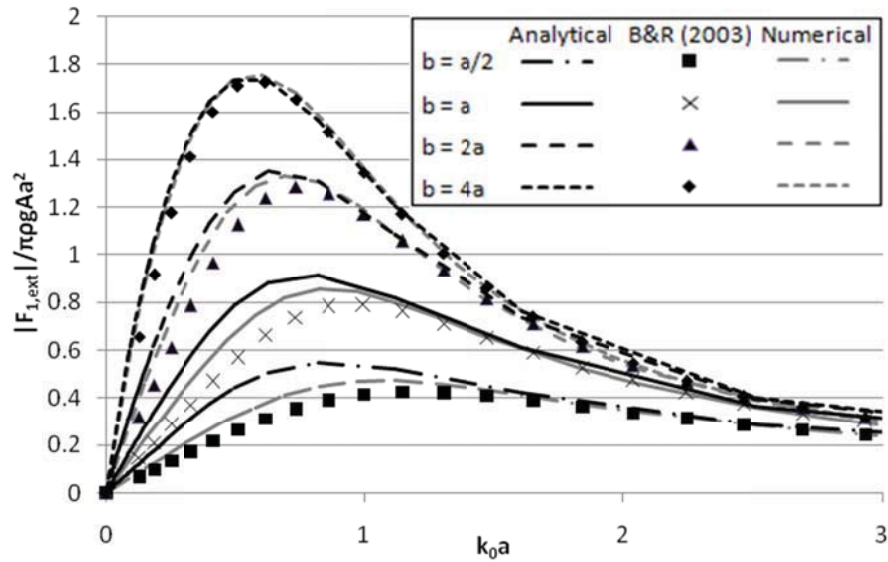


Figure 3.6: The normalised surge (or horizontal) excitation force, which is normalised by $\pi \rho g A a^2$, as a function of $k_0 a = \omega^2 a / g$, for various draft-to-radius ratios compared to Bhatta and Rahman (1995; 2003) and to the corresponding numerical CFD analysis (ANSYS AQWA).

The wave excitation forces on a truncated vertical cylinder in water of infinite depth

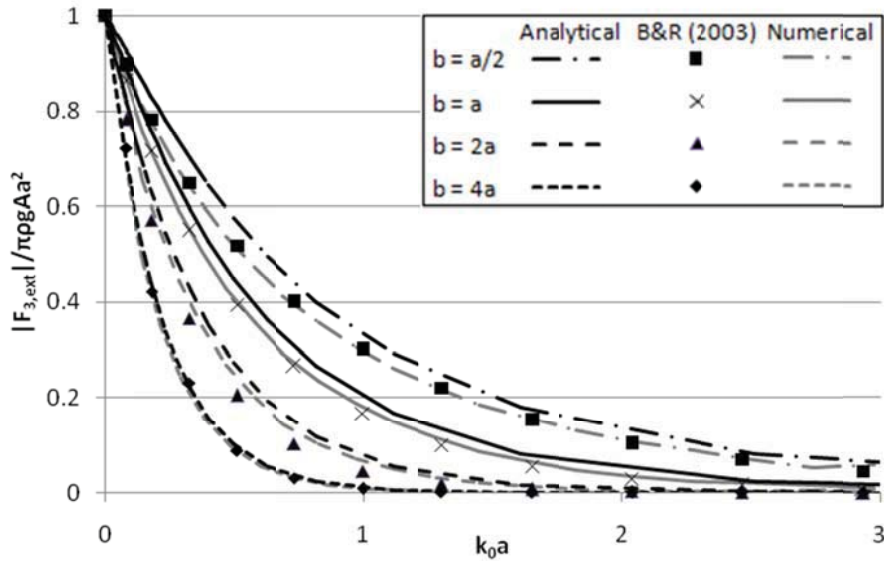


Figure 3.7: The normalised heave (or vertical) excitation force, which is normalised by $\pi \rho g A a^2$, as a function of $k_0 a = \omega^2 a/g$, for various draft-to-radius ratios compared to Bhatta and Rahman (1995; 2003) and to the corresponding numerical CFD analysis (ANSYS AQWA).

Using physical models, Fonseca et al. (2011) estimated the first order wave excitation forces on a truncated vertical cylinder with a radius, $a = 0.325$ m, and a draft, $b = 0.2$ m. Since the experimental results are being compared to an infinite depth approximation, only the regular wave observations for a water depth of 3 m are used in the comparison and are displayed in Figure 3.8. This independently observed experimental data is compared to the presented solution for a truncated vertical cylinder with a draft-to-radius ratio, $b/a = 0.62$. From Figure 3.8, it can be seen that the presented analytical expressions, given by Eqn. (3.43) and Eqn. (3.45), are in good agreement with the experimental data. The differences between the two solutions for the surge motion may be contributed to the earlier discussion that the analytical solution is more accurate for a draft-to-radius ratio greater than unity. Furthermore, the differences may be as a result of experimental or measurement errors with the experimental set-up, which is detailed in

The wave excitation forces on a truncated vertical cylinder in water of infinite depth

Figure 2.6 (c). However, error bars were not included in the results of Fonseca et al. (2011).

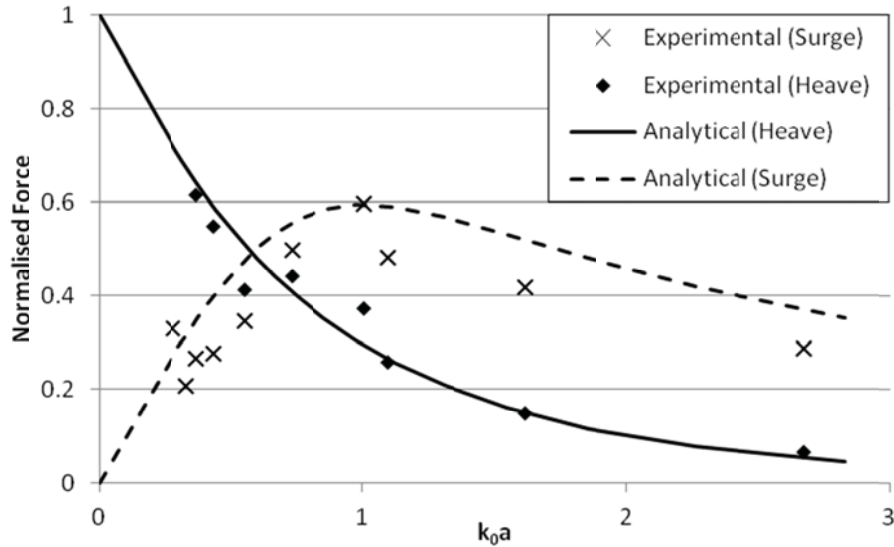


Figure 3.8: Comparison of the normalised heave and surge wave excitation forces, which is normalised by $\pi\rho g A a^2$ with the experimental results of Fonseca et al. (2011), as a function of $k_0 a = \omega^2 a/g$. The draft-to-radius ratio, $b/a = 0.62$.

3.3.2 Wave excitation forces on a cylinder of infinite depth

The scattering velocity potential, φ_S , was derived in Section 3.2.2 for a cylinder of infinite draft yielding the solution given in Eqn. (3.41). On the other hand, for a bottom mounted cylinder in water of finite depth, d , and using a concurrent axis orientation as that presented in this chapter, MacCamy and Fuchs (1954) obtained the solution:

The wave excitation forces on a truncated vertical cylinder in water of infinite depth

$$\begin{aligned} \varphi_S(r, \theta, z) = & -\frac{gA \cosh k_0(d-z)}{\omega \cosh k_0 d} \sum_{m=0}^{\infty} \epsilon_m i^{m+1} \left\{ J_m(k_0 r) \right. \\ & \left. - J_m'(k_0 a) \frac{H_m^{(1)}(k_0 r)}{H_m^{(1)'}(k_0 a)} \right\} \cos m\theta, \end{aligned} \quad (3.48)$$

for a bottom mounted cylinder in water of finite depth, d . For the infinite depth case, the z -component of the equation is replaced with $e^{-k_0 z}$. Thus, the solution presented in Eqn. (3.41) corresponds with the infinite depth version of MacCamy and Fuchs (1954) solution given in Eqn. (3.48). The surge excitation force, in the frequency domain, $\hat{F}_{1,\text{ext}}$, is then calculated as follows:

$$\begin{aligned} \hat{F}_{1,\text{ext}} &= i\rho\omega \iint_{S_B} \varphi_S(r, \theta, z) n_1 dS = i\rho\omega \int_0^{2\pi} \int_0^{\infty} \varphi_S(a, \theta, z) n_1 a dz d\theta \\ &= -\frac{\rho g A a}{k_0} \sum_{m=0}^{\infty} \epsilon_m i^m \left[J_m(k_0 a) \right. \\ &\quad \left. - J_m'(k_0 a) \frac{H_m^{(1)}(k_0 a)}{H_m^{(1)'}(k_0 a)} \right] \int_0^{2\pi} \cos m\theta \cos \theta d\theta \\ &= -\frac{2\pi i \rho g A a}{k_0} \left[J_1(k_0 a) - J_1'(k_0 a) \frac{H_1^{(1)}(k_0 a)}{H_1^{(1)'}(k_0 a)} \right], \end{aligned} \quad (3.49)$$

where $n_l = -\cos \theta$ and the only non-zero solution to $\int_0^{2\pi} \cos m\theta \cos \theta d\theta$ is when $m = 1$. Since the exterior velocity potential is calculated for the exterior domain, the solution is the same as when $b = \infty$ in Eqn. (3.43). In Figure 3.9, the presented solution is also compared to a numerical CFD solution, performed using the BEM software ANSYS AQWA (2010). Since the draft of the cylinder cannot be set to infinity in the numerical CFD solution, a draft-to-radius ratio, $b/a = 20$, is used. This comparison of the two solutions is found to be in good agreement except at low frequencies. This difference is as a result of the parameter, $b/a = 20$, in the numerical CFD solution and greater values for the draft-to-radius ratio would yield closer agreement. When this parameter is applied

The wave excitation forces on a truncated vertical cylinder in water of infinite depth to the analytical solution, i.e. $b/a = 20$, the two solutions match up very well as can be seen in Figure 3.9.

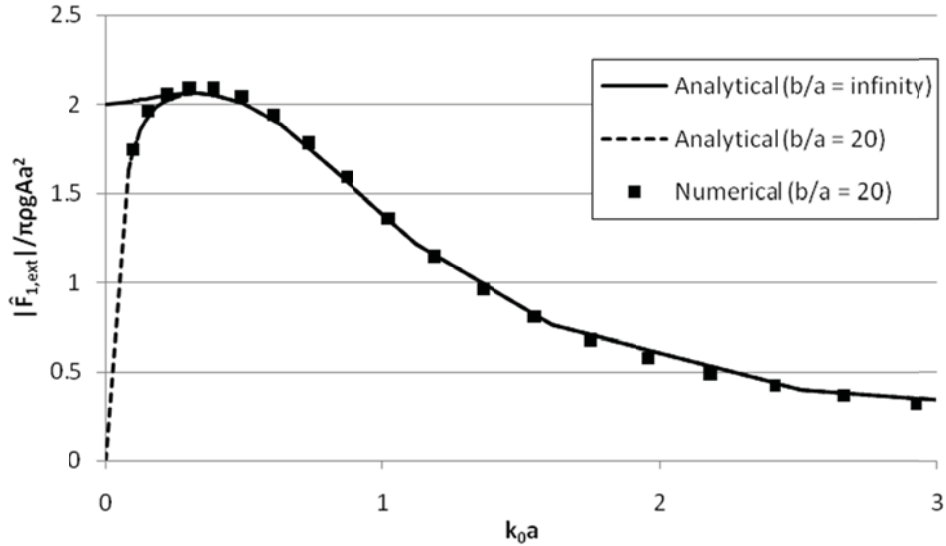


Figure 3.9: Normalised surge excitation force, which is normalised by $\pi \rho g A a^2$, as a function of $k_0 a = \omega^2 a/g$, and compared to the results from a finite depth numerical CFD analysis (ANSYS AQWA).

3.4 Discussion and conclusions

An analytical approximation to determine the wave excitation forces, by solving the scattering problem, on a floating truncated vertical cylinder in water of infinite depth has been presented in this chapter. The novel contribution of the presented analytical approximation is that it provides a solution which is far easier to use and implement than the already available analytical solutions. For example, the solution for the finite depth case provided by Bhatta and Rahman (1995; 2003) requires a considerable amount of further work if numerical values for a particular case are needed. On the other hand, the formulation presented in this chapter yields an easy to implement analytical approximation for the surge, heave and pitch wave excitation forces on a truncated

The wave excitation forces on a truncated vertical cylinder in water of infinite depth cylinder. This was achieved by imposing an approximation in deriving the unknown coefficients in the exterior region. Furthermore, the presented analytical approximation still retains a high level of accuracy in calculating the heave and surge wave excitation forces, when the draft-to-radius ratio is greater than unity.

The method of separation of variables is employed in order to formulate the velocity potentials and the unknown coefficients are derived by matching these potentials along their common boundaries. In order to create an analytical solution, the exterior velocity potential is derived for the case of a vertical cylinder of infinite draft and the interior velocity potential is calculated by matching across their common boundary. However, it should be noted that this assumption is a good approximation when the draft-to-radius ratio is greater than or equal to unity (i.e. $b/a \geq 1$), which can be seen in Figure 3.2, Figure 3.4 and Figure 3.5, where the presented analytical solution and numerical CFD solution (ANSYS AQWA) are in increasingly better agreement as the draft-to-radius ratio (b/a) increases.

The relationships between wave excitation forces and normalised wave frequency $k_0 a = \omega^2 a/g$ are shown graphically in Figure 3.2, Figure 3.4 and Figure 3.5 for a truncated cylinder having various draft-to-radius ratios. It may be noted that the pitch excitation forces are also derived in the study, along with the heave and surge excitation forces. These results are validated by comparing to a numerical CFD solution, performed using the BEM software ANSYS AQWA (2010), and they are found to be in very good agreement. A shaded region on the graph is also included indicating where a viable solution may be obtained. For surge and pitch motions, the upper bound is calculated where the draft is infinite and the lower bound is where the draft is zero, for a very thin plate. However, for heave motion, the upper bound of the viable solution region is calculated where the draft is zero, for a very thin plate, and the lower bound is where the draft is infinite. This is to be expected as the water particle velocity decreases exponentially from the still water level downwards and, therefore, the vertical force on the base will, in turn, decrease as the draft-to-radius ratio increases. These three figures (Figure 3.2, Figure 3.4 and Figure 3.5) and the associated approximations provide an

The wave excitation forces on a truncated vertical cylinder in water of infinite depth efficient and relatively quick solution to the problem for an engineer or professional investigating the wave excitation forces on a floating structure in deep water.

The phase angles of the wave excitation forces, relative to the incident wave, are also presented graphically in Figure 3.3 and compared to the results from a numerical CFD analysis. The presented analytical results were found to be in good agreement with the results from the numerical CFD analysis. Furthermore, when compared to the independently observed experimental data given in Fonseca et al. (2011), the analytical solution for a truncated vertical cylinder shows good agreement, as shown in Figure 3.8.

In addition, the presented analytical approximation is compared to a curtailed version of the finite depth solution of Bhatta and Rahman (1995; 2003), which is shown graphically for the normalised surge and heave excitation forces in Figure 3.6 and Figure 3.7, respectively. It is clear from this comparison that similar trends occur with respect to the relation between the normalised excitation forces and the normalised wave frequency $k_0 a = \omega^2 a/g$ for the presented analytical approximation and a curtailed version of the finite depth solution of Bhatta and Rahman (1995; 2003), as with the numerical CFD results. As the draft-to-radius ratio increases, the two sets of results are found to be in very good agreement.

Furthermore, when deriving the exterior velocity potential it was found to match to the infinite depth version of the MacCamy and Fuchs equation (MacCamy and Fuchs, 1954). In addition, the presented solution, for the infinite draft cylinder case, is also compared to a numerical CFD solution and they are found to be in very good agreement, which can be seen in Figure 3.9.

The analytical solution provided in this chapter provides an engineer with a very good approximation of the wave excitation forces on a structure which may be represented by a truncated cylinder. Furthermore, if only the $k_0 a$ value is known, the maximum forces can easily be calculated from the analytical solution, or estimated from the shaded regions of the graphs in Figure 3.2 and Figure 3.4, to aid in the design stage of an offshore structure.

Development of a numerical model for a wave tank

Chapter 4
**Development of a numerical model for a wave
tank**

4.1 Introduction

In the design of any floating or fixed marine structure, it is vital to test models in order to understand the fluid/structure interaction involved. Inevitably laboratory experiments will be carried out in a wave tank or wave basin, followed by tests on scale models in real sea conditions. However, with the developments in computational fluid dynamics (CFD) software and processing power of computers, it is now possible to carry out inexpensive and relatively quick initial studies. That is, provided that the numerical model used is representative of the real life environment.

The numerical models used to model wave-tanks are known as numerical wave tanks (NWTs). NWTs are developed using a variety of numerical techniques, including the boundary element method (BEM), the finite element method (FEM), finite volume technique and the finite difference method, as discussed in Section 2.6. In a NWT, a wave is generated at the input boundary and is dissipated near the output boundary.

As discussed in Section 2.6, studies relating to the development of numerical models of wave tanks have been, in general, to either model a physical wave tank in order to replicate a physical experiment or to explore the interaction of a wave on a specified structure or process. Therefore, in this chapter, an efficient NWT model is developed by altering its overall dimensions, as shown in Figure 4.1. In particular the overall height, the base length and mesh setup are varied to obtain an efficient model. These dimensions are dependent on the period of the desired deep water waves. The model works the same way as an experimental wave tank. The waves are generated at the model input boundary using a flap-type wavemaker and there is a sloped beach placed at the model output boundary in order to damp out the wave, which can be seen in Figure 4.1. The CFD software package used in this analysis is ANSYS CFX (ANSYS Inc., 2009). It uses a finite volume method in order to solve the Reynolds-averaged Navier-Stokes equations (RANSE), which accounts for turbulence and viscosity. When the analysis is extended to fluid-structure interaction, ANSYS Mechanical is used in conjunction with CFX as a motion solver.

Development of a numerical model for a wave tank

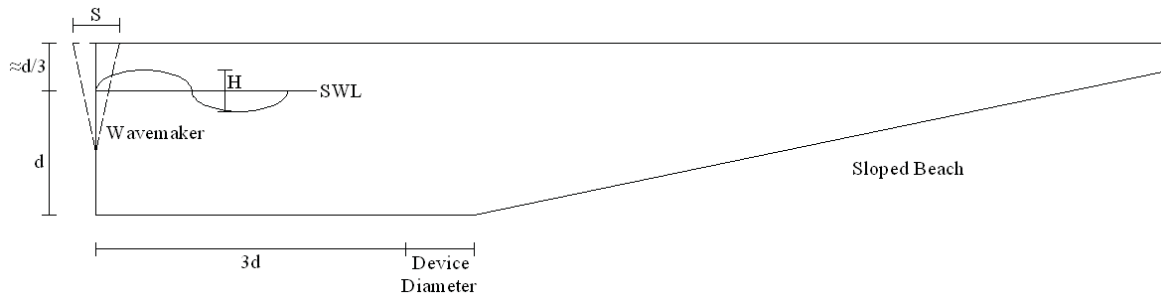


Figure 4.1: Overall dimensions of model. S , H and d are discussed in Section 4.2 and ‘Device Diameter’ refers to the horizontal length of the structure being analysed.

Furthermore, 2-dimensional CFD models are validated using wavemaker theory (WMT) for deep water waves. The experimental validation of WMT was achieved by Ursell et al. (1960) using an experimental wave tank. In addition, the water particle velocities determined by the CFD model are compared to Airy’s linear wave theory (LWT). Therefore, the waves generated by the model will be validated by comparing to both LWT and WMT. Thus, the main objective of this chapter is to present a guide to designing a CFD model that can accurately produce both linear regular deep water waves and linear regular finite depth water waves. Furthermore, the model outlined in this chapter will represent an optimised numerical model for a wave tank, as its overall dimensions will be dependent on the period of the desired waves. In order to achieve this model, a number of convergence tests were carried out. Finally, a case study of a real world application of the methodology derived is undertaken. It is an analysis of the interaction between a linear deep water wave and a floating truncated vertical cylinder.

4.2 Methodology

The CFD model developed in this chapter is similar in set-up to that of an experimental wave tank. However, the model dimensions are to be recalculated in order to optimise the model dependent on the period of the desired waves. An illustration of the dimensioning

Development of a numerical model for a wave tank

is shown in Figure 4.1, where d is the height of the still water level (SWL), S is the stroke length of the wavemaker and H is the height of the generated wave. Furthermore, since the generated waves are to be compared to LWT, the waves created are assumed to be of small amplitude relative to their length. Small amplitude waves are defined by the steepness relation $H/L_0 \leq 0.03$ (Ursell et al., 1960), where L_0 is the wavelength. The response of wave energy converters (WEC's) to small amplitude waves is of interest as their performance needs to be optimised when the resource is at its least. In other words, the WEC should be tuned to the expected properties of the dominant small amplitude waves.

The set-up for the CFD model is divided into three stages: (1) the geometry setup, which defines the physical dimensions of the model, (2) the mesh setup, where a mesh is created and is refined at the still water level (SWL) to capture the free surface accurately and (3) the wave water, or physics, setup, which defines the analysis type, the domain setup, the motion of the wavemaker, the initial water height and other characteristics of the water and air-water interaction. In defining the domain set-up, a number of assumptions are included. The surface tension at the air-water interface is assumed to be negligible. The air is specified to a temperature of 25 °C and, therefore, its density is specified to be 1.185 kg/m³. Furthermore, an isothermal heat transfer model is specified, which is homogeneous. The fluid (water) temperature is defined as 25 °C and its viscosity is 8.899 x 10⁻⁴ kg/ms. Furthermore, its density is given as 1030 kg/m³ to represent salt water.

The top boundary of the model has an '*opening boundary*' condition, which allows a fluid to cross the boundary in either direction. The Cartesian components of the flow velocity may be specified at the boundary, as follows (ANSYS Inc., 2011):

$$v_{opening} = u_{1,spec}\mathbf{i} + u_{2,spec}\mathbf{j} \quad (4.1)$$

where $v_{opening}$ is the flow velocity at the boundary and $u_{1,spec}$ and $u_{2,spec}$ are the specified horizontal and vertical flow velocities, respectively. An '*opening boundary*' condition can also be specified with a relative pressure value, as follows (ANSYS Inc., 2011):

$$p_{opening} = p_{spec} \quad (4.2)$$

where $p_{opening}$ is the relative pressure at the boundary and p_{spec} is the specified relative pressure. The value is interpreted as relative total pressure for inflow and relative static pressure for outflow. However, in this analysis, since there are two types of fluids in the model, it is specified that only air may cross the boundary. In addition, a relative pressure with a value 0 Pa normal to the plane of the boundary is specified at boundary. The boundary condition at the wavemaker is a '*wall boundary*' with a specified displacement, which is inputted using the ANSYS CFX expression language (CEL) (ANSYS Inc., 2009). There are symmetry boundary conditions specified for the adjacent sides, in order to create a model that is infinitely wide, and the remaining boundaries are assigned a static wall boundary condition. These '*wall boundary*' types are specified with a '*free slip*' condition which specifies no friction at the walls causing full velocity reflection.

4.2.1 Wave generation techniques

A number of techniques may be employed when generating the initial wave. Physical and numerical methods are explored in this study in order to determine a suitable method of wave generation. In experimental wave tanks, a number of types of physical methods of wave generation are used. The physical methods explored in this study are the paddle-type, flap-type and wedge-shaped plunger-type wavemakers, which are illustrated in Figure 4.2. However, since a numerical model for a wave tank is being developed, numerical techniques may be employed.

The numerical method being considered is to specify the water elevation and, using Airy's linear wave theory, the water particle velocities within the fluid domain at the boundary wall on the left side of the tank at each time-step. Therefore, the water elevation, in the time domain for water of finite depth, is given as:

$$\eta(t) = A \cos(-\omega t - \varepsilon_0) \quad (4.3)$$

Development of a numerical model for a wave tank

and the water particle velocities, in the time domain, are given as:

$$u_1(t) = A\omega \frac{\cosh(k_0 y')}{\sinh(k_0 d)} \cos(-\omega t - \varepsilon_0) \quad (4.4)$$

and

$$u_2(t) = A\omega \frac{\sinh(k_0 y')}{\sinh(k_0 d)} \sin(-\omega t - \varepsilon_0) \quad (4.5)$$

where ε_0 is the initial phase angle, $u_1(t)$ and $u_2(t)$ are the horizontal and vertical water particle velocities, respectively, and y' is the vertical distance from the base of the model.

For the purpose of the study in this chapter, a flap-type wavemaker was selected as the wave generation method. Two orientations of this type of wavemaker are analysed; one with the flap hinged at the base of the model and the other with the flap hinged at half the mean water depth from the base of the model.

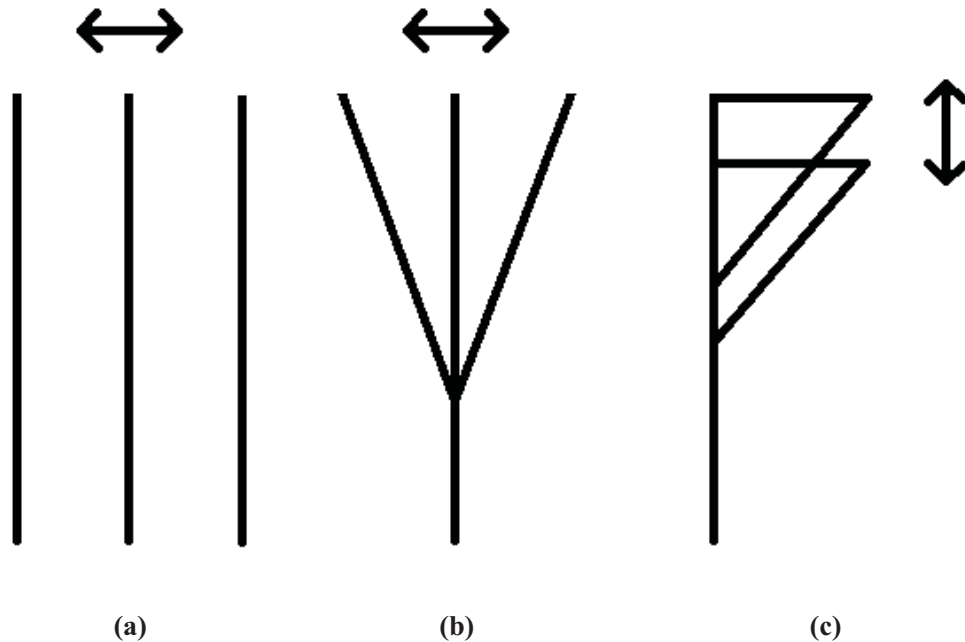


Figure 4.2: Physical wavemakers explored in this study (a) the paddle-type (b) flap-type (c) wedge-shaped plunger-type.

4.2.2 Wave energy dissipation

A variety of techniques have been employed by a number of researchers to dissipate, or damp out, the waves at the end of the model opposite the wavemaker boundary. Ning and Teng (2007) and Ning et al. (2008) used an artificial beach employed along the free surface boundary of their model. Liang et al. (2010) introduced a dissipation zone by adding terms to the momentum equations in order to eliminate wave reflection. In this study, a method of increasing the viscosity of the water in the dissipation zone and the use of a sloped beach to damp out the waves using its physical properties, a technique which is also used by Lal and Elangovan (2008), are explored. A study to determine the optimum beach slope to provide damping of the wave is detailed in Section 4.3.1. For the analysis performed in this chapter, a beach with the determined optimum slope is used to dissipate the wave energy at the end of the model opposite the wavemaker boundary. Furthermore, the effect of a coarse mesh along the SWL is used to dissipate the wave energy in the dissipation zone of the model, which is discussed further in Section 4.3.1.

4.2.3 The governing equations

The method on which the solver in ANSYS CFX is based on is the finite volume technique (ANSYS Inc., 2009). This technique divides the region of interest into sub-regions and discretises the governing equations in order to solve them iteratively over each sub-regions. Therefore, an approximation of the value of each variable at points throughout the domain is achieved.

The governing equations that need to be solved by the ANSYS CFX solver are the mass continuity equation, which is given as:

$$\frac{\partial \rho}{\partial t} + \frac{\partial(\rho u_1)}{\partial x} + \frac{\partial(\rho u_2)}{\partial y} = 0 \quad (4.6)$$

and the Navier-Stokes equations, which are given as:

$$\begin{aligned} \rho \left(\frac{\partial u_1}{\partial t} + u_1 \frac{\partial u_1}{\partial x} + u_2 \frac{\partial u_1}{\partial y} \right) \\ = -\frac{\partial p}{\partial x} + 2\mu \frac{\partial^2 u_1}{\partial x^2} + \frac{\partial}{\partial y} \left(\mu \left(\frac{\partial u_1}{\partial y} + \frac{\partial u_2}{\partial x} \right) \right) + F_1 \end{aligned} \quad (4.7)$$

$$\begin{aligned} \rho \left(\frac{\partial u_2}{\partial t} + u_1 \frac{\partial u_2}{\partial x} + u_2 \frac{\partial u_2}{\partial y} \right) \\ = -\frac{\partial p}{\partial y} + 2\mu \frac{\partial^2 u_2}{\partial y^2} + \frac{\partial}{\partial x} \left(\mu \left(\frac{\partial u_1}{\partial y} + \frac{\partial u_2}{\partial x} \right) \right) + F_2 - \rho g \end{aligned} \quad (4.8)$$

where t is time, x is the horizontal distance from the wavemaker, y is the vertical height from the SWL and increases with depth, u_1 is the horizontal flow velocity, u_2 is the vertical flow velocity, F_1 is the body force on the fluid in the horizontal direction, $F_2 - \rho g$ is the body force on the fluid in the vertical direction, p is pressure and μ is viscosity.

In order to determine the position of the free surface, or air-water boundary, the volume of fluid method is applied. This technique was also employed by Liang et al. (2010). This method adds another governing equation, given by:

$$\frac{\partial q_i}{\partial t} + u_1 \frac{\partial q_i}{\partial x} + u_2 \frac{\partial q_i}{\partial y} = 0, i = 1,2 \quad (4.9)$$

where q_i is the volume fraction of the fluid i with $\sum_{i=1}^2 q_i = 1$., where ‘1’ denotes air and ‘2’ denoting water. The free surface is then approximated as at the position of the minimum of value $|q_1 - q_2|$ along the model.

4.2.4 Optimisation of the length/height of the model

The height of the model is dictated by a number of factors; the still water level, the maximum height of the waves and the response amplitude and height of the device or structure being analysed. Therefore, since the tank is being designed for deep water wave

Development of a numerical model for a wave tank

theory, the height of the tank is estimated to be 4/3 times the still water level, as this will leave sufficient space between the SWL and the top boundary (*'opening boundary'*) of the model for the device, or structure, to oscillate as a result of the incoming wave.

As it is a numerical model, the geometry of the wave tank can be easily changed. As a result of this, the geometry can be optimised depending on the period of the incoming wave. As the incoming waves will be almost linear, Airy's linear wave theory can be used to predict the minimum depth of the water, as follows (Coastal Engineering Research Center, 1977):

$$\frac{d}{L_0} > \frac{1}{2} \quad (4.10)$$

where $L_0 = \frac{gT^2}{2\pi}$, g is gravity and T is the wave period. Thus, Eqn. (4.10) can be written as:

$$d > \frac{gT^2}{4\pi} \quad (4.11)$$

This relationship between the minimum still water level, d , and the wave period, T , is shown graphically in Figure 4.3.

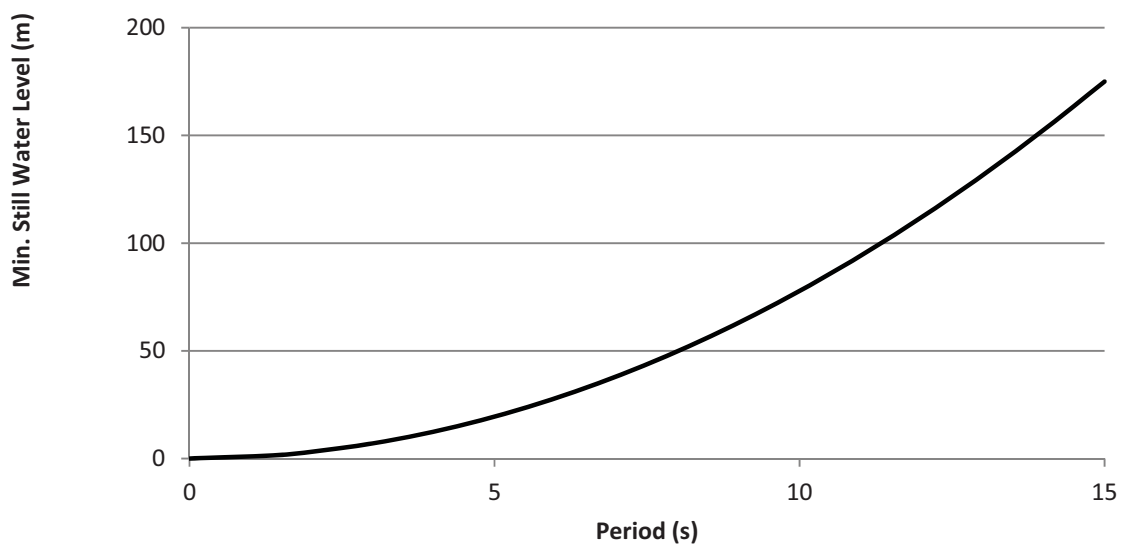


Figure 4.3: Minimum still water level as the wave period varies.

The length of the model is dictated by the SWL, the beach slope and the diameter, or width, of the WEC device being investigated. Dean and Dalrymple (1984) show that the velocity potential for a 2-D wavemaker is divided into two parts; the first is that of the progressive wave and the second of the standing wave, which decays away from the wavemaker. It is also shown that the standing wave part is negligible after a distance of three times the SWL, or $3d$, away from the wavemaker. Therefore, from this distance onwards the progressive wave is only present and, as a result, the optimum placing of a device in a wavetank is at this distance. An illustrated summary of these dimensioning techniques is shown in Figure 4.1.

4.2.5 Optimisation of the mesh for the model

It is essential to optimise the mesh size as this will reduce computational effort. This is particularly important for 3-D modelling of wave tanks. A significant observation that must be noted is the sensitivity of the wave elevation to the mesh refinement. Therefore, it is essential to optimise the method of meshing employed, which should be dependent on both the height and period of the wave being created.

In Table 4.1 and Figure 4.4, a number of meshing techniques are compared in order to determine which method would provide the most optimum mesh. The generated wave used in the comparison has a period of 1.35 s, and it adheres to finite depth theory, as $d = 1.5$ m. A beach slope of 1:5 is employed to dissipate the wave energy, as this was the optimum beach slope as found in Section 4.3.1. The variables used in the comparison are: (1) the mesh relevance, which defines the fineness of the overall mesh, (2) the maximum mesh element size and (3) the radius of the '*Sphere of Influence*' being used and its element size. The '*Sphere of Influence*' technique is a mesh refinement method of ANSYS CFX. It requires a maximum element size, coordinate in the model domain for the sphere centre and a radius to be defined by the user. In this analysis, the '*Sphere of*

Development of a numerical model for a wave tank

Influence’ technique is employed in order to perform mesh refinement along the SWL, between the wavemaker and the beginning of the beach.

Table 4.1: Summary of parametric study of mesh set-up

Model I.D.	No. of Elements	Mesh Fineness (Relevance)	Max. Element Size	Sphere of Influence		Wave Height
				Radius	Element Size	
WT1	2424	Fine 100	Undefined	0.3 m	0.02 m	0.125 m
WT2	4830	Fine 0	0.15 m	0.2 m	0.02 m	0.18 m
WT3	6231	Fine 100	0.12 m	0.3 m	0.02 m	0.17 m
WT4	6440	Fine 0	0.15 m	0.2 m	0.01 m	0.19 m
WT5	8900	Fine 0	0.15 m	0.2 m	0.005 m	0.2 m

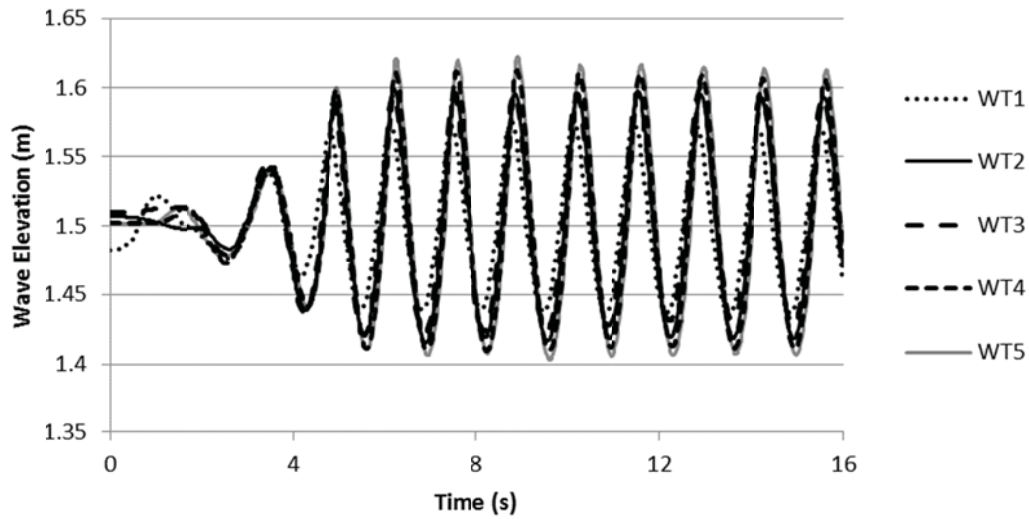


Figure 4.4: Comparison of wave elevation at 5 m, or 3d, from the wavemaker for various mesh set-ups given in Table 4.1.

Development of a numerical model for a wave tank

From Figure 4.4, it is clear that the most efficient mesh is that in model WT2, which contains 4830 elements, as it provides a wave that is insignificantly different to that obtained from model WT4, which contains 6440 element mesh. Therefore, the optimum mesh for the model utilises both a maximum element size and the ‘*Sphere of Influence*’ technique.

During the study, it was found that the radius of the sphere is dependent on the height of the wave. As a result, the radius is specified as the expected height of the wave and an element size of one tenth the radius was found to be sufficient. The optimum minimum element size was established in this study, i.e. for $T = 1.35$ s, and is affected by the wavelength, L_0 . Therefore, a simple linear relationship was established to estimate the minimum element size when $T = n$ sec and is given as:

$$\text{Min. ElementSize} = \frac{L_0[T = n \text{ sec}]}{L_0[T = 1.35 \text{ sec}]} \times 0.15 \text{ m} \quad (4.12)$$

This relationship holds true when the beach slope is at 1:5 and the meshing method above is adhered to. Furthermore, a typical mesh for the model is shown in Figure 4.5.

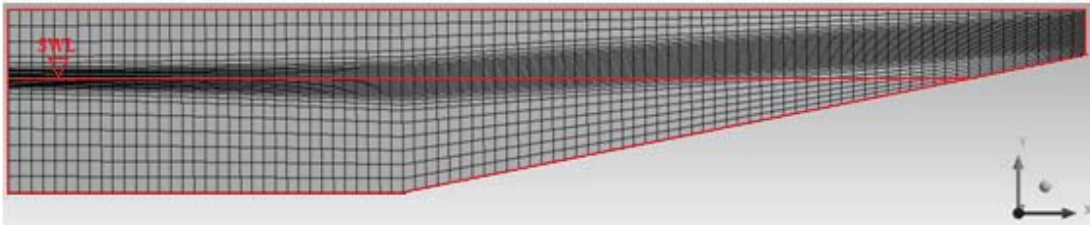


Figure 4.5: Typical longitudinal elevation of the mesh for CFD model with refinement along the SWL, which is illustrated in the schematic.

4.2.6 Time-step interval and total time

The time-step interval and total time are both dependent on the wave period. As the device is being placed at three times the still water level, $3d$, the waves of interest are those at this location. From Figure 4.6, it is clear that waves of various periods are fully

Development of a numerical model for a wave tank

developed at this location after six cycles. Therefore, a total time equal to ten times the wave period is sufficient to allow comparison between the waves generated by the numerical model and those predicted by LWT and WMT, with the waves created during the last four cycles being those of interest, i.e. fully developed waves.

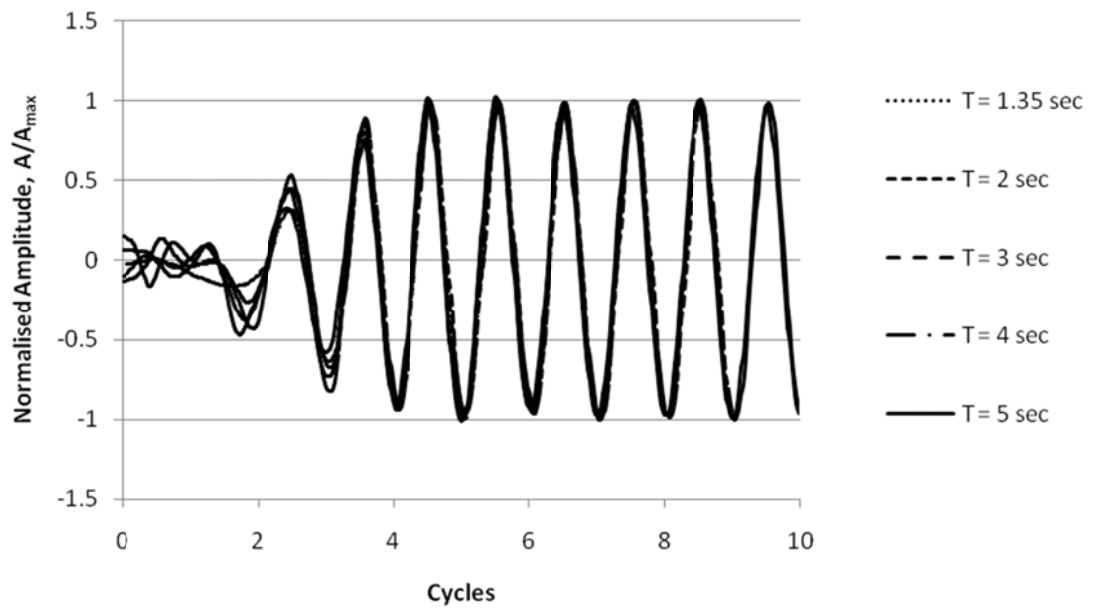


Figure 4.6: The normalised amplitude wave profile for various wave periods at a distance 3d from the wavemaker for the first ten cycles.

Furthermore, a parametric study was carried out in order to determine the optimum integration time-step interval. As accurate velocity results are one of the main requirements from the simulation, it is necessary to use a relatively small integration time-step interval. The results of this parametric study are shown in Figure 4.7 and it is clear that the optimum time-step is found by dividing the wave period into 50 intervals ($T/50$). This agrees closely with the findings of Ning and Teng (2007), which stated the maximum time-step interval is the wave period divided by 40 ($T/40$).

Development of a numerical model for a wave tank

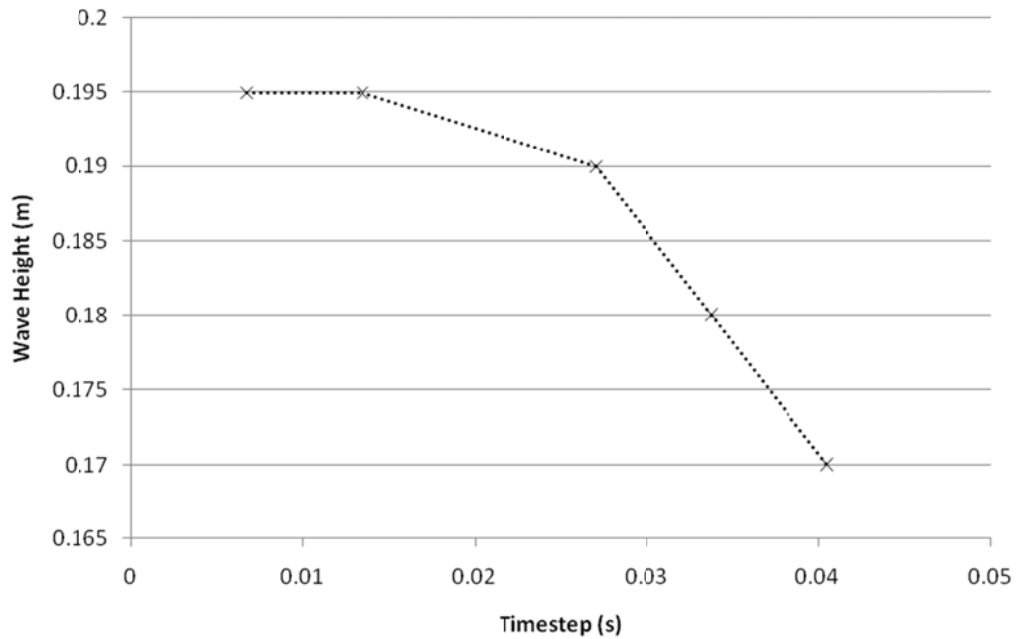


Figure 4.7: Results from a parametric study comparing the effect of the time-step on the wave height for a wave period of 1.35s.

4.3 Results

4.3.1 Beach slope study

The optimum beach slope to provide damping of the wave, or to dissipate the wave energy, at the end of the model opposite the wavemaker boundary is explored over a variety of slopes. The mesh sensitivity, discussed in Section 4.2.5, is used as an advantage near the beach, as a coarse mesh will produce a damping effect on the wave. This technique is also employed by Park et al. (1999) and Park et al. (2004) in the dissipation zone as the mesh becomes coarser horizontally along the zone. Therefore, in this chapter, a combination of the physical effect from a sloped beach and the effect of a coarse mesh along the SWL is used to dissipate the wave energy in the dissipation zone of the model.

Development of a numerical model for a wave tank

Models with beach slopes ranging from 1:3 to 1:6 were investigated. The measured transient wave elevations for various beach slopes at 1.5 m from the end of the beach are plotted in Figure 4.8. A distance of 1.5 m from the end of the beach was chosen as it was a monitoring point near the end of the beach, which was without the presence of nonlinearities, induced as a result of the wave breaking. It was found that the optimum beach slope is 1:5, as the difference in the degree of damping provided compared to a slope of 1:6 is negligible. This result contradicts the findings of Lal and Elangovan (2008), where an optimum beach slope of 1:3 was determined. As can be seen in Figure 4.8, a model containing a beach slope of 1:3 would induce the least damping of the slopes investigated. A comparison between the wave elevation of the fully formed progressive wave and the dissipated wave, near the end of the beach, is shown in Figure 4.9. It is clear to see that damping of the wave has occurred as a result of the sloped beach. The generated wave used in this study is the same as the one used in Section 4.2.5 and employs the optimum mesh method.

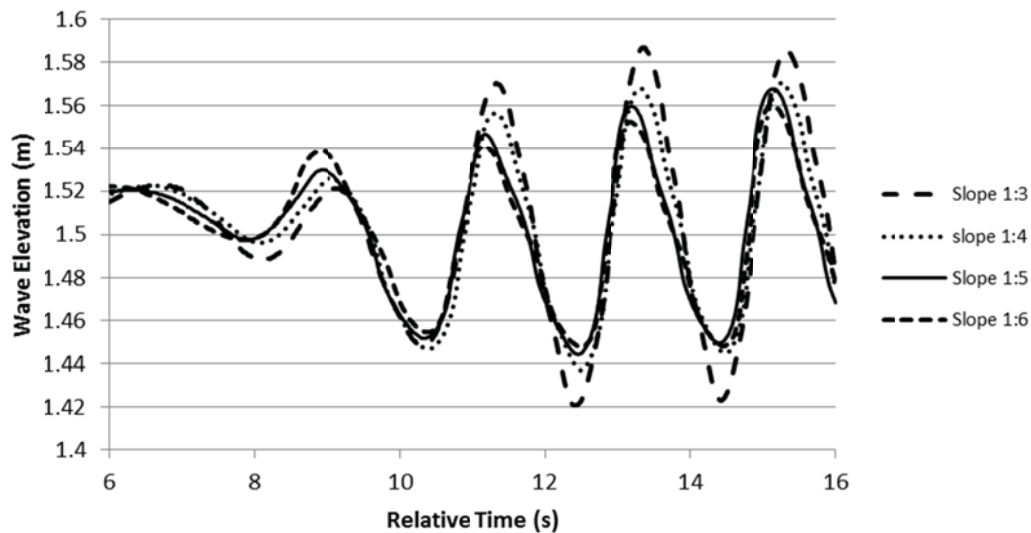


Figure 4.8: A comparison of the wave elevations for various beach slopes at 1.5m from the beach along the still water level.

Development of a numerical model for a wave tank

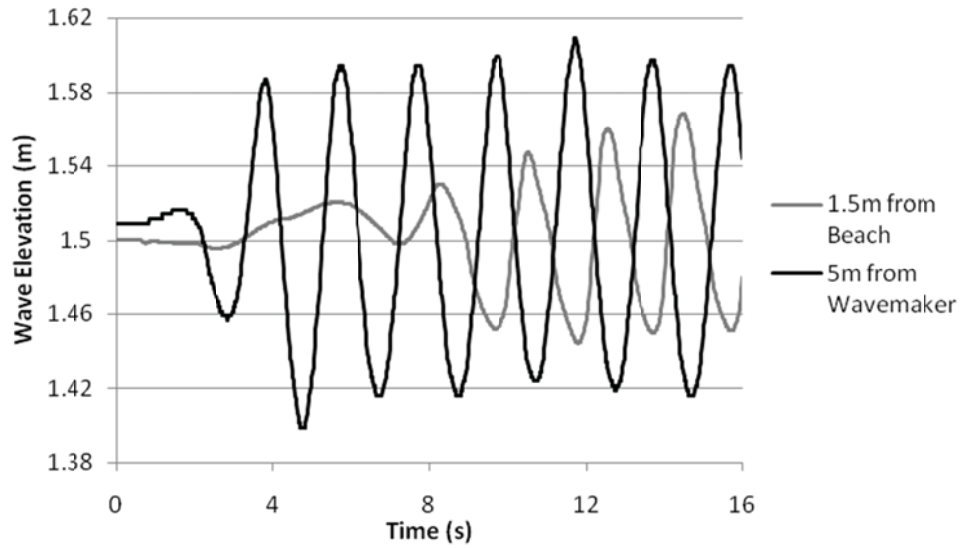


Figure 4.9: A comparison of the wave elevation at 5m from the wavemaker and 1.5m from the end of the beach.

4.3.2 Validation of CFD wave with LWT

The validation of the method presented thus far in this chapter is a vital step in this analysis. The first validation is a comparison of the generated wave in terms of the water particle velocity, v , between the SWL and model base, to linear wave theory (LWT), which uses the following equation (Coastal Engineering Research Center, 1977):

$$v = A\omega e^{k_0 y} \quad (4.13)$$

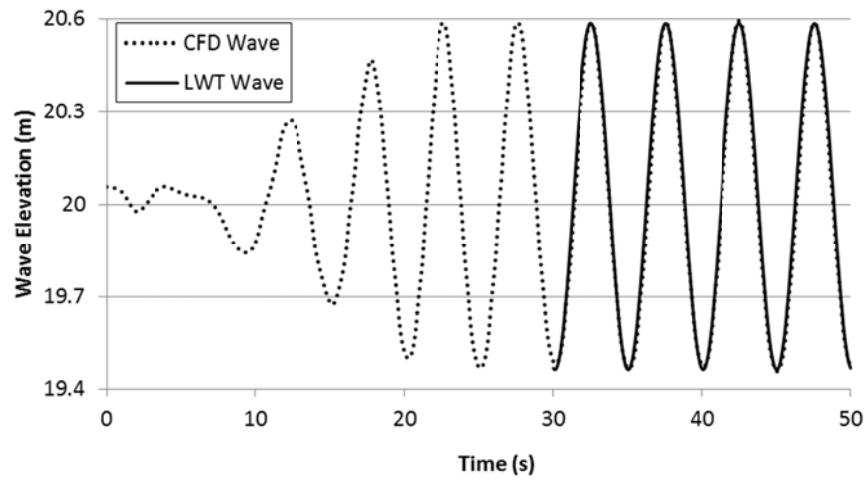
where v is the water particle velocity for the deep water case, A is the wave amplitude, ω is the angular frequency of the wave, $k_0 = \omega^2/g$ is the wavenumber for the deep water case, y increases from the SWL with depth, η_{LWT} is the wave elevation of the LWT wave, and ε_0 is the initial phase angle dependant on the initial stroke of the wavemaker and the distance from the wave maker of the profile.

Figure 4.10 (a) shows that the wave elevation of the CFD generated deep water wave is identical to that for the LWT wave, given in Eqn. (4.3), once the CFD wave has fully developed. Figure 4.10 (b) compares the scalar water particle velocity of the CFD wave,

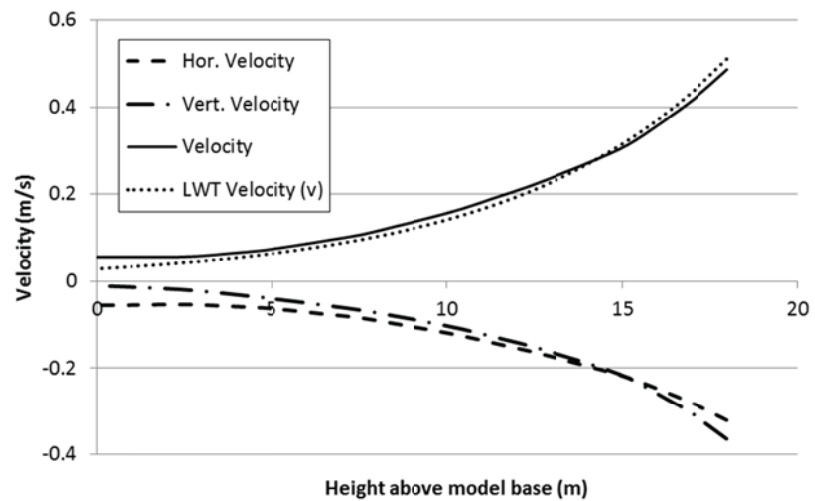
Development of a numerical model for a wave tank

which is labelled '*Velocity*', and scalar water particle velocity according to LWT, given in Eqn. (4.13), which is labelled '*LWT Velocity (v)*', which are, also, in very good agreement. Furthermore, the horizontal component of the water particle velocity, which is labelled '*Hor. Velocity*', and the vertical component of the water particle velocity, which is labelled '*Vert. Velocity*', of the CFD wave are displayed in Figure 4.10 (b). These are the vectors that combine to derive the scalar wave particle velocity. Furthermore, these vectors are compared to LWT and found to be in good agreement but this comparison is omitted from the graphs for clarity. Similarly, these comparisons and conclusions are true for the generated deep water wave in Figure 4.11.

Development of a numerical model for a wave tank



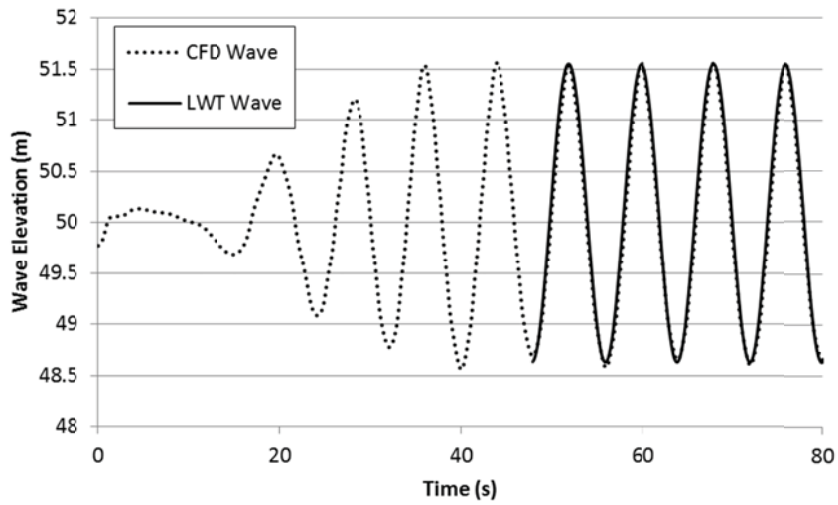
(a)



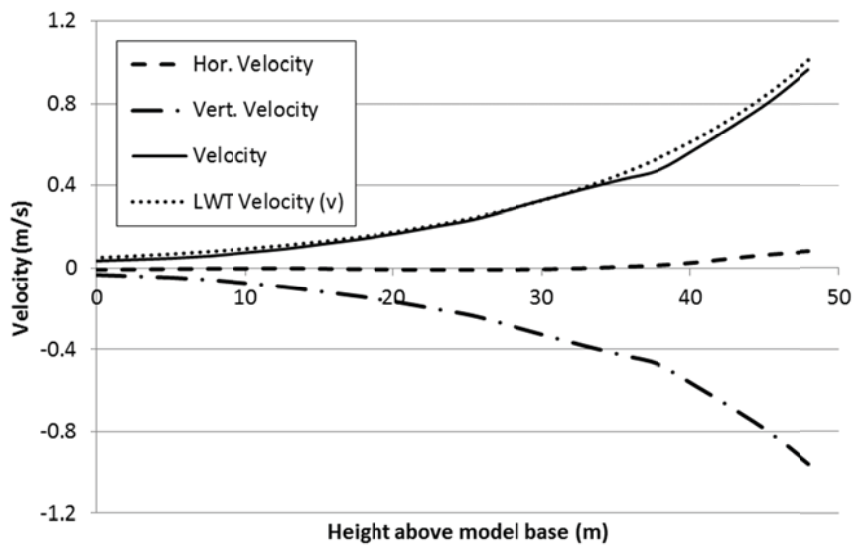
(b)

Figure 4.10: For a wave period of 5 s and a wave height of 1.12 m (i.e. $0.03L_0$) and at a distance of 60 m, or $3d$ from the wavemaker (a) Comparison of wave elevations of CFD generated wave to a linear wave (b) Comparison of CFD water velocity to LWT velocity for deep water.

Development of a numerical model for a wave tank



(a)



(b)

Figure 4.11: For a wave period of 8 s and a wave height of 2.92 m (i.e. $0.03L_0$) and at a distance of 150 m, or $3d$ from the wavemaker (a) Comparison of wave elevations of CFD generated wave to a linear wave (b) Comparison of CFD water velocity to LWT velocity for deep water.

4.3.3 Validation of CFD wave with WMT

In Figure 4.12, results from CFD analysis and WMT are plotted in terms of the wave height to stroke length ratio (H/S) against the wavenumber times the height of the wavemaker flap hinge to SWL, k_0h , where the hinge of the wavemaker flap is at the base of the tank and h is the height of the wavemaker hinge to the SWL. It was found that for the deep water case, a flap type wavemaker hinged at the bottom of the model does not satisfy wavemaker theory for deep water waves, which is valid for $k_0h \geq 3.14$, or π , according to LWT. On the other hand, it is satisfied when $k_0h \leq 2$. Hence, this only holds true for the finite/shallow depth case according to LWT and this can clearly be seen in Figure 4.12. Therefore, it is necessary to adapt the model to satisfy both linear theory and wavemaker theory. This is achieved by moving the hinge of the wavemaker to a distance of half the still water level, $d/2$, above the base of the model. However, from Figure 4.13, it can be seen that this adaption is only valid for a $k_0h \leq 1.7$. Consequently, as $2h = d$, the theory is valid for the deep water case provided the relation k_0h does not exceed 1.7.

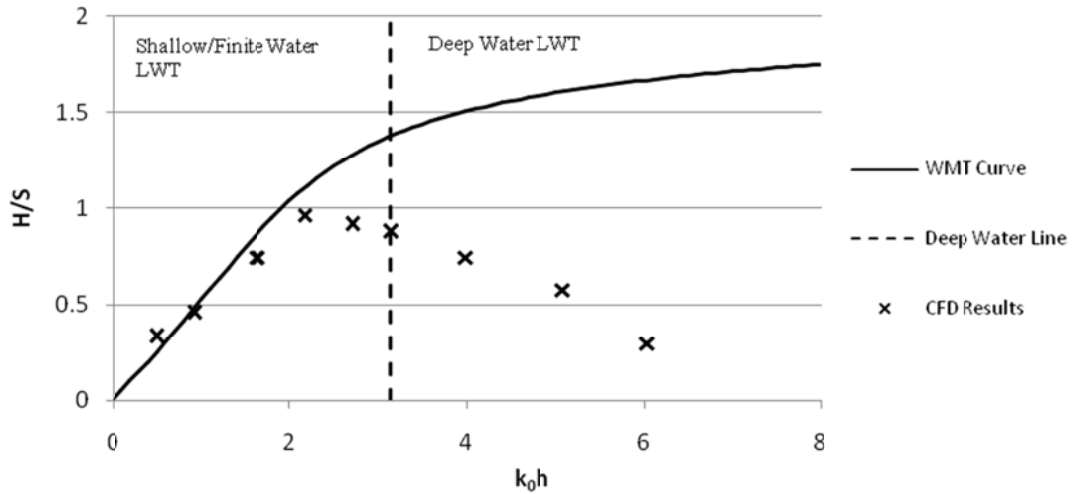


Figure 4.12: Comparison of CFD results to wavemaker theory (WMT) for the wavemaker flap hinged at the base of the model.

Development of a numerical model for a wave tank

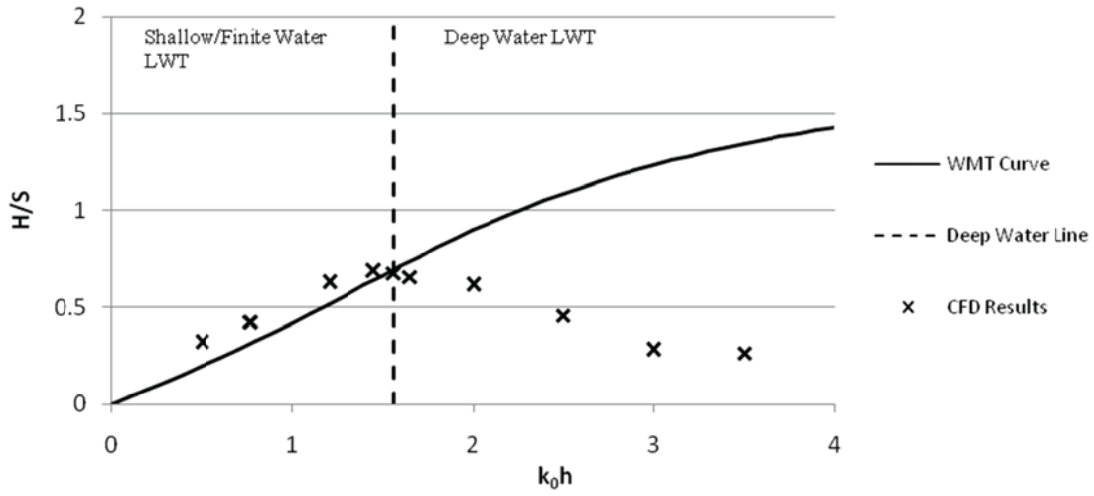


Figure 4.13: Comparison of CFD results to wavemaker theory (WMT) with the wavemaker hinged at a height, $l = 0.5d$, from the base of the model.

As the hinge of the wavemaker flap is located at a distance of half the SWL above the base of the model, it is necessary to adapt the theory in order to allow for the section of the wavemaker wall that is now stationary. Wavemaker theory, when generating two-dimensional small amplitude waves, is derived from the velocity potential of a simple boundary value problem. This velocity potential, φ , describes the simple harmonic wave motion. The boundary conditions which need to be satisfied are: the Laplace's equation, the free surface condition, the structural boundary condition, the base condition and the radiation condition, respectively (Linton and McIver, 2001):

$$\nabla^2 \varphi = \frac{\partial^2 \varphi}{\partial x^2} + \frac{\partial^2 \varphi}{\partial y^2} = 0 \quad (4.14)$$

$$\omega^2 \varphi - g \frac{\partial \varphi}{\partial y} = 0 \text{ on } y = 0 \quad (4.15)$$

$$\frac{\partial \varphi}{\partial x} = U(y) \sin \omega t \text{ on } x = 0 \quad (4.16)$$

Development of a numerical model for a wave tank

$$\frac{\partial \varphi}{\partial y} = 0 \text{ on } y = d \quad (4.17)$$

$$\lim_{x \rightarrow \infty} \left(\frac{\partial \varphi}{\partial x} \mp ik_0 \varphi \right) = 0 \quad (4.18)$$

where $U(y)$ is the prescribed horizontal velocity of the wavemaker. This problem is solved by Ursell et al. (1960), where the wave height to wavemaker stroke ratio (H/S) is given for a paddle wavemaker hinged at the base as

$$\begin{aligned} \frac{H}{S} &= \left(\frac{\omega^2 \cosh k_0 h}{g k_0} \right) \left(\frac{\int_0^h \{1 - y/h\} \cosh k_0 (h - y) dy}{\int_0^h \cosh^2 k_0 (h - y) dy} \right) \\ &= \left(\frac{4 \sinh k_0 h}{k_0 h} \right) \left(\frac{k_0 h \sinh k_0 h - \cosh k_0 h + 1}{\sinh k_0 h + 2k_0 h} \right) \end{aligned} \quad (4.19)$$

However, this takes the prescribed horizontal velocity of the wavemaker as:

$$U(y) = \frac{1}{2} S \omega \{1 - y/h\} \quad (4.20)$$

Since there is fluid now below the height of the hinge of the wavemaker, the wavemaker exerts a force on this fluid and, in turn, Eqn. (4.19) needs to be adapted to show this loss of energy. Furthermore, when the hinge of the wavemaker is taken at a height, l , from the base of model, the prescribed horizontal velocity of the wavemaker is given as

$$U(y) = \begin{cases} \frac{1}{2} S \omega \{1 - y/h\} & \text{at } 0 \leq y \leq h - l \\ 0 & \text{at } h - l \leq y \leq h \end{cases} \quad (4.21)$$

Therefore Eqn. (4.19) is adapted to allow for this change in the height of the hinge to give

$$\begin{aligned} \frac{H}{S} &= \left(\frac{\omega^2 \cosh k_0 h}{g k_0} \right) \left(\frac{\int_0^{h-l} \{1 - y/h\} \cosh k_0 (h - y) dy}{\int_0^h \cosh^2 k_0 (h - y) dy} \right) \\ &= \left(\frac{4 \sinh k_0 h}{k_0 h} \right) \left(\frac{k_0 h \sinh k_0 h - \cosh k_0 h - k_0 l \sinh k_0 l + \cosh k_0 l}{\sinh k_0 h + 2k_0 h} \right) \end{aligned} \quad (4.22)$$

where h is the height of the wavemaker from the hinge to the still water level, k_0 is obtained from the relation $\omega^2 = g k_0 \tanh k_0 h$, and l is the height of the hinge of the

wavemaker from the base of the model. The above equation is represented by the '*WMT Curve*' in Figure 4.13. It is evident from Figure 4.13 that the theory is valid for the deep water case with the wavemaker hinged at a height of half the still water level, h , provided the relation k_0h does not exceed 1.7.

4.3.4 Comparison of turbulence models

A comparison was carried out between a laminar model, a shear stress transport model and a $k-\varepsilon$ turbulence model in order to investigate the effects of viscosity. The $k-\varepsilon$ turbulence model includes the history effects such as the turbulent kinetic energy and turbulent dissipation. However, it was found that there was no difference in the generated wave elevation between the two turbulence models and, therefore, is not a factor in the generation of water waves using a wavemaker. Similar observations are noted by Lal and Elangovan (2008). In this analysis, the turbulence model used is the shear stress transport model, which is also the model used by Elangovan (2011).

4.3.5 Scaling laws in deep water wave modelling

There is a dimension restriction in ANSYS CFX (Version 12.1) of 500 m (ANSYS Inc., 2009). Therefore, as a result of the model dimensions derived in this chapter, it is necessary to scale the model when dealing with low frequencies (i.e. $f \leq 0.125$ Hz). Furthermore, when dealing with real-world models it is necessary to use the scaling factors derived in this section. These scaling factors are derived from the equations used in Airy's linear wave theory for deep water waves (Coastal Engineering Research Center, 1977), which is presented in Section 2.2. A summary of the scaling factors is given in Table 4.2. Please note that these are not all of the scaling factors, but a summary of those applicable to deep water wave modelling.

Development of a numerical model for a wave tank

Table 4.2: Summary of applicable scaling factors in deep water wave modelling.

Quantity	Symbol	Scaled Relation
Wave Period	T_{new}	sT_{in}
Wave Angular Frequency	ω_{new}	ω_{in}/s
Wave Length	L_{new}	s^2L_{in}
Wave Amplitude	A_{new}	A_{in}
Water Mass	m_{new}	m_{in}
Water Density	ρ_{new}	ρ_{in}
Still Water Level	d_{new}	s^2d_{in}
Water Particle Velocity	v_{new}	v_{in}/s
Water Particle Acceleration	a_{new}	a_{in}/s^2
Wave Force on a Body/ Structure	F_{new}	F_{in}/s^2

Note: The subscripts 'in' refers to the initial model and 'new' refers to the scaled model.

The scaling that is referred to in this chapter is a function of the wave period, T , and the scaling coefficient s , where $T_{new} = s T_{in}$. As force is directly proportional to acceleration and acceleration is given as $A\omega^2 e^{ky}$ (Coastal Engineering Research Center, 1977), it is deduced that the wave force on a body/structure is given by the relation:

$$F_{new} = \frac{F_{in}}{s^2} \quad (4.23)$$

where F_{new} is the wave force on the body or structure in the scaled model, F_{in} is the wave force on the full scale body or structure and s is the scaling coefficient.

4.4 Time-domain wave-structure interaction

4.4.1 Introduction

In this section, the methodology described previously in this chapter is advanced in order to perform wave-structure interaction in the time domain. A case study of a real world application of the methodology derived is undertaken. It is an analysis of the interaction between a linear deep water wave and a floating truncated vertical cylinder.

Again, the commercial CFD software, ANSYS CFX (ANSYS Inc., 2009), is used to perform the analysis. However, a number of additional developments must be introduced into the model in order to accurately reproduce realistic wave-structure interaction. These are described in Section 4.4.2. Furthermore, a parametric study of the heave excitation force on a fixed truncated vertical cylinder is undertaken and the results are compared to the analytical approximation derived in Chapter 3.

4.4.2 Wave-structure interaction in a numerical model for a wave tank

Since the model is to represent deep water conditions, i.e. infinite depth, it is necessary to increase the depth of the water. This change to the methodology described in Chapter 4 is required as the oscillating body generates fluid velocities beneath it and these velocities are affected by the base of the model if the depth is not sufficient. When specifying the boundary conditions on the longitudinal walls of the model, a '*symmetry boundary*' is specified on one wall in order to only model half of the problem and reduce the calculation required. On the other longitudinal wall, a '*wall boundary*' with an unspecified mesh motion, i.e. dependent on the motion of the adjacent boundaries, and no symmetry is specified. In order to model the floating structure, there is an inbuilt Fluid-structure interaction solver in ANSYS CFX. The cylinder is modelled as a 6 degree of freedom rigid body, with a specified mass and moments of inertia, which motions as an

Development of a numerical model for a wave tank

implicit result of the forces and moments which act on it. For the analysis detailed in Section 4.4.3.1, the structure is held in a fixed position. However, for the analysis detailed in Section 4.4.3.2, the structure is allowed to oscillate with one degree of freedom, which is the vertical motion. The free surface and a fixed truncated cylinder of the model are shown, for example, in for a specific moment in time.

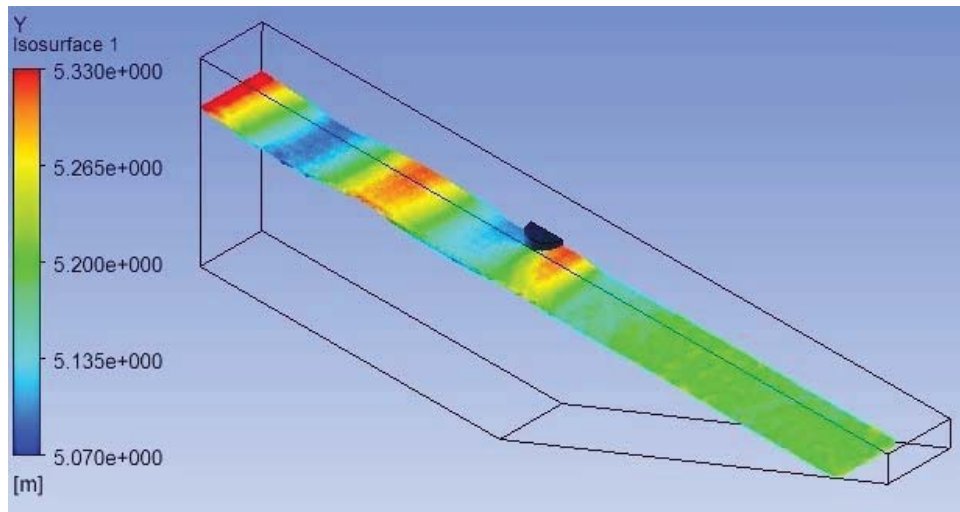


Figure 4.14: The wave-structure interaction from CFD analysis (ANSYS CFX) after 24 s. The free surface and a fixed truncated cylinder are shown.

4.4.3 Analysis of a floating structure

For the purpose of performing wave-structure interaction, a case study example is taken of a floating truncated vertical cylinder, with $a = b = 0.6$ m, and an incident wave of period 2 s and an amplitude of 0.08 m. Throughout the analysis, the model is 26 m x 2 m x 6 m with a still water level of 4 m. In this section, the analysis of the forces on a floating structure is performed by using two simulations; the first is when the structure is held in a fixed position in order to obtain the wave excitation force. The second is when the structure is free to oscillate in the vertical, or heave, motion and the heave motion dynamic response and, thus, the vertical hydrodynamic force are assessed.

4.4.3.1 Analysis with floating structure held in a fixed position

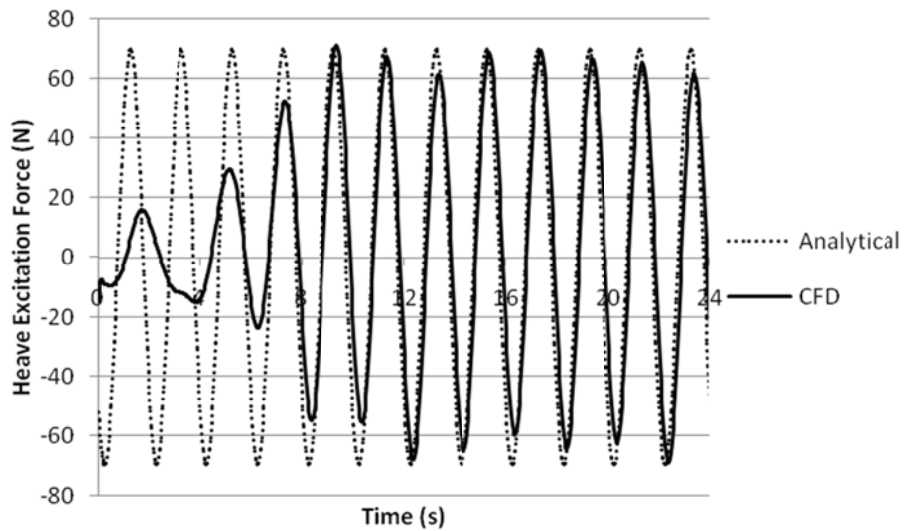
In the initial analysis, the cylinder is held in a fixed position and the wave excitation forces are calculated. Since the overall analysis is of the heave, or vertical, motion of the structure, the heave excitation force is of main concern. The results of this CFD analysis are then compared to the analytical approximation derived in Chapter 3, which is calculated from Eqn. (3.45).

A time-domain comparison between the analytical approximation and results from the CFD analysis are shown for a dimensionless wavenumber, k_0a , of 0.3 with draft-to-radius ratios, b/a , of 1 and 0.5, in (a) and (b), respectively. A similar comparison for a wavenumber, k_0a , of 0.6 is shown in and further comparisons are detailed in Appendix C. The maximum heave wave excitation forces in both are slightly overestimated in the analytical approximation and there is a slight phase difference between the two approaches for moderate dimensionless wavenumber values, $0.4 \leq k_0a \leq 1.2$, which is a similar finding to that of the phase angle comparison displayed graphically in Figure 3.3. In addition, it is clear that the magnitude of the heave wave excitation force becomes distorted as the wavenumber increases. This is as a result of interference from the side wall boundary of the model and the structure. There is a limit on the ANSYS licence of 512,000 nodes, or approximately 1.2×10^6 elements, and as a result the domain could not have been made any wider.

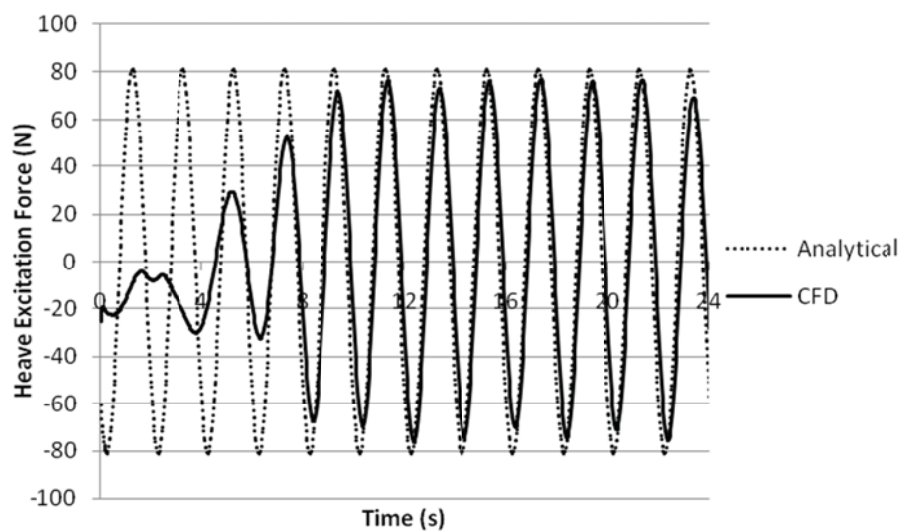
The observations from these comparisons are then summarised in the form of a parametric study. The parametric study is performed for different dimensionless wavenumbers, k_0a , and for draft-to-radius ratios, b/a , of 1 and 0.5. The study is summarised by taking the amplitude of the time-domain heave excitation force in order to obtain a frequency-domain result. The time-domain heave excitation force for each frequency is displayed graphically in Appendix C. In this study, the analytical approximation presented in Chapter 3 (Eqn. (3.45)) and the results from the CFD analysis match up closely and have the same trend, as shown in Figure 4.17. Furthermore, the

Development of a numerical model for a wave tank

results of the CFD analysis are compared to the solution derived by Bhatta and Rahman (1995; 2003) and are found to be in very good agreement.



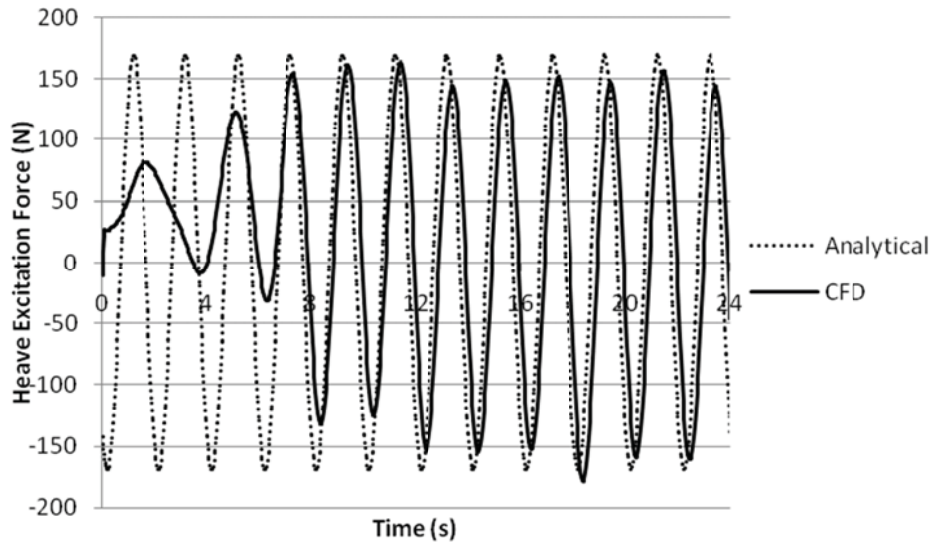
(a)



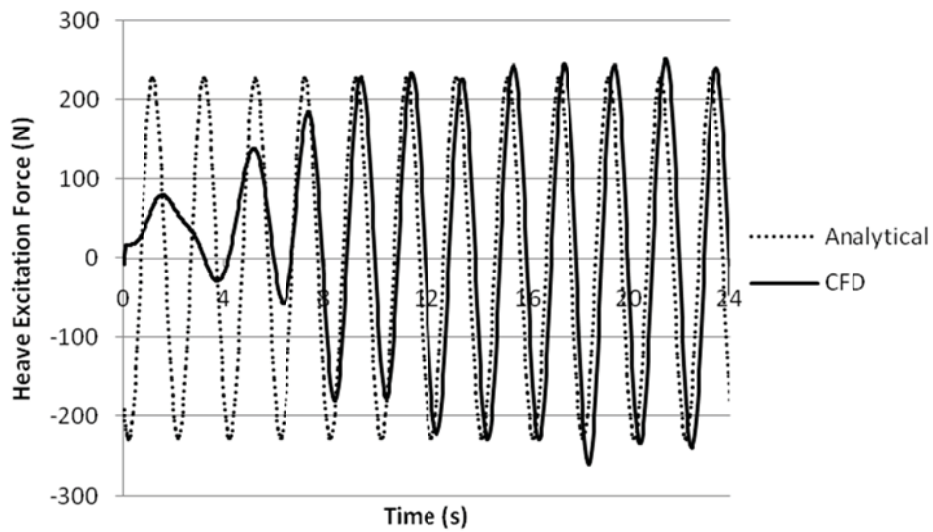
(b)

Figure 4.15: Time domain comparison between the heave excitation forces obtained from the analytical approximation presented in Chapter 3 (Eqn. (3.45)) and CFD models with $k_0 a = 0.3$, where (a): $b = a$ and (b): $b = a/2$ and the mass of the structure is 47 kg and 23 kg, respectively.

Development of a numerical model for a wave tank



(a)



(b)

Figure 4.16: Time domain comparison between the heave excitation forces obtained from the analytical approximation presented in Chapter 3 (Eqn. (3.45)) and CFD models with $k_0 a = 0.6$, where (a): $b = a$ and (b): $b = a/2$ and the mass of the structure is 336 kg and 168 kg, respectively.

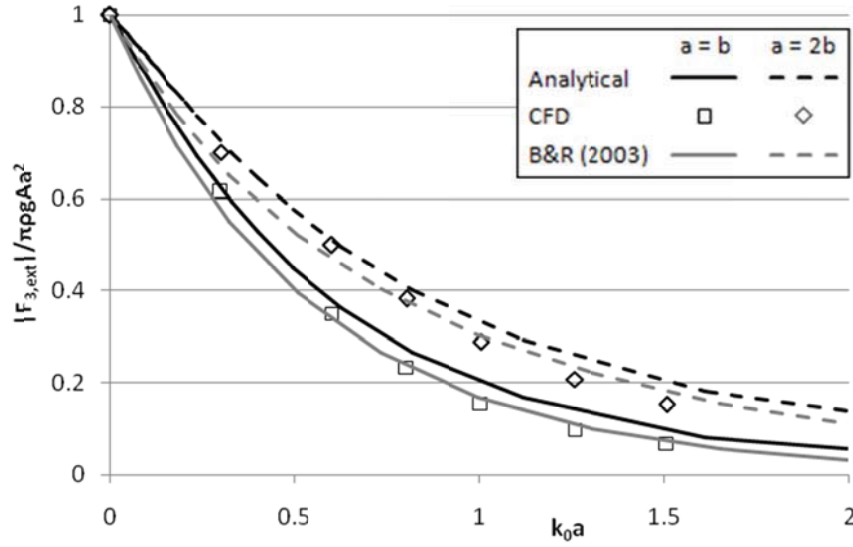


Figure 4.17: Comparison of the normalised vertical, or heave, excitation force for the analytical approximation presented in Chapter 3 (Eqn. (3.45)), the solution of Bhatta and Rahman (1995, 2003) and CFD models with ratios of $a = b$ and $a = 2b$.

4.4.3.2 Analysis when the floating structure is allowed to oscillate

The second stage of the analysis is to perform a simulation where the cylinder is free to oscillate in the heave motion, i.e. the vertical direction. Therefore, the heave motion dynamic response and the hydrodynamic force, or total wave force, on the structure is obtained. From this information, the total force on the structure can be decomposed into the various forces. Since the model deals with an unrestrained system, i.e. there are no external mechanical forces applied to the structure, the total wave force is the hydrodynamic force, which can be summarised as follows:

$$F_H = F_{ext} + F_R + F_{hs} = -M \frac{d^2 z}{dt^2} \quad (4.24)$$

where F_H is the hydrodynamic force, F_{ext} is the excitation force, F_R is the radiation force, F_{hs} is the hydrostatic force, M is mass of the body, and z is the dynamic vertical displacement response of the structure, which increases from the SWL with depth. For

Development of a numerical model for a wave tank

preliminary models of WEC's, it is reasonable to assume the excitation force is a combination of the Froude-Krylov force and the diffraction force. This assumption is only valid when the overall dimensions are large compared to the wave length and Keulegan-Carpenter parameter (Dean and Dalrymple, 1984) is less than one. Furthermore, by using Eqn. (4.24), the total hydrodynamic force may be separated into the various forces which comprise it. This may be achieved since the excitation force is calculated numerically in the previous section and the hydrostatic force can be derived from the water-plane area of the structure. An example of a summary of these forces is shown graphically, in the time-domain, for a case study in Figure 4.18.

The case study, which is detailed in this section, is a floating truncated vertical cylinder, with $a = b = 0.6$ m, and an incident wave of period 2 s and an amplitude of 0.08 m. A time domain representation of the incident wave and the dynamic response of the body are shown in Figure 4.19. The excitation force on the body is shown in (a) and the summary of the forces which make up the hydrodynamic force is shown in Figure 4.18. Furthermore, the added mass and the wave damping may be calculated from the radiation force, which is given, in the frequency domain, as:

$$\hat{F}_R = -\ddot{z}a_m - \dot{z}v = \omega^2 z a_m + i\omega z v \quad (4.25)$$

where a_m is the added mass and v is the wave damping. For the given case study the mass is 339 kg and the added mass is calculated as 196 kg, resulting in the added mass coefficient, a_m/M , of 0.579. The radiation wave damping is calculated as 185 kg/s, resulting in the radiation wave damping coefficient, $v/\omega M$, of 0.11. These figures are in good correlation with a BEM hydrodynamic analysis of the structure, which calculates the added mass coefficient and the radiation wave damping coefficient as 0.544 and 0.111, respectively.

Development of a numerical model for a wave tank

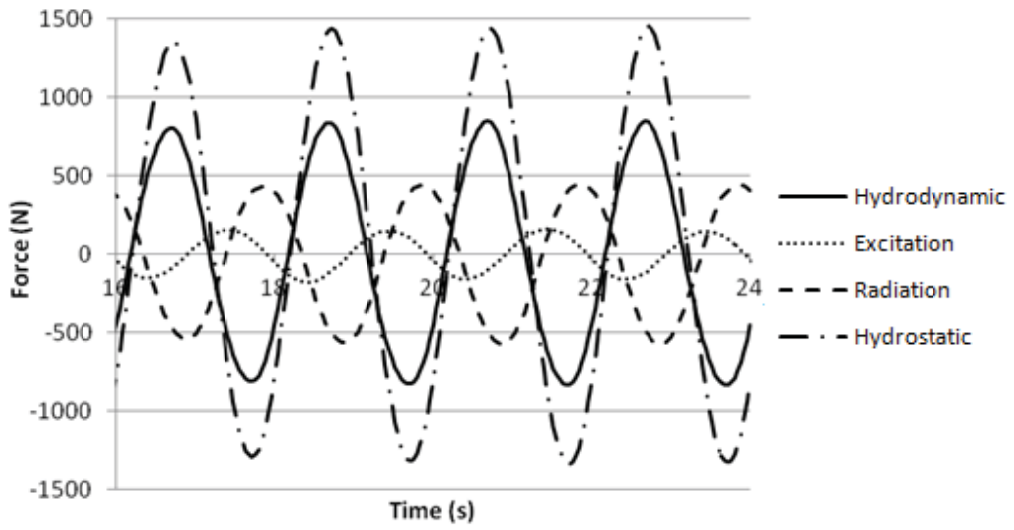


Figure 4.18: Summary of the various forces on a floating truncated vertical cylinder with $a=b$, which is allowed to oscillate in a vertical, or heave, motion from the numerical CFD analysis (ANSYS CFX).

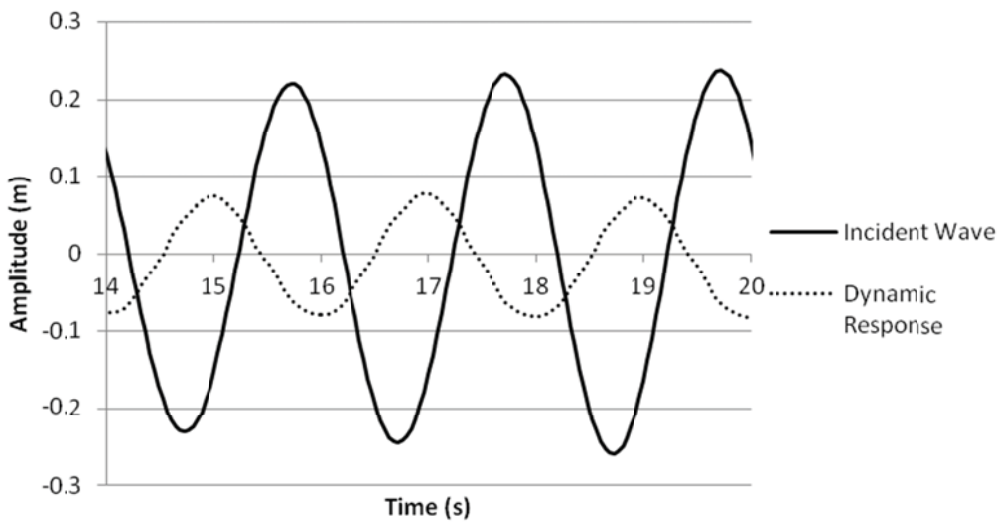


Figure 4.19: The incident wave and the dynamic response of a floating truncated vertical cylinder with $a=b$, which is allowed to oscillate in a vertical, or heave, motion from the numerical CFD analysis (ANSYS CFX).

4.5 Discussions and conclusions

A guide to designing a CFD numerical model for a wave tank that can accurately produce both linear deep water waves and linear waves for the finite depth case is presented in this chapter. Furthermore, steps required to be taken to design an optimum CFD model were outlined. In particular, the effects of the meshing method, wave dissipation beach slope, the total time and time-step interval for the transient analysis set-up were explored, while minimising the overall dimensions of the model to generate a deep water wave. The state-of-the-art contribution is the methodology for the development of an optimum numerical model of a wave tank, in terms of the desired wave period generated.

The optimum mesh for the model utilises both a maximum element size and the '*Sphere of Influence*' technique. A total time equal to ten times the wave period was found to be sufficient and the optimum time-step interval is to divide the wave period into 50 intervals ($T/50$), which can be seen in Figure 4.7. It is recommended to use a beach slope of 1:5 to dissipate, or damp out, the wave energy at the end of the numerical wave tank model.

Furthermore, it is evident from Figure 4.12 and Figure 4.13 that a limitation of ANSYS CFX is it can only conform to WMT when dealing with relatively low kh values, i.e. $kh \leq 2$ for $h = d$ and $kh \leq 1.7$ for $2h = d$. It can also be concluded from Figure 4.13 that, only when the hinge of the wavemaker is raised, can deep water waves be generated and conform to both WMT, using the adapted version of the equation described in Ursell et al. (1960), and LWT. Figure 4.10 and Figure 4.11 show two sets of comparisons and from these it is apparent that the CFD generated deep water wave is in very good agreement to LWT. Therefore, the aim of generated linear regular waves in a numerical wavetank model using a commercial CFD software package, ANSYS CFX, has been achieved.

Finally, a case study of the interaction of a linear deep water wave and a floating truncated vertical cylinder, which employs the methodology to create a NWT described in this chapter, is undertaken. A comparison between the CFD analysis and an analytical

Development of a numerical model for a wave tank

solution was undertaken to ensure the accuracy of the model set-up. It was found that the response predictions from the analytical and CFD model match up closely. Furthermore, a floating truncated vertical cylinder that oscillates in the vertical, or heave, motion was analysed to give the dynamic response and hydrodynamic forces on the structure. The added mass and wave damping were calculated from the radiation force and are in good correlation with a BEM hydrodynamic analysis of the structure.

Chapter 5
Frequency-domain wave-structure interaction
using CFD

5.1 Introduction

Computational fluid dynamics has proven to be a reliable and accurate method of evaluating fluid structure interaction for decades after first being used in the field of aeronautical and more recently for the modelling of marine structures. The subject concerning the interaction of ocean waves with floating structures is quite complex in its nature and usually requires extensive numerical analysis to solve. It is essential that numerical models can accurately and optimally perform the interaction of water waves with structures. The development of such a model is described in this chapter. The interaction of linear regular waves with structures is analysed using computational fluid dynamics (CFD) in the frequency domain by employing the boundary element method (BEM) commercial software ANSYS AQWA (ANSYS Inc., 2010). This is used to solve for the various hydrodynamic forces and dynamic responses of the structure. The methodology used in the analysis setup and its validation is included in Section 5.2. The details of this hydrodynamic analysis are described in Section 5.4.

Two applications of frequency-domain wave-structure interaction in the structural modelling of wave energy converters are detailed. The first describes how the hydrodynamic analysis is used to aid in the structural health monitoring of wave energy converters by determining the locations of high stresses on the structure over a range of frequencies. The second uses the hydrodynamic analysis, together with a coupled analytical solution, in analysing the structural dynamics of a two-body wave energy converter.

5.2 BEM analysis methodology

Similar to the set up for ANSYS CFX, ANSYS AQWA is divided into three sections; that is, geometry generation, mesh and physics.

Since the BEM is based a panel method, only surfaces need to be generated when creating the geometry. However, two separate parts must be specified; the submerged part and the part above the water surface. This is performed as the solver needs to apply certain conditions and equations on each structural boundary. The geometry is then meshed using a surface meshing, where the minimum element size is specified.

In the physics set-up, the water depth, frequency range and direction of the incoming waves is specified. Furthermore, the centre of gravity of the structure, along with either the moment of inertia or radius of gyration must be specified. For the majority of the analyses detailed in this section, the structure can be described as vertically axisymmetric. Therefore, the calculations required to derive their properties are detailed in Section 5.3.

The governing equations are then solved at each frequency and the user must specify the data which is to be outputted. For example, specifying to output the excitation force as it varies with frequency also includes specifying the direction of the force and the direction of the incoming waves. The governing equation, boundary conditions used and the hydrodynamic analysis performed are detailed in Section 5.4.

5.3 Properties calculation for a vertically axisymmetric structure

As outlined in Section 5.2, the properties of the structure which are to be calculated so to be inputted into the BEM software are the mass of the structure, the centre of gravity and either the moment of inertia or the radius of gyration. The mass of the body is simply calculated from the integral:

$$M = \rho_S \int dV \quad (5.1)$$

where ρ_S is the density of a structure and V is the volume of a structure. However, the moment of inertia, I , is quite a more complex calculation and is given by:

Frequency-domain wave-structure interaction using CFD

$$I = \int r^2 dm = \rho \int r^2 dV \quad (5.2)$$

where r is the distance between the axis and rotation mass and m is the mass of a structure. For a vertically axisymmetric body,

$$dV = r d\theta dr dz \quad (5.3)$$

where θ is the rotation polar coordinate and z is the vertical polar coordinate. Therefore, substituting Eqn. (5.3) into Eqn. (5.2), the moment of inertia about the z -axis, I_{zz} , is derived as follows:

$$\begin{aligned} I_{zz} &= \rho \iiint r^2 r d\theta dr dz = \rho \int_{b_2}^{b_1} \int_0^{a_1} \int_0^{2\pi} r^3 d\theta dr dz \\ &= \frac{\pi}{2} \rho a_1^4 (b_1 - b_2) \end{aligned} \quad (5.4)$$

where a_1 is the radius of the section, b_1 is the distance to the top of the section and b_2 is the distance to the bottom of the section. Using the perpendicular axis theorem:

$$dI_{zz} = dI_{xx} + dI_{yy} \quad (5.5)$$

where I_{xx} is the moment of inertia about the x -axis and I_{yy} is the moment of inertia about the y -axis. Since, for a vertically axisymmetric body, $I_{zz} = I_{xx} + I_{yy}$:

$$dI_{xx} = dI_{yy} = \frac{dI_{zz}}{2} \quad (5.6)$$

Therefore, using the parallel axis theorem, for any disc at a distance z from the x -axis,

$$\begin{aligned} dI_{xx} &= dI_{yy} = \frac{dI_{zz}}{2} + z^2 dm \\ \therefore I_{xx} &= I_{yy} = \frac{\pi}{4} \rho a_1^4 (b_1 - b_2) + \rho \int_{b_2}^{b_1} \int_0^{a_1} \int_0^{2\pi} z^2 r d\theta dr dz \\ &= \frac{\pi}{4} \rho a_1^4 (b_1 - b_2) + \frac{\pi}{3} \rho a_1^2 (b_1^3 - b_2^3) \end{aligned} \quad (5.7)$$

Alternatively, the radius of gyration, R , may be used which is derived from the moment of inertia, as follows:

$$R = \sqrt{\frac{I}{M}} \quad (5.8)$$

5.4 Mathematical formulation of the BEM

Assuming the fluid is irrotational and incompressible, the total pressure distribution on a floating structure is defined by Bernoulli's equation (McCormick, 1973):

$$p = -\rho \frac{\partial \Phi}{\partial t} - \rho g z \quad (5.9)$$

where p is pressure, ρ is the density of water, g is acceleration due to gravity, Φ is the velocity potential, t is time and z is the downwards distance from the still water level (SWL). The first term in Eqn. (5.9) refers to the hydrodynamic pressure distribution due to the components of the velocity field and the second term refers to the hydrostatic pressure on the body in still water. Therefore, when performing the hydrodynamic analysis on a floating or fixed structure only the first term is of interest. The velocity potential, Φ , is decomposed as follows:

$$\Phi = \Phi_I + \Phi_D + \Phi_R \quad (5.10)$$

where the incident wave velocity potential is $\Phi_I = \text{Re}[\varphi_I e^{-i\omega t}]$, the diffraction velocity potential is $\Phi_D = \text{Re}[\varphi_D e^{-i\omega t}]$, and the radiation potential is $\Phi_R = \text{Re}[-\sum_{k=1}^6 i\omega u_k \varphi_R e^{-i\omega t}]$, in which $i = \sqrt{-1}$, t is time, ω is the angular frequency, u_k is the k -component of the dynamic response and $k = 1,2,3,4,5,6$, corresponding to surge, sway, heave, roll, pitch and yaw, respectively. The calculation is then divided into two problems: the scattering and radiation problems. In the scattering problem, the structure is held in a fixed position in the presence of an incident wave, to obtain the diffraction velocity potential. In the radiation problem, where the structure is forced to oscillate and the radiation velocity potential is obtained.

Frequency-domain wave-structure interaction using CFD

In this section, the numerical method used to perform the hydrodynamic analysis is based on a non-linear approximation, Stokes' second order expansion (Coastal Engineering Research Center, 1977). The governing equation which is to be solved is the Laplace equation, which is given as:

$$\nabla^2 \Phi = 0 \quad (5.11)$$

The governing equation, given in Eqn. (5.11), can be transformed to its boundary representation, which takes the following form:

$$\alpha_c(x_c)\Phi(x_c) = \int_{S_B} \left[\frac{\partial \Phi(x)}{\partial n} G(x, x_c) - \Phi(x) \frac{\partial G(x, x_c)}{\partial n} \right] dS \quad (5.12)$$

where x_c is a collocation point, α_c is the boundary factor at location x_c , S_B is the wetted surface area of the structure, $G(x, x_c)$ is the appropriate Green's function and $\frac{\partial}{\partial n}$ denotes the outward normal derivative on S_B . Furthermore, the boundary conditions that need to be satisfied, in the boundary value problem, are: the kinematic free surface condition, the dynamic free surface condition, the deep water condition and the structural boundary condition, respectively (for further details see: Linton and McIver (2001)):

$$\frac{\partial \eta}{\partial t} + \frac{\partial \Phi}{\partial x} \frac{\partial \eta}{\partial x} + \frac{\partial \Phi}{\partial y} \frac{\partial \eta}{\partial y} = \frac{\partial \Phi}{\partial z}, \quad \text{on } z = \eta(x, y, t) \quad (5.13)$$

$$\frac{\partial \Phi}{\partial t} + \frac{1}{2} |\nabla \Phi|^2 + g\eta = 0, \quad \text{on } z = \eta(x, y, t) \quad (5.14)$$

$$|\nabla \Phi| \rightarrow 0, \quad \text{as } z \rightarrow \infty \quad (5.15)$$

$$\frac{\partial \Phi}{\partial n} = \begin{cases} 0 & \text{for scattering problem} \\ n_j & \text{for radiation problem} \end{cases} \quad (5.16)$$

where η is the vertical elevation of a point on the free surface, n_j is the unit normal in the j -direction, $j = 1,2,3,4,5,6$, corresponding to surge, sway, heave, roll, pitch and yaw, respectively, and (x, y, z) is the Cartesian coordinate system. The Green's function equation, the method for which is detailed by Garrison (1978), is utilised in order to satisfy the boundary conditions in determining the velocity potentials.

Frequency-domain wave-structure interaction using CFD

The j -component of the excitation force, in the frequency domain, $\hat{F}_{ext,j}$, is calculated from the scattering problem as follows:

$$\hat{F}_{ext,j} = i\rho\omega \int_{S_B} (\varphi_I + \varphi_D)n_j dS \quad (5.17)$$

where S_B is the wetted surface of the floating structure. The j -component of the radiation force, in the frequency domain, $\hat{F}_{R,j}$, is calculated from the radiation problem and, in turn, the hydrodynamic coefficients, the added mass and radiation damping, are determined as follows:

$$\hat{F}_{R,j} = \rho\omega^2 u_k \int_{S_B} \varphi_R n_j dS = \omega^2 u_k a_{m,jk} + i\omega u_k v_{jk} \quad (5.18)$$

where a_m is the added mass and v is the radiation damping. The dynamic response of the body can, then, be calculated using the response amplitude operator (RAO), which is given as:

$$\frac{u_k}{A} = \frac{\hat{F}_{ext,j}/A}{-\omega^2(m + a_{m,jk}) + i\omega v_{jk} + \tau_{jk}} \quad (5.19)$$

where A is the amplitude of the incident wave, m is the mass of the structure and τ is the hydrostatic stiffness of the structure.

In order to determine the various velocity potentials and calculate the hydrodynamic coefficients and forces, the boundary element method software, ANSYS AQWA (ANSYS Inc., 2010), is used.

5.5 Determining the locations of high stresses on a floating structure to aid in the structural health monitoring of wave energy converters

5.5.1 Introduction

One of the main aspects in the design of WECs is their survivability and the efficient structural health monitoring of these WECs, once they have been deployed into this harsh environment. The structural health monitoring of buildings has been undertaken for decades for both economic and social reasons, including health and safety issues. Chang et al. (2003) published a comprehensive review of the damage detection methods in the structural health monitoring of all types of civil infrastructure. Guo et al. (2004) explore the use of improved generic algorithms of structural health monitoring to determine the optimum positioning of sensors and the resulting algorithms are then compared to traditional methods. Goggins et al. (2007) used wavelet analysis to develop a structural health monitoring algorithm to investigate the seismic response of braced frames. Brownjohn (2007) details the motivations and reasons for the recent increased interest in the structural health monitoring of civil infrastructure and discusses the possible future advances in the area.

Structural health monitoring techniques have also been developed for offshore structures, although not specifically for wave energy converters. For example, Nichols (2003) experimentally examined the use of low order structural health monitoring techniques on two simple models of an articulated offshore structure undergoing ambient excitation. Murawski et al. (2010) examined measurement and calculation error estimation and damage detection of offshore structures using traditional fibre optics techniques for damaged and undamaged models.

In this section, the hydrodynamic boundary element method software, ANSYS AQWA(2010), is used to determine locations of high stresses, or strains, by examining the variance in pressure, or stress, over the submerged surface of a floating structure. This analysis is carried out over one wave period from crest to crest and over a range of ocean

wave frequencies. Particular interest is taken when the structure becomes resonant, as this is when the maximum stresses will occur. Finally, a case study of a floating vertically axisymmetric concrete structure is undertaken and optimum orientation for the placement of sensors is discussed.

5.5.2 Methodology for identifying locations of high stress

The hydrodynamic analysis is used to determine the locations of maximum pressure, p_{max} , or maximum stress, and these locations are used as critical locations for the positioning of sensors for the structural health monitoring of the structure. Examples of the type of sensors which can be used to monitor the pressure distribution, or change in force at a point on the structure, are force sensing resistors. These are a polymer thick film device which exhibit a decrease in resistance with an increase in force applied to the active surface. These can also be waterproofed so would be ideal for use on a WEC.

The other variable that must be taken into account when optimising the locations of sensors is the wave energy spectrum for the sea, or ocean location, where the WEC is being designed for, as this will define the most probable frequencies that the WEC will be exposed to. Where no wave energy spectrum is available for the design sea, a theoretical spectrum, known as the modified Pierson-Moskowitz Spectrum (Perez, 2005), $S_{PM}(f)$, may be determined using the significant wave height, H_s , and the average period, T_{av} , which is given as:

$$S_{PM}(f) = \frac{A_S}{(2\pi)^4 f^5} \exp\left(\frac{-B_S}{(2\pi)^4 f^4}\right) \quad (5.20)$$

where f is frequency and the coefficients $A_S = \frac{173H_s^2}{T_{av}^4}$ and $B_S = \frac{691}{T_{av}^4}$.

The maximum pressure, or stress, occurs when the structure is oscillating at resonance and occurs at the still water level at this frequency. This is evident from the pressure distributions shown in Figure 5.6 and the graphical summary displayed in Figure 5.4.

Therefore, it is necessary to have one or a number of sensors at the still water level depending on the direction of the incoming wave. The locations of the other sensors are defined by a combination of the factors, which are the locations of maximum pressure and the wave energy spectrum of the design sea.

5.5.3 Case study of a floating WEC

In this section, a basic floating concrete wave energy converter is used to demonstrate the methodology of analysis for structural health monitoring presented in Section 5.5.2. The structure has a radius, a , of 8m with a total draft, b , of 20m below the still water level, with the bottom 8m being a hemisphere. The results of the hydrodynamic analysis of the case study are shown graphically in Figure 5.1, Figure 5.2 and Figure 5.3, which details the added mass and radiation damping coefficients, the normalised heave and surge excitation forces and the normalised dynamic response with phase angle, respectively. The wave excitation forces are normalised as follows:

$$\frac{\hat{F}_{ext,j}}{\pi\rho g A a^2} \quad (5.21)$$

The normalised maximum pressures and the distances below the still water level at which they occur are detailed in Figure 5.4 for the WEC under consideration. The maximum pressure is normalised using the following expression:

$$\frac{p_{max}}{\rho g A} \quad (5.22)$$

The boundary element method is used to analyse the pressure distribution over the wetted surface of the structure. A wave frequency range, f , of 0.02 to 0.25 Hz is used in the analysis with the water depth set to 1000 m in order to simulate deep water conditions. A range of wave directions are specified with no forward speed. The connection details of the structure to the sea floor are specified as the default, catenary system. The structure is a floating structure which is allowed to oscillate in all directions of motion. The centre of

Frequency-domain wave-structure interaction using CFD

gravity of the structure is set equal to its centre of buoyancy and the moments of inertia for the structure are defined via its radii of gyration and coincide with this stipulation.

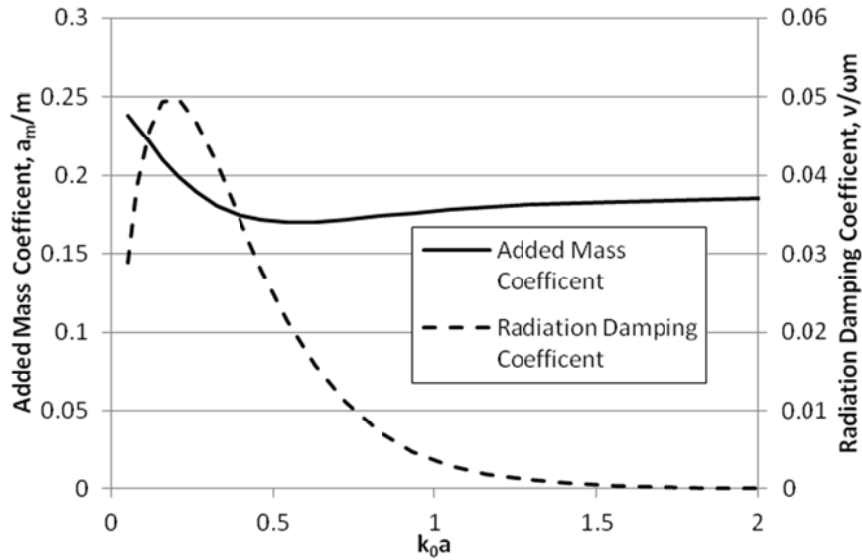


Figure 5.1: The normalised hydrodynamic coefficients for the case study using ANSYS AQWA.

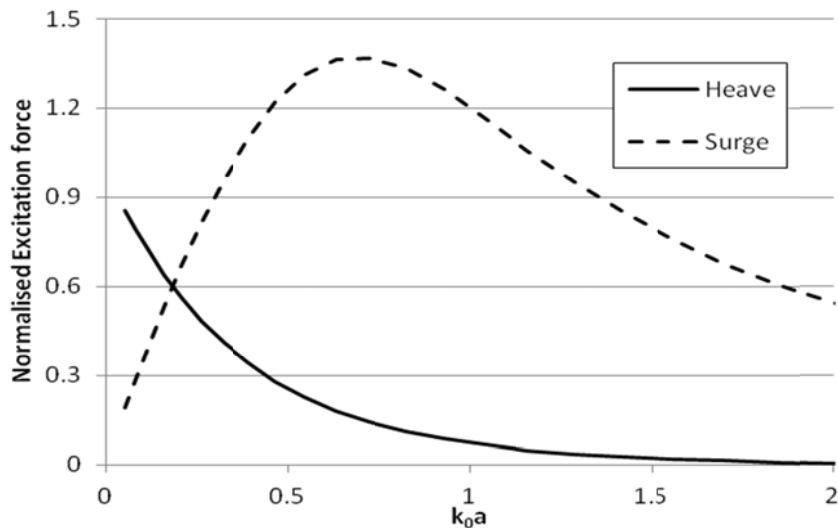


Figure 5.2: The normalised wave excitation forces, in the heave and surge motion, for the case study using ANSYS AQWA.

Frequency-domain wave-structure interaction using CFD

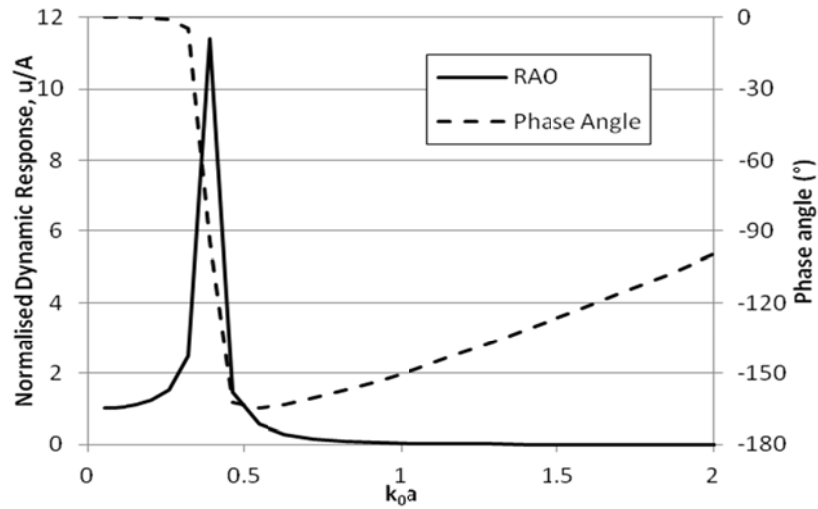


Figure 5.3: The normalised dynamic response, and its phase angle, for the case study using ANSYS AQWA.

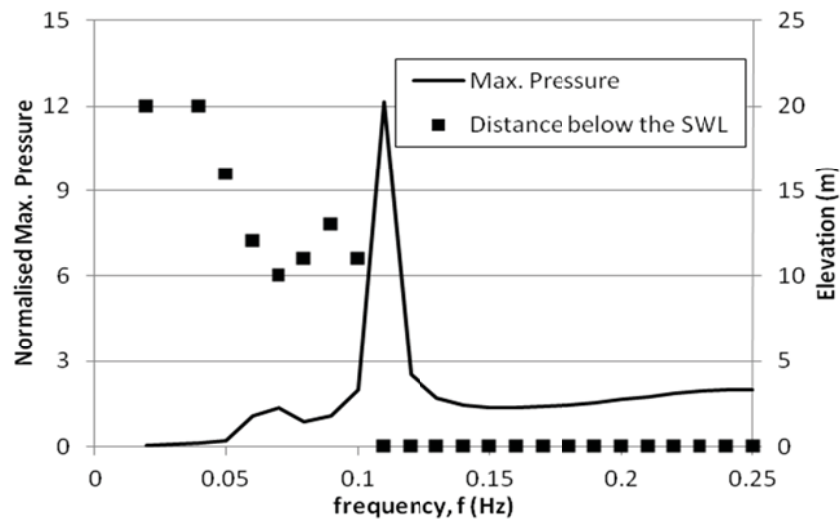
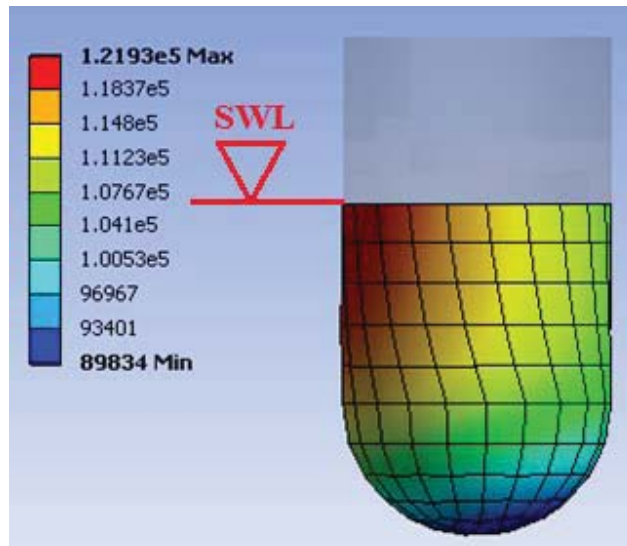


Figure 5.4: The normalised maximum pressure (Eqn. (5.22)) and depth at which it occurs below the still water level against wave frequency. Derived from the ANSYS AQWA analysis of the structure.

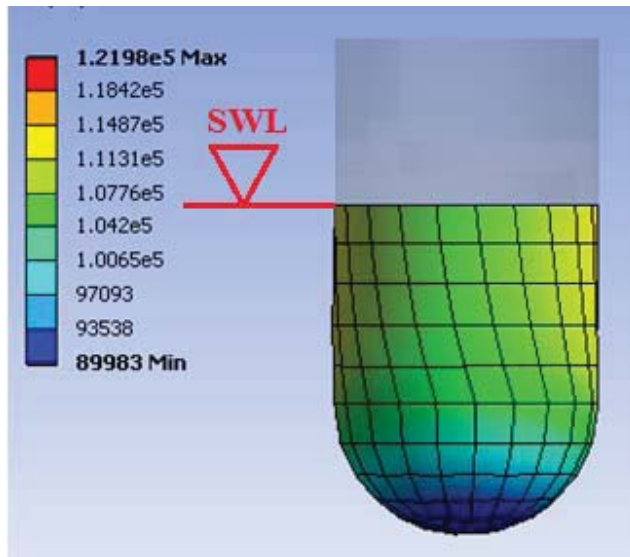
Frequency-domain wave-structure interaction using CFD

The hydrodynamic pressure distribution on the structure is shown in Figure 5.5 for the case where the structure is oscillating at resonance. A number of elevations are displayed in Figure 5.5 and this illustrates the importance of the wave direction on the location of maximum pressure. The analysis is performed with an incident wave of amplitude, A , of 1m and the units displayed are Newtons per square metre (N/m^2). Furthermore, Figure 5.6 details hydrodynamic pressure distribution on the structure for incident waves of different frequencies, above and below the resonant frequency. Again, an incident wave of amplitude, A , of 1 m is used and the units displayed are Newtons per square metre (N/m^2).

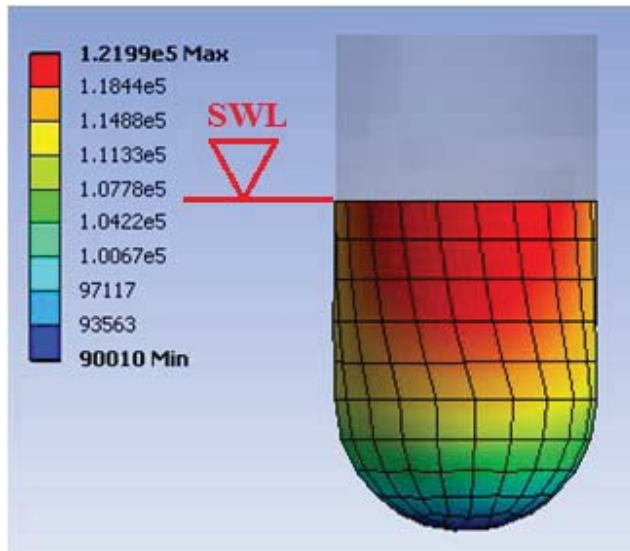


(a)

Frequency-domain wave-structure interaction using CFD



(b)



(c)

Figure 5.5: Hydrodynamic pressure distribution on the structure when it is oscillating at resonance with an incident wave coming from left to right. (a): Front elevation (b): Right end elevation (c): Left end elevation (Units in N/m^2). Structure analysed using ANSYS AQWA.

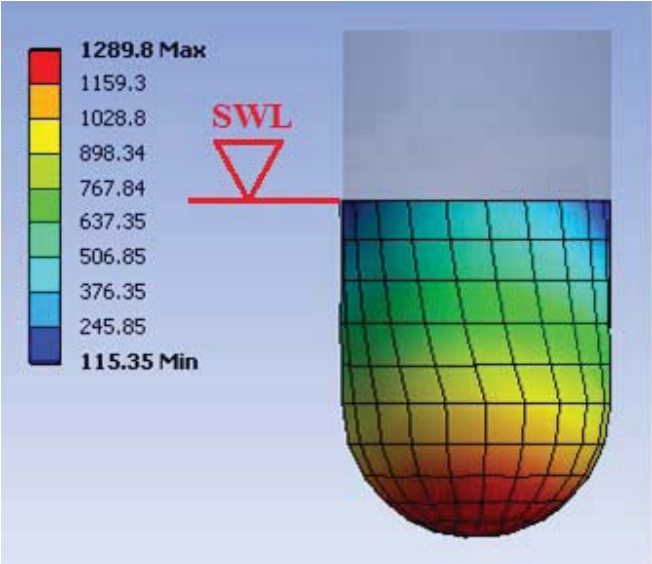
5.5.4 Discussions and conclusions

As can be seen for Figure 5.4, the maximum pressure occurs when the structure is oscillating at resonance, when the resonant frequency, f_n , of the structure matches the frequency of the incident wave, f . This occurs at a resonant frequency, f_n , of approximately 0.11 Hz for the case study presented in this section. Furthermore, the hydrodynamic pressure distribution on the structure, when it is oscillating at resonance, is illustrated in Figure 5.5. Therefore, it is necessary to place sensors at the location where this maximum pressure occurs, which is at the still water level when the wave frequency is the same as or greater than the resonant frequency of the device. In the design of WECs, mechanical tuning is used to control or adjust the resonant frequency of the converter. One of the design considerations is the avoidance of slamming and this is achieved by restricting the maximum dynamic response of the WEC by detuning away from resonance. However, high pressures will still occur close to resonance, which also can be seen in Figure 5.4.

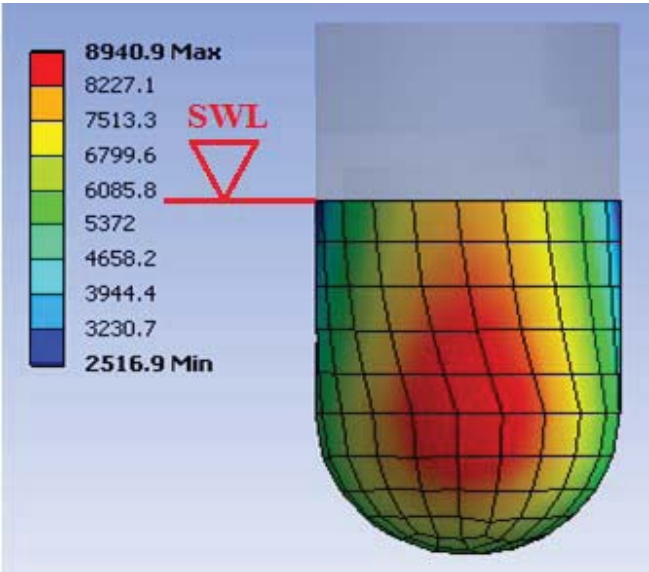
It is also noted in Figure 5.4 that the distance below the still water level where the maximum stress occurs is greatest when the maximum pressure is lowest. In other words, the greater the maximum pressure the closer to the still water level it occurs when the frequency of the waves is less than the resonant frequency of the device (i.e. $f < f_n$). When the frequency of the waves is equal to or greater than the resonant frequency of the device (i.e. $f \geq f_n$), the maximum pressure occurs at the still water level. The hydrodynamic pressure distribution on the structure shown in Figure 5.6 illustrates this observation for a number of key incident wave frequencies. For a wave of amplitude 15 m, a maximum pressure of 1.83 N/mm^2 will occur on the structure and this is much lower than the compression strength of the concrete, typically 30 N/mm^2 . Therefore, for this case, it is necessary to have a set of primary sensors in place on the structure at the still water level, as when maximum pressure, or stress, is high it occurs at this location. Furthermore, it is necessary to have a set of secondary sensors located 10 to 13 m below the still water

Frequency-domain wave-structure interaction using CFD

level. Since the maximum pressure below this point is so low compared to that at higher frequencies, this orientation of sensors is sufficient.

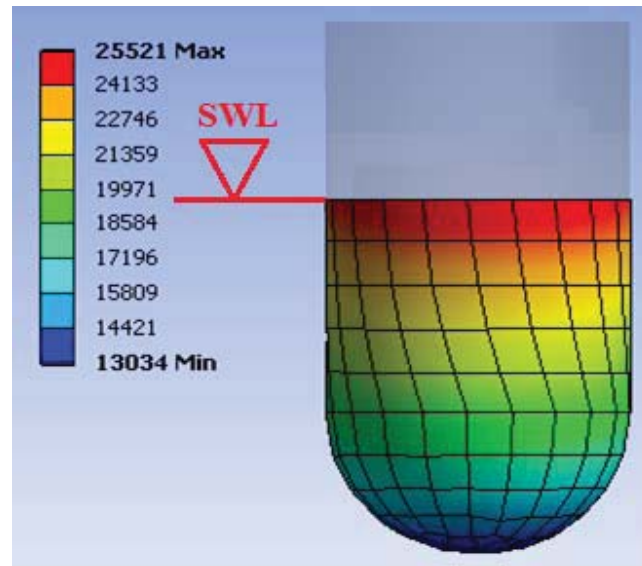


(a)



(b)

Frequency-domain wave-structure interaction using CFD



(c)

Figure 5.6: The maximum stress and the locations at which it occurs for incident waves of different frequencies. (a): $f = 0.04$ Hz (b): $f = 0.08$ Hz (c): $f = 0.12$ Hz (Units in N/m^2).

Structure analysed using ANSYS AQWA.

5.6 Structural dynamics of a heaving two-body wave energy converter

5.6.1 Introduction

The basic concept of a WEC is similar for each of the differing designs, regardless of the mode of motion of the wave in which it mainly utilizes. Generally, the ocean waves excite a mechanism and the motion of this mechanism is converted to pneumatic energy, which can easily be converted to electrical energy. The system in which the mechanical energy is converted to pneumatic energy is known as the power take-off (PTO) system. The two-body system described in this section uses the relative motion between the floating buoy and the intermediate buoy as the mechanical energy being passed to the PTO system.

In this section, the structural dynamics of this two-body system is analysed in order to derive this motion, from which wave energy is made possible. Structural dynamics has been a major topic for civil and structural engineers for decades and many topic specific books have been written, for example by Craig (1981) and Chopra (1995). The structural dynamics techniques detailed in these books will be applied to offshore structure dynamics with the ocean waves as the exciting forces. Falnes (1999) examines the load force for wave energy conversion using a two-body system where each body may only move with one degree of freedom. O’Cathain et al. (2007) explored the time-domain multi-body modeling of marine structures and took a case study of a two-body hinged barge. Furthermore, there are a number of prototype-level two body WECs being investigated, for example the Wavebob (2010) and the IPS OWEC buoy (IPS, 2012).

In recent years, many numerical approaches have been explored and developed in order to explore the wave-structure interaction using a numerical wave tank. In this section, the hydrodynamic boundary element method software, ANSYS AQWA (ANSYS-Inc., 2010), is utilised in order to perform a hydrodynamic analysis on the floating buoy and intermediate buoy individually. The structural dynamics procedure detailed in Section

5.6.2 is then used to derive the relative dynamic response between the two buoys. In Section 5.6.4, a case study of a two-body wave energy converter (WEC), which oscillates in the heave, or vertical, motion, is detailed.

5.6.2 Mathematical formulation

The system being analysed in this section is summarised using the diagram shown in Figure 5.7, where, k_i is the hydrostatic stiffness of the i th buoy, k_{ms} is the mooring system stiffness, v_i is the wave damping of the i th buoy, c_{ms} is the mooring system damping, k_{PTO} is the PTO stiffness, c_{PTO} is the PTO damping, M_i is the mass of the i th buoy, $a_{m,i}$ is the added mass of the i th buoy and F_i is the i th wave excitation force. Throughout this section, the subscript '1' denotes the floating buoy and the subscript '2' denotes the intermediate buoy.

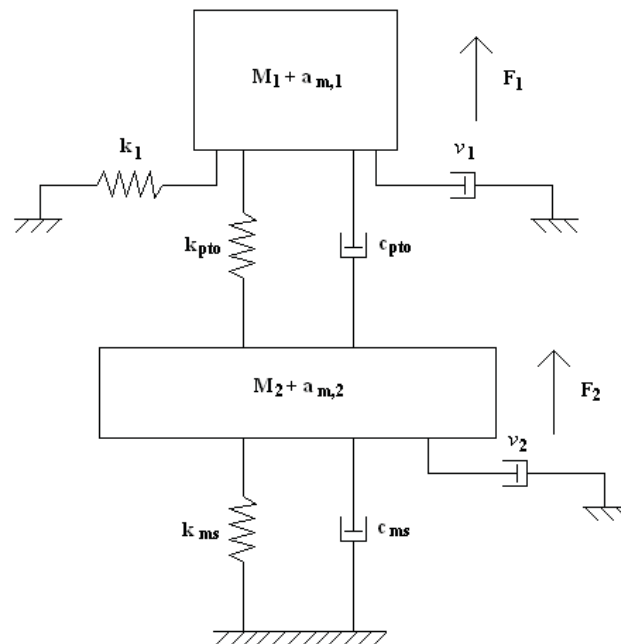


Figure 5.7: Free body diagram of the two-body system where only heaving motions are being considered.

Frequency-domain wave-structure interaction using CFD

The equation of motion for the system is given in matrix form, as follows:

$$[M]\{\ddot{u}\} + [C]\{\dot{u}\} + [K]\{u\} = \{F_{\text{ext}}\} \quad (5.23)$$

where the mass matrix:

$$[M] = \begin{bmatrix} M_1 + a_{m,1} & 0 \\ 0 & M_2 + a_{m,2} \end{bmatrix} \quad (5.24)$$

The stiffness matrix, $[K]$, terms are calculated by inducing a unit displacement individually at each of the degrees of freedom. Thus, when a unit displacement of $u_1 = 1$ and $u_2 = 0$ is induced:

$$k_{11} = k_{\text{PTO}} + k_1 \quad (5.25)$$

And when a unit displacement of $u_1 = 0$ and $u_2 = 1$ is induced:

$$k_{12} = k_{21} = -k_{\text{PTO}} \quad (5.26)$$

Therefore, the stiffness matrix is given as:

$$[K] = \begin{bmatrix} k_{\text{PTO}} + k_1 & -k_{\text{PTO}} \\ -k_{\text{PTO}} & k_{\text{PTO}} + k_{\text{ms}} \end{bmatrix} \quad (5.27)$$

Taking a similar procedure for the PTO damping and mooring system damping and, also, allowing for the wave radiation damping interaction observed by Falnes (2002), the damping matrix for the system is written as:

$$[C] = \begin{bmatrix} c_{\text{PTO}} + \nu_1 & -\sqrt{\nu_1 \nu_2} - c_{\text{PTO}} \\ -\sqrt{\nu_1 \nu_2} - c_{\text{PTO}} & \nu_2 + c_{\text{PTO}} + c_{\text{ms}} \end{bmatrix} \quad (5.28)$$

The natural frequencies, ω_n , of the system are then calculated. These may be calculated using the assumption that the system is undamped. This is a valid assumption as the damped resonant frequency, $\omega_d = \omega_n \sqrt{1 - \zeta^2}$, where the damping ratio, ζ , is small and, therefore, $\omega_d \approx \omega_n$. Also, as it is the frequency of the structure that is being calculated, the magnitude or frequency of the applied force does not affect the result. Thus, we may assume the system to be a 'free' system for this stage of the analysis. Therefore, when

Frequency-domain wave-structure interaction using CFD

calculating the natural frequencies of the system, the equation of motion, given in Eqn. (5.23) is reduced to:

$$[M]\{\ddot{u}\} + [K]\{u\} = \{0\} \quad (5.29)$$

A trial solution, where the motion of the system is assumed to be harmonic motion, is now introduced and is given as:

$$\{u\} = \{\phi\} \sin(\omega t + \theta) \quad (5.30)$$

Substituting into Eqn. (5.29), gives:

$$\begin{aligned} -\omega^2[M]\{\phi\} \sin(\omega t + \theta) + [K]\{\phi\} \sin(\omega t + \theta) &= \{0\} \\ \Rightarrow [[K] - \omega^2[M]]\{\phi\} &= \{0\} \end{aligned} \quad (5.31)$$

In order to determine a non-trivial solution, $\{\phi\} \neq 0$, and, therefore:

$$\det[[K] - \omega^2[M]] = 0 \quad (5.32)$$

where *det* is the determinant of the matrix. The only unknown value in this equation is the natural frequencies, ω_n , which are then calculated. The modal matrix can now be calculated using the natural frequencies. The fundamental harmonic mode, ϕ_1 , is derived from the first resonant frequency, ω_1 , by substituting into Eqn. (5.31) and then normalising and solving for ϕ_{11} and ϕ_{21} . The second harmonic mode, ϕ_2 , is calculated in a similar way. The second resonant frequency, ω_2 , is substituted into Eqn. (5.31) and then normalising and solving for ϕ_{12} and ϕ_{22} . The two natural modes are the two columns of the modal matrix as follows:

$$\Phi = \begin{bmatrix} \phi_{11} & \phi_{12} \\ \phi_{21} & \phi_{22} \end{bmatrix} \quad (5.33)$$

where ϕ_{ij} is the mode shape coordinate representing the position of the i^{th} buoy and j^{th} mode.

Since the system is assumed to be linear, or the elements of the stiffness matrix remain constant throughout the analysis, a convenient method in order to return a solution is modal analysis (Craig, 1981; Chopra, 1995). The original equation of motion, in Eqn.

(5.23), is now reintroduced and, since it is a coupled equation it is necessary to transform it into a set of uncoupled equations, or the modal equations. This transformation is performed using the modal matrix, as follows:

$$\begin{aligned} & \Phi^T[M]\Phi\{\ddot{u}\} + \Phi^T[C]\Phi\{\dot{u}\} + \Phi^T[K]\Phi\{u\} = \Phi^T\{F_{ext}\} \\ \Rightarrow & \begin{bmatrix} m_1 & 0 \\ 0 & m_2 \end{bmatrix} \begin{Bmatrix} \ddot{q}(t)_1 \\ \ddot{q}(t)_2 \end{Bmatrix} + \begin{bmatrix} c_1 & 0 \\ 0 & c_2 \end{bmatrix} \begin{Bmatrix} \dot{q}(t)_1 \\ \dot{q}(t)_2 \end{Bmatrix} + \begin{bmatrix} k'_1 & 0 \\ 0 & k'_2 \end{bmatrix} \begin{Bmatrix} q(t)_1 \\ q(t)_2 \end{Bmatrix} = \begin{Bmatrix} f(t)_1 \\ f(t)_2 \end{Bmatrix} \end{aligned} \quad (5.34)$$

where m_j is the modal mass in the j^{th} mode, c_j is the modal classical damping in the j^{th} mode, k'_j is the modal stiffness in the j^{th} mode, $f(t)_j$ is the modal force in the j^{th} mode and $q(t)_j$ is the modal displacement, as a function of time, in the j^{th} mode.

Therefore, each uncoupled equation is analogous to a different single degree of freedom system and can be solved in the same way as using a classic single degree of freedom solution, for example the Newmark, or average acceleration, method (Newmark, 1959). The displacements $q_1(t)$ and $q_2(t)$ of these systems identify the contribution made by the natural modes, φ_1 and φ_2 , to the actual displaced configuration, $\{u(t)\}$, of the structure at time t . However, the methodology can also be used to calculate the frequency-domain response using the response amplitude operator (RAO) to solve each uncoupled equation.

5.6.3 Mooring system design

For the purpose of this study, the type of moorings being used is catenary lines. The inelastic catenary equations (Johanning et al., 2006) are used to calculate the vertical restraint imposed by the moorings. These are more applicable to steel wire and chain and, therefore, three 100 mm chain mooring lines are used. These are distributed at intervals of equal angle (120 °) from the intermediate buoy. For the purpose of this analysis, the length of each mooring line is set to 200 m and is anchored at an average distance of 170 m, horizontally, from the WEC. From this information, the restoring force of the mooring system can be calculated, which is shown in Figure 5.8.

Frequency-domain wave-structure interaction using CFD

However, since the system described in this section is linear, it is necessary to provide a spring estimate for the restoring force. This was found to be 19.24 kN/m and a comparison between the calculated and spring estimate can be seen in Figure 5.8. From Figure 5.8, it is clear to see that, for a maximum vertical displacement of ± 5 m, this is a good estimate.

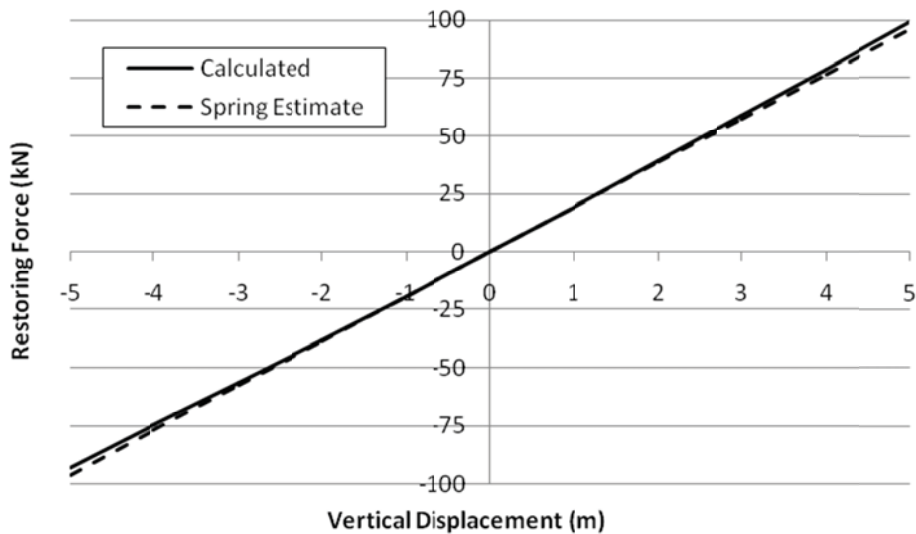


Figure 5.8: Restoring force of the mooring lines on the WEC

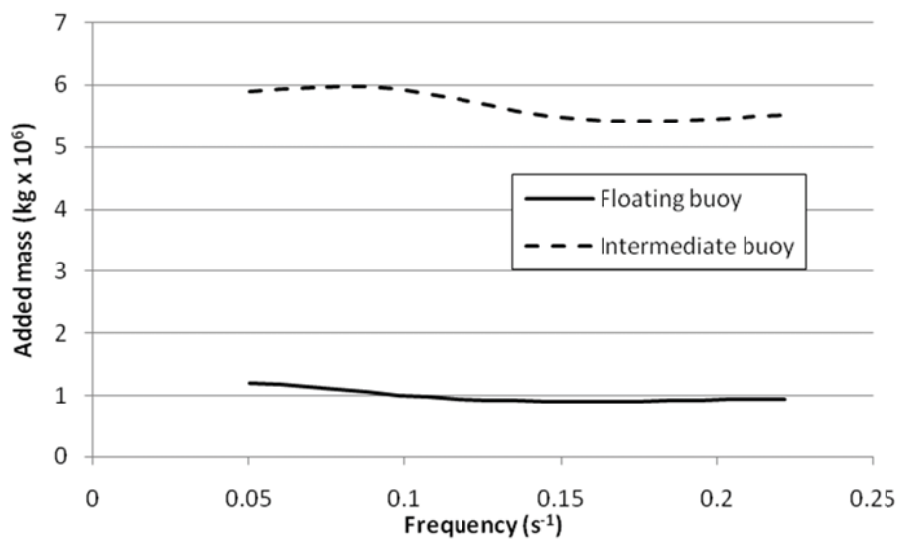
5.6.4 Case study

In this section, the methodology described in Section 5.6.2 will be applied to a case study of a two-body WEC, which has a heaving vertical cylinder floating buoy and a vertical cylinder intermediate buoy, with its upper surface located at 19 m below the still water level (SWL). The heaving vertical cylinder floating buoy has a radius of 8 m and draft of 10 m. The vertical cylinder intermediate buoy has a radius of 12 m and draft of 4 m and is anchored to the sea bed using a catenary mooring system. The WEC is restricted to operating only in the heave, or vertical, motion for the purpose of the analysis. Thus, the

Frequency-domain wave-structure interaction using CFD

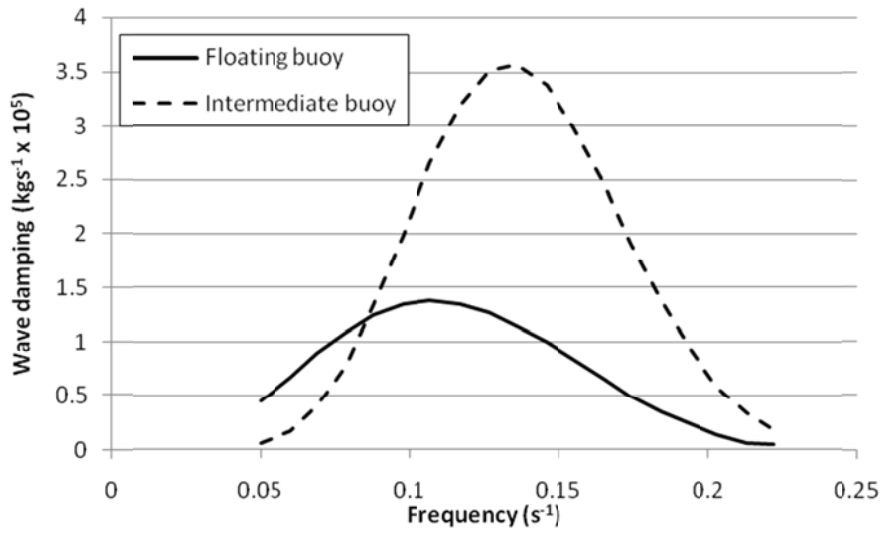
system has two degrees of freedom. The PTO system is modelled using a spring and damper system with a damping coefficient of 100,000 kg/s and an associated stiffness coefficient of 150 kN/m.

The boundary element method software, ANSYS AQWA (ANSYS Inc., 2010), is used to perform a hydrodynamic analysis on the floating and intermediate buoys. A graphical representation of this analysis is shown in Figure 5.9, detailing the added mass, wave radiation damping and the heave excitation forces on both buoys. The mooring system in the case study is assumed to be a linear system and is calculated using the procedure described in Section 5.6.3 and the spring estimate shown in Figure 5.8.

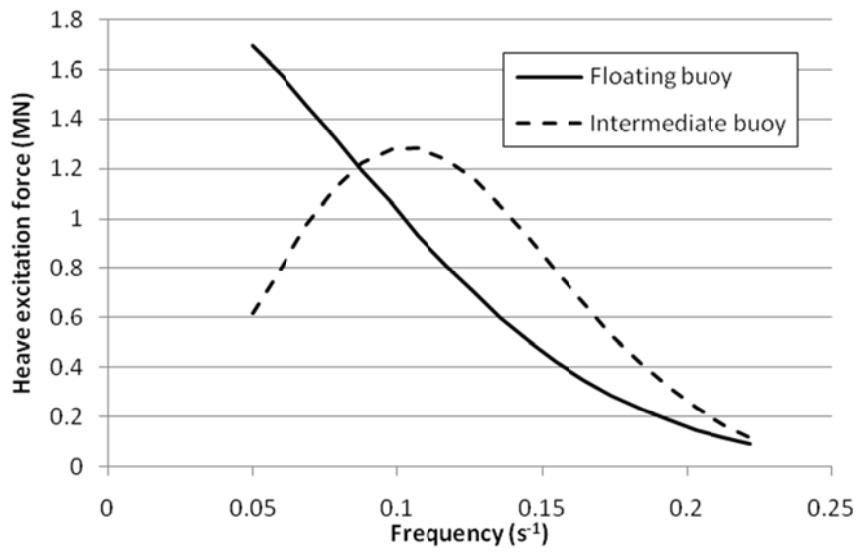


(a)

Frequency-domain wave-structure interaction using CFD



(b)



(c)

Figure 5.9: The hydrodynamic analysis, using BEM (ANSYS AQWA), for the floating buoy and intermediate buoy, detailing (a): the added mass (b): the wave radiation damping (c): the heave excitation force.

Frequency-domain wave-structure interaction using CFD

The hydrodynamic analysis is then used along with the procedure detailed in Section 5.6.2 to calculate the relative normalised dynamic response between the floating buoy and the intermediate buoy using the response amplitude operator. This is shown graphically in Figure 5.10, in the frequency domain. Furthermore, the actual normalised dynamic response of each of the two buoys is displayed.

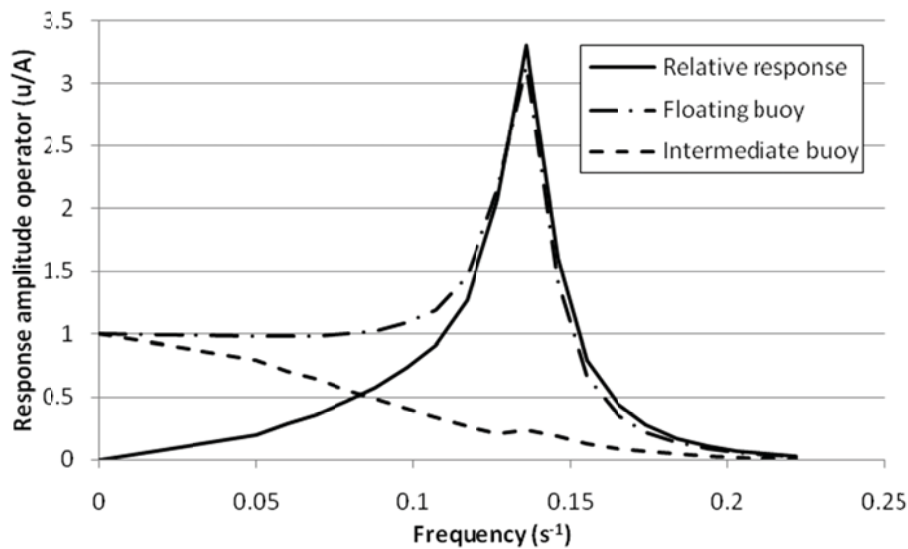


Figure 5.10: The response amplitude operator for each of the buoys and the relative response.

5.6.5 Discussion and conclusions

From Figure 5.10, it can be seen that at frequencies lower than the resonant frequency of the system, the intermediate buoy has a largely significant dynamic response, which is in phase with the floating buoy, and, therefore, the relative dynamic response is much less than that of the actual dynamic response of the floating buoy. Furthermore, it is clear from Figure 5.10 that the damping associated with intermediate buoy is well above critically damped, i.e. the buoy acts quite rigidly, to ensure there is only one resonant

frequency of the system in the frequency range investigated. This frequency is the same as the resonant frequency of the floating buoy. However, at the resonant frequency or at larger frequencies, the relative dynamic response is very close to that of the actual dynamic response of the floating buoy. Therefore, the heaving two-body WEC would perform best at or greater than the resonant frequency of the system.

In this section, the linear equations for calculating the dynamic response of a two-body WEC, which oscillates in the heave, or vertical, motion, are derived. The equations are derived using classical structural dynamics techniques, i.e. modal analysis, in order to solve the complex problem using a single degree of freedom method; for example the response amplitude operator in the frequency-domain or the Newmark method in the time-domain.

The two-body WEC comprises of a floating buoy, which is an oscillating point-absorber, and a submerged intermediate buoy, which are connected via a PTO system. The PTO system is modelled as a spring and damper system in this study. The intermediate buoy is anchored to the sea bed using a mooring system, which is three catenary lines, and is modelled using a spring derived from the inelastic catenary equations.

Chapter 6
Validation of numerical models using
experimental data

6.1 Introduction

In order to perform cost effective physical models in marine engineering, the use of small scale testing facilities is essential. These small scale marine testing facilities include wave flumes, wave tanks/basins and tidal basins. A wave tank/basin is a laboratory set-up for observing the behaviour of waves and usually has a width comparable to its length. While, a wave flume is a long narrow channel where the waves generated are two-dimensional in a vertical plane. In order to generate the waves, which mimic the characteristics of real waves, a mechanical wave generation method is usually employed.

For this project, a wave flume is employed for the validation of the numerical model for a wave tank using the results from experimental tests. A wave flume is usually characterised as a long, narrow tank with a wavemaker of some kind at one end. Furthermore, there is usually a method of dissipating the wave energy placed at the other end of the tank. The experimental wave flume used for this project is located at the National University of Ireland, Galway.

In this section, the experimental wave flume employed is described in detail in relation to its design and operation, along with the monitoring systems being employed to analyse its performance, i.e. the wave elevation gauges. An analysis of the resultant output experimental data is performed and a detailed interpretation of the results is presented. In order to reproduce the experimental waves in the numerical model for a wave tank (NWT), the wave generation method employed needs to replicate the wedged-shaped plunger-type wavemaker used in the experimental wave flume. A detailed description of the adapted NWT is included. Furthermore, an extensive time-domain comparison of the two outputs is undertaken, along with a comparison to the experimentally estimated wavemaker approximation. A floating cylindrical structure is introduced into the physical wave flume and its response is compared to simulations using the NWT.

6.2 NUI Galway experimental wave flume

The experimental wave flume located at NUI Galway, shown in Figure 6.1 and Figure 6.2, was built in 2009 by Ms. C. Killeen under the supervision of Dr. M. Bruzzi and Dr. N. Quinlan (Killeen, 2011), but was subsequently recommissioned when it was moved to the new Engineering building located on the NUI Galway main campus. It has overall dimensions of 10 m x 1 m x 1 m. For the experimental testing, the still water level (SWL) remained at a constant 0.7 m and the flume has a maximum SWL of 0.8 m. There is an error variation in the width of the flume nearing the dissipation zone of less than 25 mm. Currently, there is a rotational motor driving the wavemaker mechanism, which only has the capability of generating regular linear and non-linear waves. In this study, non-linear waves refer to waves of a single dominant frequency which have amplitude of a large enough magnitude that they don't conform to Airy's linear wave theory.

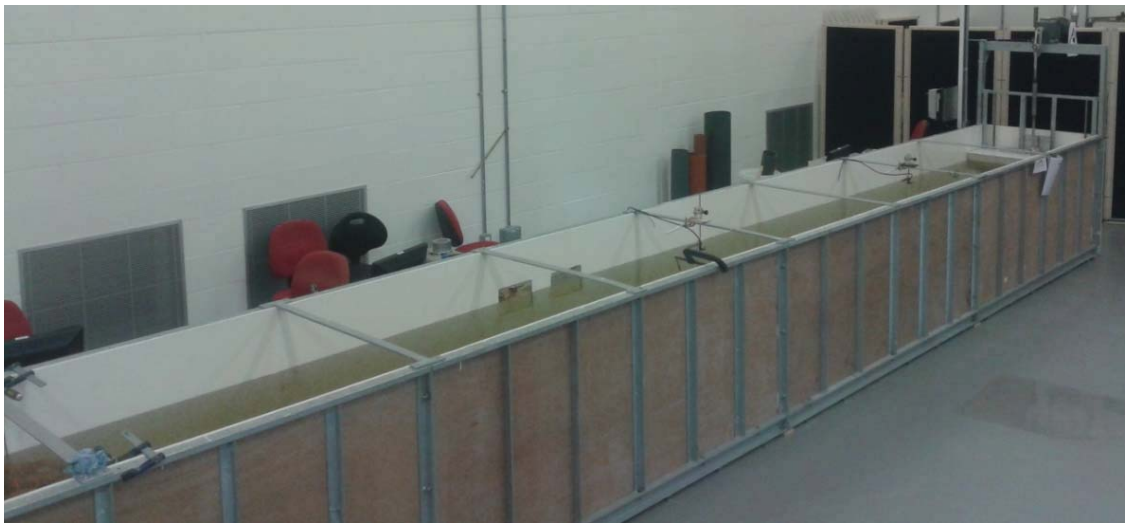


Figure 6.1: The experimental wave flume located at the National University of Ireland, Galway.

Validation of numerical models using experimental data

In order to generate the waves, a mechanical wavemaker needs to be placed at one end of the flume. There are three main types of wavemakers; flap-type, piston-type and plunger-type. In the NUI Galway experimental wave flume, there is a wedged-shaped plunger-type wavemaker in place, which is connected to linear motor ensuring that it oscillates in a sinusoidal motion. This wavemaker system is capable of accurately generating regular linear and non-linear waves with a wave period range of 0.75 to 2 s and the maximum stroke length is approximately 0.4 m. The total height of the wedge is 0.6 m with the angle of the wedge as 26.5° and plunger sectional area coefficient of 0.5. Its base oscillates around a mean position of 0.35 m from the base of the flume and, therefore, mean width of the plunger at the SWL, γ , is 0.175 m. Furthermore, the space between the wedge and the walls of the tank is 5 to 10 mm.

At the opposite end of the wave flume to the wavemaker, there is a wave energy dissipation zone. There are a number of different methods which may be implemented to achieve the desired level of wave energy dissipation. These include a constant slope beach, a parabolic beach, a gravel beach that includes porosity effects, an active wave absorption system, transverse bars, horse hair or wire screens (Khalilabadi and Bidokhti, 2012). In order to reduce the length of the wave energy dissipation zone, a combination of a varying slope beach and a wire mesh with sponges along the still water level is used in the NUI Galway experimental wave flume. The beach is at a slope of 3:1 but a wedge is added to ensure the wire mesh with sponges remain along the still water level for 0.8 m in order to increase the level of wave energy dissipation, as shown schematically in Figure 6.2. Thus, the tank has an effective length of approximately 7 m.

Validation of numerical models using experimental data

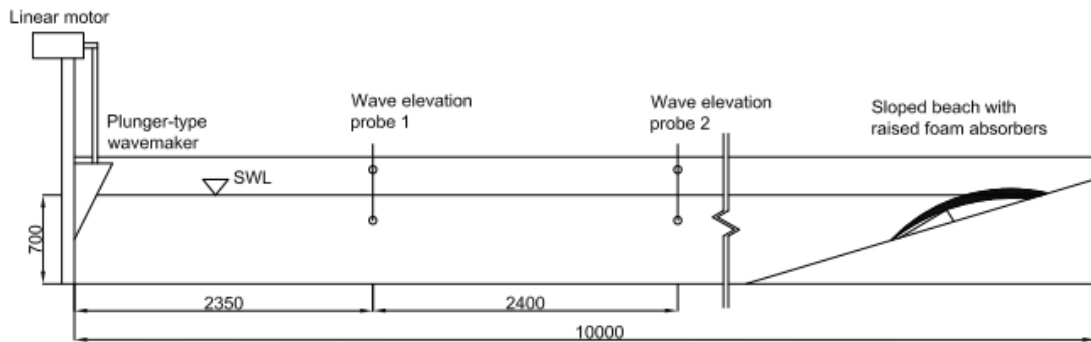


Figure 6.2: Schematic of the experimental wave flume at NUI Galway (Including positioning of wave elevation probes). Dimensions are in mm.

In order to monitor the waves been generated by the wavemaker, there are two wave elevation gauges, or probes, placed at distances of 2.35 m and 4.75 m from the vertical side of the wavemaker, which capture the free surface elevation as it varies with time, as shown in Figure 6.2. The wave elevation gauges are placed at a horizontal distance from the wavemaker of more than three times the height from the base to the SWL, or $3d$. Initially, the wavemaker generates both a progressive wave and a standing wave and this standing wave dissipates as it travels away from the wavemaker. Dean and Dalrymple (1984) found that the effects of the standing wave become negligible at a distance greater than three times the height from the base to the SWL, or $3d$, and, therefore, the wave elevation gauges are placed at two locations which only monitor the progressive wave. The wave elevation gauges are Akamina wave height gauges (Akamina Technologies, 2012), which measure capacitance through a semi-submerged vertical wire and then converts it to an output voltage. A linear relation between the output voltage and the wave elevation is determined during the calibration of the gauges, which can be seen in Figure 6.3. During the experimental testing, the wave elevation was recorded using a data acquisition system, which converts the output voltage to wave elevation at each time-step. The scaling factor used in the data acquisition system to make this conversion is the slope of their linear relation, obtained from Figure 6.3.

Validation of numerical models using experimental data

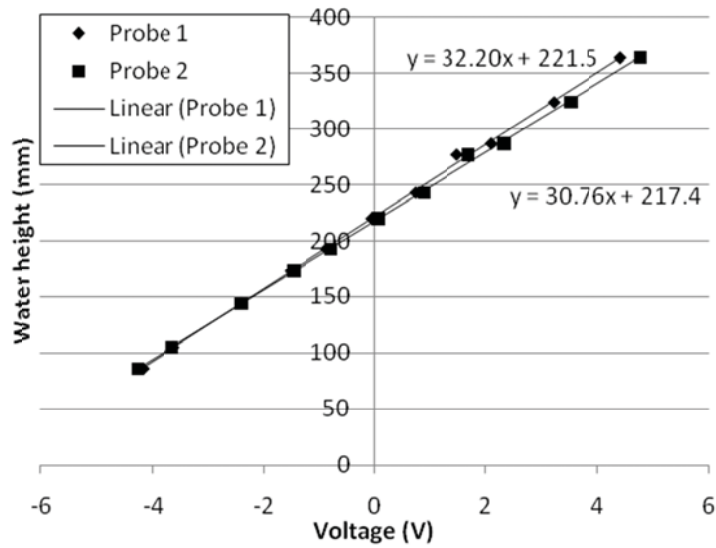


Figure 6.3: Linear relation between the output voltage and the wave elevation which was determined during the calibration of the wave elevation gauges.

6.3 Determining the parameters associated with the NUI Galway wave flume

The initial stage of the experimental analysis is to quantify the parameters associated with the NUI Galway wave flume. These parameters include the wavemaker relation associated with the flume and the frequency breaking limit of the generated waves at different strokes. Ursell (1949) and Wang (1974) showed that the wavemaker relation, the wave height to stroke length ratio, H/S , is only dependent on the dimensionless wavenumber ratio, $k_0\gamma$, where k_0 is the wavenumber and γ is the breadth of the plunger at the still water level. Therefore, the dimensionless wavenumber ratio will be used in the comparison of the experimental, theoretical and numerical wavemaker relation.

The wavemaker relation is derived for a given stroke length from the wave elevation recorded at each of the wave elevation gauges, which are placed at 2.35 m and 4.75 m from the vertical side of the wavemaker. The results of the wavemaker relation are summarized in Figure 6.4 with an experimental estimate included. The experimental

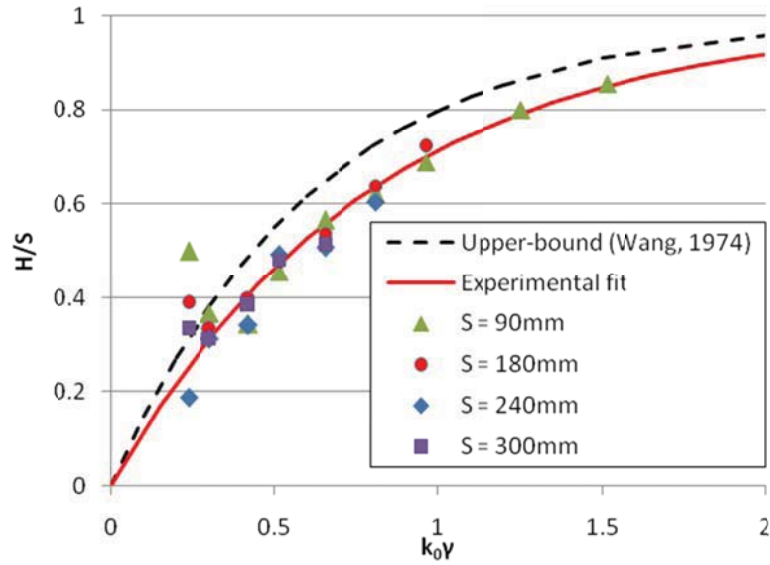
Validation of numerical models using experimental data

estimate is the best fit line through the results from the experimental data and is given by the equation:

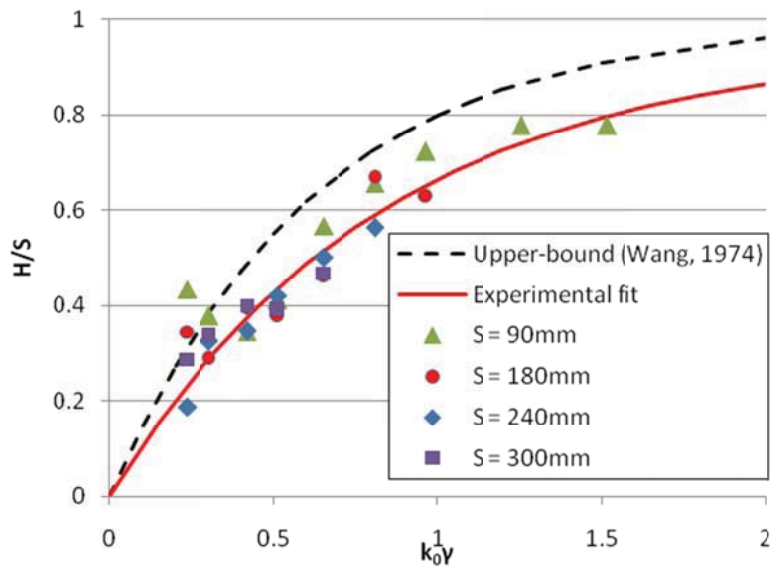
$$\frac{H}{S} = \begin{cases} 1 - e^{-1.25k_0\gamma}, & \text{at } x = 2.35 \text{ m} \\ 0.95(1 - e^{-1.2k_0\gamma}), & \text{at } x = 4.75 \text{ m} \end{cases} \quad (6.1)$$

The coefficient of determination, or r-squared value, is calculated for the best fit line and was found to be 0.84 and 0.837 for a distance of 2.35 m and 4.75 m from the wavemaker, respectively. The experimental estimate for the wavemaker relation will be used in the comparison to the output from the NWT model. The results of the experimental wave flume have also been compared to the deep water asymptotic expression for the wavemaker relation derived by Wang (1974). Since Wang assumes infinite depth and the NUI Galway wave flume has a finite depth, the asymptotic expression presented by Wang will be an ‘Upper-bound’ for H/S . It is evident from Figure 6.4 that the theory overestimates the experimental results. The reason for this is that the flume in question has a mean water depth to mean plunger depth ratio, d/h , which is below the limiting values specified by Wang (1974). Therefore, as a result of the effect of shallowness in finite depth, or, in other words, the interaction of the flume base with the water particle velocities, the height of the waves will be less than for the deep water case. However, Wang (1974) does state that the experimental values which he observed suggest that the theory would be a good approximation when the mean water depth to mean plunger depth ratio is below the limiting values, which is the case in this study. This is evident in the present study as the error between the experimental outputs and theory (Wang, 1974) is less than 15%, where in general the theory overestimates the wave height to stroke ratio for a range of dimensionless wavenumber ratios, $k_0\gamma$, which can be seen in Figure 6.4. However, the solution provided by Wang (1974) requires a rigorous calculation, whereas Eqn. (6.1) provides a convenient solution for the wavemaker relation for a wave flume with similar specifications as to what is described in this chapter.

Validation of numerical models using experimental data



(a)



(b)

Figure 6.4: Normalised comparison of wave height and wave length for different stroke lengths and the experimental estimated wavemaker relation for (a) 2.35m and (b) 4.75m from the wavemaker.

Validation of numerical models using experimental data

The frequency breaking limit of the generated waves is determined by increasing the frequency of the motion of the plunger for a given stroke length until the waves break. The breaking limit is determined for five different stroke lengths and the results of the study are detailed in Table 6.1. The breaking limit of the waves is related to the steepness, H/L , of the waves and it was found to be an average of 0.107 for the NUI Galway wave flume. The breaking limit for waves in intermediate or shallow depth water can be calculated theoretically using (Whitham, 1974):

$$\left(\frac{H}{S}\right)_{max} = \left(\frac{H_0}{S_0}\right)_{max} \tanh(k_0 d) \quad (6.2)$$

where H_0 is the deep water wave height and S_0 is the deep water stroke length. Using this equation the breaking limit of the waves in the NUI Galway flume is an average of 0.141 and a coefficient of variation, c_v , of 0.022. This is larger than the experimentally estimated result. The reason for this is the wave heights are taken at 2.35 m from the wavemaker, which measures the progressive wave, and the wavemaker generates both a progressive and standing wave initially, which is the wave which breaks.

Table 6.1: Summary of breaking limit of waves study, where T is the minimum wave period to induce wave breaking at a given stroke length, S . The average value and coefficient of variation, c_v , are included.

S (mm)	T (sec)	H (m)	L (m)	Experimental H/L	Theoretical H/L
360	1.09	0.19	1.79	0.106	0.14
300	0.97	0.15	1.45	0.104	0.141
240	0.91	0.135	1.28	0.106	0.142
180	0.8	0.11	1.0	0.109	0.142
90	0.64	0.07	0.65	0.108	0.142
Average =				0.107	0.141
c_v =				0.022	0.006

6.4 Validation of NWT model for wave generation

6.4.1 NWT model of NUI Galway experimental wave flume

In order to validate the methodology described in Chapter 4, the output from the NUI Galway experimental wave flume is compared to the corresponding output from the NWT model of the flume. However, in order for the two sets of outputs to be comparable, the wave elevation is monitored at the same locations along the NWT as the wave elevation gauges in the experimental flume. Furthermore, the method of wave generation and the wave energy dissipation method need to be adapted from that described in the methodology detailed in Chapter 4.

Therefore, the NWT model of the NUI Galway experimental wave flume uses a wall boundary with specified displacement, $\bar{x}(t)$, which mimics the movement of the experimental wavemaker to generate the linear waves.

$$\bar{x}(t) = \begin{cases} 0, & y < \bar{h}(t) \\ (y - \bar{h}(t)) \tan \alpha, & y \geq \bar{h}(t) \end{cases} \quad (6.3)$$

where

$$\bar{h}(t) = (d - h) + \frac{S}{2} \cos(\omega t + \pi) \quad (6.4)$$

where α is the angle of the plunger, h is the mean depth of the bottom of the plunger and S is the stroke length. In addition, the breadth of the plunger at the still water level, γ , may be defined with respect to these parameters as follows:

$$\gamma = (d - h) \tan \alpha \quad (6.5)$$

Furthermore, there is a ramp time specified of two times the period, $2T$, at the beginning of each simulation where the plunger is lowered from the SWL to its lowest point.

The dynamic viscosity of the fluid, μ , is adapted by increasing its value nearing the end of the model opposite the wavemaker boundary so to dissipate the wave energy. This

Validation of numerical models using experimental data

assumes an almost complete dissipation of wave energy, which is not the case, but is deemed a more accurate representation than merely putting a gradually sloping beach in place, which is the other option. In order to achieve this, the dynamic viscosity of the fluid is specified as:

$$\mu = \begin{cases} 8.899 \times 10^{-4} \text{ kg/ms}, & x < 7 \text{ m} \\ 8.899 \times 10^{-4} \text{ kg/ms} + \left(\frac{x - 7 \text{ m}}{3 \text{ m}}\right) 25 \text{ kg/ms}, & x \geq 7 \text{ m} \end{cases} \quad (6.6)$$

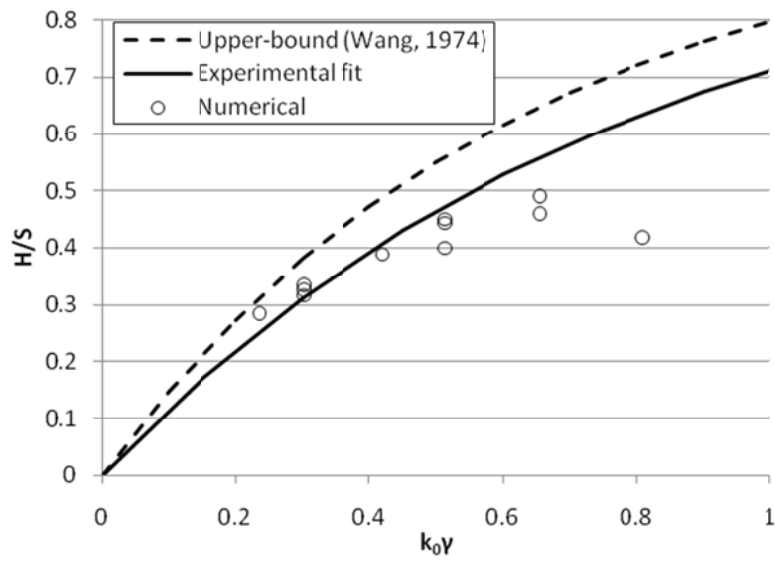
The remaining parts of the methodology, including the mesh generation and physics set-up, are as per described in Chapter 4 in the development of the NWT model of the NUI Galway experimental wave flume.

6.4.2 Comparison of numerical and experimental output

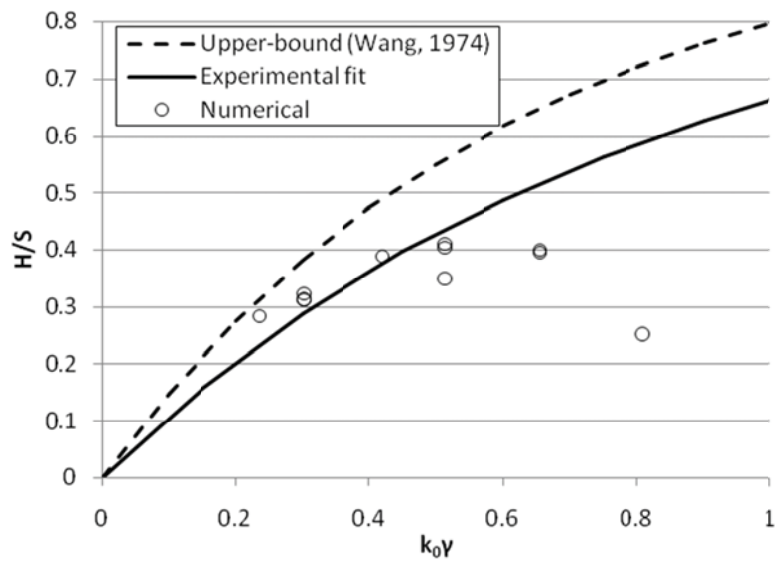
Two methods are used in order to compare the outputs from the two analyses to determine the accuracy of the NWT model; a comparison of the results of the NWT model to the experimentally derived wavemaker relation and the theoretical wavemaker relation derived by Wang (1974) and a comparison of the wave elevation output at different points along the model in the time-domain.

A number of simulations using the NWT model of the NUI Galway wave flume are performed varying the frequency and the stroke length, S , of the plunger-type wave maker and a summary of these simulations and the results derived are detailed in . The wavemaker relation at the same distance from the wavemaker as in the experimental arrangement, at the wave elevation gauges, is derived and compared in Figure 6.5. It is found that the numerical outputs are in very good agreement with the experimental outputs for $k_0\gamma < 0.7$ and then the numerical model begins to underestimate the wave height. This is a similar observation to what was found for a flap-type wavemaker, which is described in Section 4.3.3. Furthermore, the numerical model outputs are an underestimation of theoretical wavemaker relation derived by Wang (1974), which is to be expected (see Section 6.3).

Validation of numerical models using experimental data



(a)



(b)

Figure 6.5: Normalised comparison between the experimental estimate for wavemaker relation and the results of the CFD numerical model for a wave tank for (a) 2.35 m and (b) 4.75 m from the wavemaker.

Validation of numerical models using experimental data

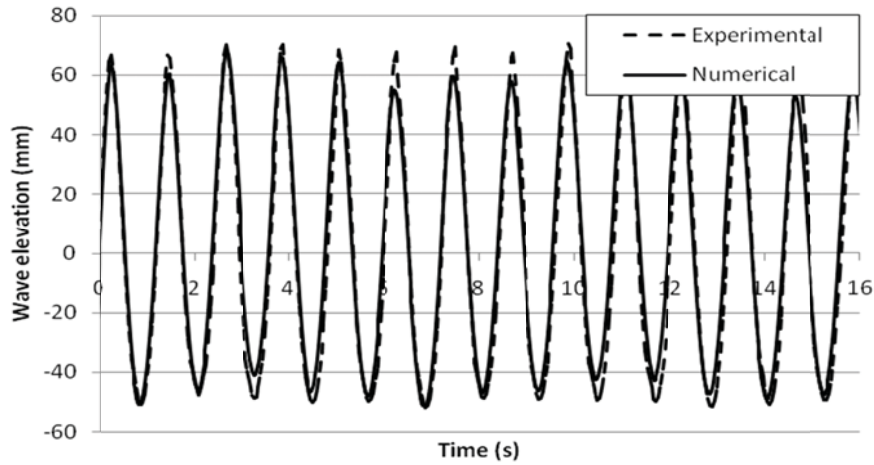
Table 6.2: Summary of comparison of NWT model and experimental results

S (mm)	T (s)	$k_0\gamma$	Experimental		Numerical	
			H/L at 2.35 m	H/L at 4.75 m	H/L at 2.35 m	H/L at 4.75 m
240	1.6667	0.303	0.325	0.313	0.313	0.325
240	1.2	0.514	0.45	0.404	0.492	0.421
240	1.05	0.654	0.458	0.396	0.508	0.5
240	0.9375	0.81	0.417	0.25	0.604	0.563
90	1.6667	0.303	0.333	0.311	0.367	0.378
90	1.2	0.514	0.444	0.411	0.456	0.411
300	2	0.236	0.283	0.283	0.333	0.287
300	1.6667	0.303	0.317	0.323	0.313	0.34
300	1.2	0.514	0.4	0.35	0.483	0.39
180	1.35	0.42	0.389	0.389	0.4	0.394
180	1.05	0.654	0.489	0.4	0.539	0.461

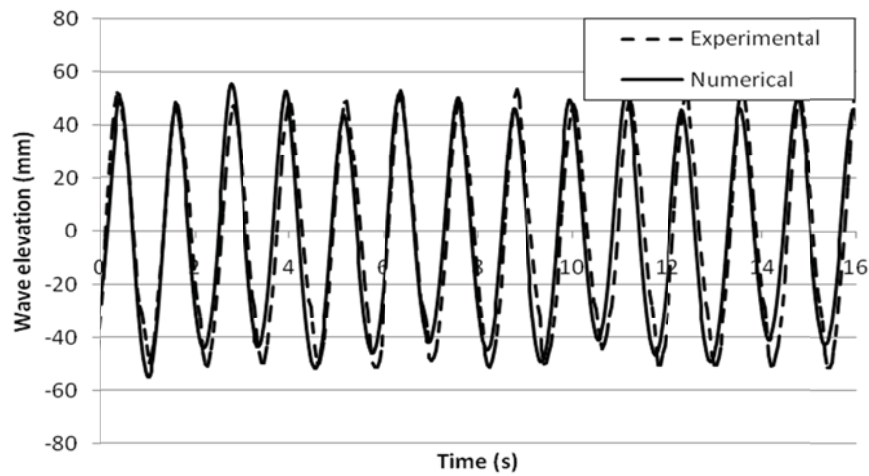
The second method of validating the numerical model against the experimentally generated data is to compare the wave elevation at each of the wave elevation gauge positions in the time-domain. The wave elevations are compared after the initial stage once the waves have become steady state in both the numerical and experimental models. A comparison for a stroke length of 240 mm and a wave period of 1.2 s is shown in Figure 6.6 and comparisons for each of the numerical simulations performed is displayed in Appendix D. The agreement between the two sets of outputs is very good, both, in terms of frequency and wave height. However, there are discrepancies when the wave period is less than 1 second, which corresponds to $k_0\gamma > 0.7$. The reason for this is that the numerical model predicts the generated wave to begin to break at a lower frequency than occurs in the experimental model. A possible reason for this prediction is the large

Validation of numerical models using experimental data

motions of the plunger wavemaker cause unrealistic nonlinearities to occur when remeshing at each time-step close to the wavemaker.



(a)



(b)

Figure 6.6: Comparison between the output from the NWT model and the experimental output from the NUIG wave flume, for $S = 240$ mm and $T = 1.2$ s, at a distance from the wavemaker: (a): 2.35 m and (b) 4.75 m.

6.5 Validation of NWT model for wave-structure interaction

In order to validate the accuracy of wave-structure interaction performed using the numerical model for a wave tank developed in Section 4.4, comparisons of the results from the model and experimental analyses are performed. Furthermore, the experimental results are compared to the results of a frequency domain hydrodynamic analysis, performed using the methodology described in Section 5.2. The floating structure which is used in the analysis is a vertical cylinder with a hemisphere base and is described in Section 6.5.1.

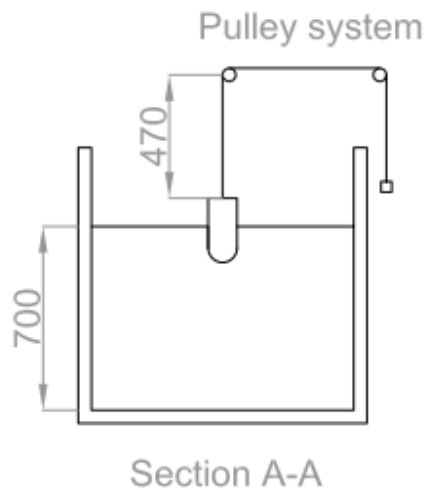
6.5.1 Experimental floating structure set-up

In order to perform wave-structure interaction in the wave flume a rig is set up which supports a structure using a mooring system, as shown in Figure 6.7. In addition, the mooring system restricts the surge, or horizontal, motion of the structure. A pulley system is employed to measure the heave, or vertical, dynamic response of the structure (Figure 6.7 (a)). When using this pulley system, the pitch rotations of the structure are assumed to be small enough to be deemed insignificant and the structure is restrained in the surge motion. Therefore, only the vertical motion of the structure is measured and no measurements of the pitch motions of the structure are recorded. The structure used in the study is a floating vertical cylinder with a hemisphere base. The diameter of the structure is 110 mm and the total draft is 137.5 mm, which gives a draft-to-radius ratio of 2.5. The structure is placed at 4 m from the wavemaker.

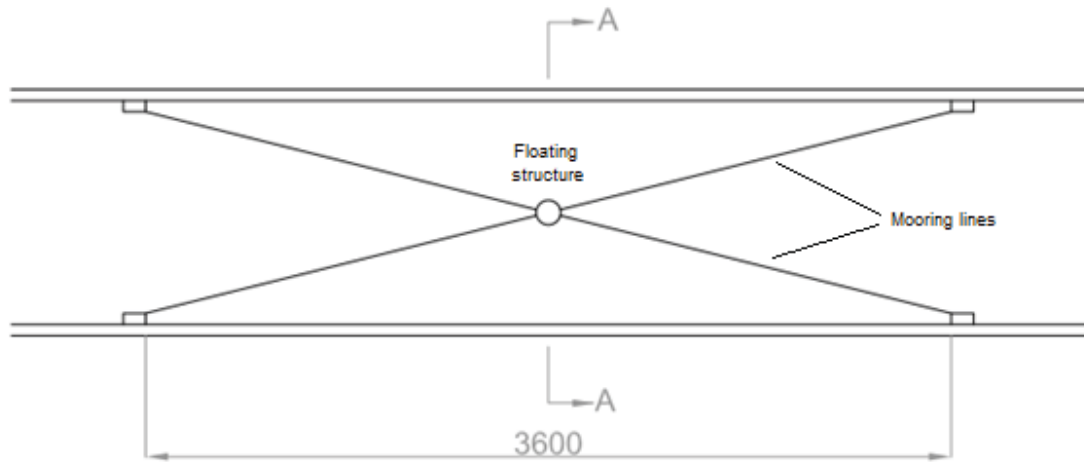
A four-line mooring system is employed, where each line is 2m in length and fixed to the side wall of the flume at the SWL. The mooring configuration can be seen in Figure 6.7 (b). However, this method would be deemed unpractical in a full-scale field but is deemed ideal for a laboratory based study such as this.

Validation of numerical models using experimental data

The vertical motion of the structure is measured with a pulley system, which is similar to that used in Stallard et al. (2009), and is shown in Figure 6.7 (a). The total vertical distance between the top of the structure and the pulley is 470 mm, which is deemed sufficient to accurately predict the actual vertical motion as the contribution of the pitch, or rotational, motions are insignificant. The heave, or vertical, dynamic response is then measured by tracking the motion of the 50 g weight on the other side of the string with a camera and measure, commonly known as a ruler, system, at 25 frames per second. However, the accuracy of this measuring scheme may be reduced where there are sudden changes in direction of the weight as the string may not remain taut. Furthermore, there may be a small experimental error associated with the measuring system employed of ± 1 mm.



(a)



(b)

Figure 6.7: Schematic of the laboratory set up for the floating structure, including horizontal mooring lines. (a) Section A-A. (b) Plan of structure. Dimensions are in mm.

6.5.2 NWT model of floating structure

In order to retain the accuracy of the model by retaining the mesh refinement, it is necessary to reduce the length of the numerical wave tank. The set-up of the model remains similar to that described in Section 6.4.1.

The method of dissipating the wave energy remains the same, but the length of the dissipation zone is reduced to 2 m from the end of the tank. An additional dissipation method of specifying a coarser mesh along the still water level in the dissipation zone, as described in Section 4.3.1, is also employed. In addition, the method of specifying the wave elevation and water particle velocities, which is given by Eqn. (4.3) - (4.5), is used to generate the waves in the analysis.

The '*Rigid Body*' fluid-structure interaction feature, which is described in Section 7.4, of ANSYS CFX is used to model the structure. The structure is restricted to two degrees of freedom; the heave, or vertical, motion and the pitch, or rotation about the z-axis, motion. The same centre of gravity, calculated at 0.0725 m below the still water level, and mass dispersion as measured in the physical structure are specified in the model.

6.5.3 Comparison of numerical and experimental output

In this section, two methods of comparison to the experimental data are used. The first is a comparison of the response amplitude operator (RAO) to the results of a hydrodynamic analysis. The second method is a comparison of the recorded experimental heave motion dynamic response, in the time domain, to the output from the NWT model, described in Section 6.5.2, for a single wave period and stroke length.

The hydrodynamic analysis, using BEM (ANSYS AQWA), of the structure is performed using the methodology described in Section 5.2 for an unrestrained system. The RAO which is determined from the experimental simulations is calculated by normalising the total displaced height of the weight with the wave height. The comparison of the two sets of results is given in Figure 6.8, where the RAO is plotted against the wave period. It is clear that the results are in very good agreement when the wave period is greater than the natural period of the structure. However, there is still reasonable agreement elsewhere. In the hydrodynamic analysis, there is an unrealistic prediction of the RAO at the natural frequency of the structure. One reason why this unrealistic prediction of the RAO will not occur in the experimental simulations is as a result of the restriction imposed by the moorings. Furthermore, the experimental set-up may have additional sources of damping, such as from the pulley system used to obtain the vertical displacement.

Furthermore, 1-DOF mechanical systems employing an equivalent viscous damping and stiffness are included in order to compare measured data from physical models to results from the BEM analysis. The equivalent viscous damping coefficient, ν/ω , and stiffness of the first 1-DOF mechanical system were determined to be 0.041 and 93.38 kN/m, respectively, to reproduce the dynamic response found in the BEM analysis over a range of wave periods. There is a very good correlation between this system and the BEM analysis as there is a mean squared error of 0.0027 and can be seen graphically in Figure 6.8. The same parameters were identified as 0.274 and 81.53 kN/m, respectively, in the second 1-DOF mechanical system, which were determined by finding a best fit approximation of the dynamic response of the system to the measured data from the

Validation of numerical models using experimental data

physical models. There is a reasonable correlation between this system and the measured data as there is a mean squared error of 0.09 and can be seen graphically in Figure 6.8. In these systems, the mass and added mass for the system remained the same. The stiffness was reduced by 11.85 kN/m (a reduction of 12.7 %) and there was an increase of the viscous damping coefficient of 0.233 to 0.274. This reduction in stiffness is the reason for the differences in peak of the graph and is expected as a result of the contribution of the moorings. The increase in damping is mainly due to the moorings and can be seen in Figure 6.8, as there is a reduction in the peak of the experimental data at the resonant frequency.

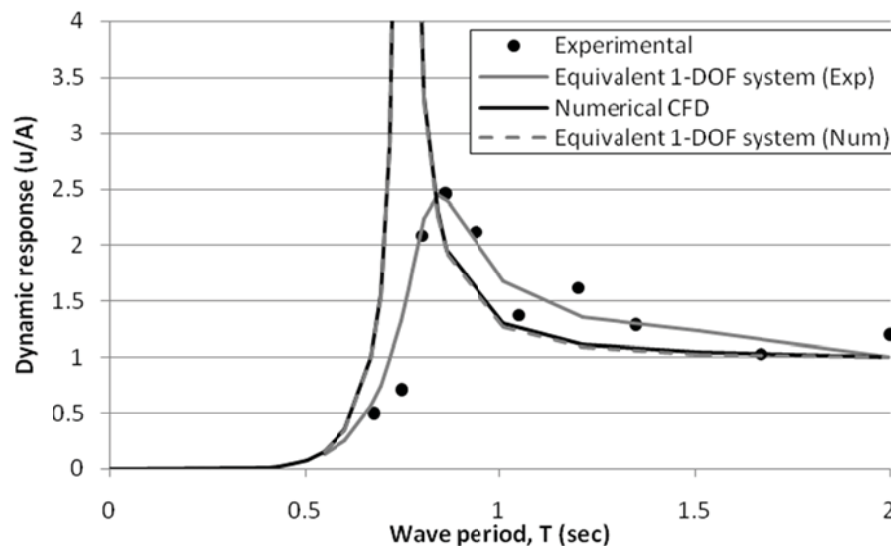


Figure 6.8: Comparison between experimental results and BEM hydrodynamic analysis using ANSYS AQWA.

The time domain comparison between the numerical model for a wave tank and the experimental simulation is performed for a wave period of 1.2 s and a wave height of 37 mm, where the stroke length is 90 mm. The dynamic heave motion response from both models and the wave elevation are displayed in Figure 6.9. The wave elevation is taken from the numerical model, but is also consistent with the experimental waves. The frequency of both sets of results are in very good agreement, but the magnitude of the

Validation of numerical models using experimental data

response in the numerical model for a wave tank is less consistent with the numerical model under predicting the dynamic heave response by 15 to 35 %, as can be seen in Figure 6.9. A reason for this is during the pitch motion, the cylinder nears its point of equilibrium and loses momentum and, therefore, there is a reduction in amplitude of some of the peaks, as shown in Figure 6.9. However, this would not occur in the experimental set-up as a result of the support provided by the mooring system.

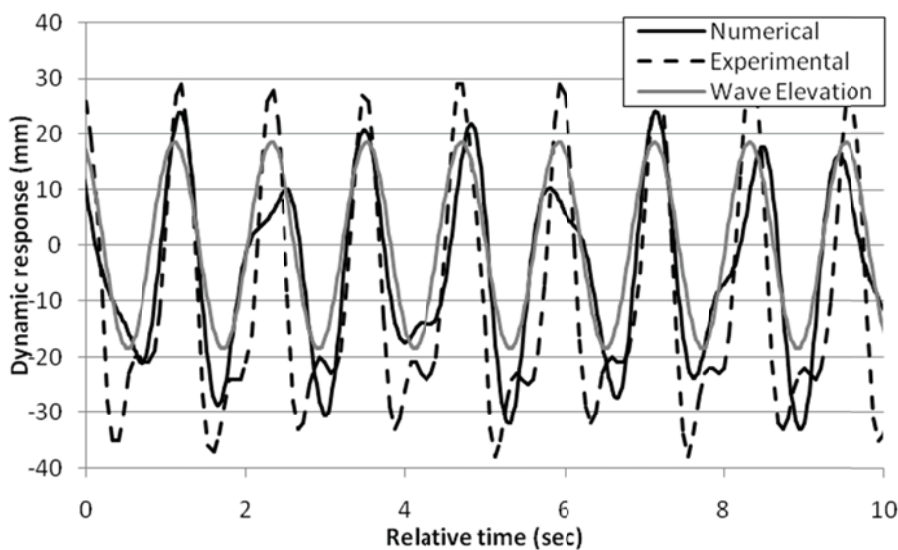


Figure 6.9: Comparison between the results from the numerical model and the experimental simulation for an incident wave with a period of 1.2 s and a height of 37mm.

Three instances in the simulations are compared in Figure 6.10. It is clear from this comparison that the magnitude of the pitch response in the numerical model is much less than that of the experimental simulation. A contributing factor to the pitch response in the experimental simulation may be the mooring system, as it generates additional rotational moments on the structure. However, the general motion response of the structure to the wave is similar in both simulations.

Validation of numerical models using experimental data

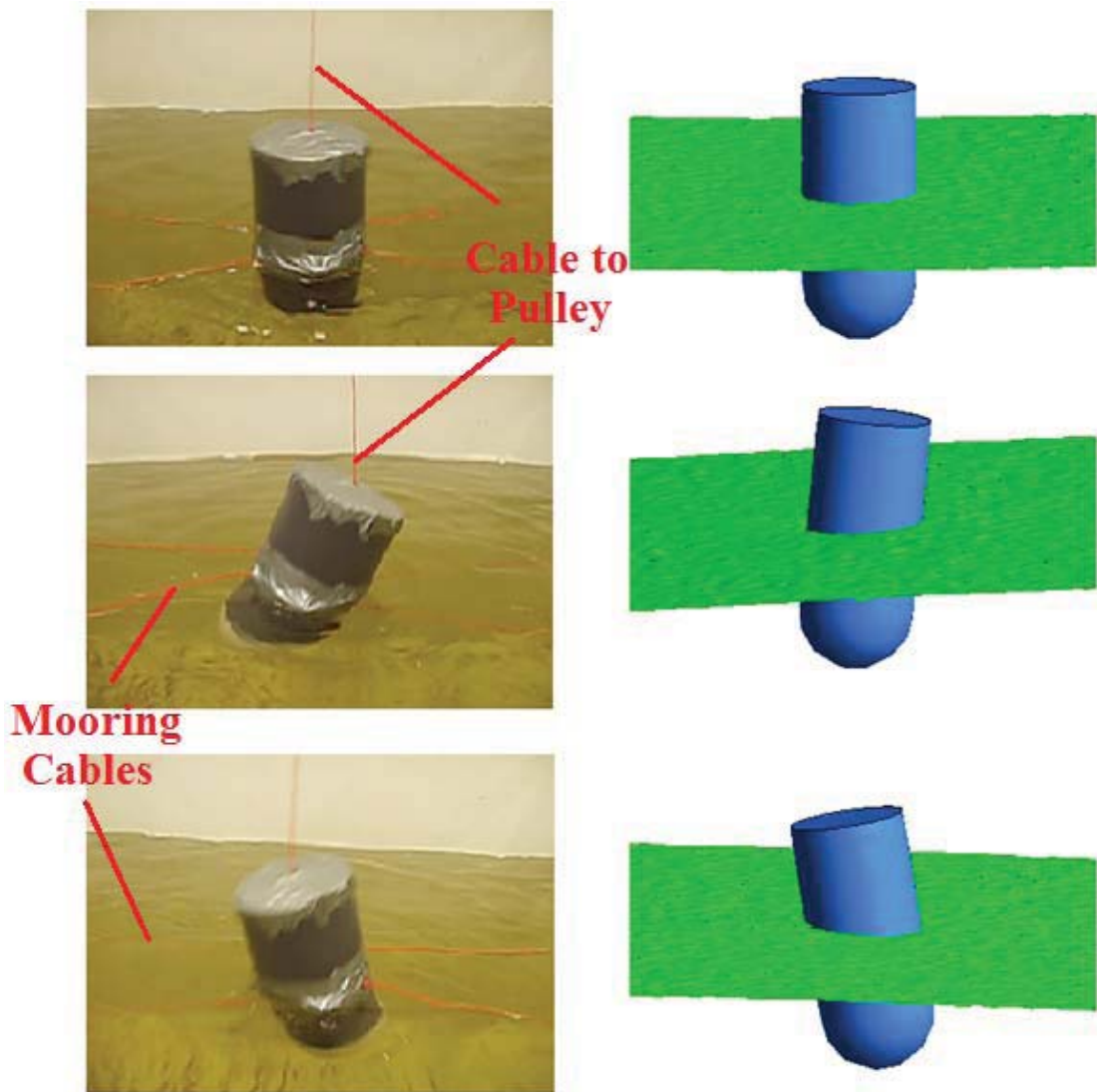


Figure 6.10: Comparison between the experimental test and the numerical simulation at
Top: 13.2 s. Middle: 13.5 s. Bottom: 13.9 s.

6.6 Discussions and conclusion

The main motivation for this section is to validate the methodology for developing a numerical model for a wave tank (NWT), which is described in Chapter 4. Therefore, the output from the NUI Galway experimental wave flume is compared to the output of a corresponding NWT model of the flume.

Initially, the parameters of the wave flume, namely the wavemaker relation and the breaking limit of the waves, are determined. The wavemaker relation is derived from the wave elevation recorded at each of the wave elevation gauges (i.e. at 2.35 m and 4.75 m from the vertical side of the wavemaker) for a given stroke length. The results of the experimental wave flume have also been compared to the deep water asymptotic expression for the wavemaker relation derived by Wang (1974). However, the theory overestimates the experimental results and the reason for this is that the flume in question has a mean water depth to mean plunger depth ratio is below the limiting values specified by Wang (1974). Furthermore, the breaking limit of the waves is related to the steepness of the waves and it was found to be an average of 0.1066 for the NUI Galway wave flume.

A number of simulations using the NWT model of the NUI Galway wave flume are performed varying the frequency and the stroke length of the plunger-type wave maker. The wavemaker relation at the same distance from the wavemaker as in the experimental arrangement is derived and compared. The numerical outputs are found to be in very good agreement with the experimental outputs for $k_0\gamma \leq 0.7$. On the other hand, the numerical model begins to underestimate the wave height when $k_0\gamma > 0.7$. The wave elevations are compared after the initial stage once the waves have become steady state in both the numerical and experimental models at the same distance from the wavemaker. The agreement between the two sets of outputs is very good, both in terms of frequency and wave height. However, there are discrepancies when the wave period is less than 1 second, which corresponds to $k_0\gamma > 0.7$. Therefore, the numerical model predicts the experimental results well for $k_0\gamma \leq 0.7$.

Validation of numerical models using experimental data

In order to perform wave-structure interaction in the wave flume a rig is set up which supports a structure using a mooring system. A pulley system is employed to measure the heave, or vertical, dynamic response of the structure. The results of the study are compared to a hydrodynamic analysis and are in very good agreement when the wave period is greater than the natural period of the structure. However, there is still reasonable agreement elsewhere. The recorded experimental heave motion dynamic response, in the time domain, is also compared to the output from the NWT model for a single wave period and stroke length. The wave frequencies of each set of results are in very good agreement. However, the magnitude of the response in the numerical model for a wave tank is less consistent but still matches reasonably well. Furthermore, three instances in the simulations are compared and it is clear from this comparison that the magnitude of the pitch response in the numerical model is much less than that of the experimental simulation. However, the general motion response of the structure to the wave is similar in both simulations, thus validating the NWT developed as part of this study.

Irregular linear wave generation in a numerical wave tank

Chapter 7
**Irregular linear wave generation in a numerical
wave tank**

7.1 Introduction

In real ocean conditions the waves are not linear or even regular in form. Therefore, it is necessary to develop a method of generating a wave which accurately represents real sea conditions. In general, when a measuring wave buoy records a wave, the wave energy spectrum is generated for that record and over time a catalogue of wave energy spectra are analysed for that site to formulate a single wave energy spectrum which is used to represent the wave climate of a given sea or ocean region. From this spectrum, a Fourier transform may be used to derive an irregular linear wave profile which represents typical waves at the location.

In this study, measured wave elevation records from a location are used and recreated. The main principle being used is the theory that real ocean waves are accurately represented by a linear irregular wave. However, these generated waves may not be an accurate representation of the typical wave climate but are, in fact, replications of real measured records. In other words, single samples are analysed and replicated and are not representative of the long-term wave climate. A major advantage of this is that extreme or exceptional wave conditions recorded at a location can be recreated accurately.

In this chapter, a CFD numerical model for a wave tank is presented for replicating measured real ocean waves at full scale. The fast Fourier transform is utilised in order to create an input wave, along with its associated water particle velocities, which replicates a measured wave record. The wave was recorded at the Atlantic marine energy test site (AMETS), as shown in Figure 7.1. Three different wave records are replicated and compared with the measured wave in the time domain, as well as their corresponding wave energy spectra. Furthermore, a rectangular prism structure is introduced into the model in order to explore the interaction between a linear irregular ocean wave and a structure. The dynamic response of the structure to the linear irregular wave is compared with the analytical prediction, which is derived from a hydrodynamic analysis.



Figure 7.1: Map showing the location of the wave data buoy at AMETS, Ireland. Adapted from: (Marine Institute, 2012).

7.2 Methodology

In this section, the methodology for replicating a measured wave in a CFD model is described. Offshore ocean waves are irregular and random in nature with each different to the previous. For the most of the time, offshore ocean waves may be described as linear irregular waves and this is the type of wave which is being detailed in this study. It is acknowledged that when dealing with near-shore waves this is not always true as a number of significant non-linearities are introduced due to the interaction of the wave with the coastline and the seabed and also with non-linearities associated with extreme wave conditions. However, this is outside the scope of this study.

Irregular linear wave generation in a numerical wave tank

The measured wave records, which are to be replicated in this analysis, have been recorded at the AMETS off Belmullet, Co. Mayo, Ireland (Marine Institute, 2012). A map detailing the location of the wave data buoy at AMETS is shown in Figure 7.1. AMETS has been selected for the full-scale testing of pre-commercial wave energy devices. The site itself provides facility for the testing of near-shore, intermediate-water and offshore devices. It was selected principally due to its deep water with sandy seabed close to shore, the quality of its wave climate, the onshore infrastructure and the suitable grid connection. A Fugro Wavescan buoy is used to record the real-time wave data and is located approximately 3 km offshore in water depth of 50 to 100m. The measured wave records are taken over a half hour time frame and three records are used in the analysis. In Section 8.2, data recorded over two years at AMETS is processed and used in the case study analysis discussed in Chapter 8.

The initial part of the study is to analytically describe the measured wave by using an irregular linear wave, which is comprised of a summation of a number of linear waves. This analytical approximation is then employed in the CFD model, which is implemented in the commercial software package ANSYS CFX (ANSYS Inc., 2009). The software uses a finite volume method in order to solve the Reynolds-averaged Navier-Stokes equations (RANSE), which accounts for turbulence and viscosity. Its governing equations are described in Section 4.2.3. In order to replicate the wave accurately at the desired location, an input wave with corresponding water particle velocities is derived and used as the input in the CFD model.

In order to validate the accuracy of the solution, the analytical wave and the output wave from the CFD model are compared in the time-domain. In addition, the wave energy spectrum from the resulting output wave from the CFD model and the wave energy spectrum from the measured data are compared.

The methodology used in this section is similar to that described by Elangovan (2011). However, Elangovan (2011) uses a flap-type wavemaker to generate the incident wave, while a numerical input of the wave elevation and the water particle velocities is used in this analysis. One of the major advantages of the numerical input is that computation time

Irregular linear wave generation in a numerical wave tank

is reduced as the initial mesh can be used throughout the analysis as there are no moving boundaries. On the other hand, a wavemaker requires a moving boundary and, thus, remeshing at each time-step.

Finally, a rectangular prism structure is introduced into the model in order to explore the interaction between a linear irregular ocean wave and a structure. This, as is the nature of the problem, will introduce a moving boundary at the structure wall and, in turn, will require extra adaptations to the model to increase its robustness. However, this subject is secondary to the primary study of the chapter of linear irregular wave generation and is detailed in Section 7.4.

7.2.1 CFD model set-up

The CFD model set-up used in this analysis is mainly based on the methodology described in Chapter 4. The set-up for the CFD model is divided into three stages: (1) the geometry setup, which defines the physical dimensions of the model, (2) the mesh setup, where the computational domain mesh is created and (3) the wave-water, or physics, setup, which defines the analysis type, the domain setup, the boundary conditions, the initial water height and other characteristics of the water and air-water interaction.

A 3-D geometry of the model is used with a thickness less than the size of an element. However, two symmetry boundaries are utilised, so the numerical model is infinitely wide. There is a limitation in the software license that the maximum dimension is 500 m. Therefore, the total length of the model is 500 m and total height of 100 m, with a still water level (SWL) of 70 m.

Since the volume fraction of a fluid method is used to define the water level, it is necessary to refine the mesh at the SWL in order to capture the free surface accurately, which is shown in Figure 7.2. This technique is similar to that employed by Lal and Elangovan (2008), Liang *et al.* (2010) and in Chapter 4. The thickness of the refined mesh at the SWL is dependent on the maximum amplitude of the wave with a maximum

Irregular linear wave generation in a numerical wave tank

element size of 0.3 m. The remainder of the domain has a maximum element size of 3.5 m. The total number of elements for the computational domain is approximately 11000 for all simulations described.

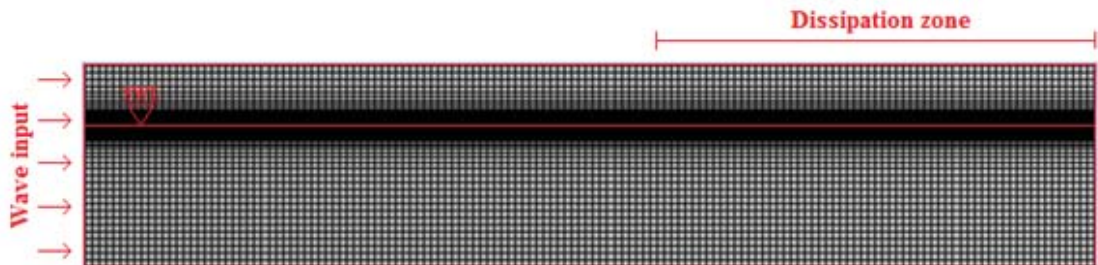


Figure 7.2: Typical longitudinal elevation of the mesh for CFD model with refinement along the SWL. Included is a schematic of the location of the wave input boundary, the SWL and the dissipation zone.

In defining the domain set-up, a number of assumptions are included. The surface tension at the air-water interface is assumed to be negligible. From previous studies (Lal and Elangovan, 2008; Finnegan and Goggins, 2012a) and in Chapter 4, it was found that the turbulence model used doesn't affect the generated wave. In this analysis a shear stress transport model is used which is also the model used by Elangovan (2011). An initial hydrostatic pressure is specified in the 'Water' region with no pressure in the 'Air' region and the entire region is static initially. The air is specified to a temperature of 25 °C and, therefore, its density is specified to be 1.185 kg/m³. Furthermore, an isothermal heat transfer model is specified, which is homogeneous. The fluid (water) temperature is defined as 25°C and its density is given as 1030 kg/m³ to represent salt water. The dynamic viscosity of the water is 8.899 x 10⁻⁴ kg/ms for the first 300 m of the model. Then the dynamic viscosity is used to dissipate the energy in the wave, increasing linearly to 125000 kg/ms as it reaches the outflow boundary. Therefore, the dynamic viscosity of the fluid is defined as:

Irregular linear wave generation in a numerical wave tank

$$\mu = \begin{cases} 8.899 \times 10^{-0} \text{ kg/ms}, & x < 300 \text{ m} \\ 8.899 \times 10^{-0} \text{ kg/ms} + \left(\frac{x - 300 \text{ m}}{200 \text{ m}}\right) 125000 \text{ kg/ms}, & x \geq 300 \text{ m} \end{cases} \quad (7.1)$$

The top boundary of the model has an ‘*opening boundary*’ condition, which allows air to pass through. At the inflow boundary, the wave elevation and horizontal and vertical water particle velocities need to be specified. An insignificant initial horizontal air velocity is also specified. The volume fraction is utilised here to differentiate between the ‘*Water*’ velocities and ‘*Air*’ velocities. The details of these inputs are described in more detail in the next section and are inputted using the ANSYS CFX expression language (CEL) (ANSYS Inc., 2009). At the outflow boundary there is a hydrostatic pressure specified over the water depth to the initial SWL to allow for overspill of excess water and allow air to pass. There are symmetry boundary conditions specified for the adjacent sides, in order to create a model that is infinitely wide, and the remaining boundaries are assigned a static wall boundary condition.

7.2.2 CFD input wave

The input wave at the inflow boundary of the CFD model is in the form of an irregular linear wave. In order to deduce this irregular linear wave, the fast Fourier transform (FFT) is used. Further details on the use of FFT for signal processing and its uses in ocean engineering can be found in Kim (2008). FFT expresses an irregular linear wave elevation, $\eta(t)$, as a summation of sinusoidal components as follows:

$$\eta(t) = \sum_{n=1}^{\infty} (\hat{A}_n \cos \omega_n t + \hat{B}_n \sin \omega_n t) \quad (7.2)$$

where

$$\hat{A}_n = \frac{2}{T_{tot}} \int_{-\frac{T_{tot}}{2}}^{\frac{T_{tot}}{2}} \eta(t) \cos \omega_n t dt \quad (7.3)$$

Irregular linear wave generation in a numerical wave tank

$$\hat{B}_n = \frac{2}{T_{tot}} \int_{-\frac{T_{tot}}{2}}^{\frac{T_{tot}}{2}} \eta(t) \sin \omega_n t dt$$

where T_{tot} is the total time of the simulation and ω_n is the wave angular frequency of the n^{th} linear wave. Introducing $N_m N$ number of time-steps, $T_{tot} = N_m \Delta t$. Therefore, the irregular linear wave elevation may be expressed as:

$$\eta(t_m) = \text{Re} \left[\sum_{n=1}^{N_m/2} (\hat{A}_n - i\hat{B}_n) e^{i2\pi f_n t_m} \right], \quad m = 1, 2, \dots, N_m N \quad (7.4)$$

where t_m is the time at the m^{th} time-step and f_n is the frequency of the n^{th} linear wave. Therefore, the Fourier transform, $\hat{X}(f_n)$, is given as:

$$\hat{X}(f_n) = \frac{\hat{A}_n - i\hat{B}_n}{2\pi} \quad (7.5)$$

And the wave energy spectrum is given as:

$$S(f_n) = \frac{|\hat{X}(f_n)|^2}{T_{tot}} \quad (7.6)$$

However, since Airy's linear wave theory is to be used in the analysis the irregular linear wave elevation has to be rewritten in the form:

$$\eta(t) = \sum_{n=1}^{\infty} A_n \cos(-\omega_n t - \varepsilon_n) \quad (7.7)$$

where

$$\varepsilon_n = \begin{cases} \tan^{-1} \left(\frac{-\hat{B}_n}{\hat{A}_n} \right), & \text{for } \hat{A}_n > 0 \\ \pi + \tan^{-1} \left(\frac{-\hat{B}_n}{\hat{A}_n} \right), & \text{for } \hat{A}_n < 0 \end{cases} \quad (7.8)$$

and

$$A_n = \sqrt{2S(f_n)\Delta f_n} \quad (7.9)$$

Irregular linear wave generation in a numerical wave tank

where A_n is the wave amplitude of the n th linear wave. Furthermore, in the CFD model, the wave is being replicated at a distance x from the input boundary so this must be accounted for in the input wave, which is achieved by using the $k_{0,n}x$ term in Eqn. (7.10), where k_0 is the wavenumber, which is obtained from the relation $\omega^2 = gk_0 \tanh k_0 h$. In addition, the wave needs to begin at the still water level (SWL) and increase, so a time offset t' is also introduced. Thus, an adapted phase angle is introduced:

$$\varepsilon_n' = \varepsilon_n + k_{0,n}x + \omega_n t' \quad (7.10)$$

This is as a result of a limitation with the method of inputting the summation of the wave elevation and water particle velocities into the CFD model. In this analysis, the thirty waves with the highest wave amplitude are taken and, thus, the number of summations, $N = 30$. Therefore, the wave elevation being inputted into the CFD model is:

$$\eta(t) = \sum_{n=1}^N A_n \cos(-\omega_n t - \varepsilon_n') \quad (7.11)$$

A comparison between the measured wave, where the full 30 minute record is given in Figure 7.3, and this filtered analytical approximation can be seen in Figure 7.4. Similar to the approach of Zhao et al. (2010), Dong et al. (2010) and Xu et al. (2011), the horizontal and vertical water particle velocities, along with the wave elevation given in Eqn. (7.11), are specified at the input boundary. From Airy's linear wave theory, the water particle velocities are given as:

$$u_1(t) = \sum_{n=1}^N A_n \omega_n \frac{\cosh(k_{0,n}y')}{\sinh(k_{0,n}d)} \cos(-\omega_n t - \varepsilon_n') \quad (7.12)$$

and

$$u_2(t) = \sum_{n=1}^N A_n \omega_n \frac{\sinh(k_{0,n}y')}{\sinh(k_{0,n}d)} \sin(-\omega_n t - \varepsilon_n') \quad (7.13)$$

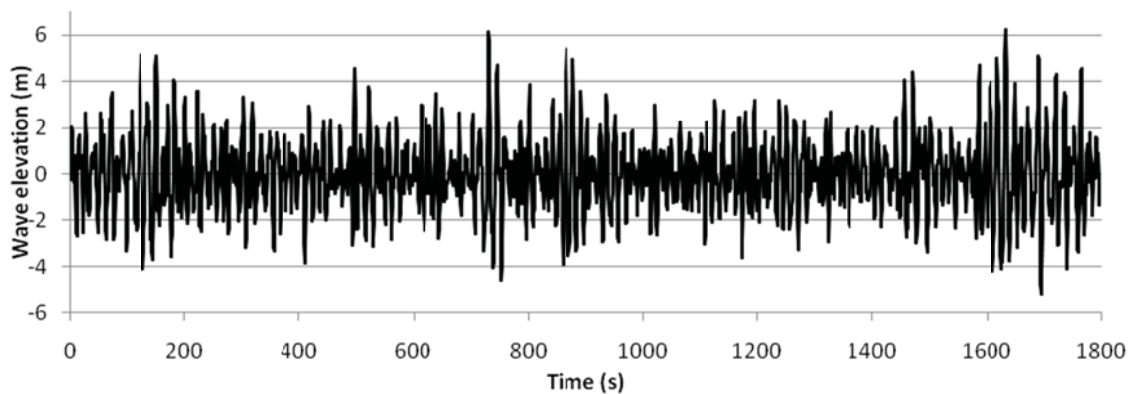
where $u_1(t)$ and $u_2(t)$ are the horizontal and vertical water particle velocities, respectively, and y' is the vertical distance from the base of the model. When entering the

Irregular linear wave generation in a numerical wave tank

water particle velocities at the input boundary, the volume of fluid method (VOF) is utilised to differentiate between the 'Air' and 'Water' regions.

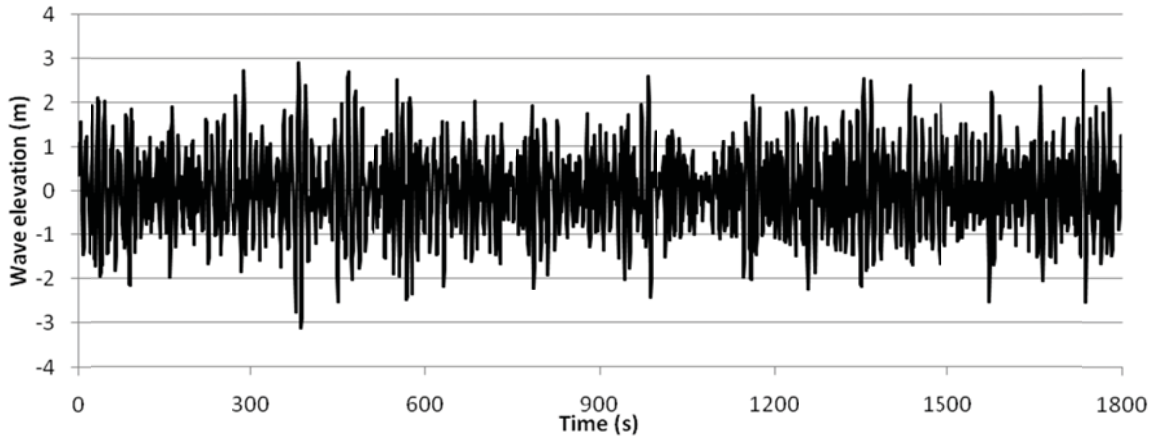
7.3 Results of linear irregular wave generation

In order to validate the integrity of the wave input methodology and the CFD model, described in Section 7.2, three measured wave records from AMETS are analysed and reproduced numerically. The records are taken on three different days and are 30 minutes in total. These records are displayed in Figure 7.3. However, in this analysis, when comparing the measured and numerical waves, only the first 200 s of each record is to be reproduced.

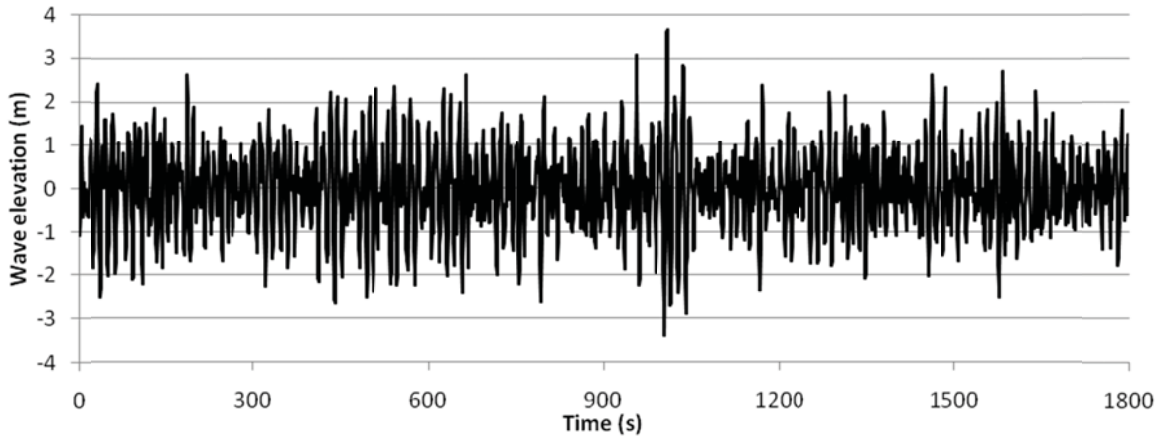


(a)

Irregular linear wave generation in a numerical wave tank



(b)



(c)

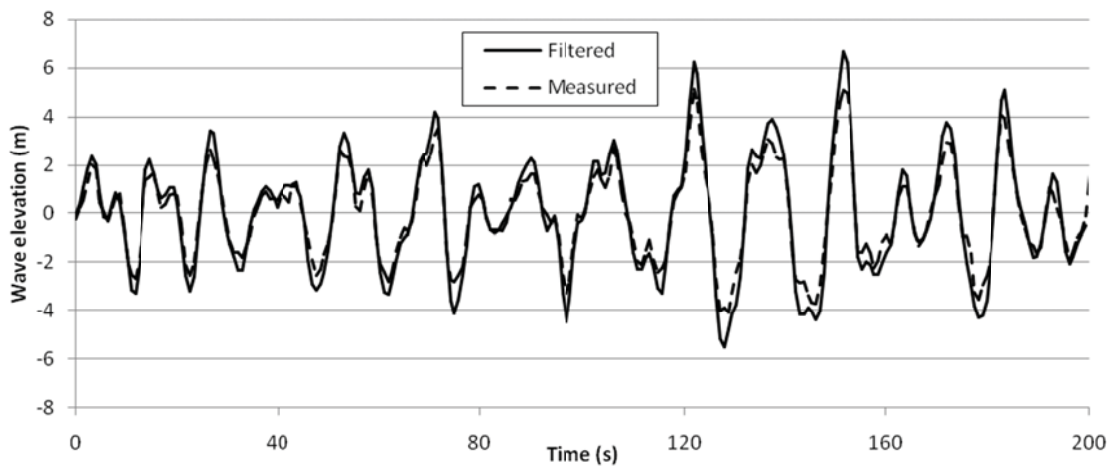
Figure 7.3: Measured wave elevation at AMETS beginning at: (a) 10:30 on 17-12-2010 (b) 4:30 on 04-10-2010 and (c) 17:00 on 02-09-2011.

The methodology detailed in Section 7.2 is then applied to these three 200 s records. The first step is to use the FFT to derive the analytical linear irregular wave approximation, given in Eqn. (7.7), of the measured wave. As stated earlier, as there is a restraint in the summation of regular waves of $N = 30$, the 30 highest amplitude regular waves are used to generate the analytical linear irregular wave approximation. The total time of the simulation analysed and replicated is also dependent on the value of N as the measured

Irregular linear wave generation in a numerical wave tank

record is sampled at 1.28 Hz. Therefore, for a 200 s record, the Fourier transform returns 128 waves and this is the limit if only the thirty highest waves are to be replicated. A comparison between the filtered analytical approximation and the measured wave record at AMETS can be seen in Figure 7.5. It is clear to see that the approximation slightly overestimates the amplitude of the peaks, but the frequencies seem to match up very well. Therefore, in all three cases, the analytical linear irregular wave approximation provides a very good representation of the measured waves.

A comparison between the filtered analytical approximation of the measured wave and the output from the CFD model can be seen in Figure 7.5. Since the model starts from a steady state, there is no correlation between the two waves in the initial stages of the simulation. However, after this stage, the two waves are found to be in very good agreement in terms of both frequency and amplitudes. It is also observed that the CFD model tends to smoothen out any dramatic changes in the elevation. In other words, it tends to replicate low frequency, high amplitude waves better than high frequency, low amplitude waves.



(a)

Irregular linear wave generation in a numerical wave tank

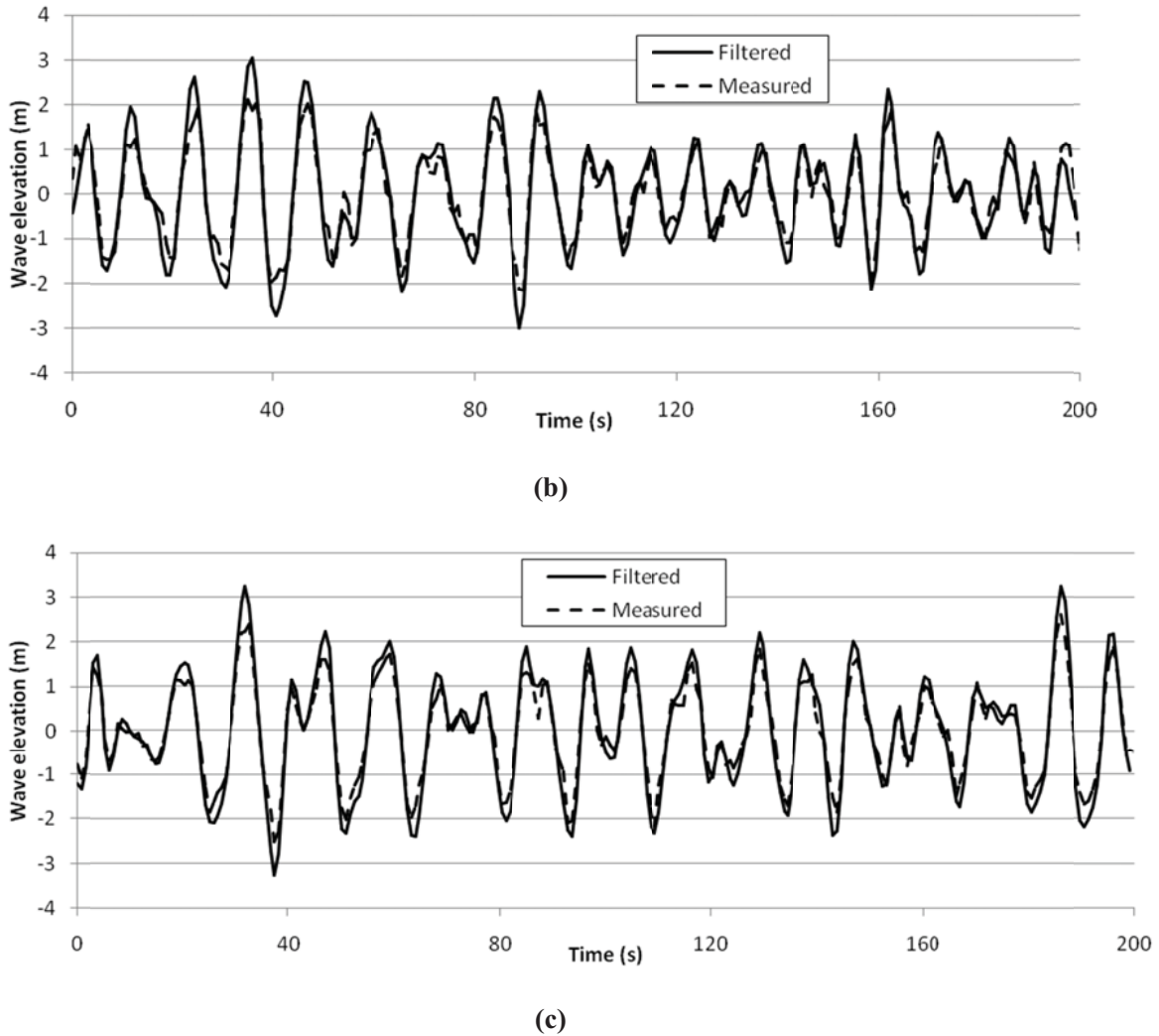
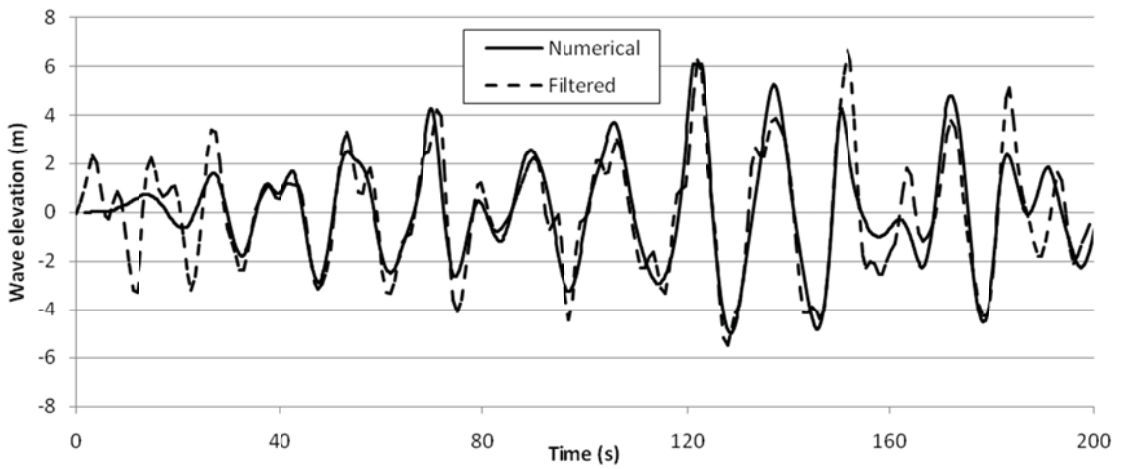


Figure 7.4: Comparison between the measured wave at AMETS and the filtered analytical approximation beginning at: (a) 10:30 on 17-12-2010 (b) 4:30 on 04-10-2010 and (c) 17:00 on 02-09-2011.

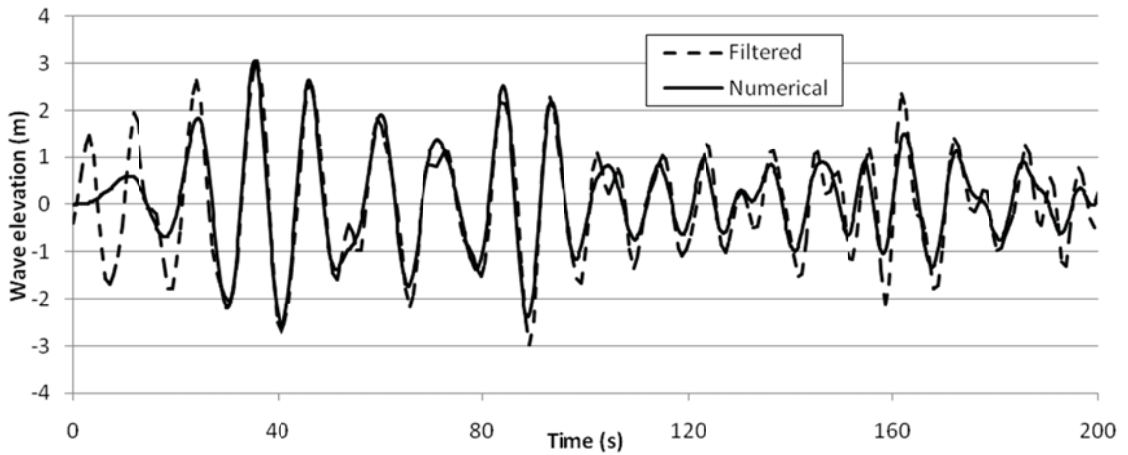
This analytical wave is then used to generate the input wave, given in Eqn. (7.11), and the corresponding horizontal and vertical water particle velocities, given in Eqn. (7.12) and Eqn. (7.13), respectively, which are to be inputted into the CFD model. In each model, the numerical wave is measured at a distance of 200 m from the input boundary. A set of wave profiles along the numerical model for a wave tank are shown in Figure 7.6 at different time-steps, for the simulation of the wave record beginning at 10:30 on 17-12-

Irregular linear wave generation in a numerical wave tank

2010. The first wave profile is at 155.4 seconds and the others are at equal intervals of 3 seconds. This set of wave profiles is an example of how waves of different frequencies move at different speeds as the two smaller peaks after the main peak are moving than the main peak. This is a further reinforcement of the need for the $k_{0,n}x$ term, in Eqn. (7.10), when deriving the CFD input wave.

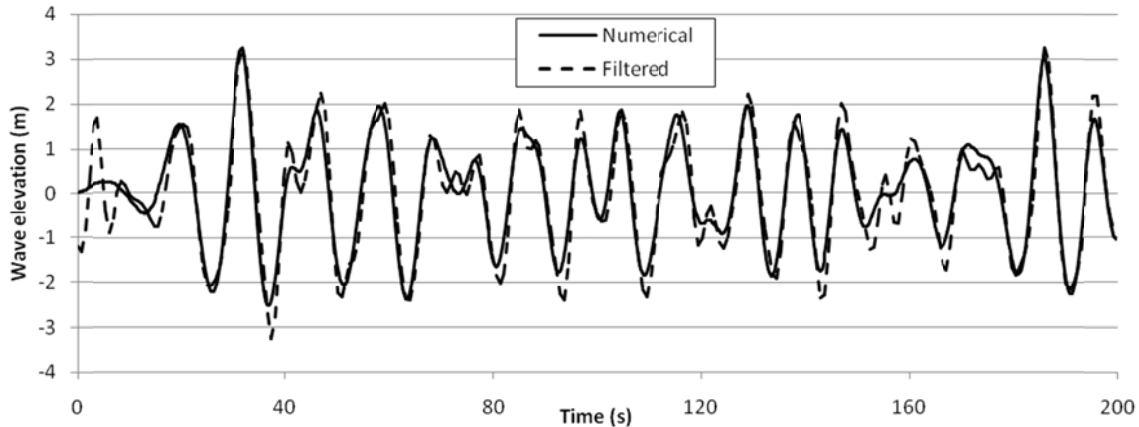


(a)



(b)

Irregular linear wave generation in a numerical wave tank



(c)

Figure 7.5: Comparison between the filtered analytical approximation wave and the output wave from the CFD model beginning at: (a) 10:30 on 17-12-2010 (b) 4:30 on 04-10-2010 and (c) 17:00 on 02-09-2011.

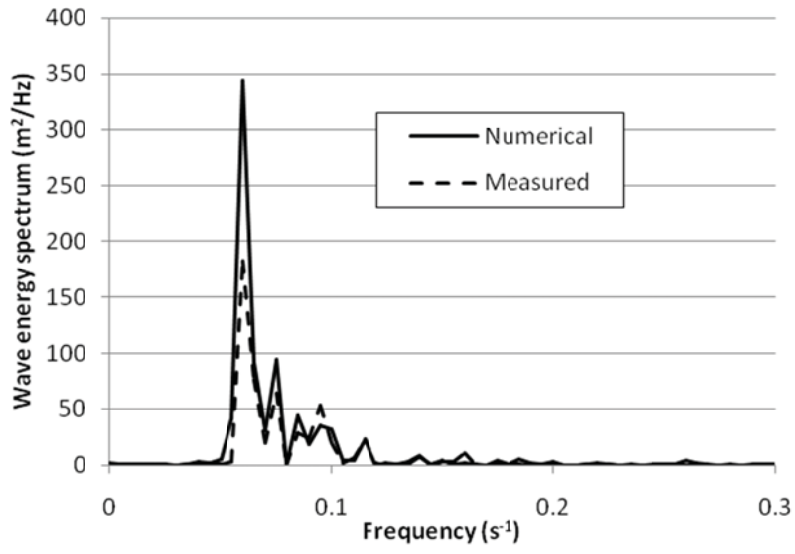
The final part of the analysis is to calculate the wave energy spectrum of the output wave from the CFD model. A FFT is performed on the output wave from the CFD model and, using Eqn. (7.6), the wave energy spectrum can be calculated. This wave energy spectrum is then compared to the wave energy spectrum of the original measured wave, which can be seen in Figure 7.7. Again, the two spectra match very well in terms of frequency. However, there is a large discrepancy in the amplitude of the spectrum at the peak frequencies and this would increase the significant wave height of the resultant irregular wave. This is to be expected as there was an increase in the amplitude of the peaks in the filtered analytical irregular wave approximation compared to the measured wave, which is evident in Figure 7.4, and this approximation was used in deriving the numerical wave. However, this error maybe reduced by reducing the amplitude of the linear wave at the peak frequency for the filtered analytical irregular wave approximation. Furthermore, there are discrepancies at high frequencies, generally greater than 0.15 s^{-1} , but these would not have a significant effect on the irregular wave elevation.

Irregular linear wave generation in a numerical wave tank

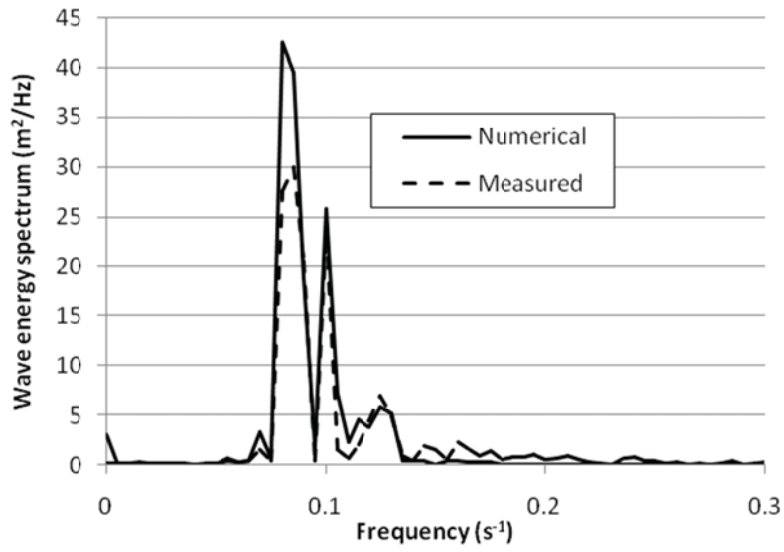


Figure 7.6: Longitudinal wave profile along the full length of the wave tank for different time-steps for the simulation of the wave record beginning at 10:30 on 17-12-2010 (beginning at 115.4 s in equal time intervals of 3 s).

Irregular linear wave generation in a numerical wave tank

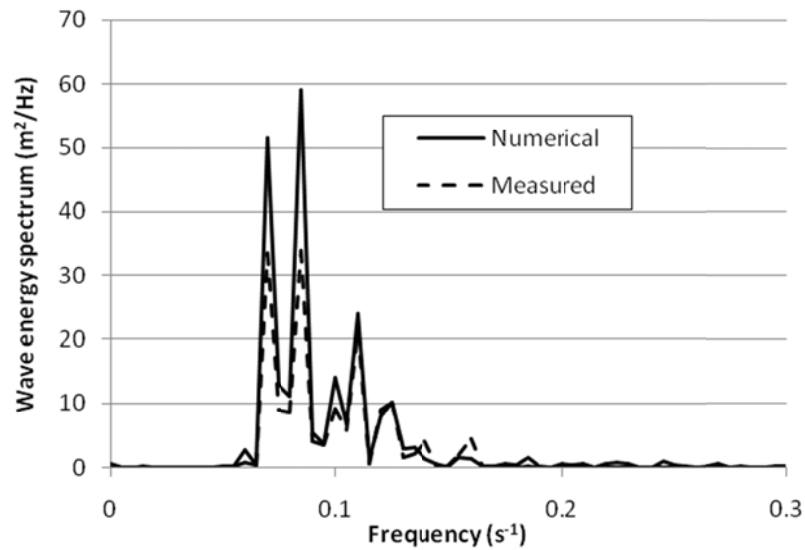


(a)



(b)

Irregular linear wave generation in a numerical wave tank



(c)

Figure 7.7: Comparison between the wave energy spectrum of the measured wave and output wave from CFD model beginning at: (a) 10:30 on 17-12-2010 (b) 4:30 on 04-10-2010 and (c) 17:00 on 02-09-2011.

7.4 Interaction of a structure with a linear irregular wave

The next stage of the analysis is to introduce a structure into the model in order to explore the interaction of the structure with a linear irregular wave. In this study, an infinitely long rectangular prism is employed as the structure in order to analyse the accuracy of the model's prediction of the heave motion dynamic response of a structure in the presence of a linear irregular wave. The infinitely long rectangular prism has a width of 30 m, a draft of 15 m with a total structural height of 20 m, and its centre is at a distance of 200 m from the inflow boundary.

The '*Rigid Body*' fluid-structure interaction feature of ANSYS CFX (ANSYS Inc., 2009) is used to model the structure. This feature requires a number of properties of the structure, including centre of gravity, moments of inertia, translational and rotational

Irregular linear wave generation in a numerical wave tank

degrees of freedom and either initial velocity or initial acceleration components. In this analysis, the movement of the structure is restricted to two degrees of freedom; the heave, or vertical, motion and the pitch, or rotation about the z-axis, motion. Furthermore, the initial velocity components of the structure are set to zero and its centre of gravity is set equal to its initial centre of buoyancy.

It may be noted that when the structure is introduced into the model, additional mesh refinement is required around the structure. The '*Sphere of Influence*' mesh refinement method is used and, therefore, the total number of elements in the mesh is increased to 40000. Further adaptations to the model are also required to ensure the robustness of the model during the analysis. At the beginning of the simulation, a ramp time-step is introduced, where the time-step is reduced from 0.1 s to 0.025 s for the first second, or first 40 time-steps, of the simulation. In addition, defined mesh stiffness is included in the model, which is the inverse of the volume of the element. Therefore, the smaller elements have greater mesh stiffness and, thus, are less likely to fold or invert during the remeshing, which will cause the simulation to crash or fail.

The interaction between a linear irregular ocean wave and a structure, which includes the wave profile and the dynamic response of the structure, over a number of time-steps, can be seen in Figure 7.8. The top model annotation in the figure is at 128.4 s of the simulation, which is replicating the wave record beginning at 17:00 on 02-09-2011, and the subsequent model annotations are in equal 4 second time intervals.

Irregular linear wave generation in a numerical wave tank

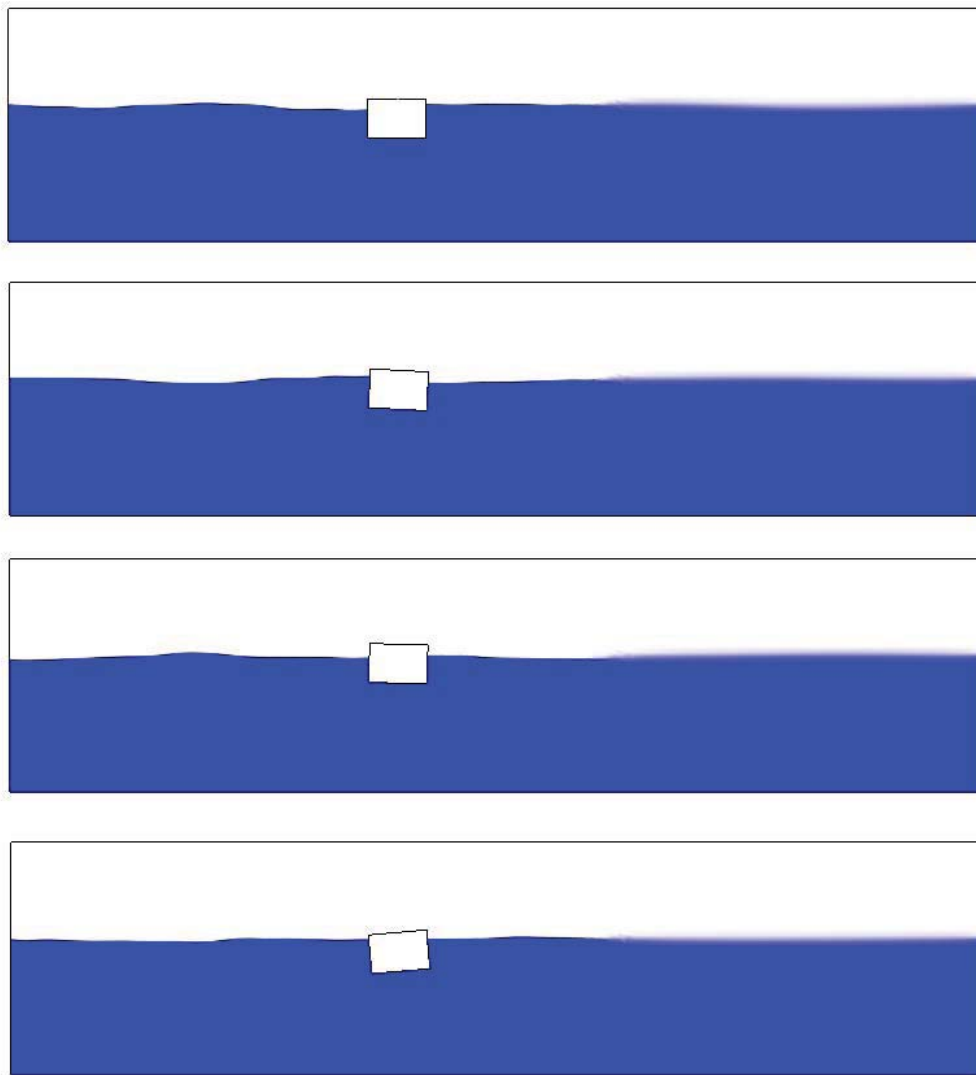


Figure 7.8: Wave profile and dynamic response of the structure for different time steps beginning at 17:00 on 02-09-2011 (beginning at 128.4 s in equal 4 s time intervals).

Furthermore, in order to assess the accuracy of the model, the heave motion dynamic response from the NWT is compared to a simple analytical solution derived from the hydrodynamic analysis of the structure. The hydrodynamic analysis is performed using the commercial boundary element method software package ANSYS AQWA (ANSYS-Inc., 2010). A parametric study was performed to determine the length of the prism

Irregular linear wave generation in a numerical wave tank

required to accurately replicate the normalised dynamic response of the infinitely long structure to beam sea conditions. From this, a length of 100 m was deemed sufficient. The normalised dynamic response, \hat{u} , and the phase angle, β , is shown graphically in Figure 7.9. It is noted in Figure 7.9 that after the initial stage, the phase angle does not behave the same as for a single degree of freedom system. The reason for this is there is a contribution from the pitch motion dynamic response of the structure that alters the phase angle of the heave motion dynamic response. The dynamic response is determined analytically, u , in the time-domain, using the following expression:

$$u(t) = \sum_{n=1}^N A_n \hat{u}_n \cos(-\omega_n t - \varepsilon'_n - \beta_n) \quad (7.14)$$

A comparison of the dynamic response of the structure from the NWT model and the analytical solution, given in Eqn. (7.14), is shown in Figure 7.10. The two solutions were found to be in good agreement. The two solutions match very well in terms of frequency, but there is a difference in the amplitude of the response. This difference may be attributed to the viscous non-linearities present in the numerical model for a wave tank around the wall, or hull, of the structure itself causing increased damping forces which are not present in the hydrodynamic analysis model. There is a large discrepancy in the initial part of the simulation between the two solutions, since the NWT model starts at a steady state. However, the two solutions begin to converge for the second half of the record.

Irregular linear wave generation in a numerical wave tank

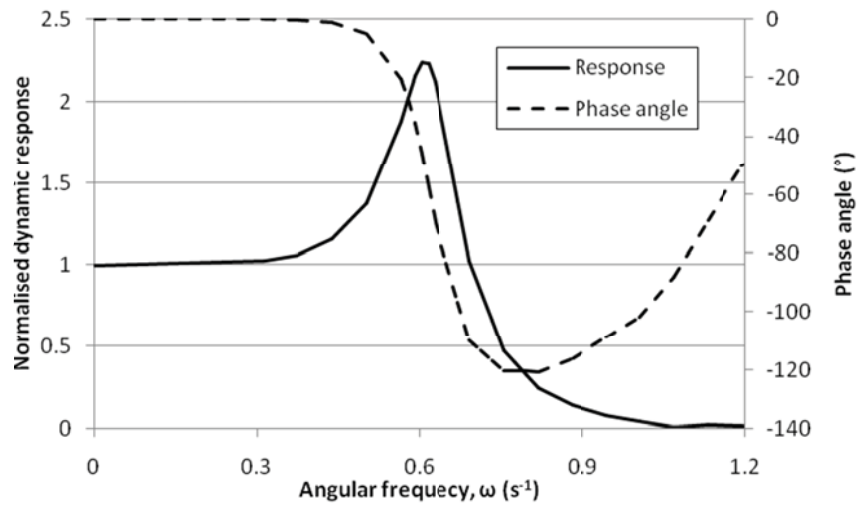
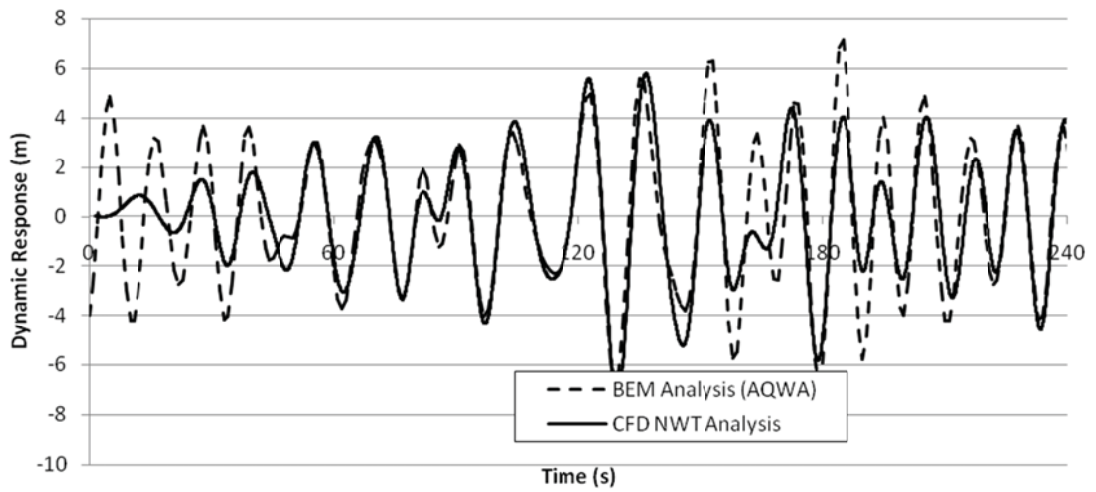
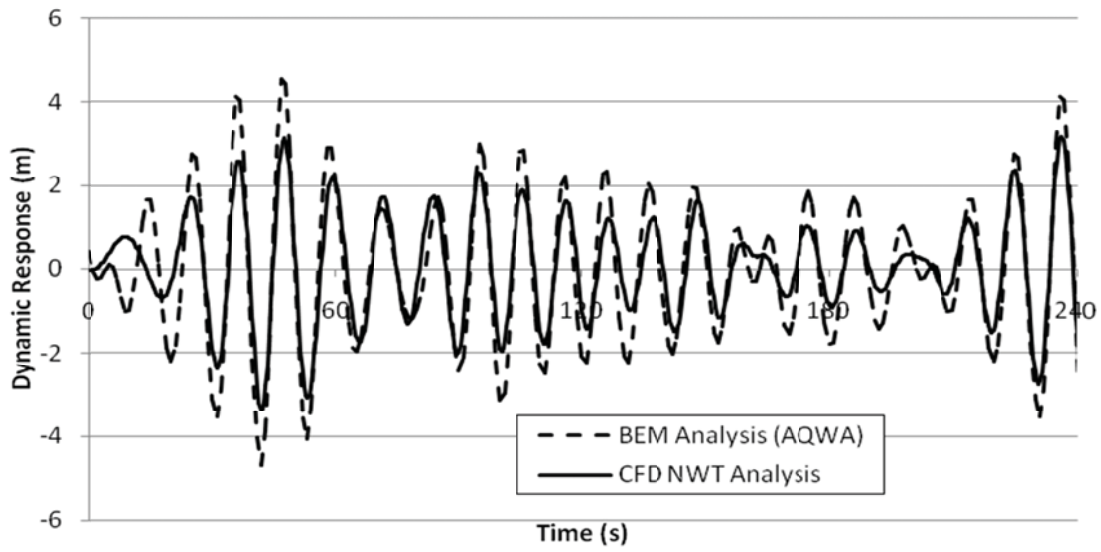


Figure 7.9: The normalised heave motion dynamic response and associated phase angle from the hydrodynamic analysis of the structure.

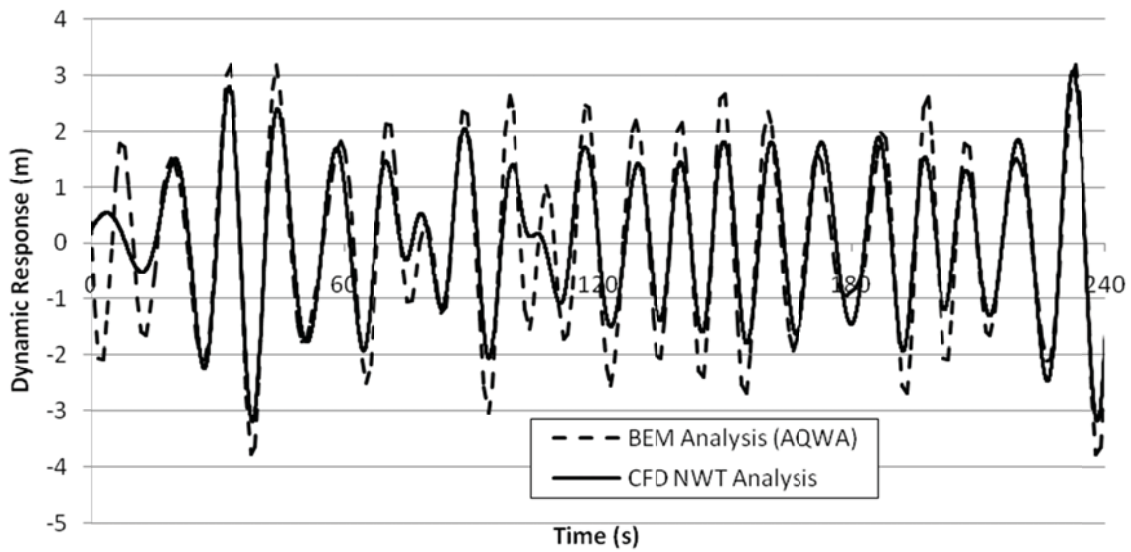


(a)

Irregular linear wave generation in a numerical wave tank



(b)



(c)

Figure 7.10: Comparison of the heave motion dynamic response of the rectangular prism from the CFD NWT analysis and analytical hydrodynamic analysis beginning at: (a) 10:30 on 17-12-2010 (b) 4:30 on 04-10-2010 and (c) 17:00 on 02-09-2011.

7.5 Discussion and conclusions

In this chapter, a numerical model for a wave tank that can accurately mimic real ocean waves is developed. It is clear from this analysis that real ocean wave conditions can be modelled accurately and relative inexpensively in comparison to physical model testing. Furthermore, numerical modelling is used to its maximum by employing full scale measured data and replicating it in a full-scale numerical wave tank. The ability of the model to accurately model measured ocean waves and their interaction with a floating structure is the novel aspect here.

The model developed in Chapter 4 is extended in order to generate linear irregular waves, which can be used to model real ocean waves. The detailed methodology for generating linear irregular waves has been used to replicate wave records measured at AMETS. In order to demonstrate the robustness of the methodology, three different wave records are analysed throughout the chapter. A comparison between the filtered analytical approximation of the measured wave and the output from the CFD model is analysed. Since the model starts from a steady state, there is no correlation between the two waves in the initial stages of the simulation. However, after this stage, the two waves are found to be in very good agreement in terms of both frequency and amplitudes. It is also observed that the CFD model tends to smoothen out any dramatic changes in the elevation. In other words, it tends to replicate low frequency, high amplitude waves better than high frequency, low amplitude waves.

A rectangular floating prism is introduced into the model in order to explore the accuracy of wave-structure interaction prediction. A comparison of the heave motion dynamic response of the structure from the NWT model and the analytical solution indicates that the two solutions were in good agreement. In particular, both solutions match very well in terms of frequency. However, there is a difference in the peak amplitude of the response. This difference may be attributed to the viscous non-linearities present in the numerical model for a wave tank around the wall, or hull, of the structure itself causing increased damping forces, which are not present in the hydrodynamic analysis model. There is a

Irregular linear wave generation in a numerical wave tank

large discrepancy in the initial part of the simulation between the two solutions, since the NWT model starts at a steady state. However, the two solutions begin to converge for the second half of the record.

Shape optimisation of a floating wave energy converter

Chapter 8
**Shape optimisation of a floating wave energy
converter**

8.1 Introduction

For every sea or ocean region around the world, the energy level and properties of the waves are unique. In general, the wave characteristics of a region are described by using a wave energy spectrum, which is detailed in Section 2.3.1, and this is used as a reference when designing a marine structure which is being constructed, or is operating at, the given location. Therefore, it is necessary to design a wave energy converter (WEC) depending on its expected location in order to maximise the energy output at that location. One method of optimising the design of a given WEC is to optimise its geometrical shape, or geometric configuration, so as it will perform to its maximum efficiency in a specified manner. Therefore, in their design, it is necessary to maximise the dynamic response of wave energy converters for the majority of the time.

In this chapter, a methodology to optimise the dynamic heave response of the floating oscillating part of the WEC through form finding of the geometric configuration of its structure is presented. The state-of-the-art aspect lies within the methodology itself as it offers a designer a method of optimising the performance of a WEC, in terms of its geometric configuration, at a given location using a single wave energy spectrum as the input. An unconstrained system is analysed in order to determine the optimum geometric configuration of the structure in terms of shape and radius. In order to clearly explain the methodology, a case study is taken of a WEC which is to be deployed at the AMETS, which is described in Section 7.2. The type of WEC investigated in this section is a floating vertically axisymmetric point absorber, which predominantly oscillates in the heave, or vertical, motion. However, the methodologies detailed may be easily adapted to be applicable to any WEC. The optimisation discussed in this chapter is limited in scope to the set of geometries defined in the geometry library of the methodology. In the case study detailed in this chapter, the geometry library is summarised in Table 8.4. In this study, a single wave energy spectrum is used as the data input and, since Babarit et al. (2012) suggest the use of the entire scatter diagram for each site, an analysis of the mean

power output of the optimum geometric configuration using this technique is also performed.

8.2 Wave energy and data processing

8.2.1 Wave energy

The most commonly used method of describing the energy in real sea waves is the wave energy spectrum, $S(f)$. This is a distribution of the wave energy of a given location as a function of the wave frequency, f . Since the sea state of a given location constantly changes, this method provides a clear representation of the energy distribution over a given time span. The two main characteristics used to describe the wave climate of a given location is the significant wave height, H_s , which is the mean wave height (trough to crest) of the top one third highest of the waves, and the average wave period, T_{av} . The significant wave height is calculated as:

$$H_s = 4\sqrt{m_0} \quad (8.1)$$

where m_0 is the integral of the wave energy spectrum, given as:

$$m_0 = \int_0^{\infty} S(f)df \quad (8.2)$$

The mean zero up-crossing period, T_z , is used to relate the average wave period to the wave energy spectrum, such that $T_{av} = 1.09T_z$ (Kim, 2008) and

$$T_z = \sqrt{\frac{m_0}{m_2}} \quad (8.3)$$

where m_2 is given as:

$$m_2 = \int_0^{\infty} f^2 S(f)df \quad (8.4)$$

Shape optimisation of a floating wave energy converter

Falnes (2007) describes the total stored energy, E , in a wave per unit area of sea surface in terms of significant wave height and the wave energy spectrum as follows:

$$E = \rho g \int_0^{\infty} S(f) df = \frac{\rho g H_s^2}{16} \quad (8.5)$$

where ρ is the density of the fluid and g is acceleration due to gravity. The wave power level, P , per unit width in a wave is given as:

$$P = \rho g \int_0^{\infty} v_g(f) S_{zz}(f) df = \frac{\rho g^2 H_s^2 T_{av}}{64\pi} \quad (8.6)$$

where $v_g(f)$ is the group velocity, which is given as:

$$v_g(f) = \frac{g}{4\pi f} = \frac{g T_{av}}{4\pi} \quad (8.7)$$

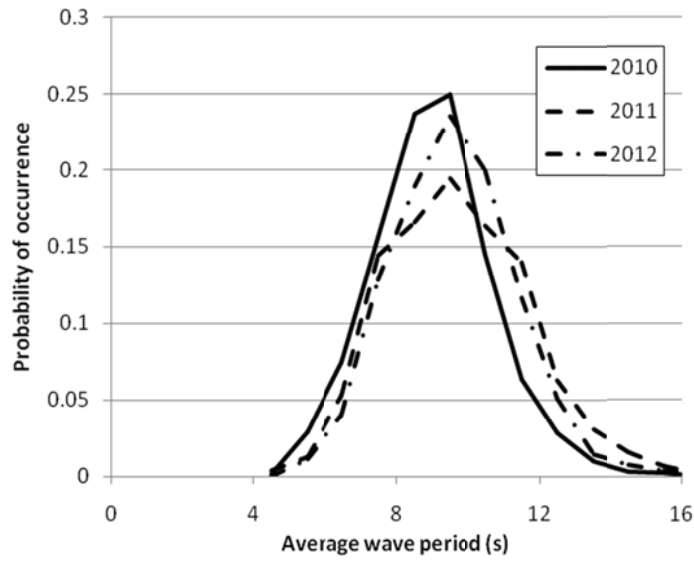
for deep water waves. For example, in 2010, seas off Belmullet, Co. Mayo, Ireland, which has latitude and longitude of [54.225N, -9.991W], at AMETS, had an average significant wave height, H_s of 2.15 m, with an average wave period, T_{av} of 9 s. Using these two figures and Eqn. (8.6), the resultant wave power level per unit width is approximately 20.5 kW/m. However, when analysing the total year's data, the total annual wave power level per unit width at the location, for 2010, is calculated to be almost 29.5 kW/m. Therefore, it's obvious that a single day's measurement is a poor estimate of a yearly average.

Table 8.1, Table 8.2 and Table 8.3, for 2010, 2011 and 2012 respectively, detail the number of half hour occurrences of bands of significant wave heights and average wave periods at AMETS and, from this, the probability of occurrence can be calculated. The probability of occurrence of average wave period and significant wave height for 2010, 2011 and 2012 can be seen graphically in Figure 8.1. These tables also give a detailed insight into the typical wave climate of the location and give a designer a great advantage when designing a WEC to perform efficiently at the location. Data monitoring at AMETS was only established in December 2009 and, therefore, there are only three full years of data available thus far. Since AMETS has been selected as Ireland's first full-scale wave

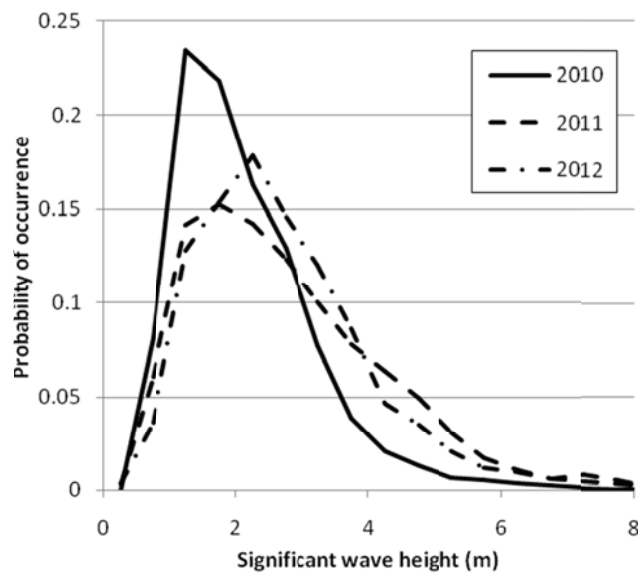
Shape optimisation of a floating wave energy converter

energy test site, this data is a good representation for a typical offshore site. However, different locations do still have different properties and, therefore, a WEC will need to be designed based on its expected deployment location. Using Eqn. (8.6) and the probability of occurrence, the annual wave power level per unit width, in kWh/m year, can be calculated and shown graphically in Figure 8.2, Figure 8.3 and Figure 8.4 for 2010, 2011 and 2012, respectively. Furthermore, the monthly distributions of average significant wave height and average wave period are shown in Figure 8.5 and Figure 8.6, respectively, for 2010, 2011 and 2012. From Figure 8.2, Figure 8.3 and Figure 8.4, there is a definite peak in the wave power level at the location. The location and magnitude at which this peak occurs, along with the overall increase in energy from 2010 to 2011, is attributable to the stormy conditions experienced at the location at the end of 2011. This is further evident as there is an overall reduction from 2011 to 2012. These stormy conditions are reflected in both Figure 8.5 and Figure 8.6.

Shape optimisation of a floating wave energy converter



(a)



(b)

Figure 8.1: Probability of occurrence at AMETS for 2010, 2011 and 2012 of (a): average wave period and (b): significant wave height.

Shape optimisation of a floating wave energy converter

Table 8.1: Number of occurrences of significant wave height and average wave period at AMETS for 2010.

	Average wave period, T_{av} (s)										
	4-5	5-6	6-7	7-8	8-9	9-10	10-11	11-12	12-13	13-14	14-16
0-0.5	0	1	0	1	1	0	0	0	0	0	0
0.5-1	18	132	290	387	262	137	28	8	0	0	0
1-1.5	0	291	434	763	929	718	395	103	7	0	0
1.5-2	0	32	333	696	1041	812	356	65	37	10	8
2-2.5	0	1	88	406	659	726	374	159	61	41	18
2.5-3	0	0	18	144	464	698	380	194	94	17	2
3-3.5	0	0	0	26	229	415	313	155	42	21	1
3.5-4	0	0	0	6	71	234	175	86	28	0	2
4-4.5	0	0	0	1	20	98	113	65	30	2	0
4.5-5	0	0	0	0	2	34	78	56	31	3	0
5-5.5	0	0	0	0	0	2	28	44	23	5	1
5.5-6	0	0	0	0	0	1	11	34	29	3	5
6-6.5	0	0	0	0	0	0	1	8	33	6	6
6.5-7	0	0	0	0	0	0	0	4	15	13	6
7-7.5	0	0	0	0	0	0	1	2	4	7	2
7.5-8	0	0	0	0	0	0	0	3	3	3	2
8-8.5	0	0	0	0	0	0	0	0	2	2	9
8.5-9	0	0	0	0	0	0	0	0	3	5	3
9-9.5	0	0	0	0	0	0	0	0	1	1	2
9.5-10	0	0	0	0	0	0	0	0	0	1	0
10-11	0	0	0	0	0	0	0	0	0	5	1
11-12	0	0	0	0	0	0	0	0	0	0	3
12-14	0	0	0	0	0	0	0	0	0	0	6

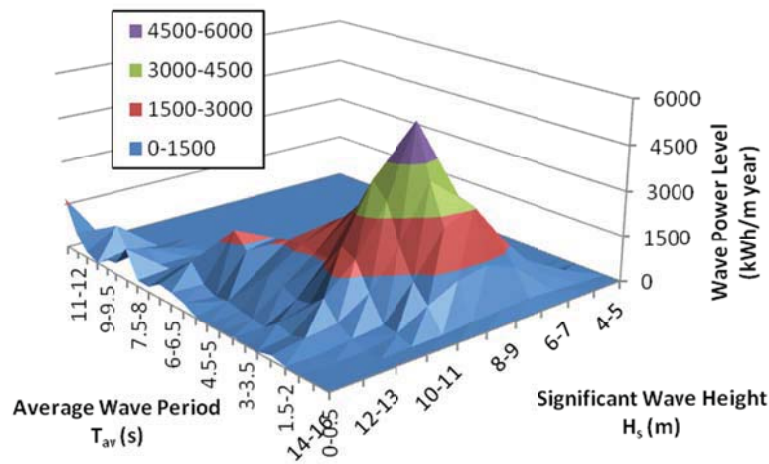


Figure 8.2: Surface chart representation of the wave power level, in kWh/m year, for significant wave height and average wave period at AMETS for 2010.

Shape optimisation of a floating wave energy converter

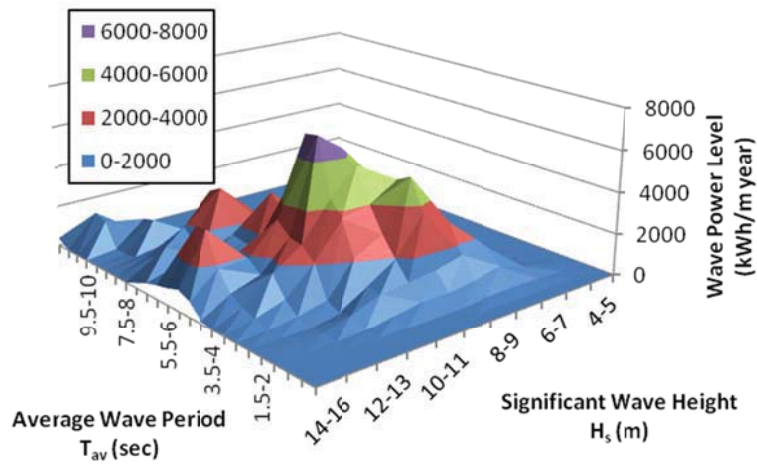


Figure 8.3: Surface chart representation of the wave power level, in kWh/m year, for significant wave height and average wave period at AMETS for 2011.

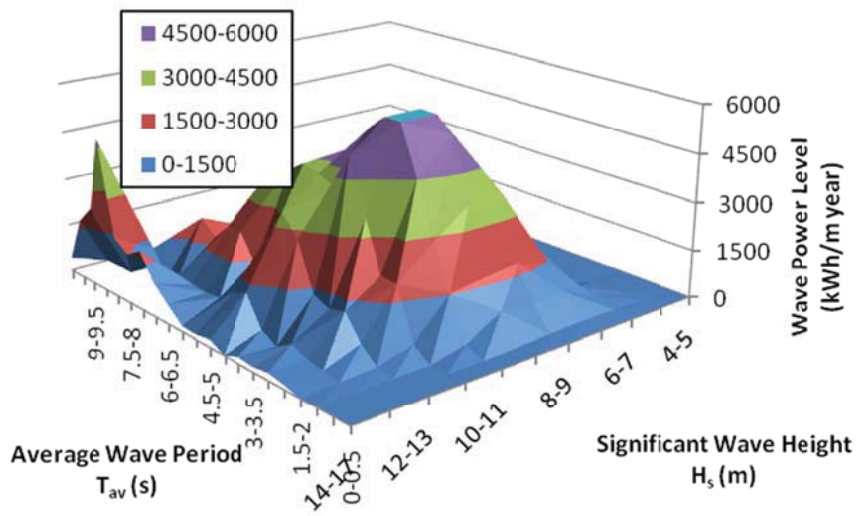


Figure 8.4: Surface chart representation of the wave power level, in kWh/m year, for significant wave height and average wave period at AMETS for 2012.

Shape optimisation of a floating wave energy converter

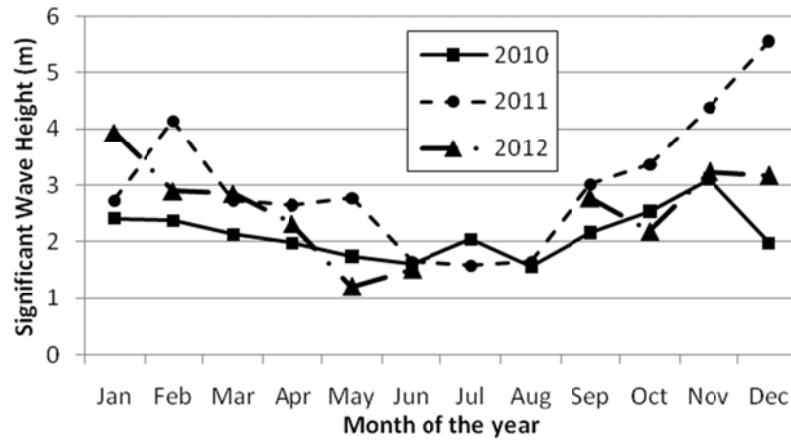


Figure 8.5: The monthly average significant wave height at AMETS for 2010, 2011 and 2012.

Table 8.2: Number of occurrences of significant wave height and average wave period at AMETS for 2011.

Significant wave height, H_s (m)	Average wave period, T_{av} (s)											
	4-5	5-6	6-7	7-8	8-9	9-10	10-11	11-12	12-13	13-14	14-16	16-20
0-0.5	27	1	0	11	1	0	0	0	0	0	0	1
0.5-1	19	99	233	252	176	33	13	0	1	0	0	0
1-1.5	1	62	318	584	360	243	226	116	21	5	0	0
1.5-2	0	11	126	529	466	335	267	221	103	21	3	0
2-2.5	0	0	39	323	515	598	282	146	34	4	0	0
2.5-3	0	0	4	225	358	554	277	189	50	23	7	0
3-3.5	0	0	0	44	252	370	278	237	122	44	19	2
3.5-4	0	0	0	2	104	242	292	210	116	71	23	1
4-4.5	0	0	0	0	23	160	249	264	94	45	28	3
4.5-5	0	0	0	0	6	81	171	208	91	48	43	14
5-5.5	0	0	0	0	0	32	102	117	44	39	65	16
5.5-6	0	0	0	0	0	8	49	61	28	22	51	11
6-6.5	0	0	0	0	0	3	15	61	24	18	17	8
6.5-7	0	0	0	0	0	0	5	28	22	14	10	5
7-7.5	0	0	0	0	0	0	6	30	43	15	15	2
7.5-8	0	0	0	0	0	0	1	15	34	18	7	0
8-8.5	0	0	0	0	0	0	0	2	18	5	4	0
8.5-9	0	0	0	0	0	0	0	1	6	4	2	0
9-9.5	0	0	0	0	0	0	0	0	1	10	1	0
9.5-10	0	0	0	0	0	0	0	0	1	8	1	0
10-11	0	0	0	0	0	0	0	0	0	3	6	0
11-12	0	0	0	0	0	0	0	0	0	1	4	0
12-14	0	0	0	0	0	0	0	0	0	0	1	0

Shape optimisation of a floating wave energy converter

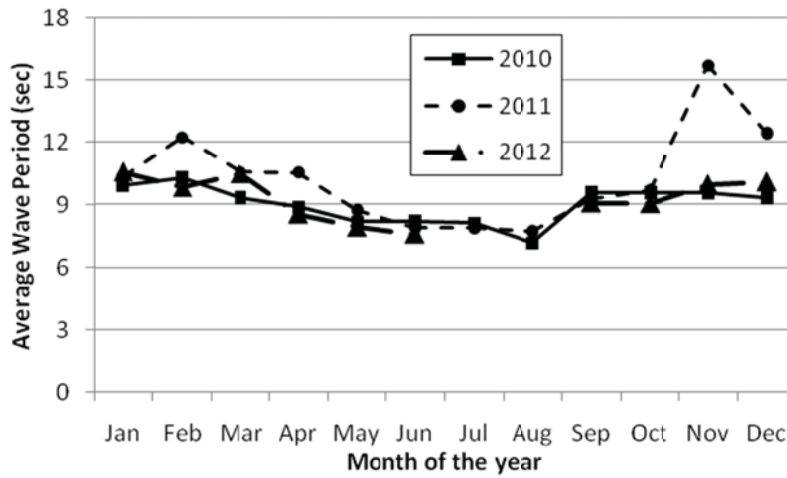


Figure 8.6: The monthly average wave period at AMETS for 2010, 2011 and 2012.

Table 8.3: Number of occurrences of significant wave height and average wave period at AMETS for 2012.

Significant wave height, H_s (m)	Average wave period, T_{av} (s)											
	4-5	5-6	6-7	7-8	8-9	9-10	10-11	11-12	12-13	13-14	14-16	16-17
0-0.5	0	5	27	21	2	0	0	0	0	0	0	0
0.5-1	4	78	163	160	96	27	3	0	0	0	0	0
1-1.5	0	60	199	535	459	494	128	7	0	0	0	0
1.5-2	0	18	152	522	573	476	395	93	21	11	0	0
2-2.5	0	0	44	412	708	631	447	277	73	18	15	0
2.5-3	0	0	8	169	517	643	472	189	111	20	17	0
3-3.5	0	0	0	55	315	574	488	238	70	26	8	0
3.5-4	0	0	0	14	99	372	439	264	63	6	6	2
4-4.5	0	0	0	0	14	149	242	162	102	13	0	0
4.5-5	0	0	0	0	2	70	168	136	100	35	6	0
5-5.5	0	0	0	0	0	25	90	115	52	24	3	0
5.5-6	0	0	0	0	0	1	47	88	28	13	3	0
6-6.5	0	0	0	0	0	0	12	74	38	10	9	0
6.5-7	0	0	0	0	0	0	3	30	32	9	13	0
7-7.5	0	0	0	0	0	0	0	23	21	9	17	2
7.5-8	0	0	0	0	0	0	0	15	23	5	12	2
8-8.5	0	0	0	0	0	0	0	5	9	11	13	2
8.5-9	0	0	0	0	0	0	0	0	6	4	30	4
9-9.5	0	0	0	0	0	0	0	0	0	0	13	2
9.5-10	0	0	0	0	0	0	0	0	0	0	6	4
10-11	0	0	0	0	0	0	0	0	0	0	2	0

8.2.2 Estimating the wave energy spectrum at a given location

In this section, a method for estimating the wave energy spectrum at a given sea or location is detailed. The energy at each significant wave height, H_s , and average wave period, T_{av} , for a given period is used to calculate wave energy spectrum for that period. This is similar to the technique utilised by Bretschneider, in 1959, where he used two parameters, the total energy and average period, to first derive the analytical Bretschneider spectrum (Bretschneider, 1959). Another, commonly used analytical wave energy spectrum is the modified Pierson-Moskowitz Spectrum (Perez, 2005), $S_{PM}(f)$, which is given as:

$$S_{PM}(f) = \frac{A_S}{(2\pi)^4 f^5} \exp\left(\frac{-B_S}{(2\pi)^4 f^4}\right) \quad (8.8)$$

where the coefficients $A_S = \frac{173H_S^2}{T_{av}^4}$ and $B_S = \frac{691}{T_{av}^4}$. This can be used as an input in time-domain calculations, as detailed in Section 8.4, where no real wave energy spectrum input is available.

In this chapter, a case study of AMETS is used as the design location, or the location where the WEC is to be deployed. An annual wave energy spectrum is calculated for 2010, 2011 and 2012, as well as an average annual wave energy spectrum for the location over the three year period. The wave energy, in kWh/m year, is estimated at each significant wave height and average wave period for a given year by utilising the probability of occurrence, which is calculated from the data displayed in Table 8.1, Table 8.2 and Table 8.3. A relation between wave energy, in kWh/m year, and frequency can be approximated and, using Eqn. (8.6), the relation is used to estimate an equivalent significant wave height at each i frequency. From this, an equivalent wave height, H_i , at each i frequency can be determined using the relation:

$$H_i = \frac{H_{s,i}}{\sqrt{2}} \quad (8.9)$$

The wave energy density, $S(f_i)$, at each i frequency is then determined using the relation:

Shape optimisation of a floating wave energy converter

$$A_i = \sqrt{2 S(f_i) \Delta f_i} \quad (8.10)$$

or

$$S(f_i) = \frac{H_i^2}{8\Delta f_i} \quad (8.11)$$

where A_i is the wave amplitude at the i^{th} frequency and Δf_i is the frequency increment at the i^{th} frequency, defined as: $\Delta f_i = \frac{f_{i+1} - f_{i-1}}{2}$. The wave energy spectra for 2010, 2011 and 2012, along with the average wave energy spectrum for the three years are shown in Figure 8.7. Furthermore, a spectrum generated using the modified Pierson-Moskowitz Spectrum (Perez, 2005), given in Eqn. (8.8), for an significant wave height, $H_s = 2.57$ m, and average wave period, $T_{av} = 9.47$ s, which are the average of the three years. It is clear to see from Figure 8.7 that this spectrum underestimates the actual average spectrum of AMETS. In addition, there is a shift in the peak frequency of this spectrum when compared to the actual peak frequency of the location. With further years' data, a more accurate wave energy spectrum for this location may be determined. However, currently, there are only three years of data available for the location. Again as discussed in Section 8.2.1, the increase in the magnitude of the wave energy spectrum and the shift in frequency where its peak occurs, between 2010 and 2011 followed by a reduction from 2011 to 2012, are attributable to the stormy conditions experienced at the location at the end of 2011.

Using the Pierson-Moskowitz Spectrum to describe the wave climate at AMETS would have an impact on the performance of a WEC being designed for deployment at the location. The shift in peak frequency predicted using this spectrum from the actual frequency would cause a design of a WEC, which would not become resonant. Furthermore, the amplitude spectrum derived from this wave energy spectrum would underestimate the magnitude of the waves at AMETS. Both of these factors would result in an inefficient design and, thus, a reduction in the potential power output of the WEC.

Shape optimisation of a floating wave energy converter

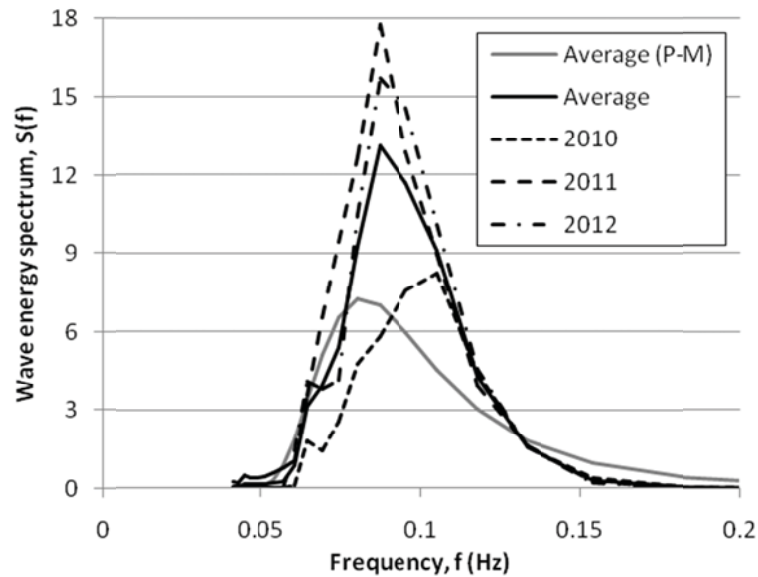


Figure 8.7: Wave energy spectra for AMETS for 2010, 2011 and 2012 and the resulting average spectrum for the site, which are calculated using Eqn. (8.11). A modified P-M spectrum for AMETS, using Eqn. (8.8), is also included.

8.3 Geometrical shape optimisation

In order to perform the geometrical shape optimisation, a computational program, the code for which is detailed in Appendix E, incorporating the geometrical shape optimisation methodology detailed in Section 8.3.1, has been developed. When optimising the geometric configuration of any wave energy converter a number of design criteria, or parameters, must be considered:

- The maximum wave energy should be extracted efficiently over an appropriate frequency range.
- The converter should perform efficiently regardless of the wave direction.
- The probability of slamming due to excessive dynamic response of the converter should be limited as much as possible.

Shape optimisation of a floating wave energy converter

In the proposed methodology, the maximum wave energy extracted is achieved by efficiently maximising the dynamic response of the unconstrained system. When dealing with a constrained system, this is incorporated into the analysis in the calculation of the response amplitude operator (RAO) of the structure. The appropriate frequency range of the analysis is defined by the desired location's wave energy spectrum. The structures being analysed are vertically axisymmetric and, therefore, the converter will perform equally with any wave direction. In order to reduce the probability of slamming, restrictions on the RAO of each structure are imposed and an optimum geometric configuration is determined at each restriction. In reality, these restrictions will be imposed by a variety of tuning, or control, techniques (Hals, 2010). Furthermore, the stability of the structure is an important factor in the design of any floating structure. This is achieved through effectively designing the mass distribution by lowering the meta-centric height insuring the structures remain in stable equilibrium, while also reducing the pitch motion of the structure. However, since this chapter only deals with geometric shape, this aspect of the design is not discussed.

In order to determine the level of performance of each geometric configuration analysed, an objective function must be defined. In this case, the objective function is the significant force or double amplitude motion, $(2s)_s$. The significant force is similar to the significant wave height, which is calculated from the input wave energy spectrum as shown in Eqn. (8.1), and is given as (Clauss and Birk, 1996):

$$(2s)_s = 4 \sqrt{\int_0^{\infty} S_{ss}(f) df} \quad (8.12)$$

where $S_{ss}(f)$ is the dynamic response spectrum density, an example of which is given in Figure 8.13. The objective function defined by Clauss and Birk (1996) has been chosen for this analysis as it is proportional to the dynamic response, which is the property of the structure that is being maximised. The significant force is calculated over a range of radii for each geometry in the geometry library. The optimum geometric configuration of the converter is the structural shape and radius yielding the maximum significant force for the input wave energy spectrum. However, if the radius of the structure is not a variable,

an optimum geometry is easily identified for the imposed radius using the methodology detailed in this section.

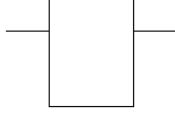
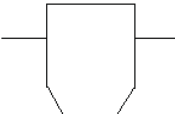
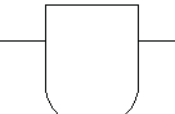
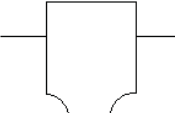
8.3.1 Geometric configuration optimisation methodology

In the geometric configuration optimisation algorithm, detailed in this section, two variables are specified: the geometric shape and the radius of the structure. Specified families of geometric shapes, which have a draft that is proportional to the radius, are used in the analysis to vary the geometrical shape, which is referred to as the geometry library. Furthermore, in the program the user specifies a range of radii that are to be analysed, which in this chapter has been specified as 1 m to 25 m. However, the radius or the geometry of the structure may be specified and, in this case, the algorithm is easily modified.

The geometric configuration optimisation algorithm is summarised in the flowchart in Figure 8.8. In order to perform the geometric configuration optimisation, a wave energy spectrum, for the design location, must be inputted. In addition to this, a geometry library of the geometric shapes being analysed must be generated. This library contains the RAO of each geometric shapes being analysed, which is used to calculate its dynamic response spectrum and, ultimately, the associated significant force. Details of the geometry library for the case study are shown in Table 8.4. Then each structural geometry is analysed and the significant force, $(2s)_s$, at each radius is calculated for a range of radii using a function defined within the computational program, the code for which is detailed in Appendix E,. The maximum significant force can then be calculated at each radius and the geometry that achieves this can be determined. The optimum geometric configuration is obtained from, for example, Figure 8.9 to Figure 8.12, where the radius and geometry that yield the maximum significant force can be selected.

Shape optimisation of a floating wave energy converter

Table 8.4: Description of the various geometry options in the geometry library.

ID	b/a	Shape description	Diagram
CYL01	0.5	A truncated cylinder	
CYL02	1		
CYL03	2		
LIN01	1	A truncated cylinder with a 45° linear chamfer dividing the radius in a ratio of 8:7	
LIN02	1.5		
LIN03	2		
HEMI	1	A half-immersed sphere	
OC01	1.5	A truncated cylinder with a hemisphere attached to its base	
OC02	2		
OC03	2.5		
IC01	1	A truncated cylinder with a quarter incircle chamfer dividing the radius in a ratio of 8:7	
IC02	1.5		
IC03	2		

Shape optimisation of a floating wave energy converter

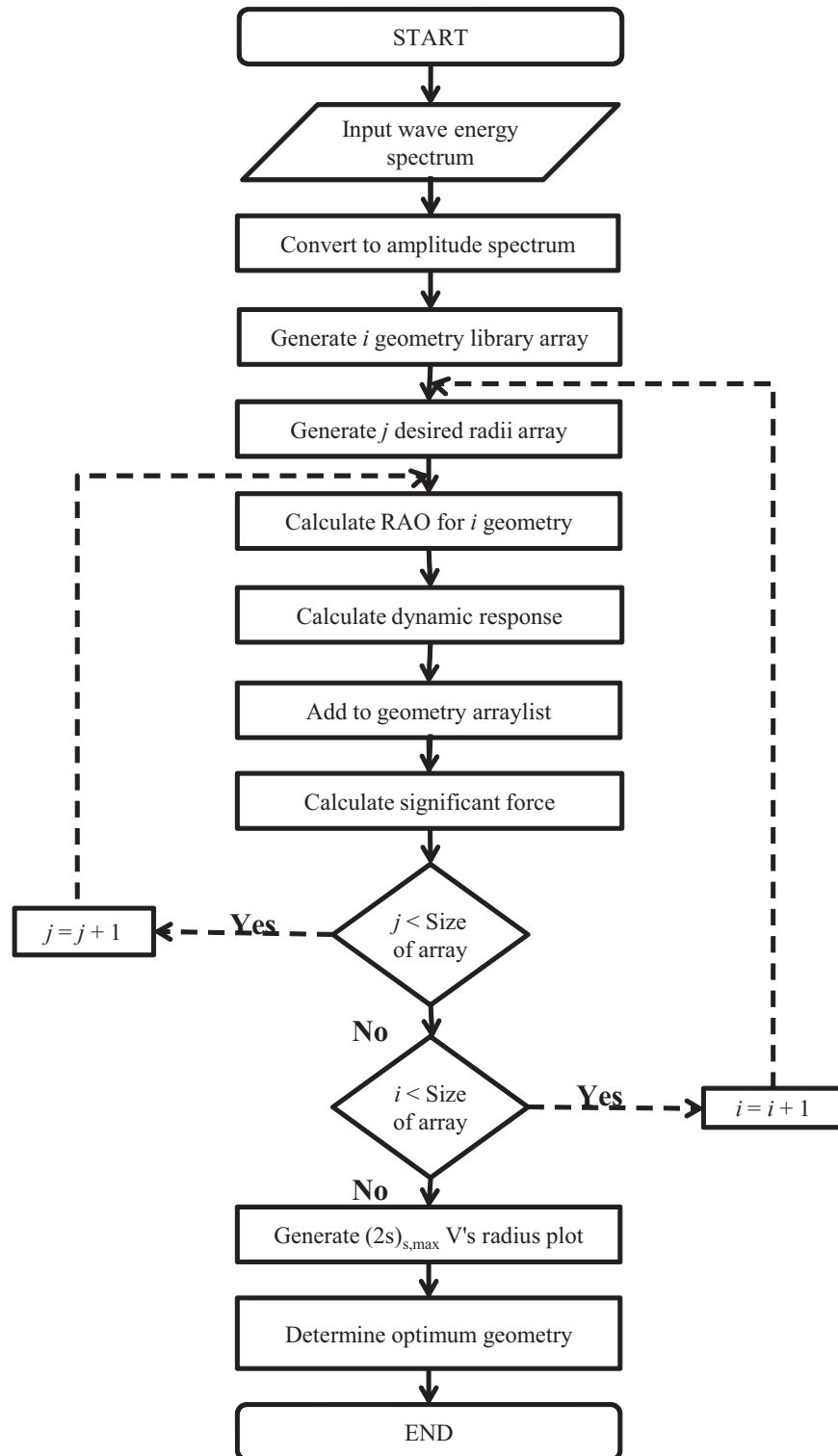


Figure 8.8: Flowchart of the shape optimisation procedure.

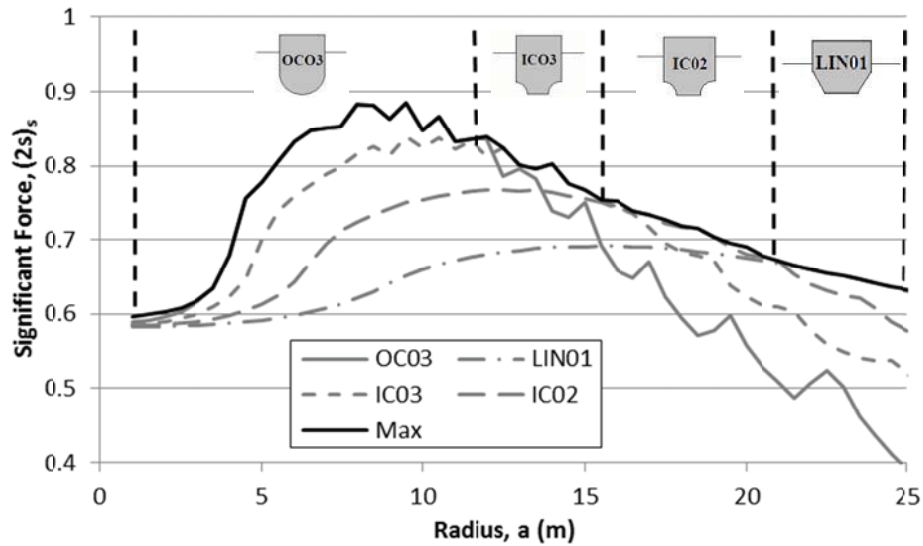
8.3.2 Case study and findings

In order to examine the geometric configuration optimisation methodology detailed in this chapter, a case study will be presented. The wave energy converter under consideration is a floating vertically axisymmetric structure, which oscillates mainly in the heave motion, for that is to be deployed at AMETS. Therefore, the average wave energy spectrum, given in Figure 8.7, is used as the input wave energy spectrum, in order to find the optimum geometric configuration that is appropriate to this location. As discussed previously, to reduce the probability of slamming of the device, a restriction on the response amplitude operator (RAO), given by Eqn. (5.19), can be imposed. Thus, to investigate the effect such a restriction would impose on the performance of the device, restrictions on the RAO of 3, 4 and 5 were imposed and compared to having no restrictions. This is shown in Figure 8.9, where the performance of the device is indicated by the significant force, $(2s)_s$, and this is plotted against the radius of the device for a number of different geometric shapes. The optimum structural geometric shape for the case study is found to be a truncated cylinder with a hemisphere attached to its base having a b/a ratio of 2.5 (i.e. geometry I.D. *OC03*) regardless of the restriction on the RAO. However, the optimum radius was found to be between 7 m and 8.5 m and this is dependent on the restriction on the RAO. On the other hand, if the radius of the structure is required to be greater than approximately 10m, other geometric shapes have been found to yield better performance. For example, for no restriction on the RAO, as seen in Figure 8.9 (a), *IC03* is found to be the optimum structural geometric shape for a range of radii from 11m to 16m and, in turn, *IC02* for 16 m to 21 m and *LIN01* for 21 m to 25 m.

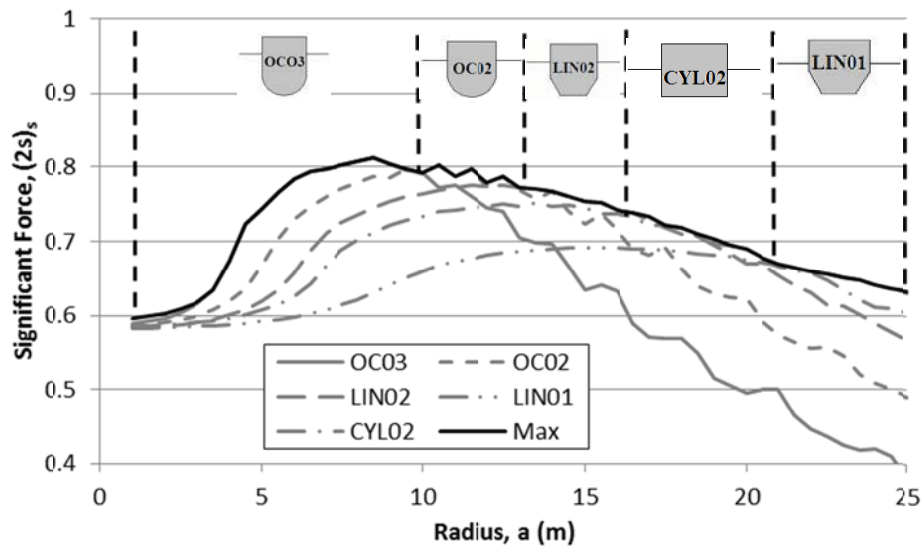
However, a developer may wish to consider a fewer number of geometric shapes without significantly affecting its optimum response. Therefore, for example, in Figure 8.9 (a), the geometry *OC03* may be deemed suitable up to a radius of 13 m and *IC02* for a radius range of 13 to 25 m. Similarly, in Figure 8.9 (b), the geometry *OC03* may be deemed suitable up to a radius of 11 m and *LIN02* for a radius range of 11 to 25m. Furthermore, when examining the data regardless of the restriction of RAO imposed, in general it can

Shape optimisation of a floating wave energy converter

be concluded that *OC03* is the optimum geometry for a radius of less than 11 m, *IC02* is the optimum geometry for a radius from 11 m to 18 m and *LIN02* is the optimum geometry for a radius range of 18 to 25 m.

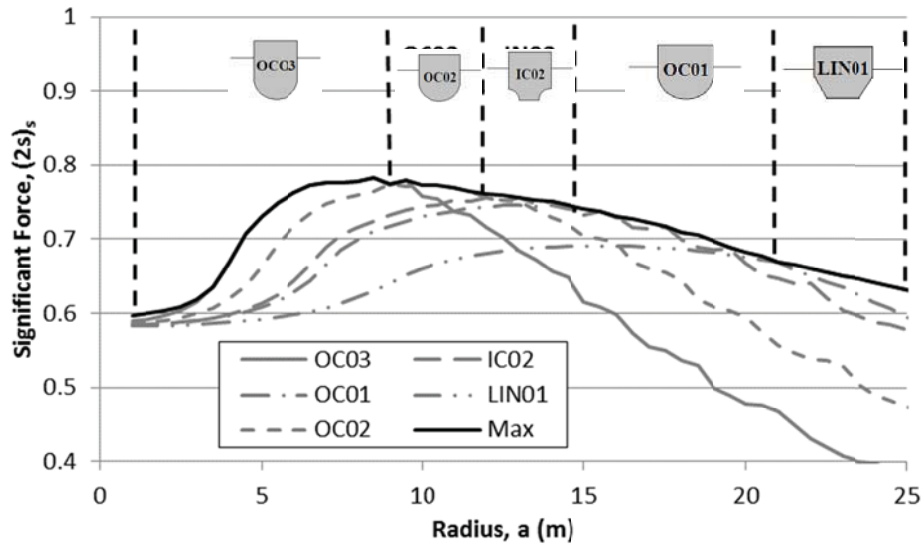


(a)

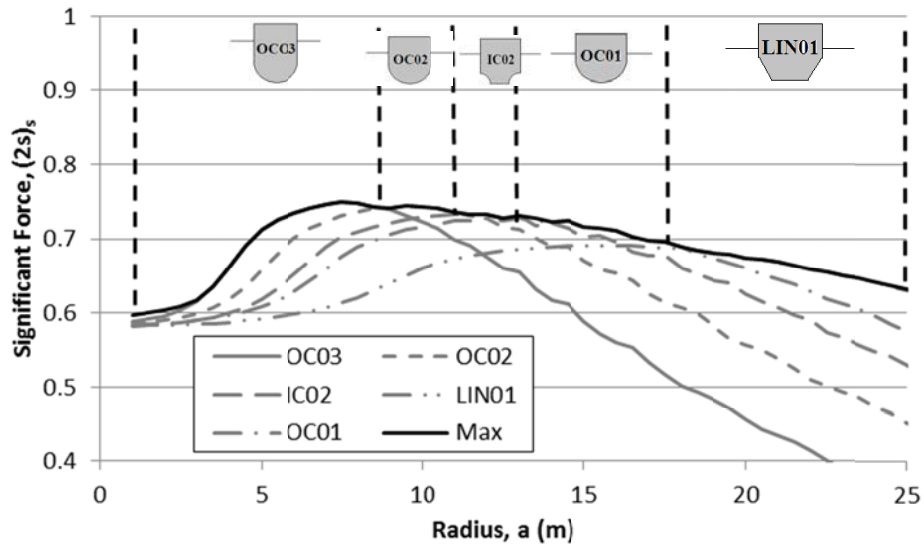


(b)

Shape optimisation of a floating wave energy converter



(c)



(d)

Figure 8.9: The significant force as a function of radius for the average spectrum over a two year period (2010-2011) for AMETS obtained by imposing the following maximum restrictions on the RAO: (a): no restriction, (b): a restriction of 5, (c): a restriction of 4, (d): a restriction of 3.

Shape optimisation of a floating wave energy converter

The algorithm was also run for an input wave spectrum for 2010, 2011 and 2012 from AMETS. The results of this are shown in Figure 8.10 to Figure 8.12, respectively. It was found that, again, the optimum structural geometry is *OC03*. A device of this geometric shape and a radius of between 7 m and 8.5 m would have yielded optimum performance at this location based on the wave energy spectrum for 2010, as can be seen in Figure 8.10. On the other hand, a similar device with a radius of between 8 m and 10 m would have performed on average better in 2011, as shown in Figure 8.11. Therefore, a suggested geometry is a vertical cylinder with a hemispherical base, with a b/a of 2.5 and a diameter of 8 m.

Furthermore, at larger radii, the optimum structural geometric shape was found to differ for this location over the three years. This is further evidence that additional years of data are required before a wave energy spectrum for design of wave energy converters at this location can be accurately determined.

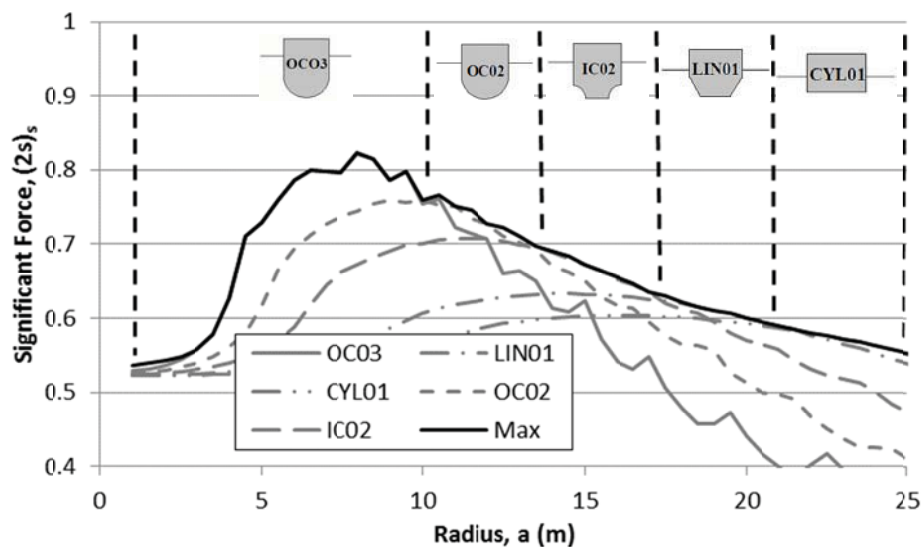


Figure 8.10: The significant force as a function of radius for the 2010 spectrum for AMETS with no restriction on the maximum value of RAO, which also details the optimum geometric shapes as the radius is varied.

Shape optimisation of a floating wave energy converter

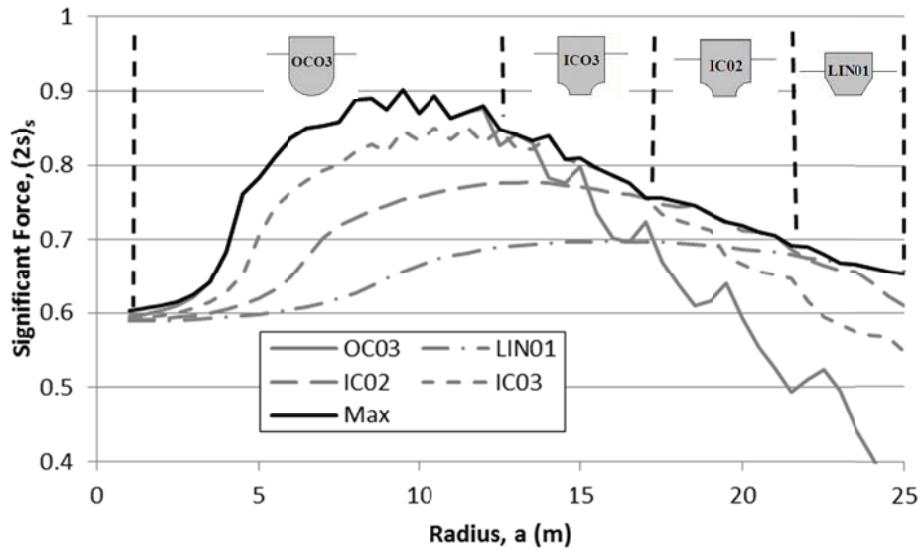


Figure 8.11: The significant force as a function of radius for the 2011 spectrum for AMETS with no restriction on the maximum value of RAO, which also details the optimum geometric shapes as the radius is varied.

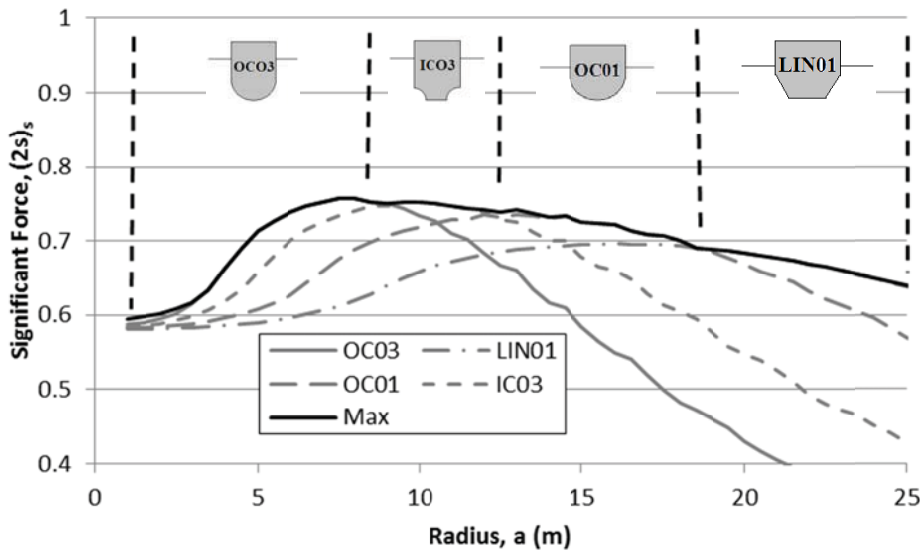


Figure 8.12: The significant force as a function of radius for the 2012 spectrum for AMETS with no restriction on the maximum value of RAO, which also details the optimum geometric shapes as the radius is varied.

Shape optimisation of a floating wave energy converter

Based on the 2010 and 2011 wave data for AMETS (Section 8.2.2), the dynamic response in the frequency-domain of the device with optimum geometric configuration (i.e. a geometrical shape of *OC03* and radius of 8 m) is shown in Figure 8.13. The wave height spectrum, which is twice the height of the amplitude spectrum, is also shown. In the analysis, a frequency increment, $\Delta f = 0.005$ Hz, is used for both the dynamic response spectrum and the wave height spectrum. It is important to keep the frequency step constant throughout the analysis, as only then is it accurate to compare the different geometric shapes and radii. This is because an increase in the frequency step will cause an increase in the amplitude spectrum and, hence, an increase in the dynamic response spectrum, as each point is representative of a defined with as shown in Figure 8.13. However, any result based on an integral over frequency should not be sensitive to Δf , provided it remains the same throughout the analysis, except for minor numerical error. It is clear from Figure 8.13 that the structure has a dynamic response which is of the same magnitude, or greater than, the wave height, for a large proportion of the wave height spectrum (between 0.06 Hz and 0.13 Hz) and, thus, would perform efficiently within this range.

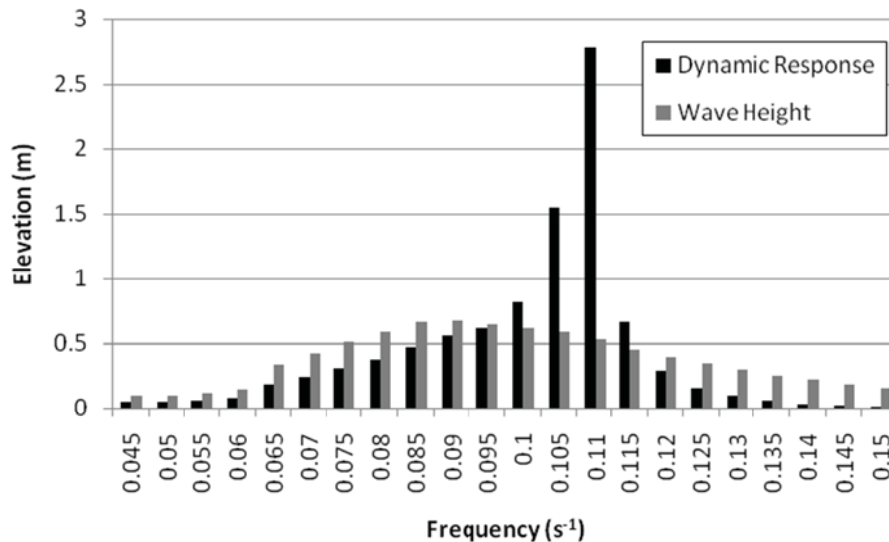


Figure 8.13: The dynamic response spectrum of the optimum structure for an input of the average wave energy spectrum for AMETS. The wave height spectrum is also displayed and, both, have a frequency step, $\Delta f = 0.005$ Hz.

8.4 Mean power output calculation

In this study, a hydrodynamic analysis of the structure is performed, using ANSYS AQWA (ANSYS-Inc., 2010), to derive the excitation forces and the hydrodynamic coefficients. In order to calculate the power output from the structure, a power take-off (PTO) mechanism is incorporated. The PTO mechanism is represented by an ideal linear damper, where the PTO damping coefficient, b_1 , is kept constant. This form lends itself to a solution in the frequency domain and, therefore, can easily be incorporated into the dynamic response calculation. Therefore, the motion of the structure is governed by the following equation:

$$(M + a_m)\ddot{u} + (b_1 + \nu)\dot{u} + \tau u = F_{ext} \quad (8.13)$$

where u is the dynamic response, M is the mass, a_m is the added mass, ν is the radiation wave damping, τ is the hydrostatic stiffness and F_{ext} is the excitation force on the structure. From Eqn. (8.13), the response amplitude operator (RAO) is calculated and is given by the following equation:

$$\frac{u}{A} = \frac{F_{ext}/A}{-\omega^2(M + a_m) + i\omega(b_1 + \nu) + \tau} \quad (8.14)$$

where A is the amplitude of the incident wave.

From the RAO, the dynamic response of a structure may be computed. However, as the value of the damping coefficient of the PTO mechanism is increased the dynamic response is decreased. This is evident from Eqn. (8.14) and is shown graphically in Figure 8.14. Therefore, it is necessary to determine the optimum value of the damping coefficient of the PTO mechanism with respect to optimising the mean power output. Oskamp and Ozkan-Haller (2012) describe the mean power output, at the i th frequency, \bar{P}_i , by the following equation:

$$\bar{P}_i = \frac{1}{2} b_1 |\dot{x}_i|^2 \quad (8.15)$$

Shape optimisation of a floating wave energy converter

where $|\dot{x}_i|$ is the amplitude of the velocity of the structure caused by the energy of the i th spectral component. Using the average wave energy spectrum at AMETS, given in Figure 8.7, the mean power output is calculated over a range of values for the damping coefficient of the PTO mechanism and is shown in Figure 8.15. From Figure 8.15, the optimum value for the damping coefficient of the PTO mechanism, b_1 , at the point where the mean power output is at its maximum, is determined as 360 kNs/m.

The optimum damping coefficient of the PTO mechanism is then used to derive the total mean power output of a structure with the optimum geometric configuration at AMETS. A technique similar to the one detailed by Babarit *et al.* (2012) is used to derive the power matrix for the structure. This power matrix is then applied to a probability of occurrence matrix for AMETS, which is derived from the data given in Tables 1 to 3, and the result is the total mean power output for the structure at the site. The results of this analysis are given in Table 8.5.

Shape optimisation of a floating wave energy converter

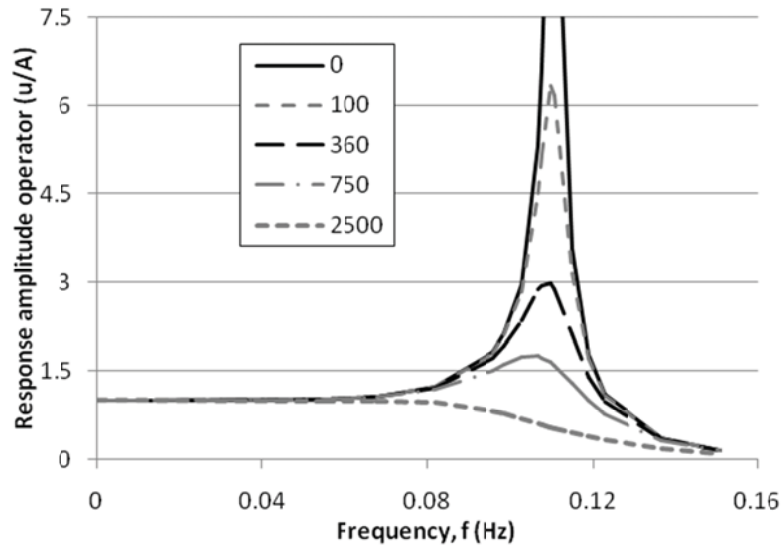


Figure 8.14: Variation of the response amplitude operator for various values of the PTO damping coefficient, b_1 .

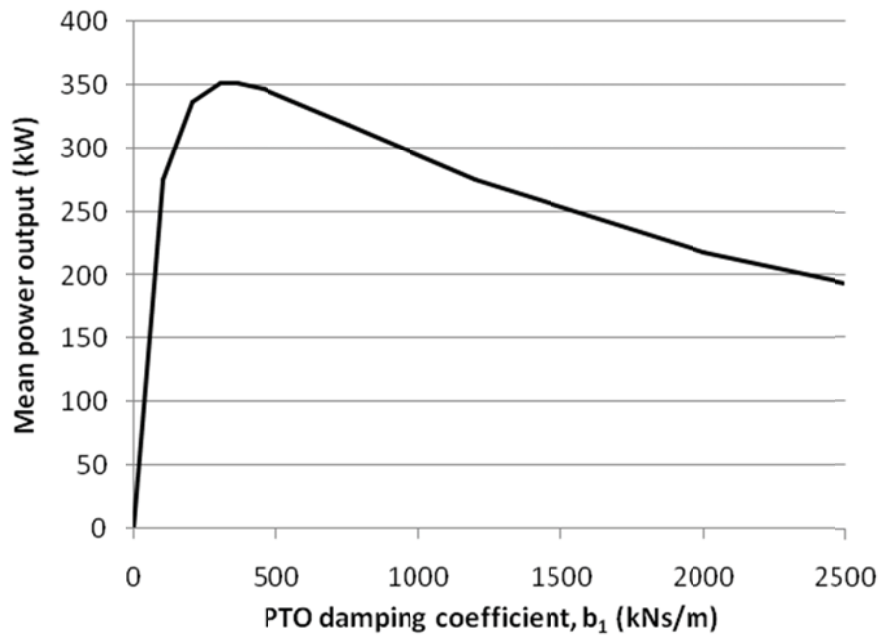


Figure 8.15: Variation of mean power output for a range of values of the PTO damping coefficient.

Shape optimisation of a floating wave energy converter

Table 8.5: Matrix representation of the mean power output (in Watts per year) for the optimum structural configuration at AMETS for 2010 to 2012.

	Average wave period, T_{av} (s)											
	4-5	5-6	6-7	7-8	8-9	9-10	10-11	11-12	12-13	13-14	14-16	16-20
0-0.5	0.1	0.0	0.0	1.4	0.6	0.0	0.0	0.0	0.0	0.0	0.0	0.0
0.5-1	1.1	5.8	9.2	303.0	748.6	276.9	13.5	2.0	0.2	0.0	0.0	0.0
1-1.5	0.1	21.4	35.3	1982.3	6807.2	5680.1	638.6	160.6	12.8	2.0	0.0	0.0
1.5-2	0.0	6.2	44.5	3606.7	15876.1	12418.4	1701.1	528.0	144.2	32.3	6.2	0.0
2-2.5	0.0	0.2	20.6	3893.9	23746.0	24727.6	3046.9	1340.3	248.7	80.0	31.0	0.0
2.5-3	0.0	0.0	5.4	2742.7	25237.8	35805.1	4658.8	1967.7	564.0	113.8	36.5	0.0
3-3.5	0.0	0.0	0.0	890.1	20954.9	35863.8	6218.8	3027.0	722.9	241.0	54.9	2.7
3.5-4	0.0	0.0	0.0	208.6	9603.3	29794.0	6952.0	3582.2	851.4	271.5	80.9	5.4
4-4.5	0.0	0.0	0.0	12.2	2566.0	18367.2	5953.0	4034.2	1193.9	271.7	93.8	7.0
4.5-5	0.0	0.0	0.0	0.0	562.3	10428.7	5133.8	4105.3	1464.9	486.5	205.1	40.7
5-5.5	0.0	0.0	0.0	0.0	0.0	4062.9	3308.7	3460.4	959.3	470.0	352.8	56.8
5.5-6	0.0	0.0	0.0	0.0	0.0	826.0	1930.4	2752.3	821.9	315.0	361.9	46.9
6-6.5	0.0	0.0	0.0	0.0	0.0	292.8	596.8	2541.0	1085.3	333.0	231.9	40.3
6.5-7	0.0	0.0	0.0	0.0	0.0	0.0	198.9	1285.0	919.5	411.3	245.1	29.4
7-7.5	0.0	0.0	0.0	0.0	0.0	0.0	200.8	1315.0	1045.4	408.6	331.6	27.1
7.5-8	0.0	0.0	0.0	0.0	0.0	0.0	32.8	901.6	1054.0	391.6	234.0	15.5
8-8.5	0.0	0.0	0.0	0.0	0.0	0.0	0.0	216.7	577.3	307.2	328.3	17.5
8.5-9	0.0	0.0	0.0	0.0	0.0	0.0	0.0	34.8	335.9	249.6	497.1	39.5
9-9.5	0.0	0.0	0.0	0.0	0.0	0.0	0.0	0.0	50.0	236.0	254.0	22.0
9.5-10	0.0	0.0	0.0	0.0	0.0	0.0	0.0	0.0	27.8	214.5	123.5	49.0
10-11	0.0	0.0	0.0	0.0	0.0	0.0	0.0	0.0	0.0	221.2	184.1	0.0
11-12	0.0	0.0	0.0	0.0	0.0	0.0	0.0	0.0	0.0	33.2	171.7	0.0
12-14	0.0	0.0	0.0	0.0	0.0	0.0	0.0	0.0	0.0	0.0	219.5	0.0

8.5 Discussion and conclusions

In this chapter, a methodology for optimising the geometric configuration of a floating wave energy converter (WEC), which considers the wave energy spectrum of its design location, is presented. The dynamic response of the floating oscillating part of the WEC is the parameter optimised in this analysis. An unconstrained system is analysed in order to determine the optimum geometric shape and radius of the structure. The type of WEC considered in this chapter is a floating vertically axisymmetric point absorber, which predominantly oscillates in the heave, or vertical, motion. However, the methodologies detailed may be easily adapted to be applicable to any WEC.

Shape optimisation of a floating wave energy converter

A case study of the Atlantic marine energy test site (AMETS) has been taken as the design location. This is a recently established full scale test site for WECs. Real wave data from the location has been analysed and the wave energy spectra for 2010 to 2012, as well as the average wave energy spectrum for the three years, was presented. Furthermore, the procedure used to derive the wave energy spectrum for the location has also been presented. However, with further years' data, a more suitable wave energy spectrum as an input in the design of WECs for this location may be determined. Currently, there are only three years of data available for the location. The derived wave energy spectrum is compared to the Pierson-Moskowitz spectrum estimate for AMETS and it was found that there was a shift in the peak frequency along with it underestimating the magnitude of the spectrum. Therefore, using this spectrum as an input would result in an efficient design for a WEC, being deployed at the location, which would have an impact on its performance. Using, the wave energy spectrum as the input, the optimum structural geometric configuration was established. This is a truncated vertical cylinder of radius 8 m with a hemisphere attached to its base and a total draft-to-radius ratio of 2.5.

Furthermore, the optimum damping coefficient of the PTO mechanism is determined. Using the average wave energy spectrum at AMETS, the mean power output is calculated over a range of values for the damping coefficient of the PTO mechanism and the optimum value is determined as $b_l = 360$ kNs/m. In addition, a technique similar to the one detailed by Babarit et al. (2012) is used to derive the power matrix for the structure. This power matrix is then applied to a probability of occurrence matrix for AMETS and the result is the total mean power output for the structure at the site, which is approximately 392 kW per year.

Conclusions and recommendations for further work

Chapter 9
Conclusions and recommendations for further
work

9.1 Introduction

This chapter summaries the findings and conclusions from the current research study. In addition, areas of the study which may require further investigation are discussed. Recommendations for further research which may stem from this study are also detailed briefly.

There are two main objectives associated with the current research, which are (1) to derive an analytical approximation in order to determine the wave excitation forces on a floating truncated cylinder in water of infinite depth and (2) to develop a computational fluid dynamics numerical model for a wave tank which can accurately simulate the interaction between an irregular ocean wave and a structure. In achieving the second objective a number of steps, or sub-objectives are required. These include (a) the development of a linear regular numerical model for a wave tank using computational fluid dynamics, (b) perform linear regular wave-structure interaction within the model, (c) validate these models by comparing the results to experimental simulations performed in the NUI Galway wave flume, (d) generate linear irregular waves which accurately replicate real ocean waves within the model and (e) perform the interaction between a linear irregular ocean wave and a structure within the model.

Furthermore, there are two other objectives associated with the current research study; to use computational fluid dynamics to develop techniques which will aid in the structural health monitoring of wave energy converters and to develop a methodology for the structural geometric optimisation of a wave energy converter and detail a case study using this methodology.

9.2 Summary and conclusions

This section gives a brief summary of the previous chapters. Furthermore, a brief discussion of the main conclusions and their potential impact and application on engineering processes and other research studies are detailed.

9.2.1 The wave excitation force on a floating truncated vertical cylinder in water of infinite depth

In Chapter 3, an analytical approximation to determine the wave excitation forces, by solving the scattering problem, on a floating truncated vertical cylinder in water of infinite depth is presented. The presented analytical approximation provides a solution which is far easier to use and implement than the already available analytical solutions, while retaining a high level of accuracy in calculating the heave and surge wave excitation forces, when the draft-to-radius ratio is greater than unity. This accuracy is displayed as the presented analytical results were found to be in good agreement with the results from the numerical computational fluid dynamics (CFD) analysis. Furthermore, when compared to the independently observed experimental data given in Fonseca et al. (2011), the analytical solution for a truncated vertical cylinder shows good agreement.

In the design of offshore structures, numerical models are used to initially explore a design or concept. However, the accuracy of these models needs to be ensured. Analytical approximations similar to the study presented here provide an efficient and easy to implement check on the results of the analysis to ensure a robust numerical model is maintained. In addition, in the current study, the pitch wave excitation forces have been calculated analytically, a solution for which was not already available in the literature. The accurate modelling of these forces is required in the engineering and structural design of risers and moorings in the oil and gas industry and, therefore, the presented analytical approximation would provide an accurate check on initial design calculations.

9.2.2 Development of a numerical wave tank

A detailed methodology for the development of a computational fluid dynamics numerical model for a wave tank, which can accurately produce both linear deep water waves and linear waves for the finite depth case, is presented in Chapter 4. However, when using numerical models, one of the greatest challenges is how computationally expensive it is. Therefore, the steps required to be taken to design an optimum numerical model for a wave tank are also outlined. In particular, the effects of the meshing method, wave dissipation beach slope, the total time and time-step interval for the transient analysis set-up were explored, while minimising the overall dimensions of the model to generate a deep water wave.

The aspect of optimising the computational cost, while retaining a high level of accuracy, is one of the main aims in the development of the numerical model for a wave tank. A major advantage of optimising the model in terms of its computational cost at a basic stage, i.e. the linear regular wave generation stage, is when the model is expanded to three-dimensions and structures or other interactions are introduced, as the savings in computational cost will be far greater. One example of this is in the design of the mesh in terms of refinement; the coarser sections will remain relatively coarse when going from the two-dimensional model to the three-dimensional model.

Furthermore, the numerical model for a wave tank is advanced to include wave-structure interaction. The use of this type of numerical model proves a relatively inexpensive alternative to physical testing, while still highlighting the major contributing factors to the dynamic response of a structure. The robustness of the numerical model analysed is confirmed when compared to the analytical solution and found to be in good agreement. Another advantage of this method is that it is ideal for analysing the nonlinear responses of structures to extreme wave conditions. This survivability testing is a major issue in the design of wave energy converters.

9.2.3 Linear regular wave-structure interaction using computational fluid dynamics

In Chapter 5, frequency-domain wave-structure interaction is performed using numerical methods. The commercial boundary element method software, ANSYS AQWA, is used to compute wave-structure interaction in the frequency domain. Two applications of using frequency-domain wave-structure interaction in the structural modelling of wave energy converters are detailed. This analysis method provides a much quicker solution and more information about a structure. However, the theory on which the analysis is based is far more basic than the time domain method and, therefore, provides less detailed results which may not accurately predict real conditions. Moreover, this method provides an easily implemented hydrodynamic analysis tool for the initial concept design and parameter optimisation associated with the engineering and structural design of marine structures.

9.2.4 Validation of numerical models using experimental data

The experimental wave flume, located at NUI Galway, is used in order to validate the methodology for developing a numerical model for a wave tank (NWT), which is described in Chapter 4. Initially, the parameters of the wave flume, namely the wavemaker relation and the breaking limit of the waves, are determined. The outputs from the numerical models are compared to the experimental results and the wavemaker relation derived by Wang (1974). It was found that the numerical model predicts the experimental results well for $k_0\gamma < 0.7$, where $k_0\gamma$ is the dimensionless wavenumber of the NUI Galway wave flume.

Furthermore, the experimental wave flume is used to perform wave-structure interaction and is compared to the results from numerical models. A rig is set up which supports a structure using a mooring system and a pulley system is employed to measure the heave, or vertical, dynamic response of the structure. The results of the study are compared to a hydrodynamic analysis and are in very good agreement when the wave period is greater than the natural period of the structure. Furthermore, the results are compared to a numerical model for a wave tank and the results were found to be in good agreement, although it is evident that the magnitude of the pitch in the model did not match that of the experimental simulation.

The experimental results observed in this study provide an improved insight into wave-structure interaction, while also providing a realistic set of data which may be used in the future to validate the results of other studies. Furthermore, the experimental study highlights issues with the model set up and, in addition, helps in improving the numerical models presented when further iterations are performed. The experimental analysis also helps highlight some of the limitations of the experimental wave flume and these are discussed further in Section 9.3.4.

9.2.5 Irregular linear wave generation in a numerical wave tank

In Chapter 7, a numerical model for a wave tank which can accurately mimic real ocean waves is developed. Three ocean wave records recorded at AMETS are taken and replicated to prove the accuracy and robustness of the methodology. After the initial stage, the measured waves and those from the model are found to be consistent both in terms of both frequency and amplitude. A rectangular floating prism is introduced into the model in order to explore the accuracy of wave-structure interaction prediction. A comparison of the heave motion dynamic response of the structure from the NWT model and the solution derived from the BEM analysis shows the two solutions were found to be in good agreement.

The methodology detailed in this section provides the user a very inexpensive method of performing wave-structure interaction in realistic ocean conditions, without the need for sea trials. The use of the numerical model is maximised here as no scaling is introduced, therefore a more realistic model and structure response is presented. This methodology also provides a far more realistic estimate of the energy extraction ability of a wave energy converter compared to the use of a linear regular wave tank.

9.2.6 Shape optimisation of a floating wave energy converter

The efficiency of a wave energy converter is primary in the design of the components which it is comprised of. In Chapter 8, a methodology for optimising the structural geometric configuration of a floating wave energy converter (WEC), which considers the wave energy

spectrum of its design location, is presented. The dynamic response of the floating oscillating part of the WEC is the parameter optimised in this analysis. The type of WEC considered in this study is a floating vertically axisymmetric point absorber, which predominantly oscillates in the heave, or vertical, motion. However, the methodologies detailed may be easily adapted to be applicable to any WEC. A case study of AMETS is taken as the design location in order to show the performance of the methodology.

The analysis provides the designer with the optimum structural geometric configuration at a given diameter, while also providing options at a diameter range, which may be specified by the designer. Furthermore, the methodology can be applied to individual components of a WEC, for example the oscillating water column turbine blades with respect to geometric design or sizing. The methodology can also be adapted for the design of other offshore floating structures, for example, breakwaters, weather/wave data buoys, or floating platforms.

9.2.7 Overview of the impact of current research study

An analytical approximation of the wave excitation forces on a floating truncated vertical cylinder in water of infinite depth derived as part of this research can be used to validate numerical CFD models, which predicts linear wave-structure interaction in both the time and frequency domain, as shown in this project. The results of a numerical CFD model developed in this work are found to be in good agreement with the analytical approximation, thus ensuring the accuracy of the model. Subsequently, a numerical CFD model which can accurately perform irregular linear wave-structure interaction is developed. This model provides a user with a method of exploring the effect of real ocean waves on a floating offshore structure, such as a breakwater, a floating platform or an offshore vessel. In the current research study, numerical CFD models are developed to aid in the design of offshore wave energy converters. Two main applications of the models are explored, which are the development of techniques to aid in the structural health monitoring of wave energy converters and the development of a methodology for the optimisation of the structural geometric configuration of a wave energy converter to maximize the power generation for a given site.

9.3 Recommendations for further work

As a result of limitations, mainly the time span of the PhD programme but also finances and resources available, there are a number of advances of the current research topics which may be explored. Furthermore, while undertaking the current research study, a number of related topics and research areas which may be performed arose, using the current research study as a base. In this section, a number of these topics are briefly discussed.

9.3.1 Analytical approximations using similar techniques

The techniques and assumptions used for deriving an analytical approximation for the forces on a structure in water of infinite depth, as detailed in Chapter 3, could be applied to other wave-structure interaction problems in order to derive useful analytical approximations.

In the current study, the wave excitation forces are derived when the scattering problem for the case of a floating truncated vertical cylinder is solved. Similar techniques, along with additional assumptions, may be employed to derive an analytical approximation in the case of the radiation problem and, thus, derive an expression of the added mass and damping coefficients. In relation to the case of a floating hemisphere in water of infinite depth, Havelock (1955) and Hulme (1982) have derived a solution for the radiation problem. However, a solution for the scattering problem has not being successfully achieved.

Although the case in the current study is for a three-dimensional structure, the techniques and approximations may be applied to two-dimensional problems in order to derive an analytical approximation which may be far less tedious and easier to employ than the currently available solutions, while retaining a high level of accuracy. For example, the solution to the problem of the heave motion of a circular cylinder in infinite depth derived by Ursell (1949) and a revision of this problem may be performed in order to find an easily implemented analytical approximation.

9.3.2 3-D the interaction between an irregular ocean wave and a structure in a NWT

In the current study, the interaction between a linear irregular ocean wave and a structure was confined to a three-dimensional numerical model, which was one element in width. The main reason for this is there is a limit on the educational license for ANSYS provided by NUI Galway. Therefore, a mesh which contained more than 512,000 nodes, or approximately 1.2×10^6 elements, could not be solved. Since linear irregular wave generation requires additional mesh refinement, along the still water level, when compared to linear regular wave generation, a high level of accuracy could not be maintained with the mesh restriction if the three-dimensional concept was to be explored. Therefore, if a full license of the software was obtained, a user may expand the study detailed in Chapter 7 to a three-dimensional simulation. Furthermore, the concept of generating multi-directional waves could be explored and this may also include the effects of currents, which were explored previously by Newell (2010).

9.3.3 Structural health monitoring of WEC's

In Chapter 5, the application of computational fluid dynamics to the topic of structural health monitoring of wave energy converters is briefly discussed. However, the topic was only touched on and there are many issues with respect to the structural health monitoring in the marine climate which need to be resolved. For example, the development of robust and reliable computational methods for detecting errors and issues with a device may be explored. Since the concept of wave energy extraction is still in its infancy, relative to other forms of energy (i.e. the oil and gas industry) there is plenty of scope for the development of such techniques which will aid in insuring the efficient in-use performance of a device.

9.3.4 The experimental wave flume at NUI Galway

The experimental wave flume at NUI Galway provides students and researchers with the opportunity to gain some invaluable hands-on experience with scale model simulations of

wave generation and wave-structure interaction. In the current study, the interaction between regular waves and a floating vertically cylindrical structure was explored. However, since the wave flume is very narrow, a prism structure which has nearly the same width as the flume, which would be more comparable to a two-dimensional model rather than a three-dimensional model, is suggested for future wave-structure interaction problems using the experimental wave flume.

However, as the equipment is a recent addition to the hydraulics laboratory and was originally designed as part of a MEngSc project, there is plenty of scope for improving the facility. The main aspects that may be investigated are as follows:

- The method of wave generation currently being employed is a plunger-type wavemaker, which is driven by a rotational motor. This wavemaker is easily removed and replaced, which gives the opportunity for exploring the use of other shapes plungers or other types of wavemakers, i.e. flap or paddle type, in order to find an optimum solution.
- Furthermore, as a result of the control system for the rotational motor, only regular, or single frequency, waves may be generated. Replacing this system with a short enough response time would introduce the possibility of generating irregular waves, which are more realistic. Alternatively, replacing the control system and motor with a piston that can be controlled at each time step may be a more suitable option.
- Another major aspect of the wave flume that would be optimised is the absorption beach. While the current system works quite well at high frequencies, there is still a noticeable amount of reflection at lower frequencies (Wave period > 2 seconds). Therefore, exploring systems used in other facilities, for example introducing a gravel, or porous, beach or a parabolic beach, may be a preferred solution to dissipating the wave energy.
- In addition, in order to increase the potential of the facility and as a result of its current location, there is scope for increasing the length of the wave flume. Currently, it is 10m long, but this could be increased to 25m as there is available space in the laboratory to do so. This would also introduce the potential for exploring the interaction between arrays of structures, for example, arrays of wave energy converters.

- The flume could also be retrofitted to incorporate a feature where water could be re-circulated to generate a current within the flume. This would then give the option of having a wave or current flume or a combined wave-current flume.

References

- Agamloh E. B., Wallace A. K. and von Jouanne A. (2008). Application of fluid-structure interaction simulation of an ocean wave energy extraction device. *Renewable Energy*. 33(4): p. 748-757.
- Akamina Technologies. (2012). *Akamina wave gauge system*. Retrieved, from the world wide web: www.akamina.com.
- Akyildiz H. (2002). Experimental investigation of pressure distribution on a cylinder due to the wave diffraction in a finite water depth. *Ocean Engineering*. 29(9): p. 1119-1132.
- Anbarsooz M., Passandideh-Fard M. and Moghiman M. (2013). Fully nonlinear viscous wave generation in numerical wave tanks. *Ocean Engineering*. 59(0): p. 73-85.
- ANSYS-Inc. (2010). ANSYS AQWA, Release 13.
- ANSYS Inc. (2009). ANSYS CFX, Release 12.1.
- ANSYS Inc. (2010). ANSYS AQWA, Release 13.
- ANSYS Inc. (2011). *ANSYS CFX-Solver Theory Guide*.
- Aquamarine-Power. (2010). *Oyster*. Retrieved on 02-11-2010, from the world wide web: <http://www.aquamarinepower.com/>.
- Babarit A., Hals J., Muliawan M. J., Kurniawan A., Moan T. and Krokstad J. (2012). Numerical benchmarking study of a selection of wave energy converters. *Renewable Energy*. 41(0): p. 44-63.
- Bai K. J. (1975). Diffraction of oblique waves by an infinite cylinder. *Journal of Fluid Mechanics*. 68(03): p. 513-535.
- Beirao P., Valerio D. and da Costa J. S. (2007). Linear model identification of the Archimedes Wave Swing in *POWERENG: International Conference on Power Engineering, Energy and Electrical Drives* Setubal, Portugal. 12-14 April.
- Bhatta D. D. and Rahman M. (1995). Wave loadings on a vertical cylinder due to heave motion. *International Journal of Mathematics and Mathematical Sciences*. 18(1): p. 151-170.
- Bhatta D. D. and Rahman M. (2003). On scattering and radiation problem for a cylinder in water of finite depth. *International Journal of Engineering Science*. 41(9): p. 931-967.
- Birk L. (2009). Application of Constrained Multi-Objective Optimization to the Design of Offshore Structure Hulls. *Journal of Offshore Mechanics and Arctic Engineering*. 131(1): p. 011301.
- Birk L. and Clauss G. F. (2001). Automated Hull Optimisation of Offshore Structures Based on Rational Seakeeping Criteria in *Eleventh International Offshore and Polar Engineering Conference*, Stavanger, Norway. 17-22 June.
- Birk L. and Clauss G. F. (2002). Parametric Hull Design and Automated Optimization of Offshore Structures in *Tenth Congress of International Maritime Association of the Mediterranean (IMAM 2002)*. 13-17 May.
- Birk L. F. and Clauss G. F. (2001). Automated Hull Optimisation of Offshore Structures Based on Rational Seakeeping Criteria. Eleventh International Offshore and Polar Engineering Conference. Stavanger, Norway.

- Black J. L. (1975). Wave forces on vertical axisymmetric bodies. *Journal of Fluid Mechanics*. 67(02): p. 369-376.
- Boo S. Y. (2002). Linear and nonlinear irregular waves and forces in a numerical wave tank. *Ocean Engineering*. 29(5): p. 475-493.
- Bretschneider C. L. (1959). Wave Variability and Wave Spectra for Wind Generated Gravity Waves. PhD Thesis. Physical (Engineering) Oceanography, Graduate School of Agriculture and Mechanical College of Texas.
- Brownjohn J. M. W. (2007). Structural health monitoring of civil infrastructure. *Philosophical Transactions of the Royal Society A: Mathematical, Physical and Engineering Sciences*. 365(1851): p. 589-622.
- Chakrabarti A. (2000). On the Solution of the Problem of Scattering of Surface-Water Waves by the Edge of an Ice Cover. *Proceedings: Mathematical, Physical and Engineering Sciences*. 456(1997): p. 1087-1099.
- Chang P. C., Flatau A. and Liu S. C. (2003). Review Paper: Health Monitoring of Civil Infrastructure. *Structural Health Monitoring*. 2(3): p. 257-267.
- Chatjigeorgiou I. K. (2012). Hydrodynamic exciting forces on a submerged oblate spheroid in regular waves. *Computers & Fluids*. 57(0): p. 151-162.
- Chopra A. K. (1995). *Dynamics of Structures: theory and applications to earthquake engineering*. Prentice-Hall international series in civil engineering and engineering mechanics. Englewood Cliffs, N.J.: Prentice-Hall.
- Clauss G. F. and Birk L. (1996). Hydrodynamic shape optimization of large offshore structures. *Applied Ocean Research*. 18(4): p. 157-171.
- Clément A., McCullen P., Falcão A., Fiorentino A., Gardner F., Hammarlund K., Lemonis G., Lewis T., Nielsen K., Petroncini S., Pontes M. T., Schild P., Sjöström B.-O., Sørensen H. C. and Thorpe T. (2002). Wave energy in Europe: current status and perspectives. *Renewable and Sustainable Energy Reviews*. 6(5): p. 405-431.
- Coastal Engineering Research Center (1977). *Shore protection manual / U.S. Army Coastal Engineering Research Center*. Fort Belvoir, Va. Washington: Supt. of Docs., U.S. Govt. Print. Off.
- Construction Industry Federation (2009). Developing the Green Economy in Ireland, Construction Industry Federation, Dublin, Ireland.
- Contento G. (2000). Numerical wave tank computations of nonlinear motions of two-dimensional arbitrarily shaped free floating bodies. *Ocean Engineering*. 27(5): p. 531-556.
- Craig R. R. (1981). *Structural dynamics: an introduction to computer methods*. New York: Wiley. xv, 527 p.
- Dean R. G. and Dalrymple R. A. (1984). *Water wave mechanics for engineers and scientists* Englewood Cliffs, N.J.: Prentice-Hall.
- Dong G.-H., Xu T.-J., Zhao Y.-P., Li Y.-C. and Gui F.-K. (2010). Numerical simulation of hydrodynamic behavior of gravity cage in irregular waves. *Aquacultural Engineering*. 42(2): p. 90-101.

- Elangovan M. (2011). Simulation of Irregular Waves by CFD. *World Academy of Science, Engineering and Technology* 55.
- Elchahal G., Lafon, P., Younes, R. (2007). Modelling and Optimizing Floating Breakwaters Using Density Distribution in *7th International Offshore and Polar Engineering Conference*, Lisbon, Portugal. 1-6 July.
- Falcão A. (2000). The shoreline OWC wave power plant at the Azores in *Proceedings of the Forth European Wave Energy Conference*, Aalborg, Denmark. 4-6 December.
- Falcão A. F. d. O. (2010). Wave energy utilization: A review of the technologies. *Renewable and Sustainable Energy Reviews*. 14(3): p. 899-918.
- Falnes J. (1999). Wave-Energy Conversion Through Relative Motion Between Two Single-Mode Oscillating Bodies. *Journal of Offshore Mechanics and Arctic Engineering*. 121(1): p. 32-38.
- Falnes J. (2002). *Ocean Waves and Oscillating Systems*: Cambridge university Press.
- Falnes J. (2007). A review of wave-energy extraction. *Marine Structures*. 20(4): p. 185-201.
- Faltinsen O. (1993). *Sea Loads on Ships and Offshore Structures (Cambridge Ocean Technology Series)*: Cambridge University Press.
- Finnegan W. and Goggins J. (2012a). Numerical simulation of linear water waves and wave-structure interaction. *Ocean Engineering*. 43(0): p. 23-31.
- Finnegan W. and Goggins J. (2012b). The Structural Dynamics of a Two-Body Wave Energy Converter in *4th International Conference on Ocean Energy*, Dublin, Ireland. 17 October 2012.
- Finnegan W. and Goggins J. (2012c). Determining the locations of high stresses on a floating concrete structure to aid in the structural health monitoring of wave energy converters in *Bridge and Concrete Research in Ireland 2012*, Dublin, Ireland. 6-7 September.
- Finnegan W. and Goggins J. (2013). Numerical modelling to aid in the structural health monitoring of wave energy converters. *Key Engineering Materials*. 569-570: p. 595-602.
- Finnegan W., Meere M. and Goggins J. (2011). The Wave Excitation Forces on a Floating Vertical Cylinder in Water of Infinite Depth in *World Renewable Energy Congress 2011*, Linkoping Sweden. 8-13 May 2011.
- Finnegan W., Meere M. and Goggins J. (2013). The wave excitation forces on a truncated vertical cylinder in water of infinite depth. *Journal of Fluids and Structures*. 40(0): p. 201-213.
- Flocard F. and Finnigan T. D. (2010). Laboratory experiments on the power capture of pitching vertical cylinders in waves. *Ocean Engineering*. 37(11-12): p. 989-997.
- Fonseca N., Pessoa J. o., Mavrakos S. and Le Boulluec M. (2011). Experimental and numerical investigation of the slowly varying wave exciting drift forces on a restrained body in bi-chromatic waves. *Ocean Engineering*. 38(17-18): p. 2000-2014.
- French M. J. (2006). On the difficulty of inventing an economical sea wave energy converter: a personal view. *Engineering for the Maritime Environment*. 220.
- Garrett C. J. R. (1971). Wave forces on a circular dock. *Journal of Fluid Mechanics*. 46(1): p. 129-139.

- Garrison C. J. (1978). Hydrodynamic loading of large offshore structures: three-dimensional source distribution methods citation. *Numerical methods in offshore engineering*, Wiley.
- Goggins J., Broderick B. M., Basu B. and Elghazouli A. Y. (2007). Investigation of the seismic response of braced frames using wavelet analysis. *Structural Control and Health Monitoring*. 14(4): p. 627-648.
- Guo H. Y., Zhang L., Zhang L. L. and Zhou J. X. (2004). Optimal placement of sensors for structural health monitoring using improved genetic algorithms. *Smart Materials and Structures*. 13(3): p. 528.
- Hadzic I., Hennig J., Peric M. and Xing-Kaeding Y. (2005). Computation of flow-induced motion of floating bodies. *Applied Mathematical Modelling*. 29(12): p. 1196-1210.
- Hals J. (2010). Modelling and phase control of wave-energy converters. PhD Thesis. Department of Marine Technology, Norwegian University of Science and Technology.
- Hassan M. and Bora S. N. (2012). Exciting forces for a pair of coaxial hollow cylinder and bottom-mounted cylinder in water of finite depth. *Ocean Engineering*. 50(0): p. 38-43.
- Havelock T. (1955). Waves due to a Floating Sphere Making Periodic Heaving Oscillations. *Proceedings of the Royal Society of London. Series A, Mathematical and Physical Sciences*. 231(1184): p. 1-7.
- Henderson D. M., Patterson M. S. and Segur H. (2006). On the laboratory generation of two-dimensional, progressive, surface waves of nearly permanent form on deep water. *Journal of Fluid Mechanics*. 559: p. 413-427.
- Henderson R. (2006). Design, simulation, and testing of a novel hydraulic power take-off system for the Pelamis wave energy converter. *Renewable Energy*. 31(2): p. 271-283.
- Hsu H.-H. and Wu Y.-C. (1997). The hydrodynamic coefficients for an oscillating rectangular structure on a free surface with sidewall. *Ocean Engineering*. 24(2): p. 177-199.
- Hulme A. (1982). The wave forces acting on a floating hemisphere undergoing forced periodic oscillations. *Journal of Fluid Mechanics*. 121: p. 443-463.
- IPS. (2012). *IPS OWEC buoy*. Retrieved, from the world wide web: <http://www.ips-ab.com/>.
- Irish Government (2007). Delivering a Sustainable Energy Future for Ireland, the Energy Policy Framework 2007-2020. M. a. n. R. Department of Communications.
- Jensen A., Pedersen G. K. and Wood D. J. (2003). An experimental study of wave run-up at a steep beach. *Journal of Fluid Mechanics*. 486: p. 161-188.
- Johanning L., Smith G. H. and Wolfram J. (2006). Mooring design approach for wave energy converters. *Proceedings of the Institution of Mechanical Engineers, Part M: Journal of Engineering for the Maritime Environment*. 220(4): p. 159-174.
- Kang H. S., Mureithi N. W. and Pettigrew M. J. (2012). Analytical solution for a vibrating simply-supported cylinder subjected to 2-D concentric annular flow, considering friction. *Journal of Fluids and Structures*. 35(0): p. 1-20.

- Khalilabadi M. R. and Bidokhti A. A. (2012). Design and Construction of an Optimum Wave Flume. *Journal of Applied Fluid Mechanics*. 5(3).
- Killeen C. (2011). Computational and experimental development of a small-scale laboratory wave flume. Masters Thesis. College of Engineering and Informatics, National University of Ireland, Galway.
- Kim C. H. (2008). *Nonlinear Waves and Offshore Structures*. Advanced Series on Ocean Engineering: World Scientific Publishing Co. Pte. Ltd.
- Kim M. H., Niedzwecki J. M., Roesset J. M., Park J. C., Hong S. Y. and Tavassoli A. (2001). Fully Nonlinear Multidirectional Waves by a 3-D Viscous Numerical Wave Tank. *Journal of Offshore Mechanics and Arctic Engineering*. 123(3): p. 124-133.
- Kofoed J. P., Frigaard P., Friis-Madsen E. and Sørensen H. C. (2006). Prototype testing of the wave energy converter wave dragon. *Renewable Energy*. 31(2): p. 181-189.
- Koo W. and Kim M. H. (2004). Freely floating-body simulation by a 2D fully nonlinear numerical wave tank. *Ocean Engineering*. 31: p. 2011-2046.
- Kramer M. M. and Frigaard P. B. (2002). Efficient Wave Energy Amplification with Wave Reflectors in *Twelfth International Offshore and Polar Engineering Conference*, Kitakyushu, Japan. 12-17 June.
- Kruckow W. (2010). The Economic Impact for Ireland of High Oil and Gas Prices. Dublin, Ireland, Seimens Limited.
- Kumar M. and Anantha Subramanian V. (2007). A numerical and experimental study on tank wall influences in drag estimation. *Ocean Engineering*. 34(1): p. 192-205.
- Lal A. and Elangovan M. (2008). CFD Simulation and Validation of Flap Type Wave-Maker. *World Academy of Science, Engineering and Technology*. 46: p. 7.
- Leppington F. G. (1973). On the radiation and scattering of short surface waves. Part 3. *Journal of Fluid Mechanics*. 59(01): p. 147-157.
- Liang X., Yang J., Li J., Xiao L. and Li X. (2010). Numerical Simulation of Irregular Wave-Simulating Irregular Wave Train. *Journal of Hydrodynamics*. 22(4): p. 537-545.
- Linton C. M. and McIver P. (2001). *Handbook of Mathematical Techniques for Wave/Structure Interactions*. Boca Raton, FL: Chapman & Hall/CRC.
- Liu Y.-y., Teng B., Cong P.-w., Liu C.-f. and Gou Y. (2012). Analytical study of wave diffraction and radiation by a submerged sphere in infinite water depth. *Ocean Engineering*. 51(0): p. 129-141.
- Liu Y., Li H.-J. and Li Y.-C. (2012). A new analytical solution for wave scattering by a submerged horizontal porous plate with finite thickness. *Ocean Engineering*. 42(0): p. 83-92.
- MacCamy R. C. and Fuchs R. A. (1954). Wave Forces on Piles: A Diffraction Theory. Tech. Memo No. 69, US Army Corps of Engineers, Beach Erosion Board.
- Mansour A. M., Williams A. N. and Wang K. H. (2002). The diffraction of linear waves by a uniform vertical cylinder with cosine-type radial perturbations. *Ocean Engineering*. 29(3): p. 239-259.
- Marine Institute (2006). Sea Change Part 2: Marine Foresight Exercise for Ireland. Marine Institute, Oranmore, Galway.

- Marine Institute (2006). *Sea Change: A Marine Knowledge, Research & Innovation Strategy for Ireland*. Marine Institute, Oranmore, Galway.
- Marine Institute (2010). *Smart Ocean Ireland Consultation Document*.
- Marine Institute. (2012). *Marine Institute*. Retrieved on 29-11-2012, from the world wide web: www.marine.ie.
- McCormick M. E. (1973). *Ocean Engineering Wave Mechanics*. New York: John Wiley & Sons Inc.
- McCormick M. E. and Kraemer D. R. B. (2001). Wave Energy. *Encyclopedia of Ocean Sciences*. J. H. Steele. Oxford, Academic Press: 3187-3191.
- Microsoft (2007). *Microsoft Visual Basic 2008 Express Edition*. Version 9.0.21022.8 RTM.
- Mohapatra S. C., Ghoshal R. and Sahoo T. (2013). Effect of compression on wave diffraction by a floating elastic plate. *Journal of Fluids and Structures*. 36(0): p. 124-135.
- Morita K. (1995). *Applied Fourier Transform*: John Wiley & Sons.
- Mousaviraad S. M., Carrica P. M. and Stern F. (2010). Development and validation of harmonic wave group single-run procedure for RAO with comparison to regular wave and transient wave group procedures using URANS. *Ocean Engineering*. 37(8-9): p. 653-666.
- Murawski L., Opoka S. and Ostachowitz W. (2010). Measurement and calculation errors estimation and damage detection possibility analysis for SHM of offshore structure in *5th European Conference on Structural Health Monitoring*.
- Newell C. (2010). *A Mathematical and Numerical Examination of Wave-Current Interaction and Wave-Driven Hydrodynamics*. PhD Thesis. Civil Engineering, national University of Ireland, Galway.
- Newmark N. M. (1959). A method of computation for structural dynamics. *Journal of Engineering Mechanics, ASCE*. 85: p. 28.
- Nichols J. M., . (2003). Structural health monitoring of offshore structures using ambient excitation. *Applied Ocean Research*. 25(3): p. 101-114.
- Ning D. Z. and Teng B. (2007). Numerical simulation of fully nonlinear irregular wave tank in three dimension. *International Journal for Numerical Methods in Fluids*. 53: p. 1847-1862.
- Ning D. Z., Teng B., Eatock Taylor R. and Zang J. (2008). Numerical simulation of non-linear regular and focused waves in an infinite water-depth. *Ocean Engineering*. 35(8-9): p. 887-899.
- O'Cathain M., Leira B. J. and Ringwood J. V. (2007). *Modelling of Multibody Marine Systems with Application to Wave-Energy Devices*. 7th European Wave and Tidal Energy Conference. Porto, Portugal.
- Ocean Energy. (2010). *Ocean Energy Buoy*. Retrieved on 09-10-10, from the world wide web: <http://www.oceanenergy.ie>.
- Oskamp J. A. and Ozkan-Haller H. T. (2012). Power calculations for a passively tuned point absorber wave energy converter on the Oregon coast. *Renewable Energy*. 45(0): p. 72-77.

- Park J.-C., Kim M.-H. and Miyata H. (1999). Fully non-linear free-surface simulations by a 3D viscous numerical wave tank. *International Journal of Numerical Methods in Fluids*. 29: p. 685-703.
- Park J. C., Uno Y., Sato T., Miyata H. and Chun H. H. (2004). Numerical reproduction of fully nonlinear multi-directional waves by a viscous 3D numerical wave tank. *Ocean Engineering*. 31(11-12): p. 1549-1565.
- Perez T. (2005). *Ship Motion Control: Course Keeping and Roll stabilisation using Rudder and Fins*. London: Springer-Verlag London Limited.
- Reilly J. (2010). Perfect waves may provide key to powering the nation. Sunday Independent. Dublin, Ireland, The Independent.
- Ruellan M., BenAhmed H., Multon B., Josset C., Babarit A. and Clement A. (2010). Design Methodology for a SEAREV Wave Energy Converter. *IEEE Transactions on Energy Conversion*. 25(3): p. 760-767.
- Salter S. H. (1974). Wave power. *Nature*. 249(5459): p. 720-724.
- Soerensen H. C., Hansen, R., Friis-Madsen, E., Panhauser, W., Mackie, G., Hansen, H.H., Frigaard, P., Hald, T., Knapp, W., Keller, J., Holmen, E., Holmes, B., Thomas, G., Rasmussen, P., Krogsgaard, J. (2000). The Wave Dragon - Now Ready for Test in Real Sea.
- Sriram V., Sannasiraj S. A. and Sundar V. (2006). Simulation of 2-D nonlinear waves using finite element method with cubic spline approximation. *Journal of Fluids and Structures*. 22(5): p. 663-681.
- Stallard T. J., Weller S. D. and Stansby P. K. (2009). Limiting heave response of a wave energy device by draft adjustment with upper surface immersion. *Applied Ocean Research*. 31(4): p. 282-289.
- Sun H. and Faltinsen O. M. (2006). Water impact of horizontal circular cylinders and cylindrical shells. *Applied Ocean Research*. 28(5): p. 299-311.
- The United States Patent and Trademark Office. (2013). *Search for patents: Wave energy converters*. Retrieved on 10-10-13, from the world wide web: www.uspto.gov.
- Thorpe T. W. (1999). An Overview of Wave Energy Technologies: Status, Performance and Costs. *Wave Power: Moving towards Commercial Viability*.
- Turnbull M. S., Borthwick A. G. L. and Eatock Taylor R. (2003). Wave-structure interaction using coupled structured-unstructured finite element meshes. *Applied Ocean Research*. 25(2): p. 63-77.
- Ursell F. (1949). On the heaving motion of a circular cylinder on the surface of a fluid *The Quarterly Journal of Mechanics and Applied Mathematics*. 2(2): p. 218-231.
- Ursell F., Dean R. G. and Yu Y. S. (1960). Forced small-amplitude water waves: a comparison of theory and experiment. *Journal of Fluid Mechanics*. 7(01): p. 33-52.
- Valério D., Beirão P. and Sá da Costa J. (2007). Optimisation of wave energy extraction with the Archimedes Wave Swing. *Ocean Engineering*. 34(17-18): p. 2330-2344.
- Vantorre M., Banasiak R. and Verhoeven R. (2004). Modelling of hydraulic performance and wave energy extraction by a point absorber in heave. *Applied Ocean Research*. 26(12): p. 61-72.

- Wang S. (1974). Plunger-Type Wavemakers: Theory And Experiment. *Journal of Hydraulic Research*. 12(3): p. 357-388.
- Wavebob. (2010). *Wavebob*. Retrieved on 10-09-2010, from the world wide web: www.wavebob.ie.
- Weller S. D., Stallard T. J. and Stansby P. K. (2013). Experimental measurements of the complex motion of a suspended axisymmetric floating body in regular and near-focused waves. 39: 137-145.
- Whitham G. B. (1974). *Linear and Nonlinear Waves*: John Wiley & Sons.
- Wu G. X. and Hu Z. Z. (2004). Simulation of nonlinear interactions between waves and floating bodies through a finite-element-based numerical tank. *Proceedings of the Royal Society of London. Series A: Mathematical, Physical and Engineering Sciences*. 460(2050): p. 2797-2817.
- Wu Y.-C. (1991). Waves generated by a plunger-type wavemaker. *Journal of Hydraulic Research*. 29(6): p. 851-860.
- Xu T.-J., Dong G.-H., Zhao Y.-P., Li Y.-C. and Gui F.-K. (2011). Analysis of hydrodynamic behaviors of gravity net cage in irregular waves. *Ocean Engineering*. 38(13): p. 1545-1554.
- Yan H. and Liu Y. (2011). An efficient high-order boundary element method for nonlinear wave-wave and wave-body interactions. *Journal of Computational Physics*. 230(2): p. 402-424.
- Yeung R. W. (1981). Added mass and damping of a vertical cylinder in finite-depth waters. *Applied Ocean Research*. 3(3): p. 119-133.
- Zhao Y.-p., Xu T.-j., Dong G.-h. and Li Y.-c. (2010). Numerical simulation of a submerged gravity cage with the frame anchor system in irregular waves. *Journal of Hydrodynamics, Ser. B*. 22(5, Supplement 1): p. 433-437.
- Zheng Y.-H., Shen Y.-M. and Ng C.-O. (2008). Effective boundary element method for the interaction of oblique waves with long prismatic structures in water of finite depth. *Ocean Engineering*. 35(5-6): p. 494-502.

Appendix A

**Full analytical derivation of the unknown functions
for the wave excitation forces on a truncated vertical
cylinder in water of infinite depth**

In this appendix, a full analytical solution for deriving the unknown functions for the wave excitation forces on a floating truncated vertical cylinder in water of infinite depth is presented. The integral equation determining $q_m(\xi)$ is given by Eqn. (A.22). It should be noted that $B(\xi)$ and $D(\xi, \bar{\xi})$, which are defined in Eqn. (A.23) and Eqn. (A.24), respectively, are known, albeit quite complicated, functions and that the only unknown quantity appearing in Eqn. (A.22) is $q_m(\xi)$. Hence the integral equation, given in Eqn. (A.22), may in principle be solved numerically for $q_m(\xi)$. Once $q_m(\xi)$ has been determined, $q_{m,0}$ and $p_m(\xi)$ follow from Eqn. (A.21) and Eqn. (A.18) and the solution to the scattering problem is complete.

The boundary conditions which are to be satisfied are detailed in Eqn. (3.32)-(3.34). Taking Eqn. (3.18) and Eqn. (3.31) and imposing the condition in Eqn. (3.32) gives:

$$\begin{aligned}
& \sqrt{\frac{2}{\pi}} \int_b^\infty p_m(\xi) \cos \xi(z-b) d\xi \\
&= -\frac{gA}{\omega} \epsilon_m i^{m+1} \{J_m(k_0 a) + q_{m,0}\} e^{-k_0 z} \\
&\quad - \frac{gA}{\omega} \epsilon_m i^{m+1} \sqrt{\frac{2}{\pi}} \int_0^\infty \frac{q_m(\xi)}{\xi^2 + k_0^2} [\xi \cos \xi z \\
&\quad - k_0 \sin \xi z] d\xi
\end{aligned} \tag{A.1}$$

Inverting the Fourier cosine transform gives:

$$\begin{aligned}
p_m(\xi) = & -\frac{gA}{\omega} \epsilon_m i^{m+1} \sqrt{\frac{2}{\pi}} \int_b^\infty \left\{ \{J_m(k_0 a) + q_{m,0}\} e^{-k_0 z} \right. \\
& \left. + \sqrt{\frac{2}{\pi}} \int_0^\infty \frac{q_m(\bar{\xi})}{\bar{\xi}^2 + k_0^2} [\bar{\xi} \cos \bar{\xi} z - k_0 \sin \bar{\xi} z] d\bar{\xi} \right\} \cos \xi(z-b) dz
\end{aligned} \tag{A.2}$$

Next, taking Eqn. (3.18) and Eqn. (3.31) and imposing the conditions in Eqn. (3.33) and Eqn. (3.34) gives:

$$\begin{aligned}
& -\frac{gA}{\omega} \epsilon_m i^{m+1} k_0 \left\{ J_m'(k_0 a) + q_{m,0} \frac{H_m^{(1)'}(k_0 a)}{H_m^{(1)}(k_0 a)} \right\} e^{-k_0 z} \\
& -\frac{gA}{\omega} \epsilon_m i^{m+1} \sqrt{\frac{2}{\pi}} \int_0^\infty \frac{\xi K_m'(\xi a)}{K_m(\xi a)} \frac{q_m(\xi)}{(\mu^2 + k_0^2)} [\xi \cos \xi z - k_0 \sin \xi z] d\xi \quad (A.3) \\
& = R(z)
\end{aligned}$$

where,

$$R(z) = \begin{cases} 0, & \text{if } 0 \leq z \leq b \\ \sqrt{\frac{2}{\pi}} \int_b^\infty p_m(\xi) \frac{\xi I_m'(\xi a)}{I_m(\xi a)} \cos \xi(z-b) d\xi, & \text{if } b \leq z \leq \infty \end{cases} \quad (A.4)$$

Now, applying Havelock's expansion theorem to Eqn. (A.4) and Eqn. (A.5), obtaining:

$$\begin{aligned}
& -\frac{gA}{\omega} \epsilon_m i^{m+1} \frac{\xi K_m'(\xi a)}{K_m(\xi a)} q_m(\xi) \\
& = \frac{2}{\pi} \int_b^\infty \int_0^\infty p_m(\bar{\xi}) \frac{\bar{\xi} I_m'(\bar{\xi} a)}{I_m(\bar{\xi} a)} \cos \bar{\xi}(z-b) d\bar{\xi} [\xi \cos \xi z \\
& - k_0 \sin \xi z] dz \quad (A.5)
\end{aligned}$$

and,

$$\begin{aligned}
& -\frac{gA}{\omega} \epsilon_m i^{m+1} k_0 \left\{ J_m'(k_0 a) + q_{m,0} \frac{H_m^{(1)'}(k_0 a)}{H_m^{(1)}(k_0 a)} \right\} \\
& = 2k_0 \int_b^\infty \sqrt{\frac{2}{\pi}} \int_0^\infty p_m(\xi) \frac{\xi I_m'(\xi a)}{I_m(\xi a)} \cos \xi(z-b) d\xi e^{-k_0 z} dz \quad (A.6)
\end{aligned}$$

In Eqn. (A.2), the following integral may be evaluated:

$$\int_b^\infty e^{-k_0 z} \cos \xi(z-b) dz = \frac{e^{-k_0 b} k_0}{\xi^2 + k_0^2} \quad (A.7)$$

Changing the order of integration in Eqn. (A.2) and defining:

$$\begin{aligned}
\mathcal{L}(\xi, \bar{\xi}) &= \int_b^\infty [\bar{\xi} \cos \bar{\xi} z - k_0 \sin \bar{\xi} z] \cos \xi (z - b) dz \\
&= \frac{\pi}{2} (\delta(\xi - \bar{\xi}) + \delta(\xi + \bar{\xi})) (\bar{\xi} \cos(b\bar{\xi}) \\
&\quad - k_0 \sin(b\bar{\xi})) + \frac{\bar{\xi} (\bar{\xi} \sin(b\bar{\xi}) - k_0 \cos(b\bar{\xi}))}{\xi^2 - \bar{\xi}^2}
\end{aligned} \tag{A.8}$$

obtaining:

$$\begin{aligned}
p_m(\xi) &= -\frac{gA}{\omega} \epsilon_m i^{m+1} \sqrt{\frac{2}{\pi}} \{J_m(k_0 a) + q_{m,0}\} \frac{e^{-k_0 b} k_0}{\xi^2 + k_0^2} \\
&\quad - \frac{gA}{\omega} \epsilon_m i^{m+1} \frac{2}{\pi} \int_0^\infty \frac{q_m(\bar{\xi})}{(\bar{\xi}^2 + k_0^2)} \mathcal{L}(\xi, \bar{\xi}) d\bar{\xi}
\end{aligned} \tag{A.9}$$

Further, Eqn. (A.5) can be similarly written using Eqn. (A.8) as follows:

$$\begin{aligned}
&-\frac{gA}{\omega} \epsilon_m i^{m+1} \frac{\xi K_m'(\xi a)}{K_m(\xi a)} q_m(\xi) \\
&= \frac{2}{\pi} \int_b^\infty p_m(\bar{\xi}) \frac{\bar{\xi} I_m'(\bar{\xi} a)}{I_m(\bar{\xi} a)} \mathcal{L}(\bar{\xi}, \xi) d\bar{\xi}
\end{aligned} \tag{A.10}$$

And, using Eqn. (A.7), Eqn. (A.6) can be written as follows:

$$\begin{aligned}
&-\frac{gA}{\omega} \epsilon_m i^{m+1} k_0 \left\{ J_m'(k_0 a) + q_{m,0} \frac{H_m^{(1)'}(k_0 a)}{H_m^{(1)}(k_0 a)} \right\} \\
&= 2 \sqrt{\frac{2}{\pi}} k_0^2 e^{-k_0 b} \int_b^\infty \frac{\bar{\xi} I_m'(\bar{\xi} a)}{I_m(\bar{\xi} a)} \frac{p_m(\bar{\xi})}{\bar{\xi}^2 + k_0^2} d\bar{\xi}
\end{aligned} \tag{A.11}$$

Then, defining the following functions:

$$S_1(\xi) = -\frac{gA}{\omega} \epsilon_m i^{m+1} \sqrt{\frac{2}{\pi}} \frac{e^{-k_0 b} k_0}{\xi^2 + k_0^2} \tag{A.12}$$

$$S_2(\xi) = -\frac{gA}{\omega} \epsilon_m i^{m+1} \frac{(\xi \cos(b\xi) - k_0 \sin(b\xi))}{\xi^2 + k_0^2} \tag{A.13}$$

$$S_3(\xi, \bar{\xi}) = -\frac{gA}{\omega} \epsilon_m i^{m+1} \frac{2 \bar{\xi}(\bar{\xi} \sin(b\bar{\xi}) - k_0 \cos(b\bar{\xi}))}{\pi (\xi^2 - \bar{\xi}^2)(\bar{\xi}^2 + k_0^2)} \quad (\text{A.14})$$

$$S_4(\xi) = -\frac{\omega}{gA\epsilon_m} i^{-m-1} (\xi \cos(b\xi) - k_0 \sin(b\xi)) \frac{I_m'(\xi a) K_m(\xi a)}{I_m(\xi a) K_m'(\xi a)} \quad (\text{A.15})$$

$$S_5(\xi, \bar{\xi}) = -\frac{\omega}{gA\epsilon_m} i^{-m-1} \frac{2 \bar{\xi} I_m'(\xi a)}{\pi I_m(\xi a)} \frac{\bar{\xi}(\bar{\xi} \sin(b\bar{\xi}) - k_0 \cos(b\bar{\xi}))}{\xi^2 - \bar{\xi}^2} \frac{K_m(\xi a)}{K_m'(\xi a)} \quad (\text{A.16})$$

$$S_6(\bar{\xi}) = 2 \sqrt{\frac{2}{\pi}} k_0^2 e^{-k_0 b} \frac{\bar{\xi} I_m'(\bar{\xi} a)}{I_m(\bar{\xi} a)(\bar{\xi}^2 + k_0^2)} \quad (\text{A.17})$$

Eqn. (A.9) may be rewritten as:

$$p_m(\xi) = S_1(\xi) \{J_m(k_0 a) + q_{m,0}\} + S_2(\xi) q_m(\xi) + \int_0^\infty S_3(\xi, \bar{\xi}) q_m(\bar{\xi}) d\bar{\xi} \quad (\text{A.18})$$

and Eqn. (A.10) takes the form:

$$q_m(\xi) = S_4(\xi) p_m(\xi) + \int_0^\infty S_5(\xi, \bar{\xi}) p_m(\bar{\xi}) d\bar{\xi} \quad (\text{A.19})$$

Finally, Eqn. (A.6) may be written as:

$$-\frac{gA}{\omega} \epsilon_m i^{m+1} k_0 \left\{ J_m'(k_0 a) + q_{m,0} \frac{H_m^{(1)'(k_0 a)}}{H_m^{(1)}(k_0 a)} \right\} = \int_0^\infty S_6(\bar{\xi}) p_m(\bar{\xi}) d\bar{\xi} \quad (\text{A.20})$$

Solving between Eqn. (A.18) and Eqn. (A.20) gives:

$$q_{m,0} = \frac{J_m(k_0 a) \int_0^\infty S_6(\bar{\xi}) S_1(\bar{\xi}) d\bar{\xi} - \frac{gA}{\omega} \epsilon_m i^{m+1} k_0 J_m'(k_0 a) + \int_0^\infty \{S_6(\bar{\xi}) S_2(\bar{\xi}) + \int_0^\infty S_6(\bar{\xi}) S_3(\bar{\xi}) d\bar{\xi}\} q_m(\bar{\xi}) d\bar{\xi}}{-\frac{gA}{\omega} \epsilon_m i^{m+1} k_0 \frac{H_m^{(1)'(k_0 a)}}{H_m^{(1)}(k_0 a)} - \int_0^\infty S_6(\bar{\xi}) S_1(\bar{\xi}) d\bar{\xi}} \quad (\text{A.21})$$

and

$$q_m(\xi) = B(\xi) + \int_0^\infty D(\xi, \bar{\xi}) q_m(\bar{\xi}) d\bar{\xi} \quad (\text{A.22})$$

where

$$B(\xi) = \frac{\left(J_m(k_0 a) + \frac{J_m(k_0 a) \int_0^\infty S_6(\bar{\xi}) S_1(\bar{\xi}) d\bar{\xi} - \frac{gA}{\omega} \epsilon_m i^{m+1} k_0 J_m'(k_0 a)}{-\frac{gA}{\omega} \epsilon_m i^{m+1} k_0 \frac{H_m^{(1)'(k_0 a)}}{H_m^{(1)}(k_0 a)} - \int_0^\infty S_6(\bar{\xi}) S_1(\bar{\xi}) d\bar{\xi}} \right) (S_4(\xi) S_1(\xi) + \int_0^\infty S_5(\xi, \bar{\xi}) S_1(\bar{\xi}) d\bar{\xi})}{1 - S_4(\xi) S_2(\xi)} \quad (\text{A.23})$$

$$D(\xi, \bar{\xi}) = \frac{(S_4(\xi) S_1(\xi) + \int_0^\infty S_5(\xi, \bar{\xi}) S_1(\bar{\xi}) d\bar{\xi}) (S_6(\bar{\xi}) S_2(\bar{\xi}) + \int_0^\infty S_6(\bar{\xi}) S_3(\bar{\xi}, \bar{\xi}) d\bar{\xi})}{\left(-\frac{gA}{\omega} \epsilon_m i^{m+1} k_0 \frac{H_m^{(1)'(k_0 a)}}{H_m^{(1)}(k_0 a)} - \int_0^\infty S_6(\bar{\xi}) S_1(\bar{\xi}) d\bar{\xi} \right) (1 - S_4(\xi) S_2(\xi))} + \frac{S_4(\xi) S_3(\xi, \bar{\xi}) + S_5(\xi, \bar{\xi}) S_2(\xi) + \int_0^\infty S_5(\xi, \bar{\xi}) S_3(\bar{\xi}, \bar{\xi}) d\bar{\xi}}{1 - S_4(\xi) S_2(\xi)} \quad (\text{A.24})$$

Appendix B

MATLAB code for the analytical approximation

In this appendix, the MATLAB code used to generate the plots of the analytical approximation of the wave excitation forces on a floating truncated vertical cylinder in water of infinite depth is presented.

```

clc
clearall
closeall

%%%%%%%%%% define constants %%%%%%%%%%%
g =9.81;           % gravity
rho =1000;        % water density
pi =3.14159;
A = 1.0;          % wave amplitude

%%%%%%%%%% define the buoy geometry %%%%%%%%%%%
a =1.0;           % buoy's radius
b =1.0;           % buoy's draft

symsxz
ct=0;
for k0a=[0 0.0005 0.2 0.3:0.2:2.1]
ct=ct+1;
k=k0a/a;

%%%%%%%%%% Bessel functions %%%%%%%%%%%
J0=besselj(0,k.*a);
J1=besselj(1,k.*a);
dJ0=-besselj(1,k.*a);
dJ1=-0.5*(besselj(0,k.*a)-besselj(2,k.*a));
H0=besselh(0,1,k.*a);
dH0=-besselh(1,1,k.*a);
dH1=-0.5*(besselh(0,1,k.*a)-besselh(2,1,k.*a));

%%%%%%%%%% Surge excitation force calculation %%%%%%%%%%%
r1=-2*pi*1i*rho*g*A*a/k;
r2=J1-(dJ1*besselh(1,1,k.*a))/dH1;
r3=1-exp(-k.*b);

Fle= r1*r2*r3;
absNormFle(ct)=abs(Fle)/(pi*rho*g*A*a*a);

%%%%%%%%%% Heave excitation force calculation %%%%%%%%%%%
ss=(1/((k.^2)+(x.^2)))*(besseli(1,x*a)/(x*besseli(0,x*a)));
s1=(int(ss,x,0,inf));

s2=-g*A*1i*sqrt(2/pi)*(J0-dJ0.*H0./dH0).*k.*exp(-k.*b);

F3e= -2*pi*1i*rho*a*sqrt(2/pi).*s1*s2;

```

```

absNormF3e(ct)=abs(F3e)/(pi*rho*g*A*a*a);

%%%%%%%%%%%%%%%%%%%%%%%%%%%%%%%%%%%%%%%%%%%%%%%%%%%%%%%%%%%%%%%%%%%%%%%%%% Pitch excitation force calculation %%%%%%%%%%%%%%%
t1=-2*pi*li*rho*g*A*a;
t2=(J1-((0.5*J0-
besselj(2,k.*a))*besselh(1,k.*a))/((besselh(1,k.*a)/(k.*a))-
besselh(2,k.*a)));

tt3=(z-b)*exp(-k.*z);
t3=int(tt3,z,0,b);

t4=(-g*A)*(2)*(li^2)*(sqrt(2/pi))*(J1-((0.5*(besselj(0,k.*a)-
besselj(2,k.*a))*besselh(1,k.*a))/((besselh(1,k.*a)/(k.*a))-
besselh(2,k.*a))))*k.*exp(-k.*b));

tt5=(1/((k.^2)+x^2))*((besseli(2,x*a))/(x*besseli(1,x*a)));
t5=(int(tt5,x,0,inf));

F5e=t1*t2*t3+(pi*li*rho*(a^2)*(sqrt(2/pi))*t4*t5);
absNormF5e(ct)=abs(F5e)/(pi*rho*g*A*(a^3));
end

k0a=[0 0.0005 0.2 0.3:0.2:2.1];

fig1=figure;
gridon
plot(k0a,absNormF1e,'-r','LineWidth',1.5)
xlabel('k0a');
ylabel('Normalised Surge Force');
saveas(fig1,'Surge Force.pdf','pdf');

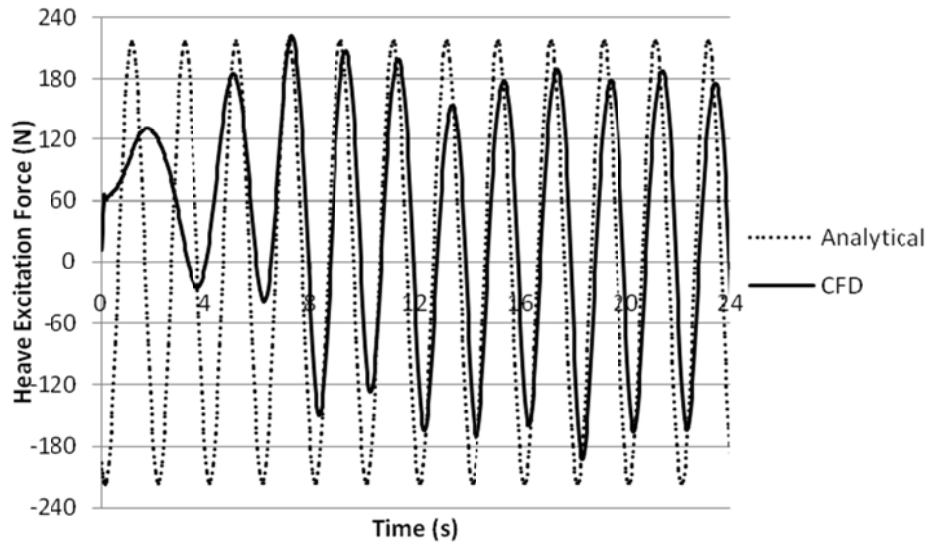
fig2=figure;
gridon
plot(k0a,absNormF3e,'-r','LineWidth',1.5)
xlabel('k0a');
ylabel('Normalised Heave Force');
saveas(fig2,'Heave Force.pdf','pdf');

fig3=figure;
gridon
plot(k0a,absNormF5e,'-r','LineWidth',1.5)
xlabel('k0a');
ylabel('Normalised Torque');
saveas(fig3,'Torque Force.pdf','pdf');

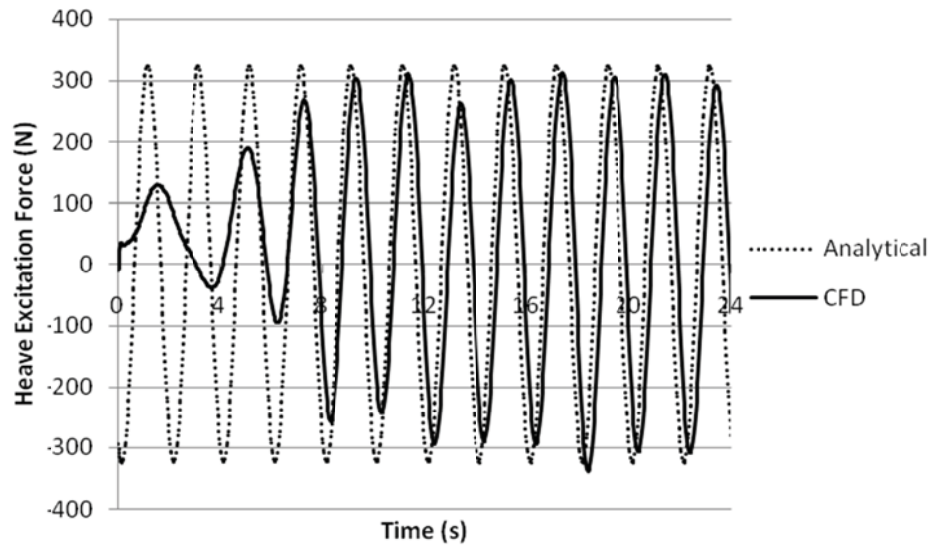
```

Appendix C
**Time-domain comparison between the analytical
approximation and results from the CFD analysis**

In this appendix, the numerical CFD results of the excitation force on fixed cylinder, detailed in Chapter 4, are compared to the analytical approximation, given in Eqn. (3.45). These results are summarised in Figure 4.17.

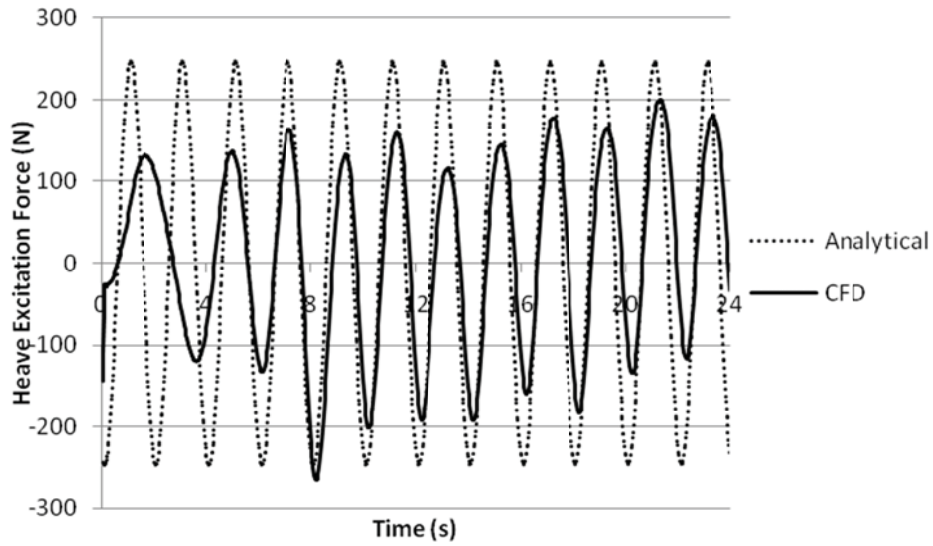


(a)

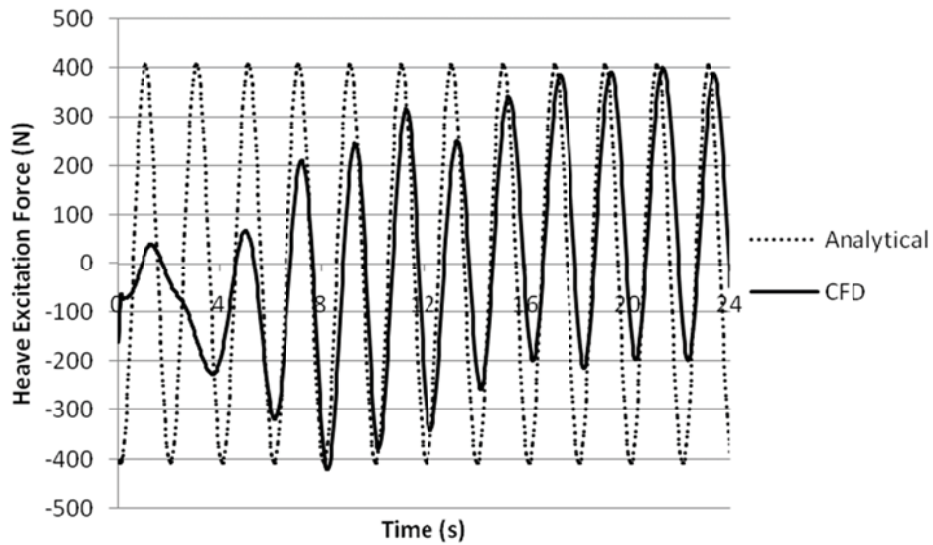


(b)

Figure C.1: Time domain comparison between the heave excitation forces obtained from the analytical and CFD models with $k_0a = 0.8$, where (a): $b = a$ and (b): $b = a/2$.

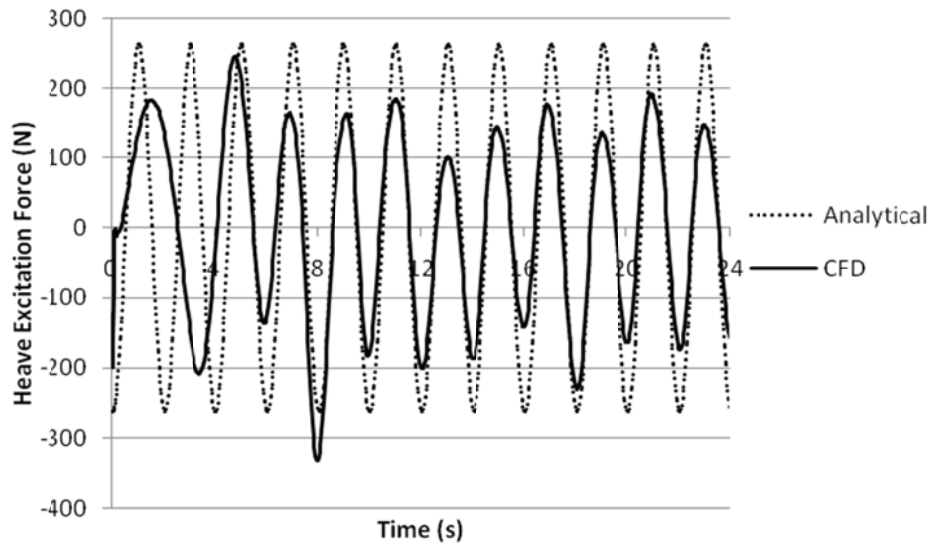


(a)

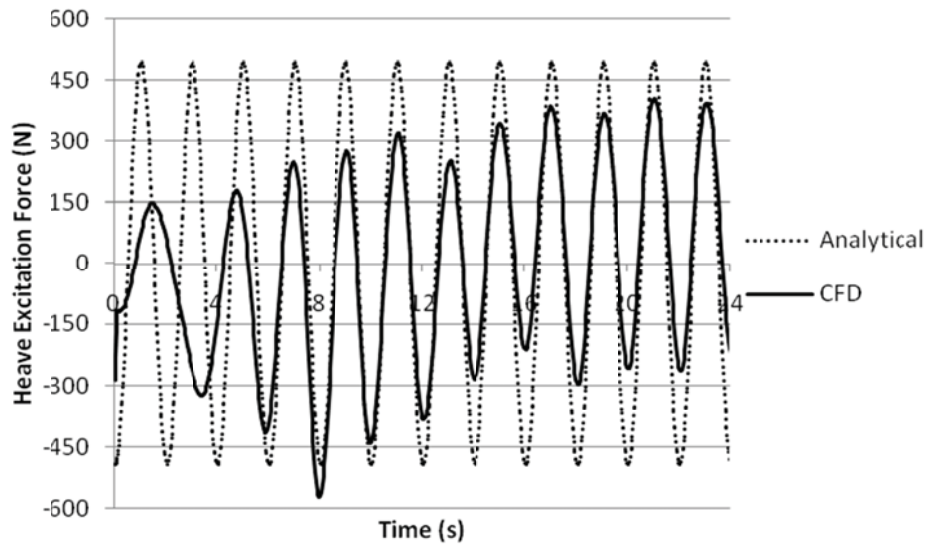


(b)

Figure C.2: Time domain comparison between the heave excitation forces obtained from the analytical and CFD models with $k_0 a = 1$, where (a): $b = a$ and (b): $b = a/2$.

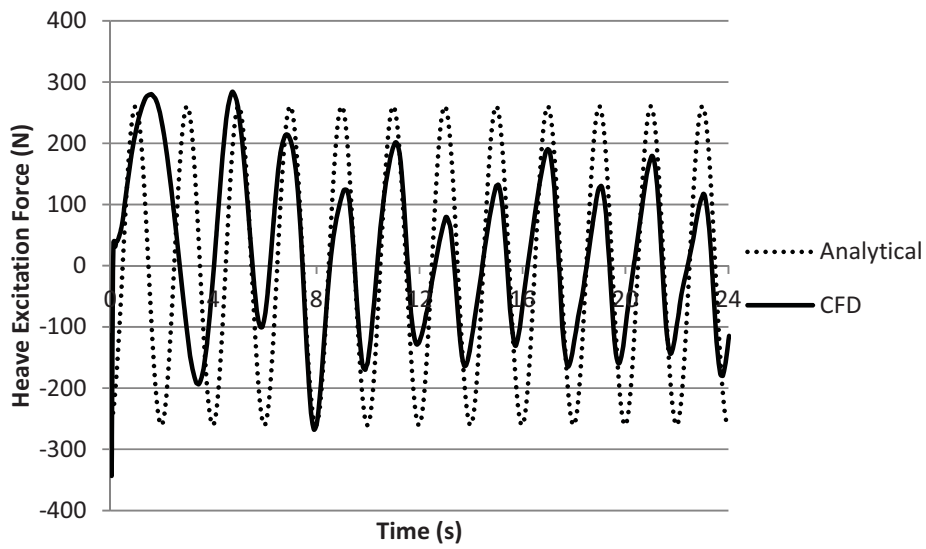


(a)

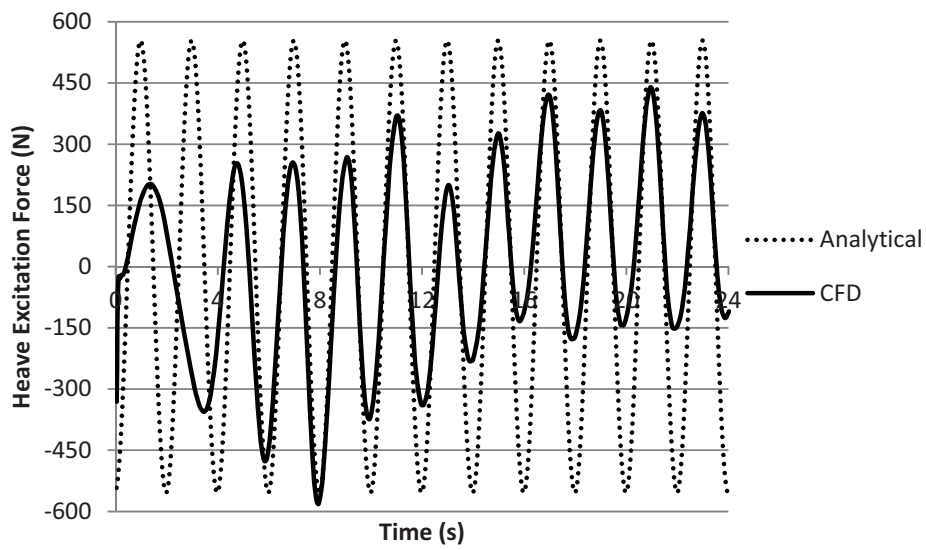


(b)

Figure C.3: Time domain comparison between the heave excitation forces obtained from the analytical and CFD models with $k_0 a = 1.25$, where (a): $b = a$ and (b): $b = a/2$.



(a)

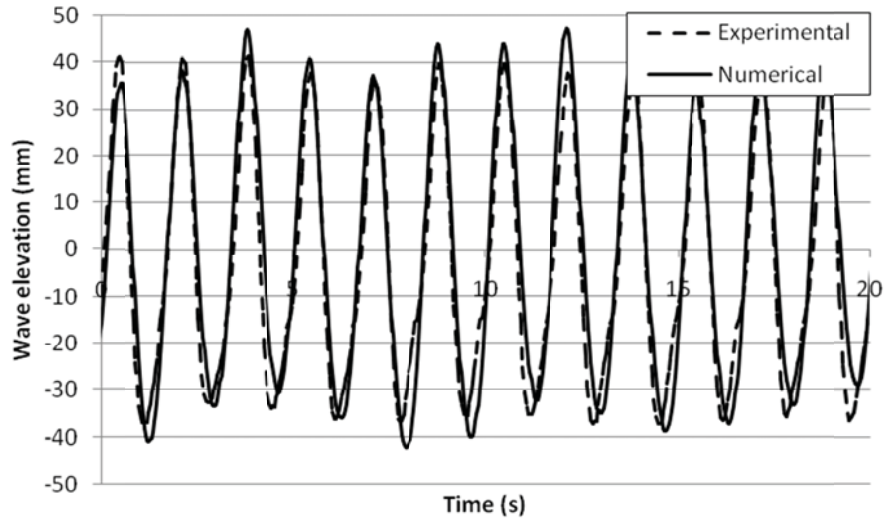


(b)

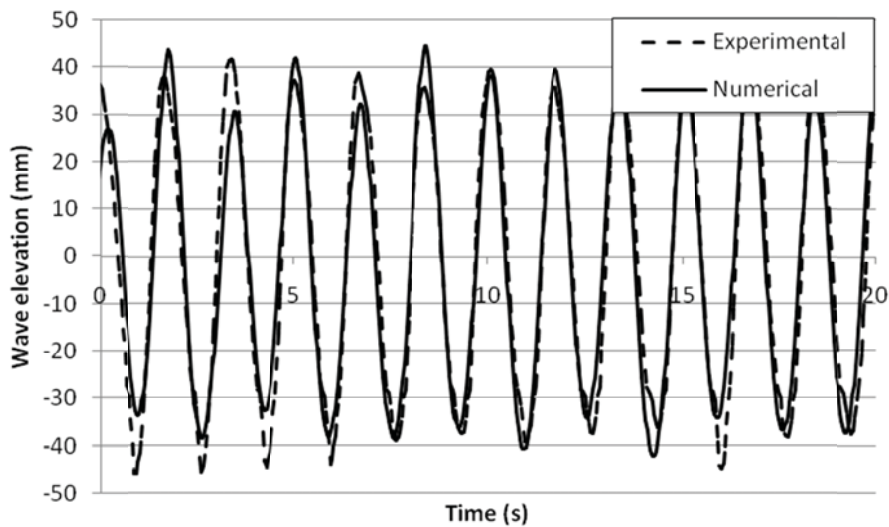
Figure C.4: Time domain comparison between the heave excitation forces obtained from the analytical and CFD models with $k_0a = 1.5$, where (a): $b = a$ and (b): $b = a/2$.

Appendix D
Validation comparison of NWT model and
experimental data

In this appendix, the results of the numerical CFD model, using ANSYS CFX, of the NUI Galway wave flume are compared to experimental data. These results are summarised in Figure 6.6.

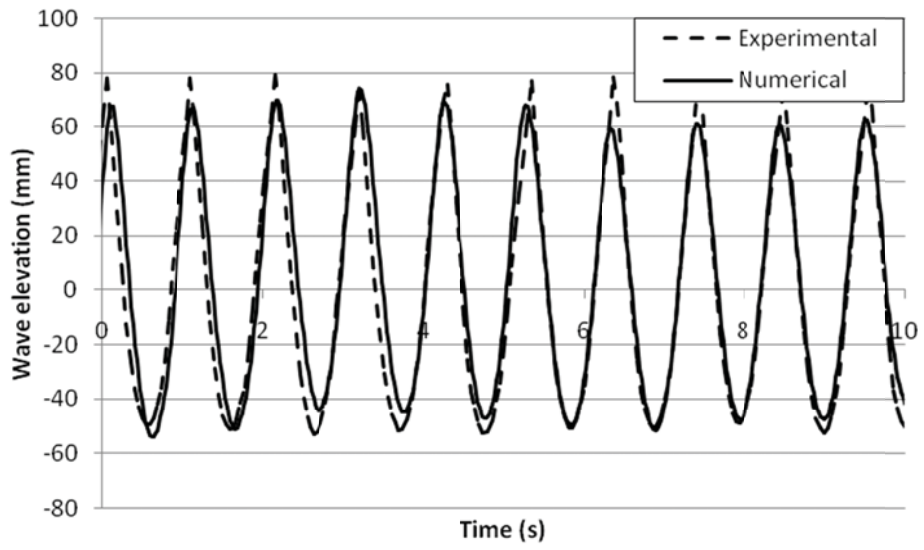


(a)

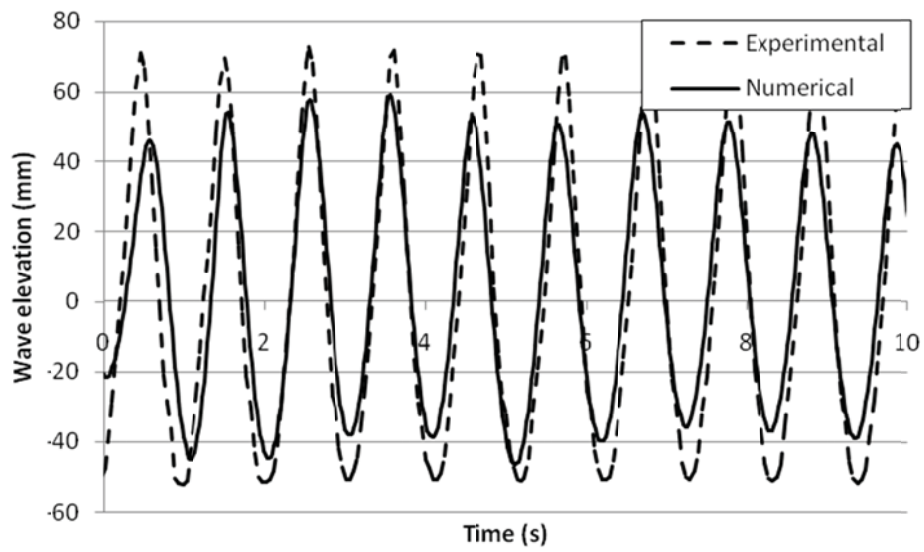


(b)

Figure D.1: Comparison between the output from the NWT model and the experimental output from the NUIG wave flume, for $S = 240\text{mm}$ and $T = 1.6667\text{s}$, at a distance from the wavemaker: (a): 2.35m and (b) 4.75m.

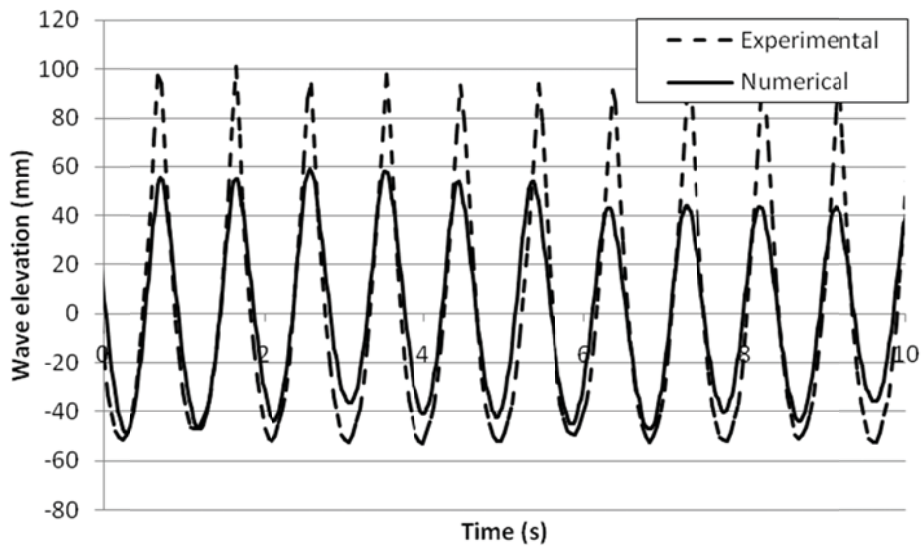


(a)

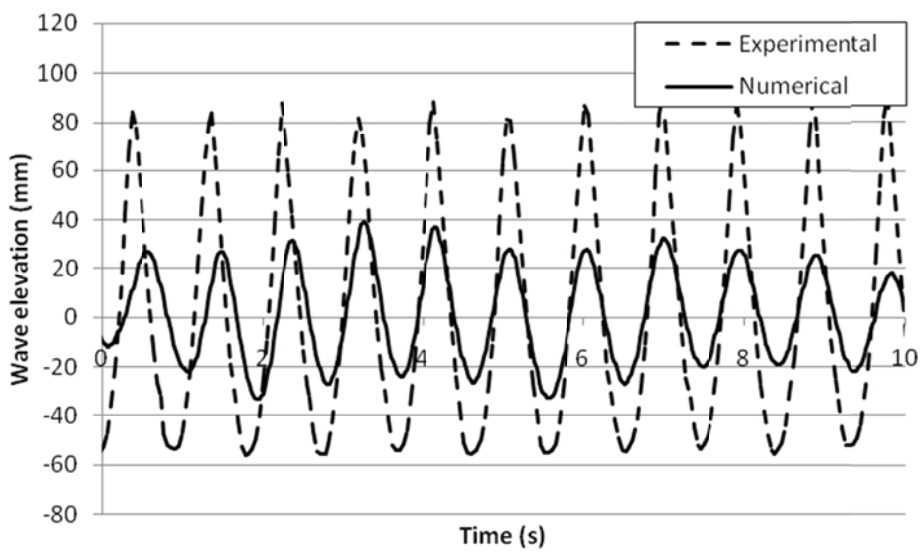


(b)

Figure D.2: Comparison between the output from the NWT model and the experimental output from the NUIG wave flume, for $S = 240\text{mm}$ and $T = 1.05\text{s}$, at a distance from the wavemaker: (a): 2.35m and (b) 4.75m .

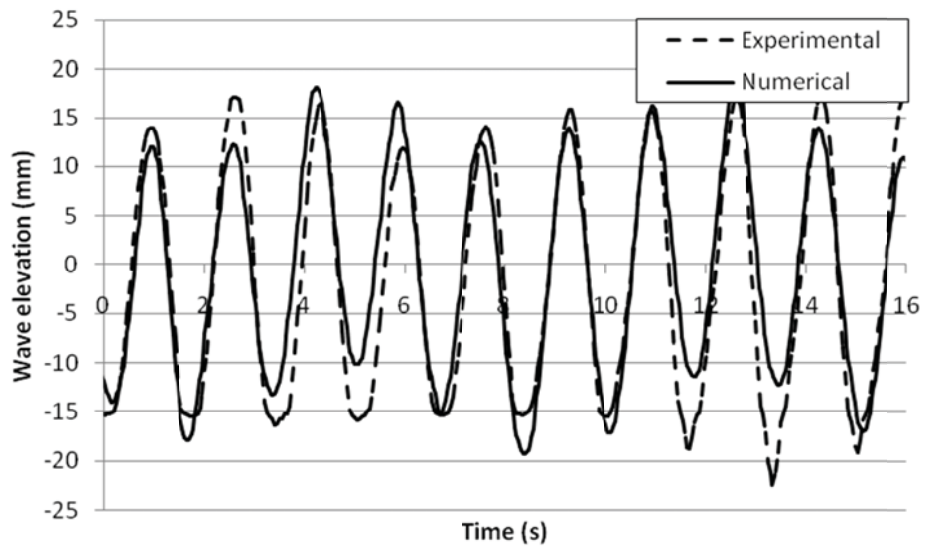


(a)

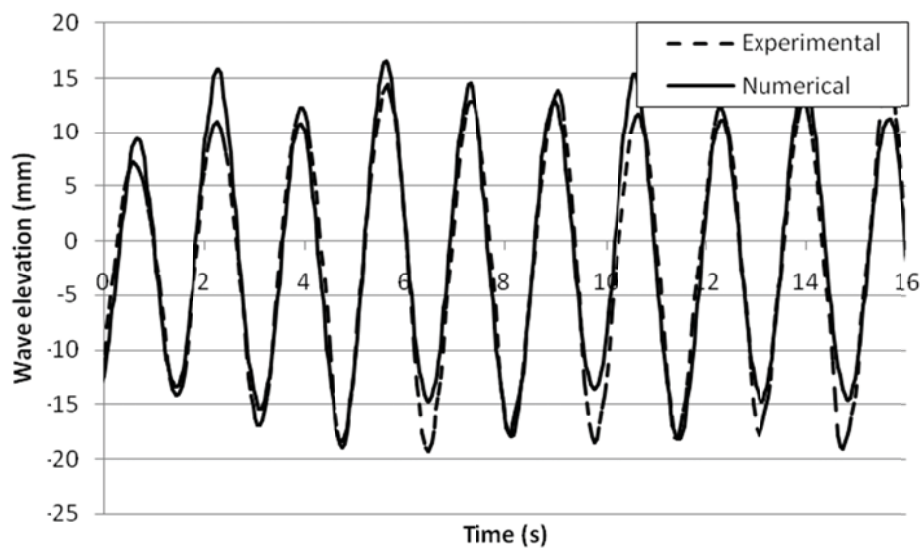


(b)

Figure D.3: Comparison between the output from the NWT model and the experimental output from the NUIG wave flume, for $S = 240\text{mm}$ and $T = 0.9375\text{s}$, at a distance from the wavemaker: (a): 2.35m and (b) 4.75m .

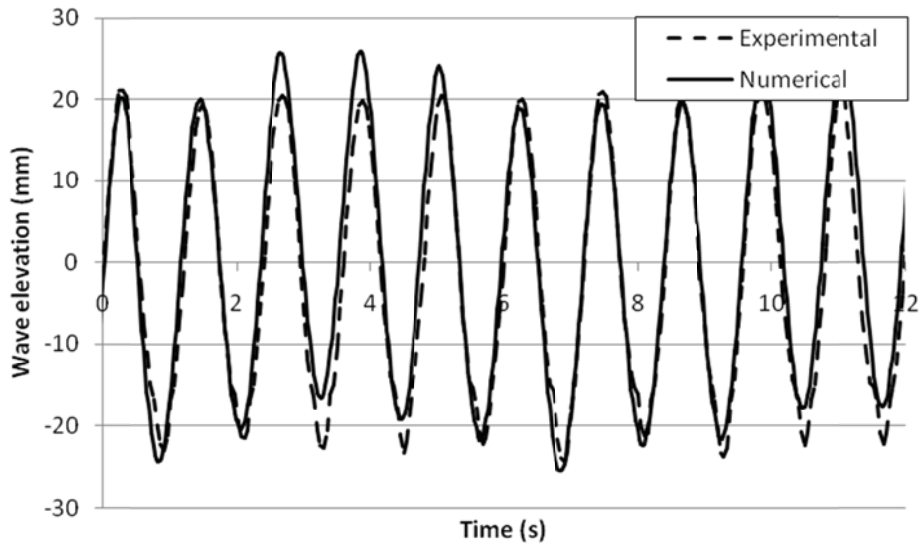


(a)

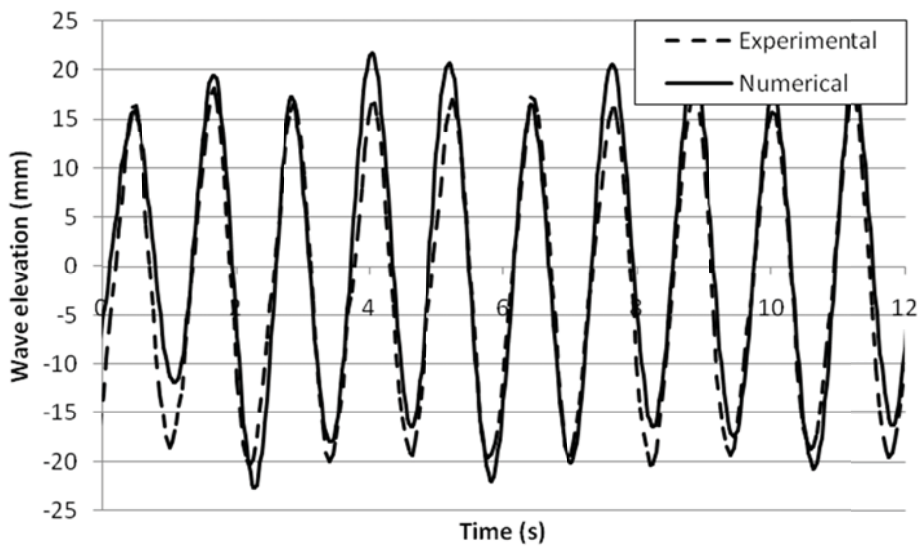


(b)

Figure D.4: Comparison between the output from the NWT model and the experimental output from the NUIG wave flume, for $S = 90\text{mm}$ and $T = 1.6667\text{s}$, at a distance from the wavemaker: (a): 2.35m and (b) 4.75m .

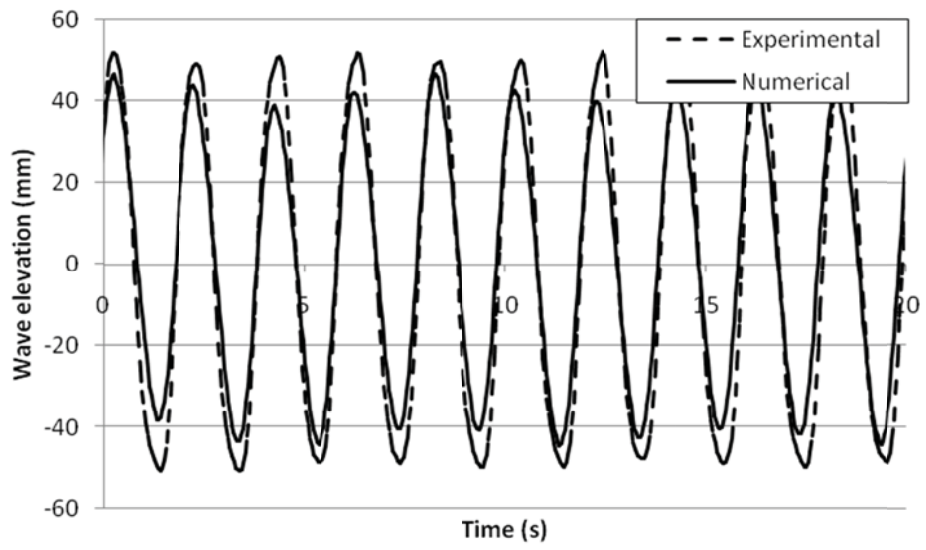


(a)

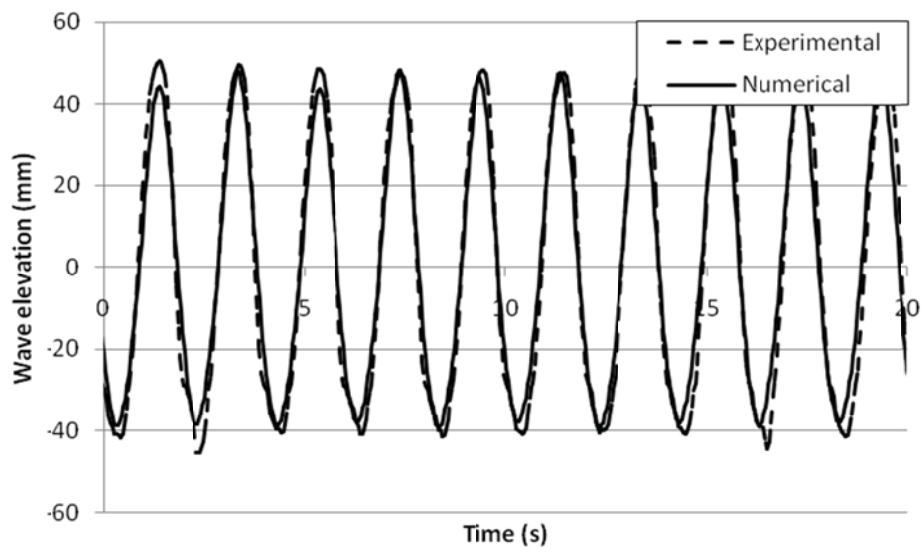


(b)

Figure D.5: Comparison between the output from the NWT model and the experimental output from the NUIG wave flume, for $S = 90\text{mm}$ and $T = 1.2\text{s}$, at a distance from the wavemaker: (a): 2.35m and (b) 4.75m .

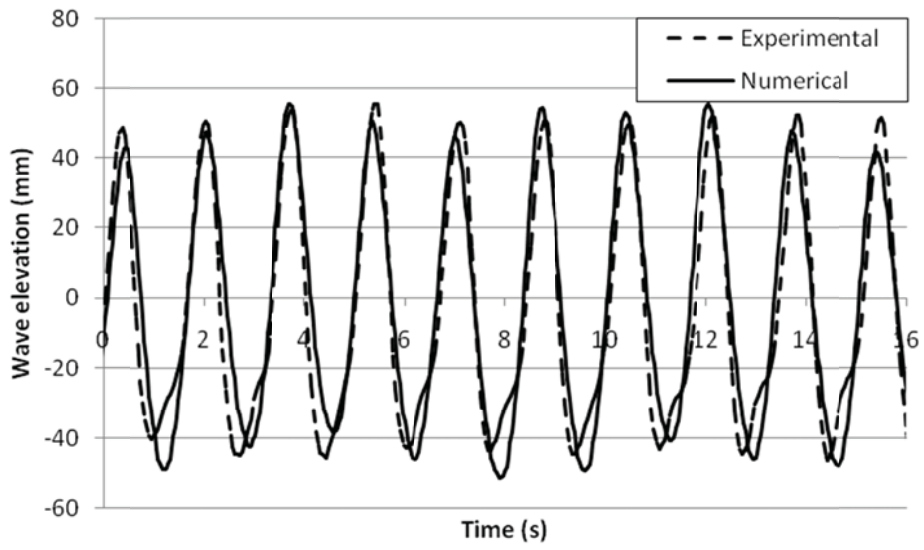


(a)

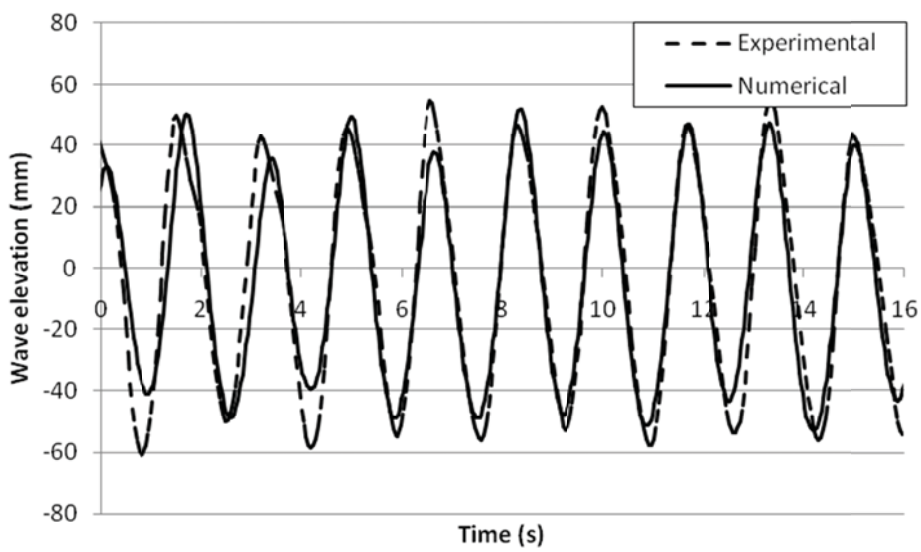


(b)

Figure D.6: Comparison between the output from the NWT model and the experimental output from the NUIG wave flume, for $S = 300\text{mm}$ and $T = 2\text{s}$, at a distance from the wavemaker: (a) 2.35m and (b) 4.75m .

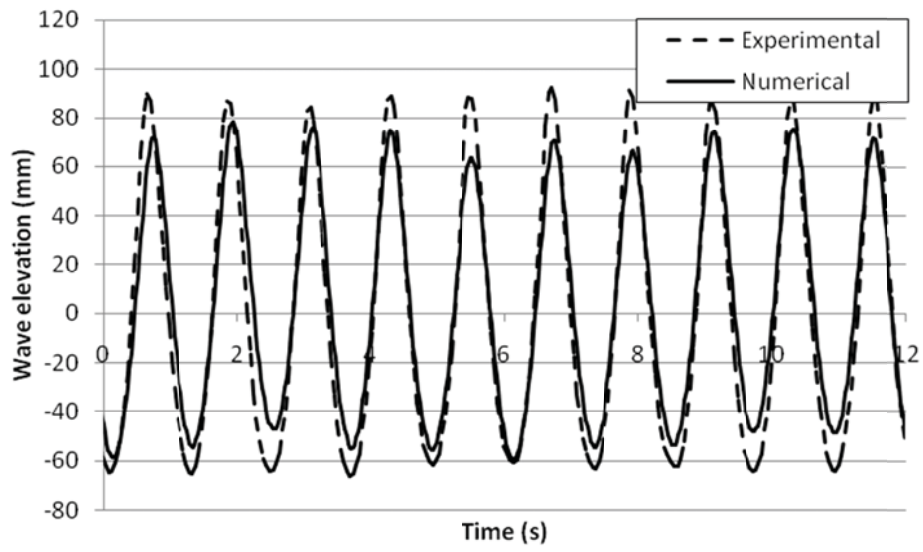


(a)

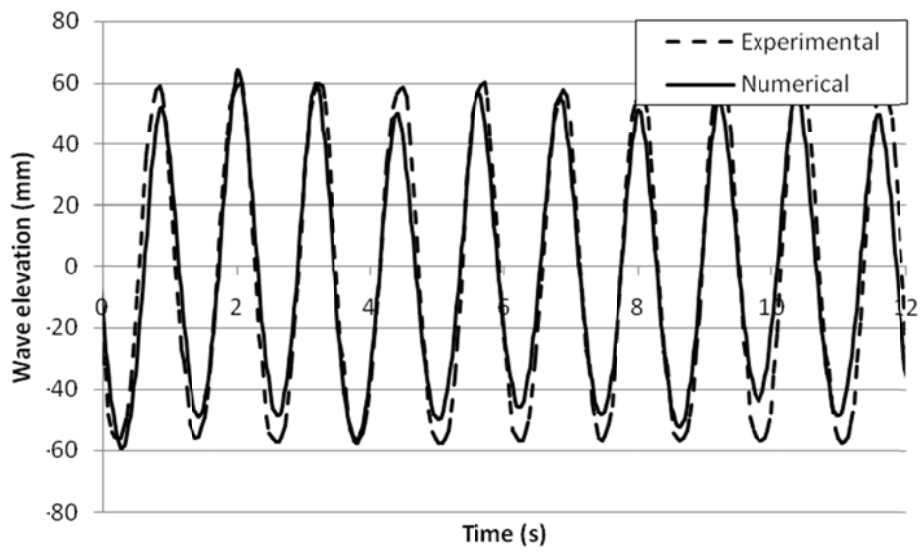


(b)

Figure D.7: Comparison between the output from the NWT model and the experimental output from the NUIG wave flume, for $S = 300\text{mm}$ and $T = 1.6667\text{s}$, at a distance from the wavemaker: (a): 2.35m and (b) 4.75m .

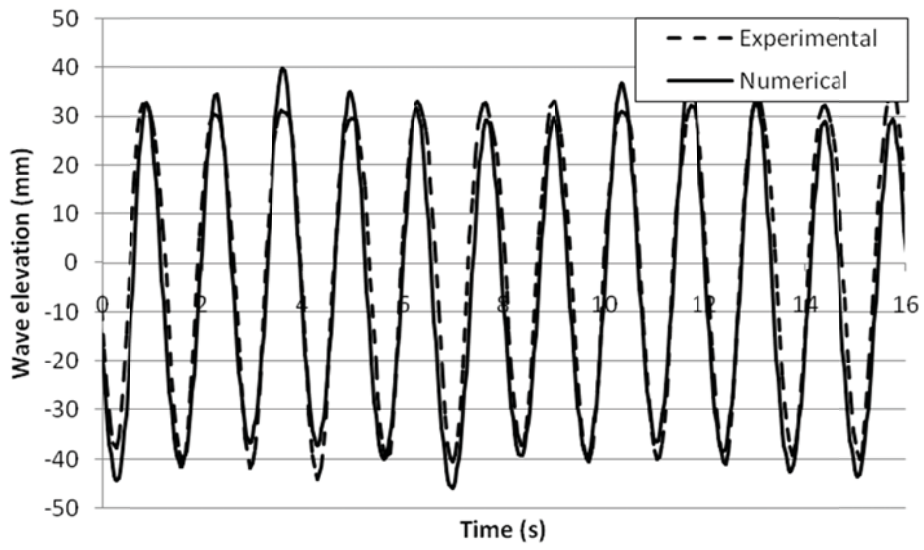


(a)

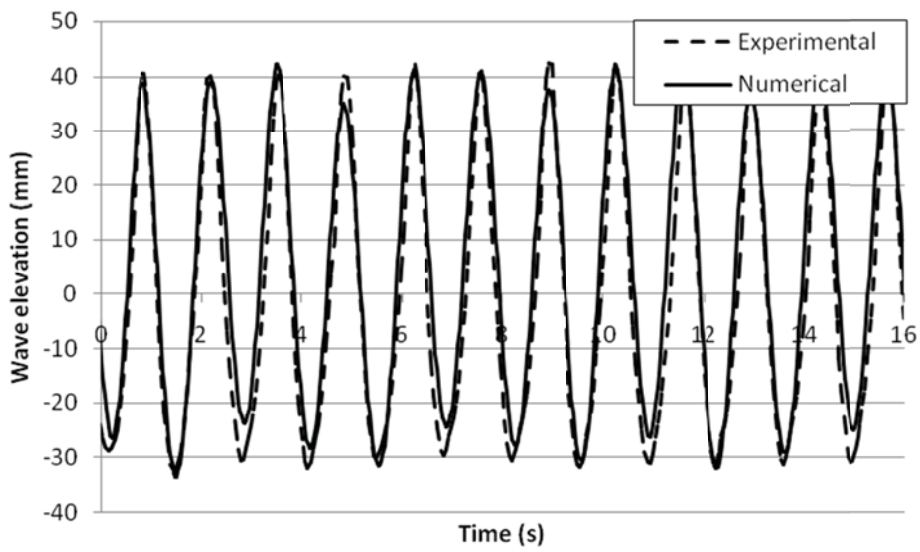


(b)

Figure D.8: Comparison between the output from the NWT model and the experimental output from the NUIG wave flume, for $S = 300\text{mm}$ and $T = 1.2\text{s}$, at a distance from the wavemaker: (a): 2.35m and (b) 4.75m .

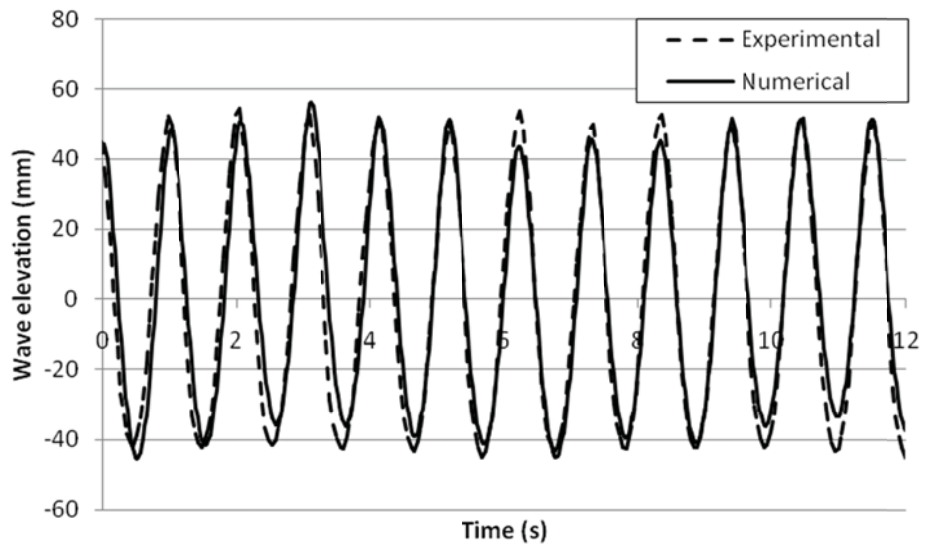


(a)

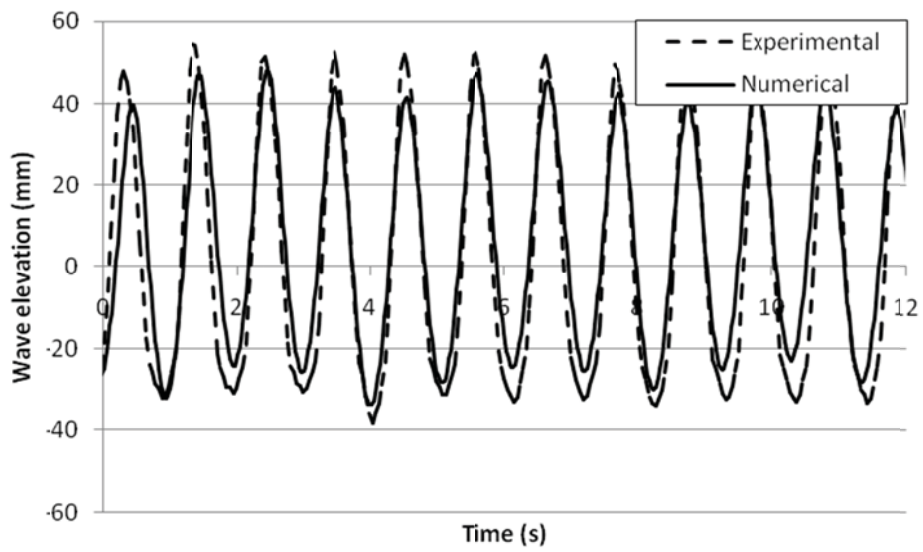


(b)

Figure D.9: Comparison between the output from the NWT model and the experimental output from the NUIG wave flume, for $S = 180\text{mm}$ and $T = 1.35\text{s}$, at a distance from the wavemaker: (a): 2.35m and (b) 4.75m .



(a)



(b)

Figure D.10: Comparison between the output from the NWT model and the experimental output from the NUIG wave flume, for $S = 180\text{mm}$ and $T = 1.05\text{s}$, at a distance from the wavemaker: (a): 2.35m and (b) 4.75m .

Appendix E
Shape optimisation algorithm programme code

Shape optimisation algorithm programme code

In this appendix, the computer programme code for the main function used in the shape optimisation algorithm is presented. The function calculates the response spectrum for each geometric configuration over a range of radii and then calculates the significant force associated with each structure. The computer programme used to perform the analysis is Microsoft Visual Basic 2008 (Microsoft, 2007).

```
Private Function CalculateResponse(ByVal arlRAO As ArrayList) As
    ArrayList

    'Function to calculate the response spectra and significant
    force
    For i As Integer = 0 To 50
        Dim VaryingRadius As New strVaryingRadius
        Dim FrequencyArraySize As Integer = 30
        ReDim VaryingRadius.arrFrequency(FrequencyArraySize)
        ReDim VaryingRadius.arrSpectrum(FrequencyArraySize)
        ReDim VaryingRadius.arrAmplitude(FrequencyArraySize)
        ReDim VaryingRadius.arrResponse(FrequencyArraySize)
        ReDim
        VaryingRadius.arrNormalisedResponse(FrequencyArraySize)
        ReDim VaryingRadius.arrRAOFrequency(arlRAO(0).arrka.length
        - 1)
        VaryingRadius.Radius = 1 + i * 0.5
        'Generate frequency array
        Dim DeltaFrequency As Double = 0.005
        For j As Integer = 0 To FrequencyArraySize
            VaryingRadius.arrFrequency(j) = j * DeltaFrequency
        Next j
        'Generate corresponding RAO frequency array
        For j As Integer = 0 To arlRAO(0).arrka.length - 1
            VaryingRadius.arrRAOFrequency(j) =
            Math.Round(Math.Sqrt(9.81 * arlRAO(0).arrka(j) /
            VaryingRadius.Radius) / (2 * Math.PI), 4)
        Next j
        'Generate corresponding RAO array
        VaryingRadius.arrNormalisedResponse(0) = 1
        For j As Integer = 1 To VaryingRadius.arrFrequency.Length-1
            For k As Integer = 0 To
                VaryingRadius.arrRAOFrequency.Length - 1
                Select Case VaryingRadius.arrFrequency(j) =
                    VaryingRadius.arrRAOFrequency(k)
                Case True
                    VaryingRadius.arrNormalisedResponse(j) =
                    arlRAO(0).arrNormalisedResponse(k)
                    Exit For
                Case False
                    Select Case VaryingRadius.arrFrequency(j) <
                    VaryingRadius.arrRAOFrequency(k)
                    Case True
```

```

        Select Case
        VaryingRadius.arrFrequency(j) >
        VaryingRadius.arrRAOFrequency(k-1)
            Case True
                VaryingRadius.arrNormalisedResponse(j) =
                arlRAO(0).arrNormalisedResponse(k - 1) +
                (VaryingRadius.arrFrequency(j) -
                VaryingRadius.arrRAOFrequency(k - 1)) *
                (arlRAO(0).arrNormalisedResponse(k) -
                arlRAO(0).arrNormalisedResponse(k - 1)) /
                (VaryingRadius.arrRAOFrequency(k) -
                (VaryingRadius.arrRAOFrequency(k - 1)))
            Exit For
        End Select
        Case False
            Select Case k =
            VaryingRadius.arrRAOFrequency.Length - 1
                Case True
                    VaryingRadius.arrNormalisedResponse(j)=0
                Exit For
            End Select
        End Select
    End Select
Next k
Next j
'Generate corresponding Spectrum array
For j As Integer = 0 To VaryingRadius.arrFrequency.Length-1
    For k As Integer = 0 To arlWaveSpectrum.Count-1
        Select Case VaryingRadius.arrFrequency(j) =
            Math.Round(arlWaveSpectrum(k).Frequency, 3)
            Case True
                VaryingRadius.arrSpectrum(j) =
                arlWaveSpectrum(k).spectrum
            Exit For
            Case Else
                VaryingRadius.arrSpectrum(j) = 0
        End Select
    Next k
Next j
'Generate corresponding Amplitude array
For j As Integer = 0 To VaryingRadius.arrSpectrum.Length-1
    VaryingRadius.arrAmplitude(j) = Math.Sqrt(2 *
    VaryingRadius.arrSpectrum(j) * DeltaFrequency)
Next j
'Generate corresponding Response array
For j As Integer = 0 To VaryingRadius.arrAmplitude.Length-1
    'A restriction on the RAO is imposed
    Dim Restriction As Double = 300
    Select Case VaryingRadius.arrNormalisedResponse(j) >
        Restriction
        Case True
            VaryingRadius.arrResponse(j) =
            VaryingRadius.arrAmplitude(j) * Restriction
        Case False
            VaryingRadius.arrResponse(j) =

```

```

        VaryingRadius.arrAmplitude(j) *
        VaryingRadius.arrNormalisedResponse(j)
    End Select
Next j
'Calculate the Significant Force of the Response
Dim Area As Double = 0
For j As Integer = 0 To VaryingRadius.arrResponse.Length-1
    Area = Area + VaryingRadius.arrResponse(j) *
    DeltaFrequency
Next j
VaryingRadius.SigForce = 4 * Math.Sqrt(Area)
arlRAO.Add(VaryingRadius)
Next i

'Print output to console window
For i As Integer = 0 To arlRAO(1).arrFrequency.length - 1
    Console.WriteLine(arlRAO(1).arrResponse(i))
Next i
For i As Integer = 1 To arlRAO.Count - 1
    Console.WriteLine(arlRAO(i).Radius & Chr(9) &
arlRAO(i).SigForce)
Next i

Return arlRAO

```

```
End Function
```